

SAPIENZA
UNIVERSITÀ DI ROMA

SAPIENZA UNIVERSITÀ DI ROMA

DIPARTIMENTO DI SCIENZE DELLA TERRA

SCUOLA DI DOTTORATO IN SCIENZE DELLA TERRA

CICLO XXIX

STRUCTURE, FLUID FLOW, AND MECHANICAL PROPERTIES OF CARBONATE/CLAY-HOSTED SEISMOGENIC FAULTS: CASE STUDIES FROM THE CENTRAL APENNINES, ITALY

Supervisore: *Prof. Eugenio Carminati*

Cotutore: *Dr. Andrea Billi*

Dottorando: *Luca Smeraglia*

2016

Table of contents

Introduction **I**

Chapter 1. Phyllosilicate injection along extensional carbonate-hosted faults and implications for co-seismic slip propagation: case studies from the central Apennines, Italy **1**

1. Introduction 2
2. Geological framework 4
2.1 Central Apennines: evolution and seismotectonic setting 4
2.2 Geological setting of the Pietrasecca area 6
3. Methods 10
4. Terminology 11
5. Pietrasecca fault 1 (PSF1) 12
5.1 Structural setting 12
5.2 Hangingwall damage zone (D1) 12
5.3 Footwall damage zone (D2) 14
5.4 Fault core (FC) 16
5.5 Phyllosilicate-rich layer 17
5.5.1 Mineralogical and microstructural observations 17
5.5.2 Clast size distribution analyses 22
6. Pietrasecca fault 2 (PSF2) 23
7. Mineral composition of siliciclastic sandstones and hemipelagic marls 27
8. Further instances of phyllosilicate occurrence along extensional faults 27
8.1 Fiamignano Fault 28
8.2 Val Roveto Fault 29
8.3 Tre Monti Fault 29
9. Discussion 31
9.1 PSF1 and PSF2 activity and exhumation depth 31
9.2 Origin of phyllosilicate-rich material 32
9.3 Model for clay injection and smearing within carbonate fault zone 35
9.4 Deformation mechanisms within the phyllosilicate-rich layer (PSF1) 37
9.5 Implications for seismic-slip propagation 38
10. Conclusions 40
11. References 41

Chapter 2. Origin and role of fluids involved in the seismic cycle of extensional faults in carbonate rocks **49**

1. Introduction 50
2. Geological setting 52
2.1 Apennines evolution and seismotectonic setting 52
2.2 The Tre Monti Fault 55
3. Methods 56
4. Structural and cathodoluminescence data 57
4.1 Fault zone setting and general architecture 57
4.2 Principal fault (D1) 59
4.3 Damage zone (D2) 64
4.4 Secondary fault zone (D3) 66
5. Stable isotope data and whole rock geochemistry 67
5.1 Sampling strategy 67
5.2 Results 67
6. Discussion 69
6.1 Fluid sources 69
6.2 Spatio-temporal evolution of fault zone architecture and fluid flow 72
6.3 Fluid involvement in the seismic cycle 75
7. Conclusions 77
8. References 78
9. Supplementary Material 82

Chapter 3. Ultra-thin clay layers facilitate seismic slip in carbonate faults **86**

1. Introduction 87
2. Methods 89
2.1 Description of starting materials 89
2.2 Description of XRD analyses performed on natural rocks 90
2.3 Description of experimental rotary shear apparatus and gouge holder 90
2.4 Description of experimental conditions 91
3. Results 92
3.1 Natural fault zone structure 92
3.2 Laboratory experiments and comparison with natural fault products 95
4. Discussion and conclusions 100
5. References 101
6. Supplementary Material 104

Chapter 4. Seismic cycles in carbonate/clay-hosted faults **113**

1. Introduction 114
2. Geological setting 115
3. Methods 118
4. Field- to nano-scale observations on the Tre Monti principal fault 119
5. In situ elastic properties micromeasurements 124
6. Low to high velocity friction experiments 128
6.1 Experimental procedure 128
6.2 Results 130
6.3 Experimental microstructures 134
7. Discussion 136
7.1 Rationale 136
7.2 Synthetic model of seismic cycles 136
7.3 Implications 141
8. Conclusions 143
9. References 144
10. Supplementary Material 147

General conclusions and future perspectives **156**

Introduction

In many seismically active countries (e.g., Italy, Greece, Turkey, China, USA) moderate to large earthquakes nucleate in and propagate through heterogeneous (i.e., consisting of carbonate, marly, and clayey deposits) sedimentary successions within the brittle upper crust (< 5 km depth), often causing surface displacement with associated damages and casualities. In particular, in the central Apennines of Italy, moderate earthquakes (< M_w 7.0) propagate through the heterogeneous carbonatic-clayey sedimentary cover up to the Earth's surface, possibly causing surface faulting (e.g., 1915, M_w 7.0, Avezzano Earthquake; 2009, M_w 6.3, L'Aquila Earthquake; Figs. 1a and 1b). For instance, the mainshock of the recent M_w 6.0 Amatrice earthquake of August 24th, 2016, nucleated at ~7-8 km depth and the seismic slip propagated upward through carbonate rocks causing a ~6 km long surface rupture and deformation.

Indirect studies (i.e., through seismological, geophysical, and geodetic techniques) lack of sufficient spatio-temporal resolution to constrain the detailed three-dimensional fault-zone architecture, the deformation mechanisms, and the seismic-related fluid circulation within seismogenic faults at depth. The study of exposed fault zones exhumed from shallow depth (i.e., depths < 3 km) can narrow this knowledge gap and can help in understanding how the shallow fault zone structure can promote or inhibit seismic slip propagation up to the Earth's surface. For these reasons, in this thesis, I used a multidisciplinary approach to study exposed carbonate/clay-hosted active faults, which can be reliable analogues of buried seismogenic faults at depth, in the seismogenic domain of the central Apennines, Italy (Fig. 1a). In particular, I combined fieldwork (geological mapping and structural analysis) with laboratory studies. I used optical microscopy and FESEM (Field Emission Scanning Electron Microscopy) to study fault rock microstructures from micro- to nanoscale. I used stable isotope analyses on calcite veins/cement, whole rock geochemistry, cathodoluminescence, and X-ray powder diffraction to study the origin and paleotemperatures of geofluids, which circulated in the fault zones, and fault rock mineralogy. I used low to high velocity friction experiments (using the Slow to High Velocity Apparatus, SHIVA,

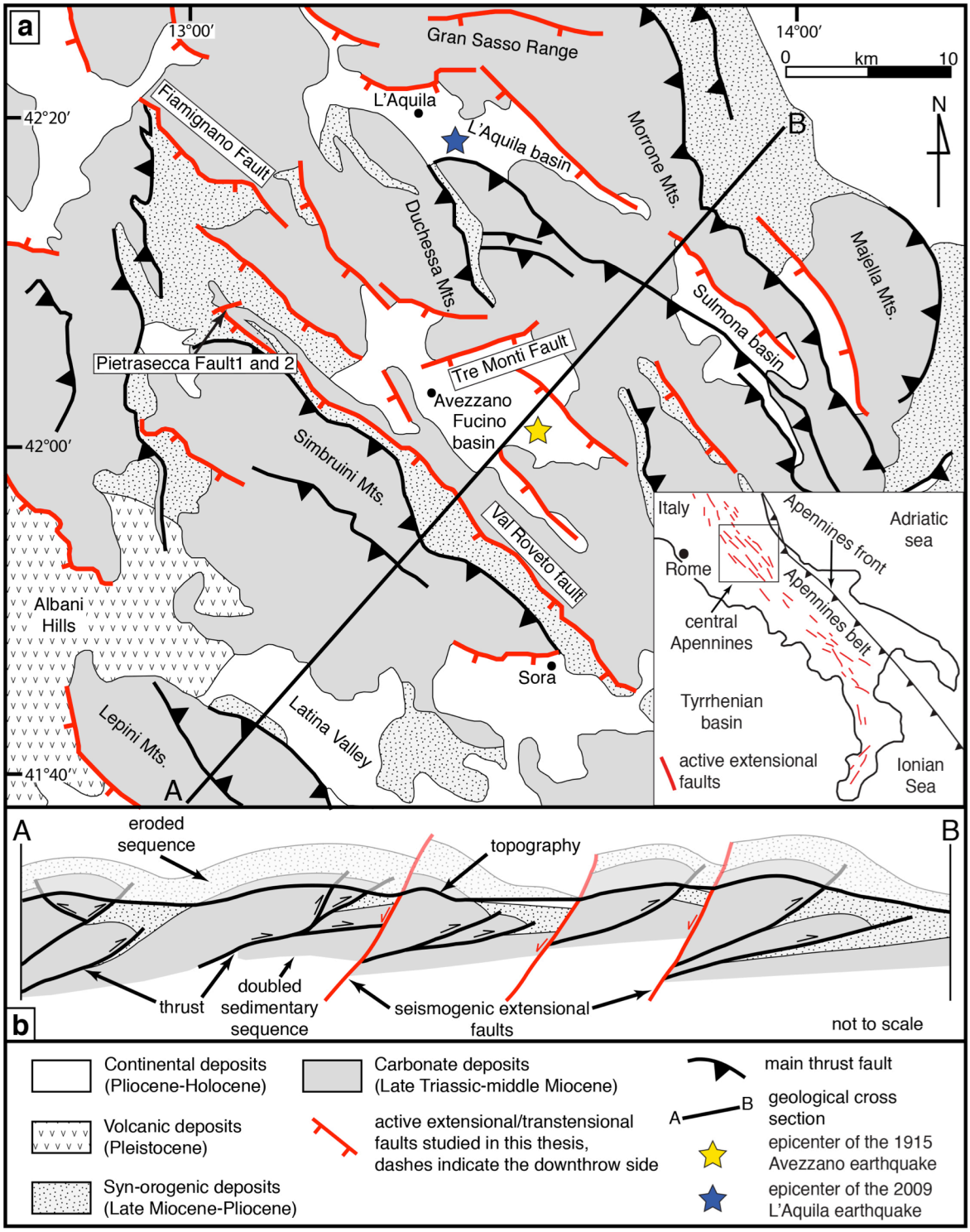


Figure 1. (a) Simplified geological map of the central Apennines (Italy) showing main thrusts, active extensional faults, and location of the studied faults in this thesis. **(b)** Schematic geological cross section across the central Apennines showing extensional seismogenic faults cutting through a carbonate-clayey sedimentary succession. Cross-section trace is shown in (a).

at INGV in Rome) to understand fault rock frictional properties during earthquake propagation and in situ mechanical analyses using Atomic Force Microscopy to understand fault rocks elastic properties (Young's modulus and viscoelasticity) down to nanoscale. In particular, the main focus

of this thesis is to understand the roles both of fluids and phyllosilicates during the seismic cycle within carbonate-hosted faults in the shallow carbonate-dominated brittle crust. The thesis is divided into four chapters, which are described as follows.

In Chapter 1, "*Phyllosilicate injection along extensional carbonate-hosted faults and implications for co-seismic slip propagation: case studies from the central Apennines, Italy*", I described fault-zone architecture and deformation mechanisms of five carbonate/clay-hosted extensional faults (i.e., the Pietrasecca 1 and 2 Faults, the Tre Monti Fault, the Fiamignano Fault, and the Val Roveto Fault; Fig. 1a). In particular, I focused on Pietrasecca 1 and 2 Faults within which I documented clay-rich layers occurring along carbonate-hosted fault planes. Eventually, I developed a conceptual model for clay injection and smearing along faults cutting through carbonate-dominated sedimentary successions. This work has been done in collaboration with L. Aldega (Sapienza University of Rome, Italy), A. Billi (CNR, National Research Council, Rome, Italy), E. Carminati (Sapienza University of Rome, Italy), and C. Doglioni (Sapienza University of Rome and INGV, National Institute of Geophysics and Volcanology, Rome, Italy) and is accepted for publication on *Journal of Structural Geology*.

In Chapter 2, "*Origin and role of fluids involved in the seismic cycle of extensional faults in carbonate rocks*", I focused on the Tre Monti Fault (Fig. 1a) and described fault-zone architecture, deformation mechanisms, and seismic-related fluid circulation (using stable isotope analyses and cathodoluminescence) within carbonate/clay-hosted faults. In this work I propose a general model for seismic-related fluid circulation within seismically active faults during fault exhumation from 3 to ≤ 1 km depths and concurrent fluid cooling from ~68 to <30◦C. This work has been done in collaboration with F. Berra (University of Milan, Italy), C. Boschi (CNR-IGG, National Research Council Institute of Geosciences and Georesources, Pisa, Italy), A. Billi (CNR, National Research Council, Rome, Italy), E. Carminati (Sapienza University of Rome, Italy), E. Carminati (Sapienza University of Rome, Italy), and C. Doglioni (Sapienza University of Rome and INGV, National

Institute of Geophysics and Volcanology, Rome, Italy) and is published on *Earth and Planetary Science Letters 450, 292-305, doi:10.1016/j.epsl.2016.06.042*.

In Chapter 3, *"Ultra-thin clay layers facilitate seismic slip in carbonate faults"*, I focused on ultra-thin phyllosilicate-bearing (5 wt.% of clay content) layers discovered along the Tre Monti principal fault. I performed high-velocity (i.e., at co-seismic slip rates) friction experiments using SHIVA (Slow to High Velocity Apparatus, SHIVA, at INGV in Rome) to study frictional behaviors of ultra-thin phyllosilicate-bearing layers, simulating the natural setting observed along the Tre Monti principal fault. I concluded that ultra-low (< 3 wt.%) clay content localized along micrometer-thick layers within pure calcite gouges can facilitate upward earthquake-slip propagation, possibly enhancing surface faulting and displacement. This work has been done in collaboration with A. Billi (CNR, National Research Council, Rome, Italy), E. Carminati (Sapienza University of Rome, Italy), E. Carminati (Sapienza University of Rome, Italy), G. Di Toro (Manchester University, UK, and INGV, Rome), E. Spagnuolo (INGV, Rome), A. Cavallo (CERTEM, multidisciplinary laboratory, Grosseto, Italy), and F. Zorzi (University of Padova) and is currently under review on *Scientific Reports*.

In Chapter 4, *"Fingerprints of seismic cycles in natural and laboratory carbonate/clay-hosted faults"*, I focused our study on micro to nanoscale deformation mechanisms along the Tre Monti principal fault. In addition, I performed in situ mechanical analyses (Young's modulus and viscoelasticity) of clay and calcite clasts along the Tre Monti principal fault using Atomic Force Microscopy (at CNIS Research Center for Nanotechnology applied to Engineering, Sapienza University of Rome, Italy). I integrated these new data with previous results from high-velocity friction experiments (in Chapter 3) to propose a model for deformation mechanisms acting during seismic cycles within carbonate/clay-hosted faults and to explain several seismological observations documented during seismic sequences. In addition, I empathized the use of direct and in situ studies of fault rock friction and mechanical properties as fundamental instruments to obtain natural parameters to be used for future seismic cycles modeling. This work has been done in collaboration

with A. Billi (CNR, National Research Council, Rome, Italy), E. Carminati (Sapienza University of Rome, Italy), E. Carminati (Sapienza University of Rome, Italy), G. Di Toro (Manchester University, UK, and INGV, Rome), E. Spagnuolo (INGV, Rome), A. Cavallo (CERTEMA, multidisciplinary laboratory, Grosseto, Italy), M. Rossi (Dipartimento di scienze di base e applicate, Sapienza University of Rome, Italy and CNIS, Research Center for Nanotechnology applied to Engineering, Sapienza University of Rome, Italy), D. Passeri (Dipartimento di scienze di base e applicate, Sapienza University of Rome, Italy), M. Natali (Dipartimento di scienze di base e applicate, Sapienza University of Rome, Italy), and A. Bettucci (Dipartimento di scienze di base e applicate, Sapienza University of Rome, Italy) and is currently under review on *Journal of Geophysical Research*.

Chapter 1. Phyllosilicate injection along extensional carbonate-hosted faults and implications for co-seismic slip propagation: case studies from the central Apennines, Italy

Abstract

We document phyllosilicates occurrence along five shallow (exhumed from depths < 3 km) carbonate-hosted extensional faults from the seismically-active domain of the central Apennines, Italy. The shallow portion of this domain is characterized by a sedimentary succession consisting of ~5-6 km thick massive carbonate deposits overlain by ~2 km thick phyllosilicate-rich deposits (marls and siliciclastic sandstones). We show that the phyllosilicates observed within the studied carbonate-hosted faults derived from the overlying phyllosilicate-rich sedimentary deposits and were involved in the faulting processes. We infer that, during fault zone evolution, the phyllosilicates downward injected into pull-aparts (i.e., dilational jogs) that were generated along staircase extensional faults. With further displacement accumulation, the clayey material was smeared and concentrated into localized layers along the carbonate-hosted fault surfaces. These layers are usually thin (a few centimeters to decimeters thick), but can reach also a few meters in thickness. We suggest that, even in tectonic settings dominated by high frictional strength rocks (e.g., carbonates), localized layers enriched in weak phyllosilicates can occur along shallow fault surfaces thus reducing the expected fault strength during earthquakes, possibly promoting co-seismic slip propagation up to the Earth's surface.

This study was performed in collaboration with L. Aldega, A. Billi, E. Carminati, and C. Doglioni. This chapter is in press on Journal of Structural Geology as the following paper: Smeraglia, L., Aldega, L., Billi, A., Carminati, E., Doglioni C. Phyllosilicate injection along carbonate-hosted extensional faults and implications for seismic slip propagation: case studies from the central Apennines, Italy. Doi: 10.1016/j.jsg.2016.10.003.

1. Introduction

Faults and fault zones in heterogeneous sedimentary sequences are common in many active tectonic settings, including subduction zones, accretionary prisms, fold-and-thrust belts, and extensional basins (e.g., Bally et al., 1986; Rowe et al., 2011; Williams et al., 2015). During the spatio-temporal evolution of these faults, tectonic deformation can mix and smear along fault zones various lithologies from the hosting sedimentary sequences (e.g., carbonate, clayey, marly, and siliciclastic rocks; e.g., Kettermann et al., 2016; Vrolijk et al., 2015). The involvement of different lithologies can affect fault-related fluid circulation (e.g., water, geothermal fluids, and hydrocarbons), deformation mechanisms, and fault friction (e.g., Faulkner et al., 2003; Keranen et al., 2013). In particular, fault friction modulates the fault-slip behaviors (from aseismic creep to seismic slip) of seismogenic faults and both earthquake nucleation and co-seismic slip propagation (e.g., Marone and Richardson, 2010; Faulkner et al., 2011; Tesei et al., 2014; Bullock et al., 2015; Carpenter et al., 2015; Giorgetti et al., 2015; Ikari et al., 2016). Specifically, the occurrence of phyllosilicate minerals, which can be important constituents of fault rocks within shallow crustal domains (< 3 km depth), can strongly influence the strength of faults (e.g., Faulkner et al., 2003; Carpenter et al., 2011; Tesei et al., 2013; Bullock et al., 2014; Balsamo et al., 2014). In many seismically active regions, in fact, co-seismic slip propagates along phyllosilicate-rich fault zones up to the Earth's surface, generating surface displacements and seafloor breakout, occasionally associated with tsunami generation (e.g., Chi Chi earthquake, Taiwan, M_w 7.6, 1999, Ma et al., 1999; Sumatra, Indonesia, 2004, M_w 9.0 earthquake, Fujii and Satake, 2007; Wenchuan, China, 2008, M_w 7.9 earthquake, Xu et al., 2009; Tohoku-Oki, Japan, 2011, M_w 9.0 earthquake, Ide et al., 2011). Therefore, the study of exposed analogues of shallow faults cutting through phyllosilicate-bearing sedimentary sequences can significantly contribute to understanding how mixing and smearing of phyllosilicates can affect fault deformation mechanisms and, in particular, earthquake slip propagation.

In this paper, we describe two case studies of exhumed extensional faults within massive carbonate rocks (Pietrasecca Fault 1 and Pietrasecca Fault 2, PSF1 and PSF2, respectively) from the seismically active extensional domain of the central Apennines, Italy (Fig. 1a). PSF1 and PSF2 were exhumed from a depth ≤ 2.5 km since Pliocene time and presently have excellent exposures allowing geoscientists to study in situ the complete fault-zone structure (i.e., both hangingwall and footwall are preserved). Therefore, we consider both the PSF1 and PSF2 as exposed analogues of the shallow portion (< 3 km depth) of subsurface seismogenic extensional faults in the central Apennines (e.g., Demurtas et al., 2016; Smeraglia et al., 2016). Within these faults, we report for the first time in the central Apennines, the occurrence of phyllosilicate-rich layers injected along extensional carbonate-hosted fault surfaces (i.e., carbonate-on-carbonate faults).

We combine mesostructural, microstructural (image analyses, optical and electron microscopy), and mineralogical (X-ray diffraction, XRD) analyses to understand the phyllosilicate origin and propose a general model for the phyllosilicate injection along carbonate-hosted extensional fault zones. To show that the two examples are not isolated at least in the study region, we briefly report further examples of phyllosilicates occurrence along other seismogenic or potentially-seismogenic faults in the central Apennines cutting through carbonate rocks. Our main goal is to show that, even in a tectonic setting dominated by lithologies characterized by high frictional strength (i.e., carbonates), phyllosilicate-rich layers can occur along carbonate-hosted fault zones, presumably reducing the expected frictional strength (e.g., Saffer and Marone, 2003; Collettini et al., 2009; Bolognesi and Bistacchi, 2016).

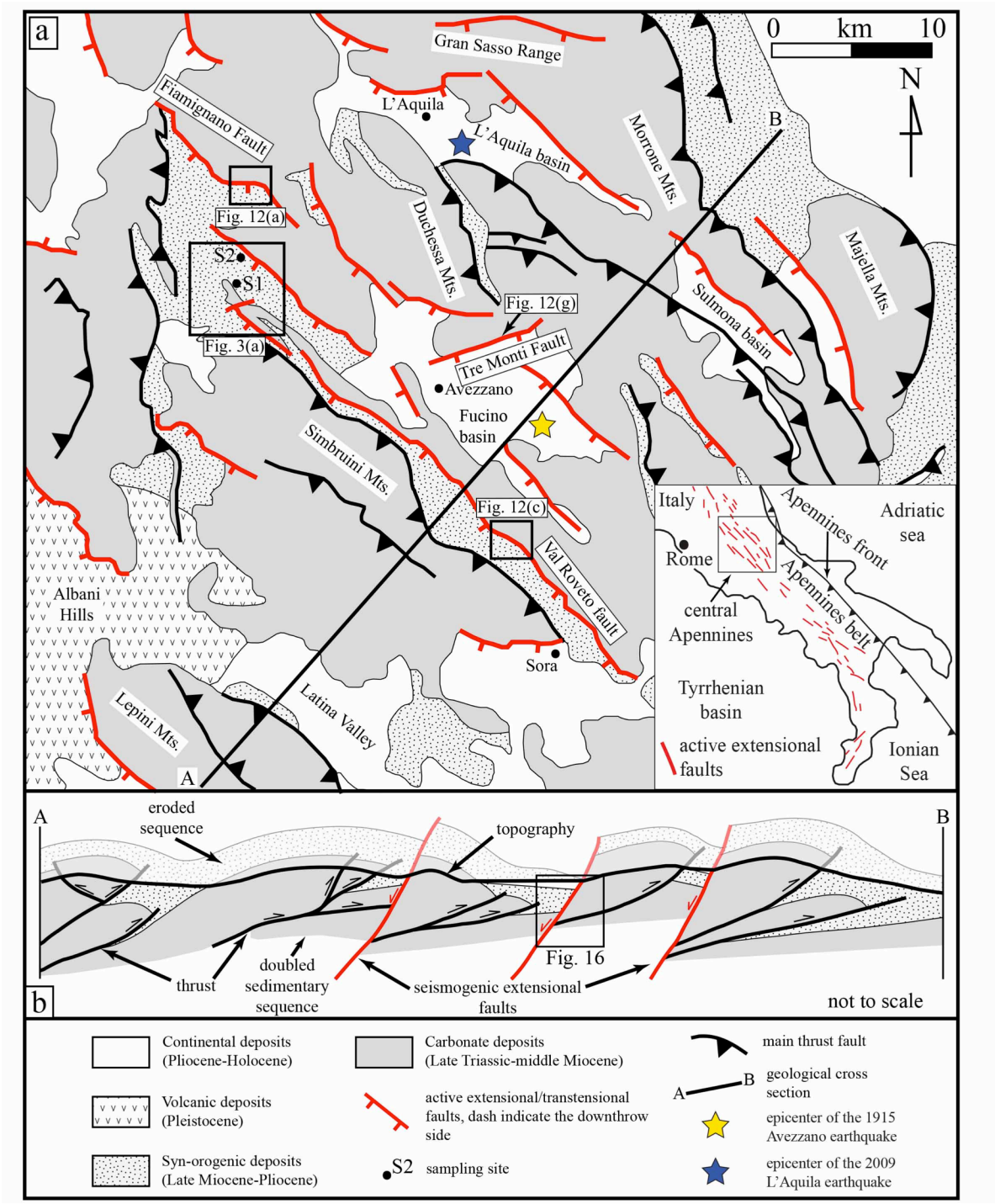


Figure 1. (a) Simplified geological map of the central Apennines (Italy) showing main thrusts, active extensional faults, and location of the studied faults. (b) Schematic geological cross section across the central Apennines (modified after Cavinato et al., 2002 and Patacca et al., 2008). Cross-section trace is shown in (a).

2. Geological framework

2.1 Central Apennines: evolution and seismotectonic setting

The Apennines are a late Oligocene-to-Present fold-thrust belt related to west-directed subduction and eastward rollback of the Adriatic plate under the European plate (e.g., Doglioni,

1991; Carminati et al., 2012). Shortening was accommodated by the off-scraping and piling up of pre-orogenic and syn-orogenic sedimentary deposits of the Adriatic plate (Figs. 1a and 1b; e.g., Doglioni, 1991). In the central Apennines, the pre-orogenic sedimentary sequence consists of ~4,000-5,000 m thick Late Triassic-Middle Miocene massive limestones and dolostones deposited within shallow-water carbonate platform and ramp environments above the underlying crystalline basement of the Adriatic plate (Fig. 2; e.g., Dondi et al., 1966; Parotto and Praturlon 1975; Damiani, 1977; Damiani et al. 1991; Cosentino et al., 2010; Carminati et al., 2013). Since Late Miocene time, hemipelagic and syn-orogenic clastic sedimentation occurred within foreland and foredeep environments respectively, as a result of Adriatic plate flexure and orogenic wedge accretion (e.g., Cipollari et al., 1995). This sedimentary succession consists of a maximum of ~100 m thick hemipelagic marls and ~3,000 m thick siliciclastic sandstones with marly and clayey interbeds (Fig. 2; e.g., Milli and Moscatelli, 2000; Carminati et al., 2007; Bigi et al., 2009). The northeastward migration of NW-SE-oriented thrust faulting has sliced and duplicated the pre- and syn-orogenic sedimentary succession (Figs. 1a and 1b; e.g., Dondi et al., 1966; Bally et al., 1986; Mostardini and Merlini, 1986; Billi et al., 2006; Patacca et al., 2008). In this framework, thrust sheets are composed of repeated sequences of both pre-orogenic and syn-orogenic deposits, which can be traced up to depths of ~8–10 km (Fig. 1b; Billi et al., 2006; Patacca et al., 2008).

Since early Pliocene time, the internal and axial part of the central Apennines belt underwent post-orogenic exhumation (e.g., Galadini et al., 2003), volcanic activity (the Albani Hills, Fig. 1a; e.g., Carminati et al., 2012), and extensional faulting associated with the development of the Tyrrhenian backarc basin (e.g., Doglioni, 1991; Doglioni et al., 1997). This extensional regime is still active and has generated a system of main NW-SE-oriented extensional faults and subordinate ENE-WSW-oriented extensional/transtensional transfer faults, which have generated historical and instrumental seismicity (Fig. 1a; Doglioni et al., 1998; Cavinato and De Celles, 1999; Cavinato and Miccadei, 2000; Morewood and Roberts, 2000; Cavinato et al., 2002). PSF1 and PSF2 belong to this tectonic setting.

In particular, in the central Apennines, moderate to large earthquakes (Figs. 1a and 1b; e.g., Avezzano, 1915, M_w 7.0 earthquake, Oddone, 1915; L'Aquila, 2009, M_w 6.3 earthquake, Chiaraluce, 2012; Amatrice, 2016, M_w 6.0 earthquake, Gruppo di lavoro INGV sul terremoto di Amatrice, 2016) nucleated at < 10 km depth (probably within the crystalline basement, and co-seismic slip upward-propagated along faults that cut through the sedimentary cover consisting of massive carbonate rocks (limestones and dolostones), clayey to marly rocks, and siliciclastic sandstones (e.g., Bally et al., 1986; Cosentino et al., 2010; Chiaraluce, 2012; Valoroso et al., 2013). Moreover, many studies regarding historical and instrumental earthquakes documented that co-seismic slip propagated up to the Earth's surface producing fault scarps and displacements (e.g., Pantosti et al., 1993; Cello et al., 1998; Galli et al., 2008; Alessio et al., 2009; Galli et al., 2011; Benedetti et al., 2013; Martino et al., 2014; Mildon et al., 2016). For instances, during the recent (24th August, 2016) M_w 6.0 Amatrice earthquake a surface rupture up to ~20 cm high was mapped along the M. Vettoretto fault scarp (EMERGEO Working Group, 2016). This evidence indicates that the shallow fault zone structure, as those analyzed in this paper, must have significantly influenced and modulated co-seismic slip propagation up to the Earth's surface.

2.2 Geological setting of the Pietrasecca area

Within the Pietrasecca area, pre-, syn-, and post-orogenic deposits are exposed (Fig. 2). The pre-orogenic succession consists of Late Cretaceous carbonate platform deposits paraconformably overlain by Early-Middle Miocene carbonate ramp deposits (Lithothamnion and Bryozoan Limestone Fm., LBL Fm.). The LBL Fm. is between ~100 m and ~150 m thick and is divided into three lithostratigraphic units: LS1, LS2, and LS3 units from the bottom to the top (Fig. 2; Civitelli and Brandano, 2005; Brandano et al., 2010). The LBL Fm. is characterized by compaction stylolites, developed during burial as roughly parallel to bedding (Civitelli and Brandano, 2005), and by pressure-solution cleavage oblique to bedding and related to shortening within the central Apennines fold-thrust belt (Tavani and Cifelli, 2010).

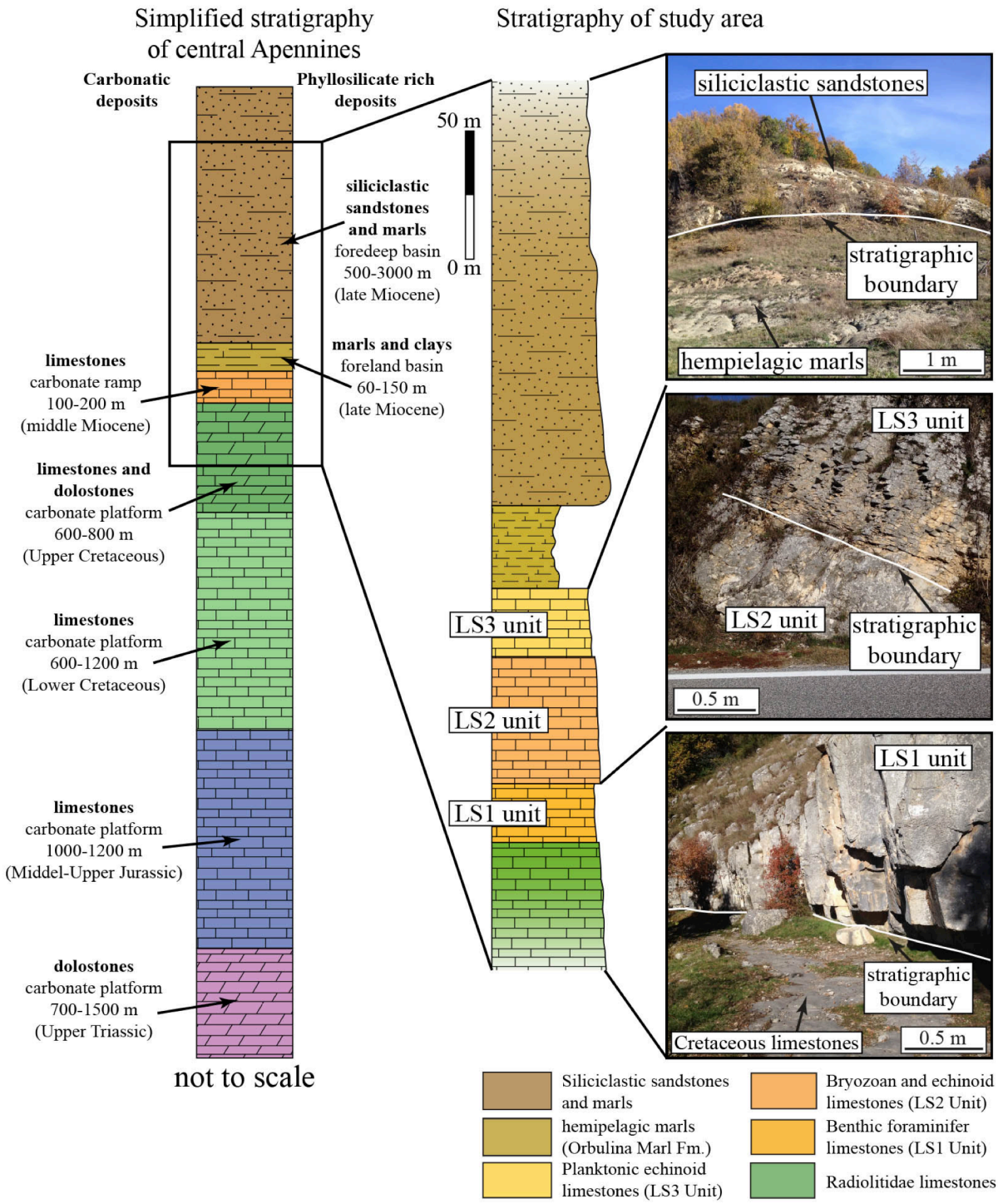


Figure 2. Stratigraphic column of the sedimentary succession in the central Apennines (left) and in the Pietrasecca study area (right with related outcrops exposures). Within the sedimentary succession, the difference between phyllosilicate-rich deposits and carbonate deposits is highlighted.

In this area, the Late Miocene succession consists of ~60 m thick hemipelagic marls (Orbulina Marl Fm.; Cosentino et al., 1997) followed by ~1,600 m thick siliciclastic sandstones (i.e., syn-orogenic deposits) with marly and clayey interbeds (Fig. 2; Milli and Moscatelli, 2000; Carminati et al., 2007; Brandano et al., 2010). Stratigraphic and vitrinite reflectance data constrain the maximum

burial depth of siliciclastic sandstones to ~2,000 m (Milli and Moscatelli, 2000; Corrado et al., 2010).

In Late Miocene time, both pre- and syn-orogenic deposits were folded and thrust during the Apennines belt evolution. Shortening generated the Pietrasecca-Tufo anticline, which is a NW-SE-oriented asymmetric fold with no overturned strata or thrust breakthrough evidence (Figs. 3a and 3b; Tavani and Cifelli 2010). Following this contractional phase, the early Pliocene extensional tectonics occurred with exhumation and uplift of the Apennines belt, creating both NW-SE- and ENE-WSW-oriented extensional faults (Fig. 3a), which cut across the compressional structures. The PSF1 and PSF2 belong to the ENE-WSW- and NW-SE-oriented sets, respectively.

In the Pietrasecca area, erosion of the Apennines belt caused the deposition of post-orogenic continental deposits (Holocene in age) within topographic depressions (Fig. 3a). These deposits consist of eluvial-colluvial and gravel deposits enriched in reworked volcanoclastic material derived from the volcanic deposits of the Albani Hills (Compagnoni et al., 1993).

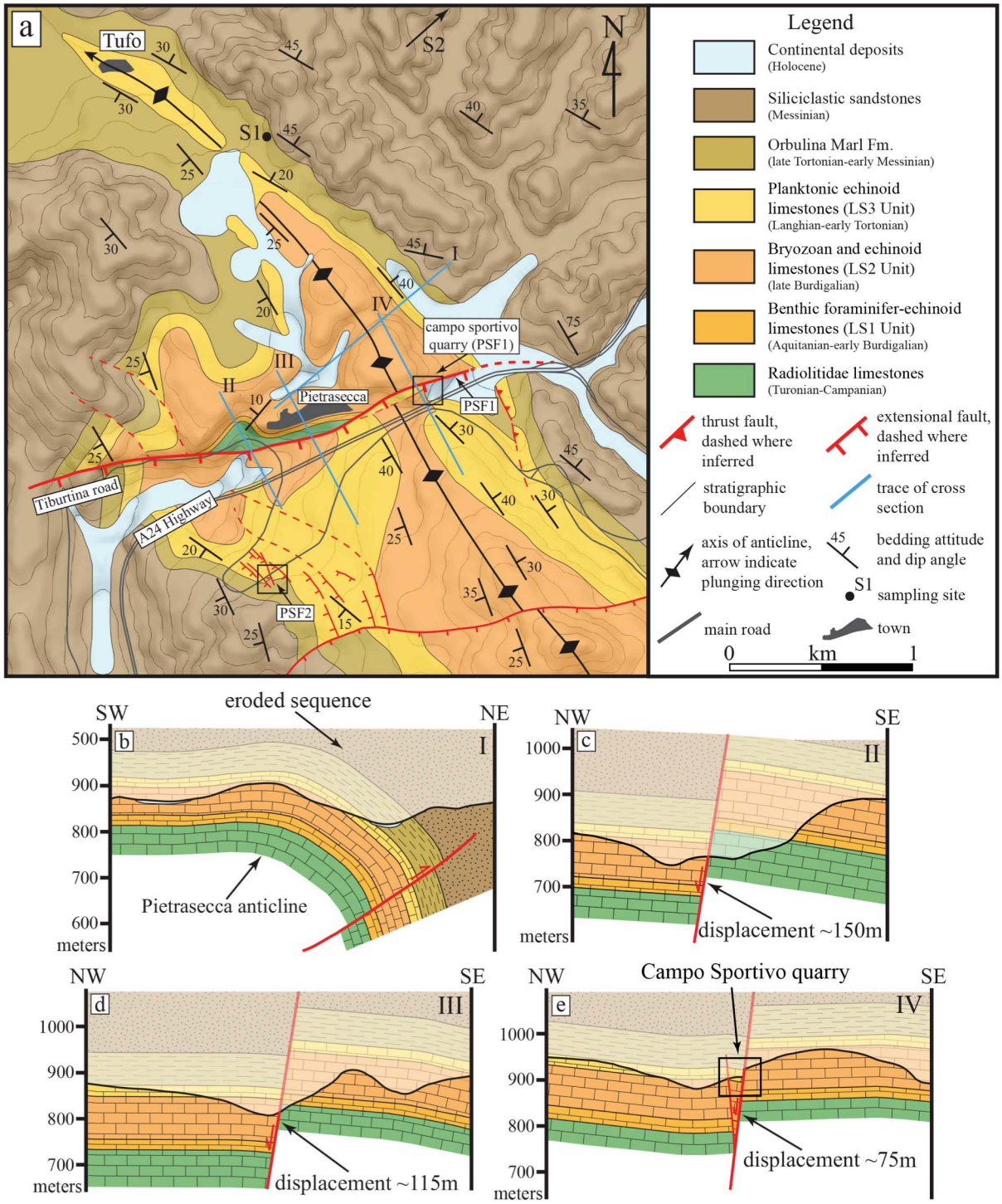


Figure 3. (a) Geological map of the Pietrasecca area with location of the studied faults (Pietrasecca Fault 1, PSF1, and Pietrasecca Fault 2, PSF2). (b) Geological cross-sections across the Pietrasecca anticline. Cross-section trace is in (a). (c), (d), and (e) Geological cross-sections through the PSF1. Cross-section traces are in (a).

3. Methods

To reconstruct the general architecture of the PSF1 and PSF2 zones, we collected original field data and performed geological mapping at the 1:10,000 and larger scales. Moreover, to determine the fault displacements and stratigraphic juxtapositions, we drew four geological cross sections across PSF1 (Fig. 3) and one across PSF2. Then, to reconstruct the mesoscale fault zone architecture, we conducted detailed structural analyses within the Campo Sportivo quarry (latitude N 42°08'08'' longitude E 13°08'01'') and along the Tiburtina Road (latitude N 42°07'36'' longitude E 13°07'29''), where large and accessible exposures of PSF1 and PSF2 occur. We collected a set of samples from the Campo Sportivo quarry and studied the microstructures occurring in a phyllosilicate-rich and isolated layer located along the PSF1 principal fault surface. We prepared polished cuts of impregnated hand samples and thin sections, which we analyzed under both optical and scanning electron microscopes. For electronic microscopy, we used the FESEM Zeiss Auriga of the CNIS (Center for Nanotechnologies Applied to Engineering) Laboratory at the Sapienza University of Rome, Italy. To study the mineral composition and determine the fault-zone exhumation depth, we used low temperature geothermometers (illite content in mixed layer illite-smectite; Srodon, 1980). For this analysis, we collected three samples across the PSF1 phyllosilicate-rich layer at increasing distance from the principal fault surface: sample SL1 at 0.5 cm, sample SL2 at 4 cm, and sample SL3 at 8 cm. We also collected two additional samples from the top of the hemipelagic marls (Orbulina Marls Fm., sample 1) and the top of the siliciclastic sandstones (sample 2) in the study area. Whole-rock composition and the illite content in mixed illite-smectite (I-S) layers were determined by X-ray diffraction analyses (XRD) using a Scintag X1 X-ray system (CuKα radiation) at 40 kV and 45 mA (at the XRD Laboratory, Science Department, Roma Tre University, Italy). We ran randomly oriented whole-rock powders in the 2-70° 2θ interval with a step size of 0.05° 2θ and a counting time of 3 s per step. Oriented air-dried and ethylene-glycol solvated samples of the <2 μm grain-size fraction were scanned from 1 to 48° 2θ and from 1 to 30° 2θ, respectively, with a step size of 0.05° 2θ and a

count time of 4 s per step. Following Moore and Reynolds (1997), we determined the illite content in mixed I-S layers using the delta two-theta method after decomposing the composite peaks between 9-10° 2θ and 16-17° 2θ. We determined the I-S ordering type (Reichweite parameter, R; Jagodzinski, 1949) through the position of the I001-S001 reflection between 5 and 8.5° 2θ (Moore and Reynolds, 1997). Finally, we performed two-dimensional clast-size distributions of fault and host rocks to constrain microdeformation mechanisms. In thin sections, under optical microscope, we traced clasts and measured their dimensions semi-automatically through the *ImageJ* software (http://rsbweb.nih.gov/ij/). As clasts have a sub-angular to rounded shape, we expressed clast size as the diameter d of a circle with the same area A of the clast ($d=2(A/\pi)^{0.5}$; Marone and Scholz, 1989). We measured size-frequency data at 4x magnification and plotted the cumulative number of clasts (N) larger than a given diameter d (i.e., normalized to the maximum clast number n) in a log(N>d/n)-log(d) diagram.

4. Terminology

In the present study, we adopt the texture-based fault rock terminology by Woodcock and Mort, (2008). This terminology is primarily defined by grain size: fault rocks with >30% large clasts (≥ 2 mm in diameter) are classified as breccias, whereas fault rocks with <30% large clasts (≥ 2 mm in diameter) are classified as cataclasites. We define the fine-grained particulate material < 0.1 mm in diameter as matrix. Matrix can be produced by local fragmentation of larger particles and/or by introduction of exotic material into the fault rock. Moreover, we define any neo-formed mineralization as cement (e.g., calcite crystals precipitated from a fluid).

Cataclasites are characterized by few (< 30%) large clasts (> 2 mm in diameter), generally sub-rounded to well rounded, surrounded by a fine-grained matrix (< 0.1 mm in diameter; e.g., Woodcock and Mort, 2008). Following the classification of fault breccias by Woodcock and Mort (2008), we further divide breccias on the basis of clast/matrix proportions, fitting of adjacent clast sides, and evidence of clast rotation: (1) Crackle breccia texture is characterized by > 75% of large

clasts (> 2 mm in diameter), which can fit together like a jigsaw puzzle and have no evidence of rotation. Spaces between clasts can be filled by matrix and/or cement. (2) Mosaic texture is characterized by < 75% and > 65% of large clasts (> 2 mm in diameter), which show more separation and rotation, but some fitting to adjacent clasts is still preserved. Voids between clasts can be filled by matrix and/or cement. (3) Chaotic texture is characterized by < 60% of large clasts (> 2 mm in diameter), which are strongly rotated and lack geometric fit to formerly adjacent clasts. Voids between clasts are filled by matrix and/or cement.

5. Pietrasecca fault 1 (PSF1)

5.1 Structural setting

PSF1 is a ~3 km long SSE-dipping (60°-80°) extensional fault with some evidence of transtensional movements, which displaces the Pietrasecca-Tufo anticline perpendicularly to the fold axis (Fig. 3a). Based on stratigraphic offsets, the minimum displacement along the principal fault decreases from ~160 m at the center of the fault (Fig. 3c) to ~75 m and ~115 m toward the eastern and western fault tips, respectively (Figs. 3d and 3e). The eastern tip of PSF1 crops out at the Campo Sportivo quarry (Fig. 3a), where the fault-zone internal architecture is exposed both toward the hangingwall and toward the footwall. There, we identified three principal structural domains (Figs. 4a and 4b): (1) the hangingwall damage zone (Domain 1, D1); (2) the footwall damage zone (Domain 2, D2); and (3) the fault core (Fault Core, FC).

5.2 Hangingwall damage zone (D1)

The ~80 m thick hangingwall damage zone consists of carbonate deposits from the LS3 and LS2 units (Fig. 3). The bedding of the LS3 unit is preserved and dips gently (~20°) toward the west. Hemipelagic marls, which nowadays are not exposed due to erosion, were located a few meters above the exposed LS3 beds. The two lithostratigraphic units (LS2 and LS3) are juxtaposed by a

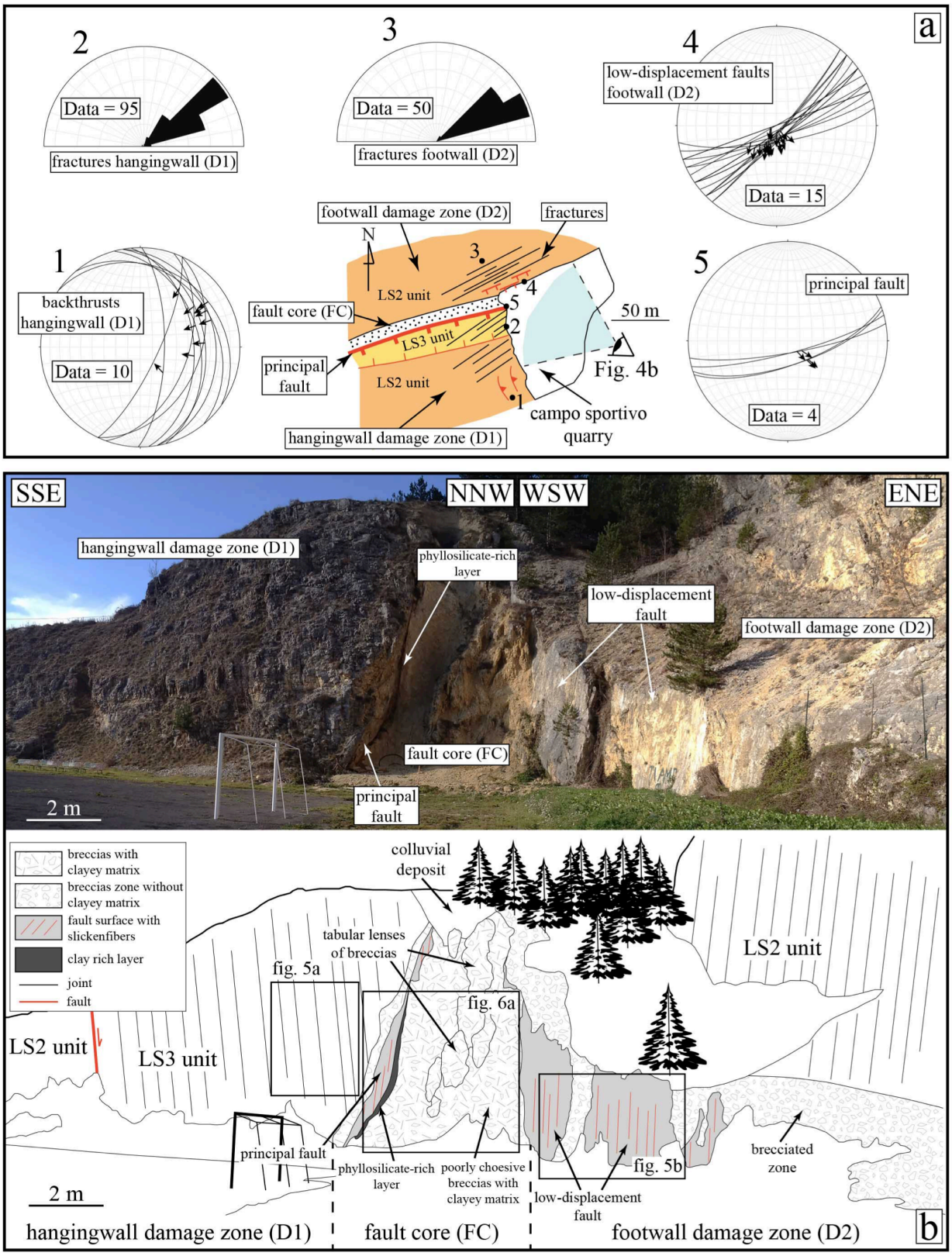


Figure 4. (a) Schmidt nets (lower hemisphere) showing attitude of low displacement faults with related slip vectors (plot 1, dip-slip extensional movements and right-lateral transtensional movements) and attitude of the PSF1 principal surface with related slip vectors (plot 4, dip-slip extensional movements and left-lateral transtensional movements). Rose diagrams showing attitude of joints (plots 2 and 3). Simplified structural map of the Campo Sportivo quarry (PSF1). **(b)** Panoramic view of the Campo Sportivo quarry (photograph above and line drawing below) showing exposures of the main structural domains. View of (b) shown in (a).

NNW-dipping (80°) extensional fault (Figs. 4a and 4b). Within the two lithostratigraphic units, the brittle deformation is accommodated by:

(1) SW-dipping (60°-80°) low-displacement faults, characterized by kinematic indicators showing extensional dip-slip motions with some evidence of transtensional right-lateral motions (plot 1, Fig. 4a);

(2) steeply dipping empty (no mineralization or filling) joints that isolate rock lithons, which have cubic or parallelepiped shapes, generating a crackle-like breccia texture (Fig. 5a). The most penetrative set of joints dips toward NNW by 80°-90° (plot 2, Fig. 4a) and pervasively cuts through LS3 unit (Figs. 4b and 5a).

5.3 Footwall damage zone (D2)

The ~90 m thick footwall damage zone consists of carbonate deposits from the LS2 unit (Figs. 4a and 4b), and contains:

(1) a dense network of joints showing a wide range of orientations. The most continuous and penetrative set is SW-dipping (70°-90°; plot 3, Fig. 4a). Joints have no mineralization or filling, and isolate rock lithons, which have cubic or parallelepiped shapes, generating crackle-like breccia texture (Fig 5b);

(2) low-displacement SE-dipping (70°-90°) faults with kinematic indicators showing extensional dip-slip motions with some evidence of transtensional right-lateral motions (plot 1, Fig. 4a). Fault surfaces are smooth and sharp and cut across both chaotic breccias and cataclasites (Figs. 5b, 5c, and 5d), often truncating carbonate clasts (Fig. 5d inset);

(3) patches and lenses of chaotic breccias located below low-displacement fault surfaces (Figs., 5b, 5c, and 5d). Breccias are clast-supported and the matrix consists of fine-grained carbonate clasts. We did not observe any cement between clasts;

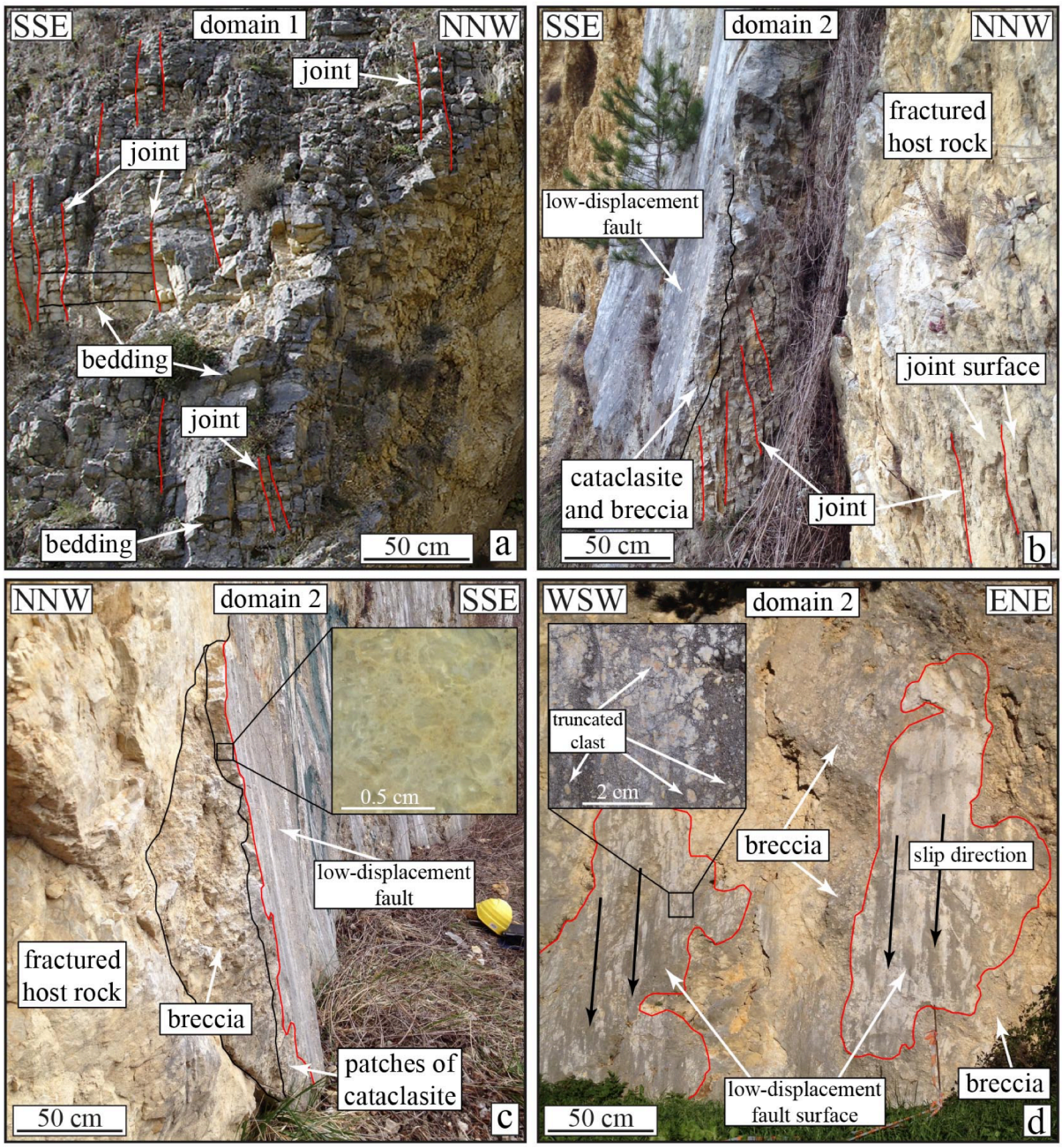


Figure 5. PSF1 structures both in the hangingwall damage zone (domain 1, D1) and in the footwall damage zone (domain 2, D2). **(a)** Fractured hangingwall damage zone (domain 1, D1) showing the pervasive network of WSW-ENE-oriented joints (example joints traces in red). **(b)** and **(c)** Footwall damage zone (domain 2, D2) showing the pervasive network of WSW-ENE-oriented joints, chaotic breccias, and low-displacement fault planes cutting through cataclasites. Inset shows a high resolution scan of a hand sample cut through the cataclasite, which is characterized by sub-rounded to well-rounded carbonate clasts within a fine-grained carbonate matrix. **(d)** Low-displacement fault showing a smooth and sharp fault surface cutting through chaotic breccias. Inset shows a close-up from the fault surface with truncated carbonate clasts.

(4) highly-cohesive patches and lenses of cataclasite, up to ~10 cm thick, heterogeneously distributed below low-displacement fault surfaces (Figs. 5b and 5c). Large carbonate clasts (up to 10 mm in diameter) are dispersed within a fine-grained matrix consisting of carbonate particles (< 0.1 mm in diameter; Fig. 5c inset).

5.4 Fault core (FC)

The fault core is ~14 m thick and juxtaposes the LS3 unit in the hangingwall with the LS2 unit in the footwall, for a minimum of ~75 m of cumulative displacement (Fig. 3d) accomodated by the principal fault (Figs. 4a and 4b). The fault core contains:

(1) poorly cohesive breccias heterogeneously distributed through the fault core (Fig. 6a) and

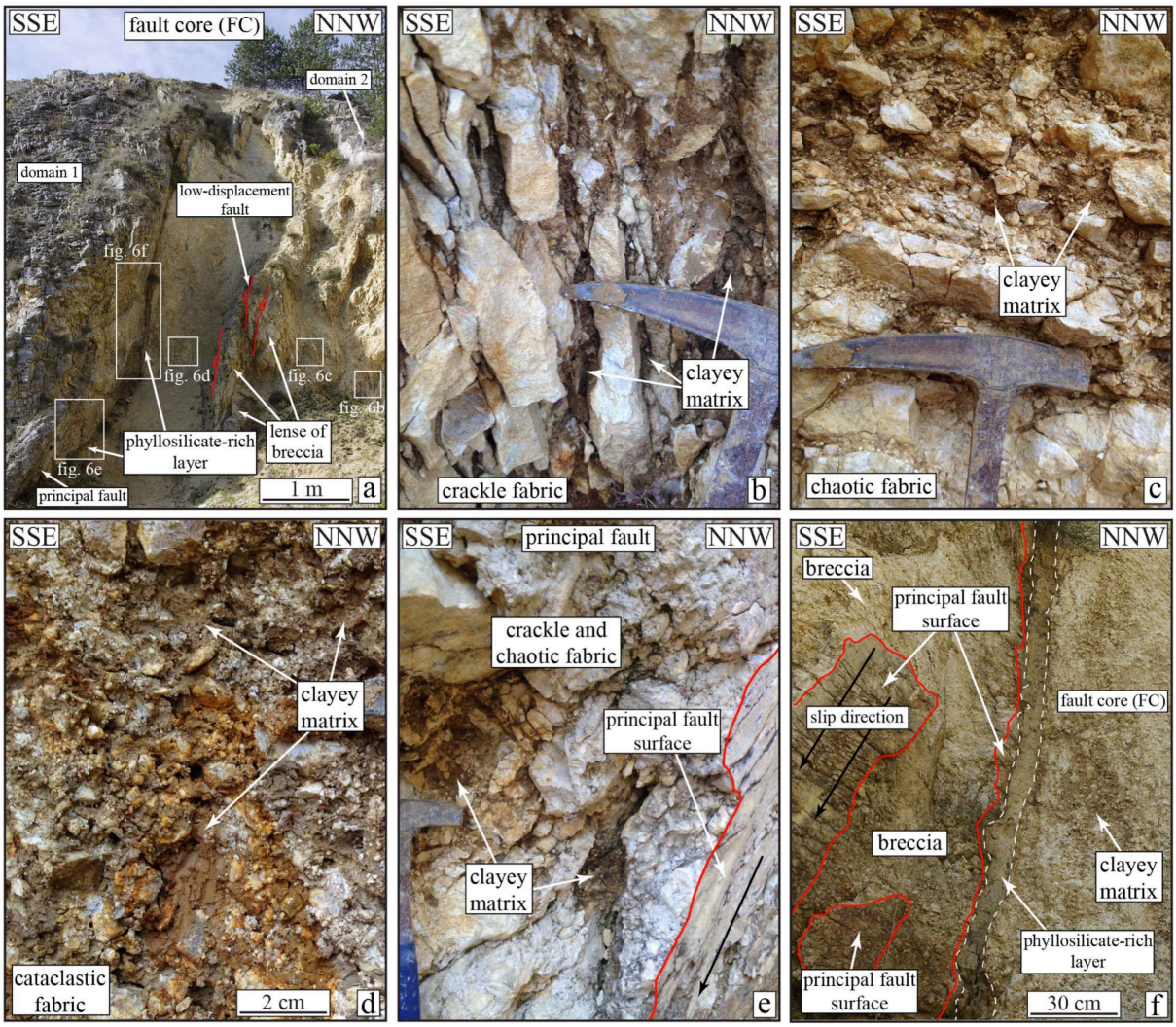


Figure 6. PSF1 structures within the fault core (FC). **(a)** Overview of the fault core showing the brecciated zone, the principal fault, and the phyllosilicate-rich layer. **(b)** Mosaic breccia texture with parallelepiped rock lithons bounded by joints. Joints are filled by a clayey matrix. **(c)** Chaotic breccia texture showing joints and voids filled by a clayey matrix. **(d)** Cataclasite showing sub-rounded carbonate clasts within a clayey matrix. **(e)** Smooth and sharp surface of the principal fault cutting through a fault breccias and cataclasites. Fractures and voids within breccias and cataclasites are filled by a clayey matrix. **(f)** The phyllosilicate-rich layer interposed between the principal fault surface and the brecciated zone of the fault core.

exhibiting two main textures: mosaic and chaotic. Within the mosaic breccias, fractures isolate parallelepiped rock lithons and are filled by a clayey matrix (Fig. 6b). Within the chaotic breccias, 1-5 cm large carbonate clasts are surrounded by a clayey matrix (Fig. 6c). We did not observe any cement within clasts;

(2) patches and lenses of cataclasite heterogeneously distributed through the fault core. Cataclasite is poorly cohesive and consists of carbonate clasts surrounded by an abundant clayey matrix (Fig. 6d);

(3) low-displacement SE-dipping (70°-90°) faults that cut across breccias and cataclasites (Fig. 6a). Fault surfaces are smooth and undulated forming an anastomosing set, which isolates tabular bodies of breccias (Fig. 6a);

(4) the principal fault (Figs. 4a, 4b, and 6a), which juxtaposes the hangingwall damage zone (D1) with the footwall damage zone (D2) through a SSE-dipping (70°) undulated surface. Kinematic indicators show extensional dip-slip motions with some evidence of transtensional left-lateral motions (plot 4, Fig. 4a). The principal fault cut through the brecciated zone of the fault core (Figs. 6e and 6f) and a ~15 cm thick phyllosilicate-rich layer lies parallel to the fault surface (Figs. 6a and 6f).

5.5 Phyllosilicate-rich layer

5.5.1 Mineralogical and microstructural observations

The ~15 cm thick phyllosilicate-rich layer is interposed between the PSF1 principal surface and the brecciated zone of the fault core, lying parallel to the fault surface (Figs. 6f and 7a):

(1) The average whole-rock composition (Table 1) of the phyllosilicate-rich layer consists of clay minerals (~35%), quartz (~35%), plagioclase (~27%), and K-feldspar (~3%). Calcite or dolomite cement are absent, although macroscopic carbonate clasts are dispersed within the layer (Fig. 8a). We measured the relative amount of both clay and non-clay minerals (i.e., quartz,

Lithology	Sample name	Quartz (%)	K-feldspar (%)	Plagioclase (%)	Clay minerals (%)	Calcite (%)	Dolomite (%)
Hemipelagic marls (Orbulina Marls Fm.)	S1	5	0	3	52	39	1
Siliciclastic sandstones	S2	15	1	22	47	8	6
Clay rich layer	SL1	34	3	14	48	0	0
Clay rich layer	SL2	40	4	27	29	0	0
Clay rich layer	SL3	30	3	41	27	0	0
Lithology	**Sample name**	**Illite (%)**	**Illite-Smectite (%)**	**Kaolinite (%)**	**Chlorite (%)**		
Hemipelagic marls (Orbulina Marls Fm.)	S1	47	22	18	14		
Siliciclastic sandstones	S2	70	15	11	4		
Clay rich layer	SL1	50	21	26	2		
Clay rich layer	SL2	53	10	33	5		
Clay rich layer	SL3	48	9	39	3		

Table 1. Summary of mineralogical XRD analyses for the **(a)** > 2 μm and **(b)** < 2 μm fractions, respectively.

plagioclase, and K-feldspar) within the phyllosilicate-rich layer toward the principal fault surface (i.e., from SL3 to SL1; Fig. 7a). Results show that toward the fault, the clay-mineral content increases from 26% to 48% whereas and plagioclase content decreases from 41% to 14% (Fig 7b). The amount of K-feldspar is ~3-4% within all samples, whereas the amount of quartz varies between 30 and 40% independent of distance to the fault (Fig 7b).

The average composition of the < 2 μm grain-size fraction of the phyllosilicate-rich layer consists of illite (~50%), kaolinite (~33%), mixed illite-smectite layers (~13%), and chlorite (~4%). In this fraction, we observed traces of quartz, K-feldspar, and lepidocrocite, as well. Mixed layered minerals correspond to two populations of illite-smectite crystals. The first population consists of random-ordered illite-smectite structures (R_0) with an illite content of 40%, whereas the second one is characterized by short-range ordered illite-smectite (R_1) with 67% illitic layers. The mineralogy does not change moving closer to the fault surface, and we did not find any mineralogical evidence indicating high temperature occurrences, for instance, as a function of co-seismic fault slip (e.g., Balsamo et al., 2014).

(2) The phyllosilicate-rich layer is characterized by a sharp contact both with the principal fault surface and with the brecciated zone of the fault core (Fig. 7a). In the layer, mm-thick phyllosilicate bands alternating with cm-thick granular bands, which are characterized by quartz, plagioclase, K-feldspar, and carbonate clasts, form a strong foliation (Figs. 7a and 8a). Foliation

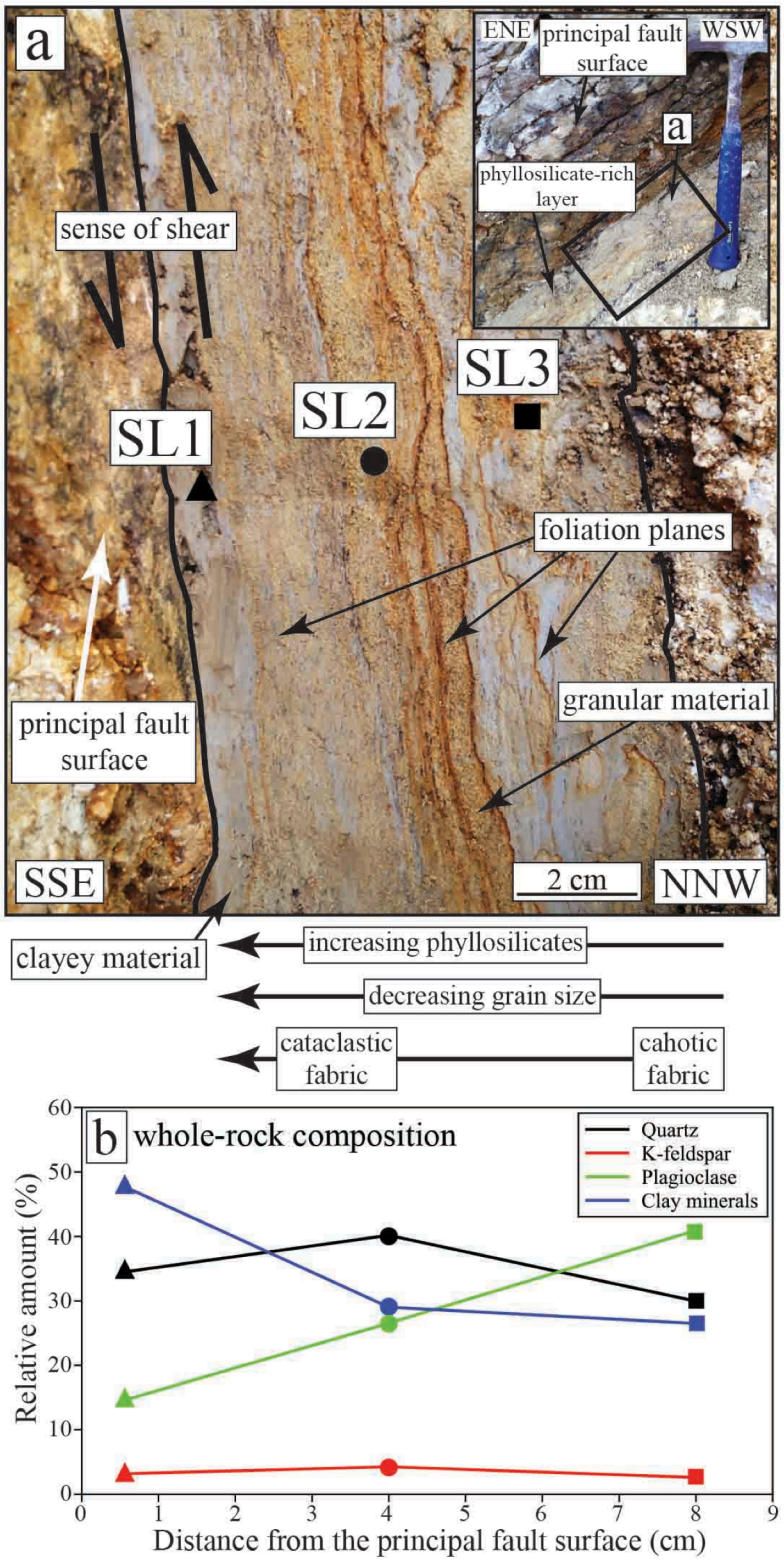


Figure 7. (a) Detail of the PSF1 phyllosilicate-rich layer and sample locations. Note the phyllosilicate bands alternating with granular bands rich in quartz, plagioclase, K-feldspar, and carbonate clasts. Foliation planes are oriented roughly parallel to the principal fault surface. **(b)** Variation of the relative content of both clay minerals and non-clay minerals as a function of the distance from the principal fault surface. Triangles-SL1, Circles-SL2, Squares-SL3.

planes are oriented roughly parallel to the principal fault surface (Figs. 7a and 8a). In addition, carbonate clasts with long axes oriented roughly parallel to the principal fault surface are dispersed within the phyllosilicate-rich layer (Fig. 8a).

(3) At the microscale, texture of the phyllosilicate-rich layer toward principal fault surface is charachterized by a transition from chaotic breccia to cataclasite. Chaotic breccia texture is characterized by large clasts, often in reciprocal contact, surrounded by a clayey matrix (Figs. 8b and 8c). Clasts that are in contact have, in places, indented boundaries typical of pressure solution seams (i.e., stylolites; Figs. 8b and 8c). Clasts are well sorted and often exhibit internal crackle-like textures where extensional microfractures are filled by phyllosilicates (Figs. 8b and 8c). The chaotic breccia texture is comparable to that of the undeformed siliciclastic sandstones (Fig. 8i). The cataclasite consists of few large and many small clasts surrounded by a phyllosilicate-bearing matrix. Clast sorting is poor and clasts are rarely in reciprocal contact (Figs. 8d and 8e). We observed a clast size decrease from the chaotic-textured breccia to the cataclasite. At microscale, layering is defined by alternating phyllosilicate and granular bands (Fig. 8a, 8f-h). Within these bands, phyllosilicate [001] planes and clast long axes (in 2D) are preferentially oriented and roughly parallel to the principal fault surface (Figs. 8f and 8g). Phyllosilicate bands typically develop within granular rocks rich in phyllosilicates (phyllosilicates content >15%; e.g., Antonellini et al., 1994; Fossen, 2007). Along the contact with the principal fault surface, a ~2 mm thick phyllosicate band occurs, where phyllosilicate [001] planes are aligned roughly parallel to the principal fault surface and clasts are scattered within the clayey matrix. Also in this case, clasts have apparent long axes aligned roughly parallel to the principal fault surface (Figs. 8g and 8h).

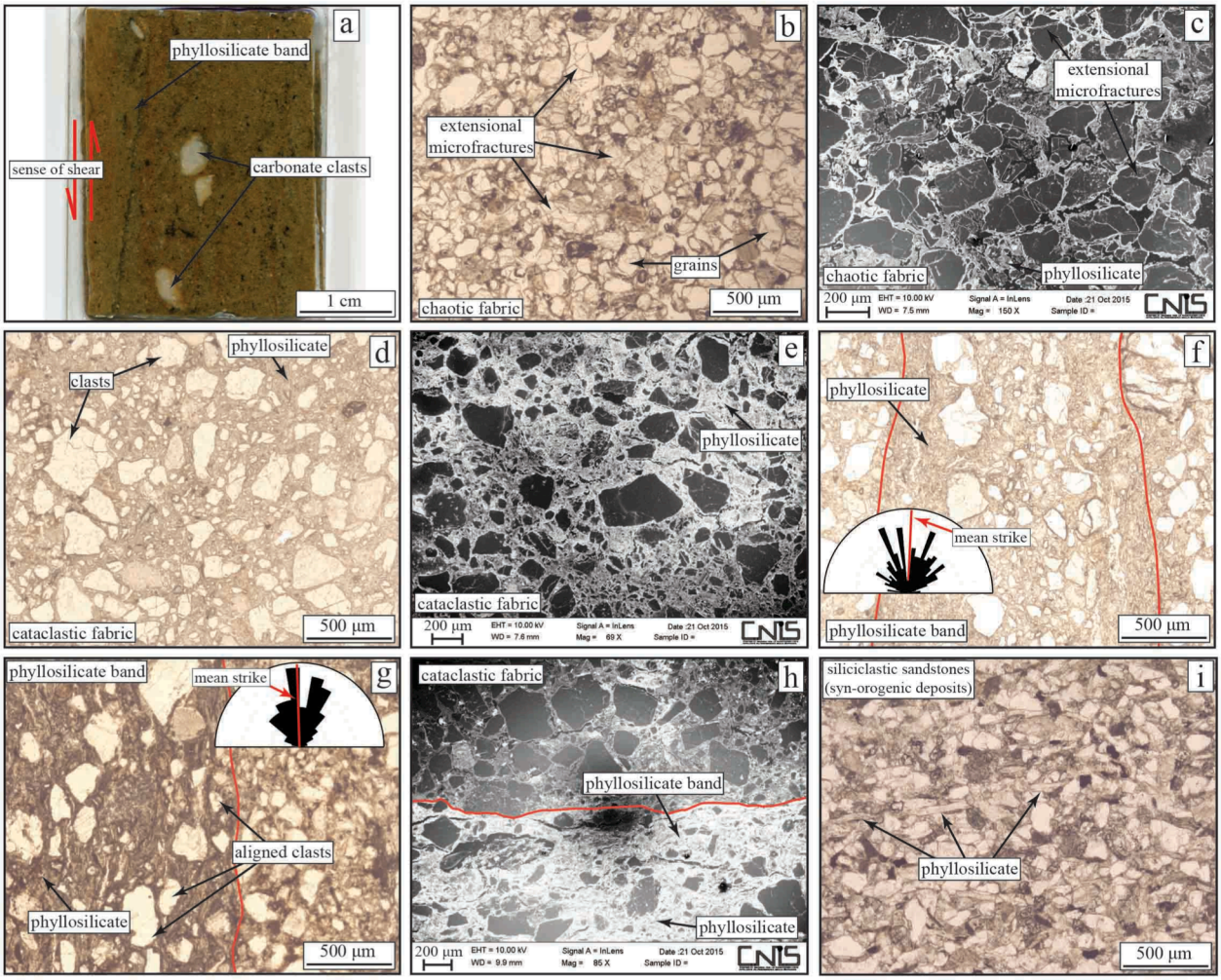


Figure 8. Microstructures from the PSF1 phyllosilicate-rich layer in thin sections photographed under optical microscope (plane-polarized light) and electron microscope (FESEM Zeiss Auriga). **(a)** High resolution scan of hand sample cut perpendicular to the phyllosilicate-rich layer and parallel to the slip direction. Note the carbonate clasts scattered within the granular material and phyllosilicate bands roughly parallel to the principal fault surface. **(b)** and **(c)** Chaotic texture within granular material. Clasts are characterized by an internal extensional microfractures pattern defining a crackle-like texture. Phyllosilicates fill the voids and fractures between clasts. **(d)** and **(e)** Cataclasites showing clasts supported by a matrix of phyllosilicates. Clasts are sub-rounded to well rounded and poorly sorted. **(f)** Phyllosilicate and granular bands defining a strong foliation oriented roughly parallel to the principal fault. Rose diagram shows attitude of clast long axes (2D), which are aligned roughly parallel to principal fault. **(g)** and **(h)** Phyllosilicate band along the principal fault surface. Clasts are scattered within a phyllosilicate-bearing matrix. Rose diagram shows attitude of clast long axes (2D). Both phyllosilicate [001] planes and clast long axes are oriented roughly parallel to the principal fault surface. **(i)** Typical texture of siliciclastic sandstones from the syn-orogenic deposits sampled outside the fault zone.

5.5.2 Clast size distribution analyses

We analyzed seven thin sections, six from the phyllosilicate-rich layer (Figs. 8b and 8d) and one from the siliciclastic sandstones (Fig. 8i) sampled outside the fault zone. The six samples are representative of the cataclasite (Fig. 8b) and chaotic-textured breccia (Fig. 8d).

The cataclasite is characterized by a clast-size distribution within the 0.1-1 mm size (diameter) interval (Fig. 9a), where the lower boundary (0.1 mm) is determined by the resolution of the optical microscope, whereas the upper boundary (1 mm) is a real boundary, at least in the given

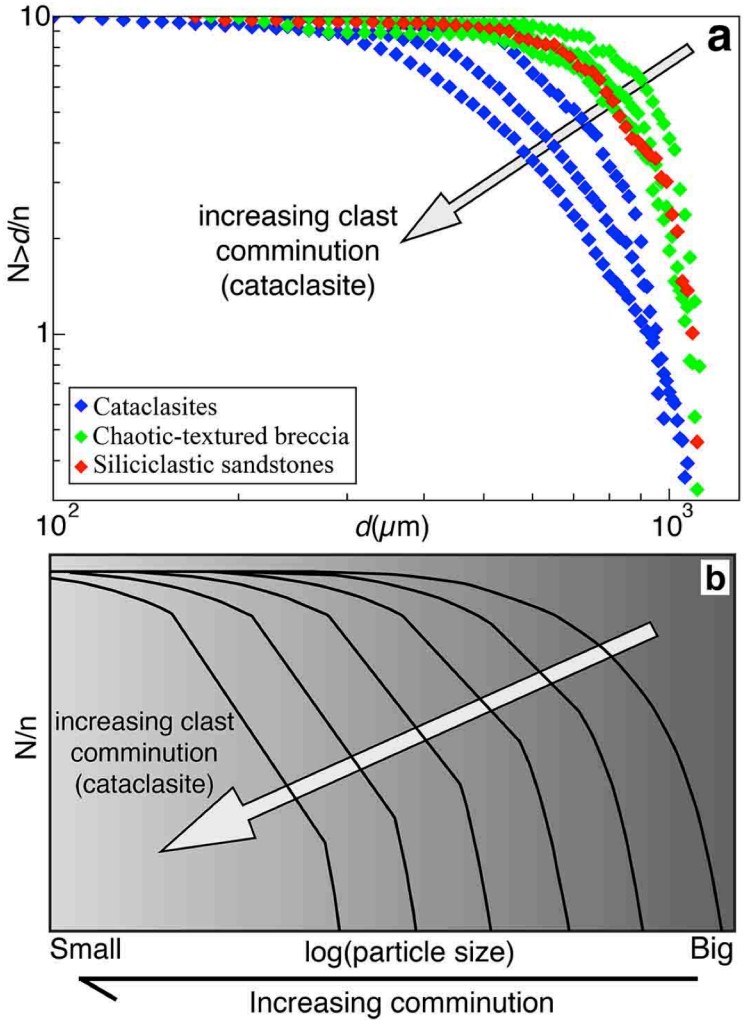


Figure 9. (a) Clast size distribution of cataclasite and breccia from the PSF1 phyllosilicate-rich layer and of the siliciclastic sandstones from syn-orogenic deposits. The log-log plot shows the number of clasts (N) larger than a particular diameter, *d*, normalized to the maximum number of clasts (n). Moving from breccia to cataclasite towards the principal fault, clast comminution increases and the log-log curves become steeper. **(b)** Schematic conceptual evolution

of clast-size distributions from fractured to cataclastic rocks thorough increasing clast comminution. (modified from Melosh et al., 2014).

sample magnification (4x). Within the 0.5-0.9 mm size interval, the clast-size distribution is linear (Fig. 9a) and very similar to the linear distribution of natural cataclasites from the literature (e.g., Storti et al., 2003; Billi, 2007; Fondriest et al., 2012). Chaotic-textured breccia and siliciclastic sandstones are characterized by a clast-size distribution within the 0.1-1 mm size (diameter) interval. In this interval, the clast size distribution is arcuate (i.e., non-linear; Fig. 9a). The transition from the arcuate (chaotic-textured breccia) towards the linear (cataclasite) clast-size distribution indicates increasing clasts comminution (Figs. 9a and 9b; e.g., Mort and Woodcock, 2008; Melosh et al., 2014).

6. Pietrasecca fault 2 (PSF2)

The geological map shown in Fig. 10a synthesizes the geological and structural setting of PSF2. This structure is a SW-dipping and ~200 m long, extensional fault with a minimum cumulative displacement of ~25 m (Fig. 10a). PSF2 belongs to a network of SW- or NE-dipping extensional faults (Fig. 10b), which displace the backlimb of the Pietrasecca-Tufo anticline. A road cut along the Tiburtina Road, perpendicular to PSF2 strike provides an excellent cross-sectional view across the fault zone both toward the hangingwall and toward the footwall (Figs. 11a and 11b). Moving from NE to SW across the fault zone we found:

(1) Within the hangingwall, NE-dipping (10°) LS3 beds are overlain by hemipelagic marls (Figs. 11b and 11c), which are partially eroded. Conversely, within the footwall, NE-dipping (10°) beds of the LS2 unit are exposed (Fig. 11b), although the upper LS2 is absent due to erosion. In contrast to PSF1, no brecciated fault core occurs. Displacement is accumulated along two main SW-dipping faults cutting through the carbonate rocks (Fig. 11b). The fault surfaces are manifestly undulated with dip angles ranging between 55° and 10° (Fig. 11b). Similarly to PSF1, a thick phyllosilicate-rich layer lies roughly parallel to the PSF2 principal surfaces (Figs. 11b, 11d, and 11e

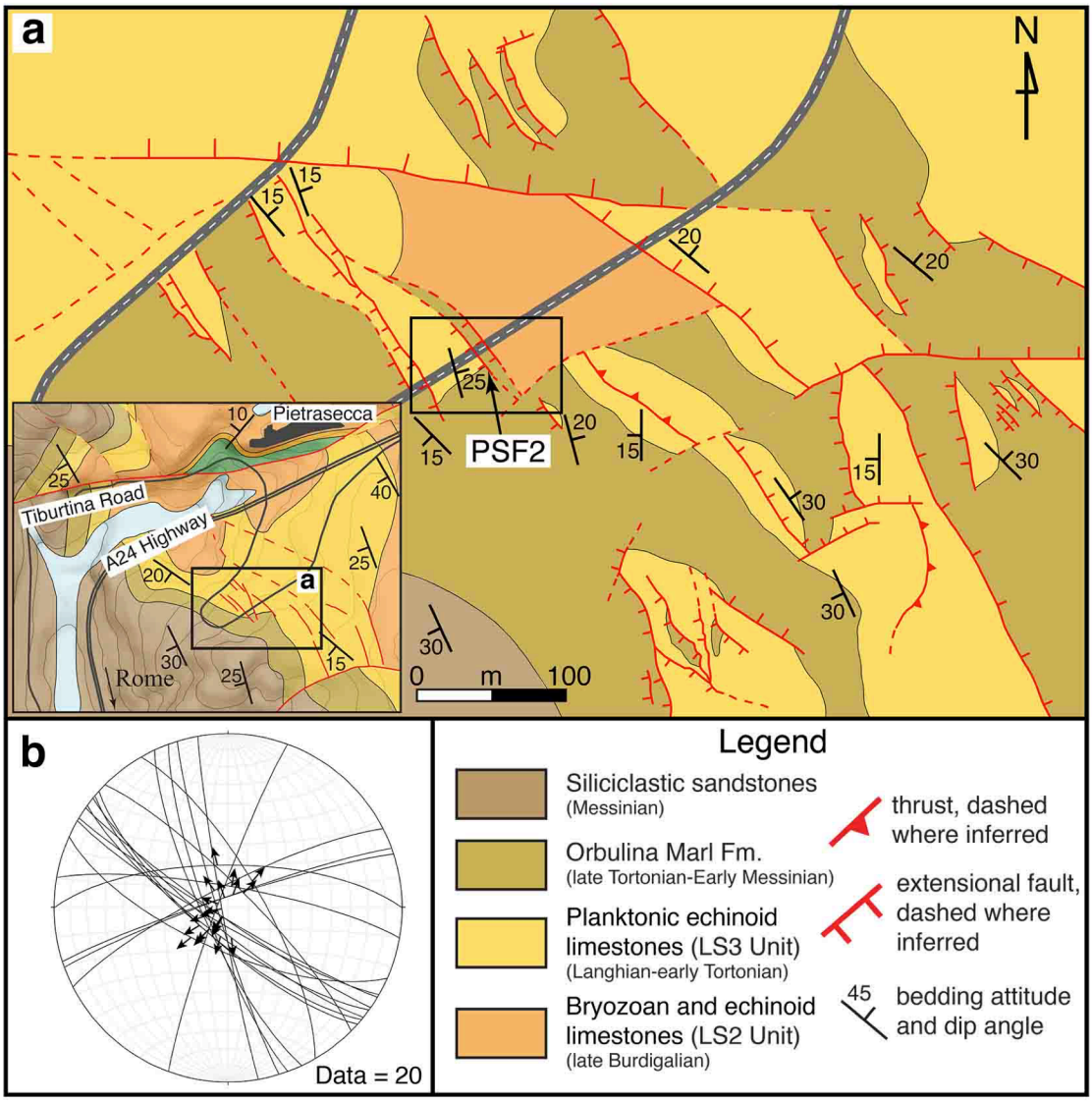


Figure 10. (a) Geological and structural map of the PSF2 area. Inset shows the PSF2 location in the Pietrasecca area. See Figs. 3(a) for the PSF2 location with respect to the PSF1 location. **(b)** Schmidt net (lower hemisphere) showing orientations of mesoscale faults and related slip vectors (dip-slip extensional movements) in the PSF2 area.

and is interposed between the hangingwall and the footwall. The PSF2 phyllosilicate-rich layer is much thicker (~6 m) than that observed along PSF1 (~15 cm). The phyllosilicate-rich layer is located immediately below the hangingwall hemipelagic marl, from which it originated. This layer is strongly foliated, as observed within the PSF1 phyllosilicate-rich layer, with SW-dipping (70°-80°) foliation planes oriented roughly parallel to the PSF2 main surfaces (Figs. 11d and 11e). Based on the lack of thrust-related doublings and overturned strata in the study area, we reject the

hypothesis that the occurrence of phyllosilicate layers along the PSF1 and PSF2 surfaces can be the result of a simple juxtaposition between marly and carbonate rocks arising from normal faulting of tectonically doubled successions or of overturned folds.

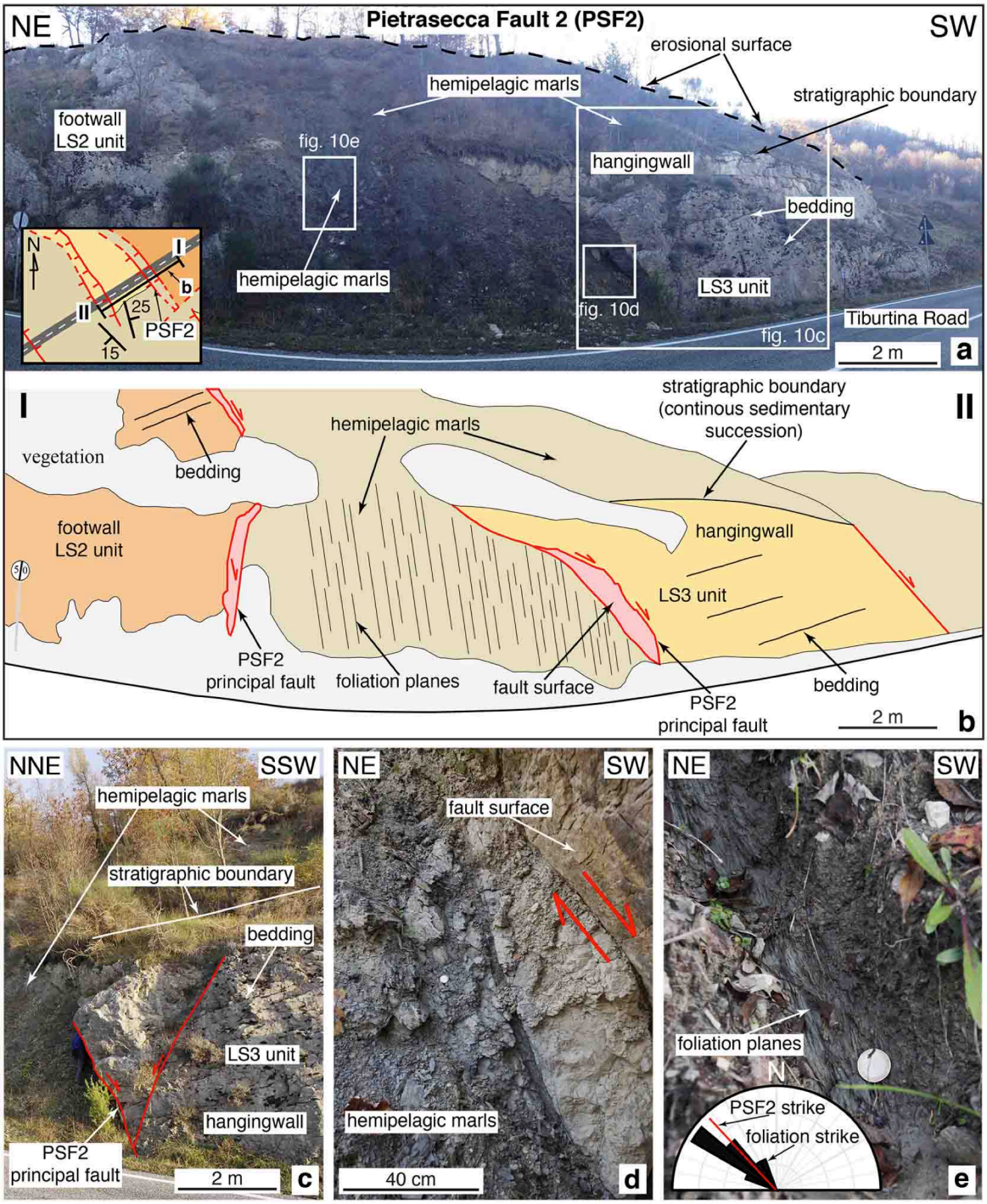


Figure 11. (a) Panoramic view of PSF2 along the Tiburtina Road and **(b)** line drawing showing exposures of the main fault structures (the Tiburtina Road is straight and its apparent curved shape in the photograph is due to the distortion related to the wide-angle lens). Note the continuous sedimentary succession in the hangingwall consisting of the LS3 unit carbonate deposits overlain by the hemipelagic marl deposits (Orbulina Marl. Fm.). The same marls are interposed within the PSF2 principal fault surfaces. **(c)** Detail of the hangingwall showing the stratigraphic boundary between LS3 unit and hemipelagic marl deposits. **(d)** Detail of the contact between the strongly foliated hemipelagic marls and the PSF2 principal surface. **(e)** Strongly foliated hemipelagic marls interposed along the PSF2 principal surfaces. Rose diagram shows foliation strike that is roughly parallel to the PSF2 strike (red line).

7. Mineral composition of siliciclastic sandstones and hemipelagic marls

Figs. 1a and 3a show the sampling sites of the siliciclastic sandstones (S1) and hemipelagic marls (S2) samples and complete mineralogical results are listed in Table 1. S1 consists essentially of phyllosilicate minerals (47%), plagioclase (22%), quartz (15%), calcite (9%), dolomite (6%), and K-feldspar (1%). The <2 μm grain-size fraction is characterized by illite (70%), mixed illite-smectite layers (15%), kaolinite (11%), and subordinate chlorite (4%). We identified non-clay minerals such as quartz, calcite, plagioclase, and gismondine in the clay fraction as well. Mixed illite-smectite are randomly ordered structures with an illite content of 30%.

S2 consists of phyllosilicate minerals (52%), calcite (39%), quartz (5%), plagioclase (3%), and dolomite (1%). In the <2 μm grain size fraction, among the phyllosilicates, illite is the most abundant mineral (47%) followed by mixed illite-smectite (22%), kaolinite (18%), and chlorite (13%). We identified two sub-populations of mixed illite-smectite layers. The first population corresponds to randomly ordered illite-smectite with an illite content of 40%, whereas the second population, is characterized by short-range ordered structures with an illite content of 70%. Overall, mineralogical compositions of S1 (siliciclastic sandstones) and S2 (hemipelagic marls) are similar to those of syn-orogenic deposits in central Apennines (Aldega et al., 2007; Critelli et al., 2007; Bigi et al., 2009; Smeraglia et al., 2014).

8. Further instances of phyllosilicate occurrence along extensional faults

We report and briefly describe further evidence of phyllosilicates occurrence along seismogenic or potentially-seismogenic extensional faults in carbonate rocks from the central Apennines, namely: (1) the Fiamignano Fault, (2) the Val Roveto Fault, and (3) the Tre Monti Fault (Table 2).

Fault	Displacement (m)	Lithology (hangingwall)	Lithology (footwall)	Phyllosilicate-rich layers	Phyllosilicate-rich fault rocks
Pietrasecca Fault 1 (PSF1)	75	limestones	limestones	yes	yes
Pietrasecca Fault 2 (PSF1)	25	limestones	limestones	yes	no
Fiamignano Fault	500-2000	marls, clay, and sandstones	limestones	yes	yes
Val Roveto Fault	100-2000	marls, clay, and sandstones	limestones and dolostones	no	yes
Tre Monti Fault	700-2000	marls, clay, and sandstones	limestones	no	yes

Table 2. Summary of studied faults.

8.1 Fiamignano Fault

The Fiamignano Fault is a SW-dipping and ~12 km long, active extensional fault (e.g., Bosi, 1975; Mariotti and Capotorti, 1988; Morewood and Roberts, 2000; Roberts and Michetti, 2004) with a vertical throw ranging from ~500 m to ~2000 m (Morewood and Roberts, 2000; Bigi and Costa Pisani, 2003; Bigi and Costa Pisani, 2005). Most displacement accumulated along the principal fault, which juxtaposes syn-orogenic deposits in the hangingwall with carbonate deposits in the footwall. The ~100 m thick, carbonate-hosted footwall damage zone consists of fractured carbonate rocks, patches of breccias, and low-displacement extensional faults. Within this damage zone, we observed the occurrence of several phyllosilicate-rich layers along low-displacement extensional faults (Fig. 12a). These layers, which are up to ~15 cm thick, lie parallel to fault surfaces and toward faults have a transition from clasts-supported to clay-supported cataclasites (Fig. 12b). Carbonate clasts are scattered within a clayey matrix and phyllosilicate content increases moving toward the fault surfaces (Fig. 12b). The phyllosilicate-rich layers are strongly foliated, with foliation planes oriented roughly parallel to the fault surfaces (Fig. 12b). These layers display structures similar to that of the phyllosilicate-rich layer along PSF1 (Fig. 7a). In the Fiamignano Fault case, the syn-orogenic deposits crop out only a few tens of meters above the footwall damage zone (Bigi and Costa Pisani, 2003; Bigi and Costa Pisani, 2005).

8.2 Val Roveto Fault

The Val Roveto Fault is a SW-dipping and ~60 km extensional/transtensional active fault (e.g., Montone and Salvini, 1991, 1993; Ciotoli et al., 1993; Galadini and Galli, 2000; Roberts and Michetti, 2004) with a vertical throw ranging from ~100 m to ~2000 m (e.g., Roberts and Michetti, 2004). Most displacement accumulated along the principal fault, which juxtaposes syn-orogenic deposits in the hangingwall with carbonate deposits in the footwall (Fig. 12c; e.g., Roberts and Michetti, 2004).

Along the Val Roveto principal fault, we observed the occurrence of a phyllosilicate-bearing foliated cataclasite (Fig. 12d). The foliated cataclasite is characterized by an anastomosed network of phyllosilicate-rich foliation planes oriented roughly parallel to the principal fault surface (Figs 12d-f). Foliation planes isolate carbonate sigmoids, which have their long axes oriented parallel to the principal fault surface (Figs. 12e and 12f). Foliation planes can be smooth and continuous, or rough and teeth-shaped, having geometries comparable to that of pressure solution seams (i.e., stylolites; Fig. 12f).

8.3 Tre Monti Fault

The Tre Monti Fault is a SSE-dipping and ~8 km extensional/transtensional active fault (Benedetti et al., 2013) with a vertical throw ranging from ~700 m up to ~2000 m (e.g., Morewood and Roberts, 2000; Cavinato et al., 2002; Smith et al., 2011; Smeraglia et al., 2016). The Tre Monti principal fault juxtaposes syn-orogenic deposits in the hangingwall with carbonate deposits in the footwall (Cavinato et al., 2002; Smeraglia et al., 2016). Synthetic faults are hosted within the carbonate bedrock of the footwall and juxtapose carbonate deposits in the hangingwall with carbonate deposits in the footwall (Smith et al., 2011; Smeraglia et al., 2016). Patches and lenses of phyllosilicate-bearing brownish ultracataclasite only occur above a grey carbonate cataclasite along the principal fault (Figs. 12g and 12h; Smeraglia et al., 2016).

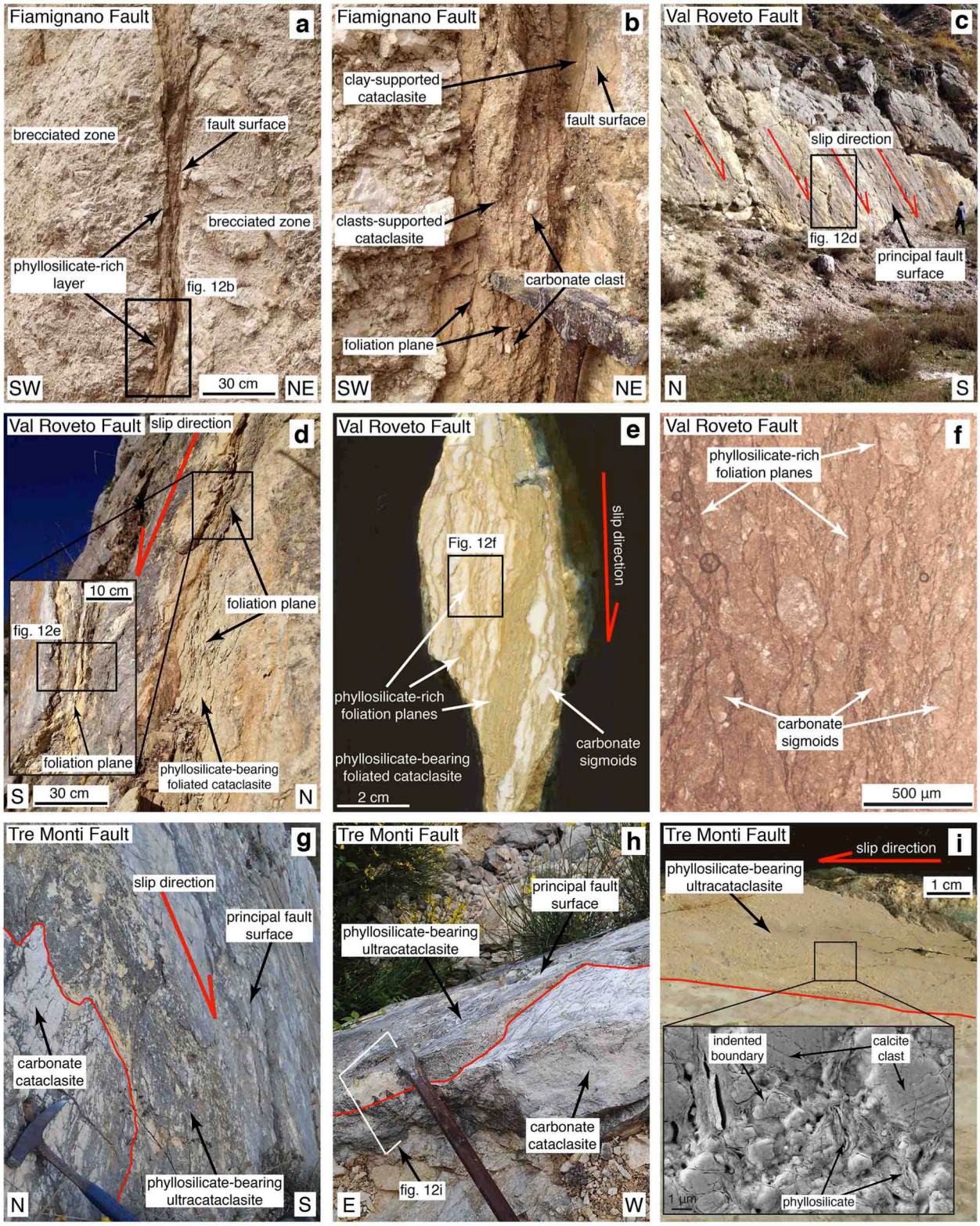


Figure 12. (a) and **(b)** Phyllosilicate-rich layers along low-displacement faults within the Fiamignano Fault footwall damage zone (latitude N 42°16'17" longitude E 13°11'11"). Carbonate clasts are scattered within a phyllosilicate-rich matrix. Foliation planes are oriented parallel to the fault surface. **(c)** Panoramic view of the Val Roveto principal fault (latitude N 41°55'25" longitude E 13°26'45"), juxtaposing syn-orogenic deposits (hemipelagic marls and siliciclastic sandstones) in the hangingwall with carbonate deposits in the footwall. **(d)** Detail of the Val Roveto principal fault showing the strongly foliated cataclasite. Foliation planes are oriented roughly parallel to principal fault surface. **(e)**

High resolution scan of hand sample from the foliated cataclasite cut parallel to slip direction. Note that phyllosilicate-rich foliation planes isolate carbonate sigmoids and define a strong foliation oriented roughly parallel to the principal fault surface. **(f)** Microphotograph of thin section under optical microscope (plane-polarized light) showing microstructures of the foliated cataclasite. Phyllosilicate-rich foliation planes are often characterized by teeth-shaped boundaries typical of pressure solution seams. **(g)** and **(h)** detail of the Tre Monti principal fault surface (latitude N 42°4'34" longitude E 13°29'57") showing patches and plagues of phyllosilicate-bearing ultracataclasite above the carbonate cataclasite. **(i)** High resolution scan of hand sample cut parallel to the slip direction showing the phyllosilicate-bearing ultracataclasite above the carbonate cataclasite. Inset for microstructures of phyllosilicate-bearing ultracataclasite (from thin section under electron microscope, FE-SEM Zeiss Auriga) showing carbonate clasts within a phyllosilicate-bearing matrix.

The phyllosilicate-bearing ultracataclasite consists of carbonate clasts, derived from the underlying carbonate cataclasite, scattered within a fine-grained matrix consisting of small carbonate clasts and phyllosilicates (Fig. 12i). Carbonate clasts, which are usually in contact with one another, have indented boundaries typical of pressure solution seams (i.e., stylolites; Fig. 12i).

9. Discussion

9.1 PSF1 and PSF2 activity and exhumation depth

PSF1 and PSF2 cut through the Pietrasecca-Tufo anticline, which developed during the Apennines compressional phase. Moreover, PSF1 and PSF2 are structurally compatible with the post-orogenic extensional regime that affected this area of the Apennines fold-thrust belt since about Pliocene time and is still (seismically) active (D'Agostino et al., 2001; Cavinato et al., 2002; Hunstad, 2003). However, no evidence of Holocene tectonic activity is available for PSF1 and PSF2, which cannot therefore be considered as active faults. Our hypothesis is that these two faults were mostly active during the post-orogenic phase probably in Pliocene time.

We used structural and thermal maturity data from syn-orogenic deposits to constrain the maximum exhumation depth of the exposed portions of PSF1 and PSF2. The hemipelagic marl deposits at the bottom of the syn-orogenic sedimentary succession are characterized by two sub-populations of mixed illite-smectite layers. The first population (illite content 40%) represents the

diagenetic component of the deposit, whereas the second population (illite content 70%) represents the detrital supply. The first population indicates a shallow burial and maximum paleotemperatures between 70° and 100 °C (Hoffman and Hower, 1979; Srodon, 1999). Assuming a pre-erosional geothermal gradient of 30°C/km (i.e., typical of the extensional tectonic setting of the Apennines; e.g., Mongelli et al., 1989), the burial depth of these hemipelagic marls was 2-2.5 km. This range is consistent with stratigraphic data from syn-orogenic deposits in this (~1,600 m thick; Milli and Moscatelli, 2000) and other areas of the central Apennines (e.g., Bigi et al., 2009), and with vitrinite reflectance data (Corrado et al., 2010). Excluding relevant erosion between the end of compressional tectonics and the beginning of post-orogenic extensional faulting, the exhumation depth for the exposed portion of these faults is ≤ 2.5 km.

9.2 Origin of phyllosilicate-rich material

Understanding the origin of phyllosilicate-rich materials observed along the studied faults is a fundamental pre-requisite for proposing a model for phyllosilicate involvement within carbonate fault zones during tectonic activity. From the geological, lithological, and stratigraphic setting of central Apennines, we infer that potential sources for the phyllosilicate-rich materials may include: (1) reworked eluvial-colluvial and gravel continental deposits (for the PSF1 and PSF2 case); (2) insoluble residue derived from pressure solution of the host carbonate rocks; and (3) materials derived from hemipelagic marls and phyllosilicate-rich syn-orogenic deposits (siliciclastic sandstones).

Reworked continental deposits can be excluded as potential source for the lack of typical mineral assemblage within the PSF1 phyllosilicate-rich layer. Both Compagnoni et al. (1993) and Aldega et al. (2009) showed that, in the Pietrasecca area, Holocene continental deposits bear volcanic minerals (leucite, augite, and phlogopite) and related weathering minerals (chabazite, phillipsite, and analcime), that were not observed in our X-ray diffraction analyses (Table 1).

We can also exclude the hypothesis that implies the phyllosilicates as the insoluble residue due to pressure solution of carbonate rocks (e.g., Viti et al., 2014; Petracchini et al., 2012) on the basis of the following observations:

(a) previous geochemical analyses of carbonate rocks (limestones and dolostones) from the central Apennines showed that insoluble residues (clay minerals and oxides) are < 0.5% of the bulk volume (e.g., Masi et al., 1996; De Vito et al., 2004; Tucci and Morbidelli, 2004; Anigrisani et al., 2011). Hence, considering a clayey insoluble residue of 0.5% in the PSF1 carbonate host rock, the 15 cm thick phyllosilicate-rich layer (35% of phyllosilicates) observed along PSF1 would require the solution of ~10.5 m of carbonates localized along the principal fault. Although this process cannot be theoretically excluded, we did not find evidence of such a pervasive pressure solution cleavage (i.e., stylolites) within the PSF1 and PSF2 carbonate-hosted fault rocks. Given little evidence for pressure solution within the studied fault rocks (Figs. 8b, 12f, and 12i) and the low insoluble residue of carbonate rocks in central Apennines, we suggest that their contribute of insoluble minerals is negligible.

(b) Anigrisani et al. (2011) showed that the insoluble residue of PSF1 carbonate host rocks consists of quartz, smectite, kaolinite, illite, rutile (Ti-bearing oxides), and feldspar. This mineralogical composition only partially overlaps that of PSF1 phyllosilicate-rich layer (Table 1). Conversely, plagioclase and chlorite, which do not occur in the Anigrisani et al. (2011) insoluble residue, indicate the input of syn-orogenic deposits within PSF1 phyllosilicate-rich layer;

(c) several carbonate-hosted fault zones in the central Apennines show evidence of pressure solution within carbonate fault rocks (e.g., Agosta and Kirschner, 2003; Storti et al., 2003; Agosta and Aydin, 2006; Billi, 2007, 2010; Smith et al., 2011). However, despite this evidence of pressure solution processes, previous authors did not document any evidence of phyllosilicates occurring within those carbonate-hosted fault zones. Therefore, we propose that the most suitable sources for the phyllosilicate-rich material within carbonate-hosted faults are hemipelagic marls and phyllosilicate-rich syn-orogenic deposits. The following observations corroborate this hypothesis:

(a) the mesoscale architecture of PSF2 show that phyllosilicate-rich layer derive from the overlying hemipelagic marls (Orbulina Marl Fm.; Fig. 11a);

(b) geological mapping and structural analysis (Fig. 3a) show that hemipelagic marls and phyllosilicate-rich syn-orogenic deposits are located right above the exposed fault zones (at a distance of a few meters in the case of PSF1 and PSF2, and up to a few tens of meters in the case of the Fiamignano Fault). In addition, phyllosilicate-rich fault rocks occur only along principal fault surfaces juxtaposing phyllosilicate-rich deposits with carbonate deposits (e.g., Tre Monti Fault and Val Roveto Fault).

(c) XRD results (Table 1) show that the phyllosilicate-rich layer of PSF1 consists of clay minerals (illite, mixed layers illite-smectite, kaolinite and chlorite), quartz, plagioclase, and K-feldspar. We interpret compositional suite to result from the mixing of siliciclastic sandstones with hemipelagic marls (Orbulina Marl Fm.) during fault activity. However, both calcite and dolomite, which are present in the siliciclastic sandstones and the hemipelagic marls, are absent within the phyllosilicate-rich layer. The lack of carbonates within the PSF1 phyllosilicate-rich layer suggests slightly acidic fluids circulated along the principal fault surface during tectonic activity and/or superficial weathering, or pressure solution mechanism acting during tectonic activity, which dissolved the carbonate minerals. Fluids circulation focused along the PSF1 principal surface may also account for the neoformation of clay minerals (e.g., van der Pluijm et al. 2001) within the PSF1 phyllosilicate-rich layer, such as kaolinite, which increases its content in the phyllosilicate-rich layers with respect to that observed in siliciclastic sandstones and hemipelagic marls (Table1).

(d) microstructural observations and clast-size distributions show that the siliciclastic sandstones texture is comparable to the chaotic breccia texture within the PSF1 phyllosilicate-rich layer (Figs. 8b, 8i, and 9a).

9.3 Model for clay injection and smearing within carbonate fault zone

The PSF1 and PSF2 principal surfaces are strongly undulated along the dip direction (Figs 4b and 11a). This kind of fault surfaces generally develops when faults cut through multilayers characterized by strong rheological contrasts, based on field studies, laboratory experiments, and numerical simulations (e.g., Childs et al., 1996; Schöpfer et al., 2006; Schöpfer et al., 2007a, 2007b; Welch et al., 2009; Roche et al., 2012). With displacement, these faults generate pull-aparts and dilational jogs, within which material can inject (e.g., Lehner and Pilaar, 1997; Ferrill and Morris, 2003; van der Zee et al., 2003; Ferrill and Morris, 2008). Based on this prior work and our observations, we propose a fault evolution where the rheological contrast is controlled by the occurrence of thin (~80 m thick) less competent hemipelagic marl deposits (Orbulina Marls Fm.) interposed between more competent carbonates (~4,000-5,000 m thick) and siliciclastic sandstones (~2,000 m thick) deposits. Consequently the fault evolves by:

(1) early-stage fault development, where the extensional fault propagated upward throughout the sedimentary succession (Fig. 13a), with steeply dipping (70°-90°; Fig. 4a) segments in competent carbonates and sandstones, and shallow dipping (10°-20°; Fig. 11a) segments in less competent marls (Fig. 13a; e.g., Roche et al., 2012);

(2) the staircase fault geometry led to the development of pull-apart (i.e., dilational jog), as fault walls with different fault dip geometries were juxtaposed (Fig. 13b). Horizontal dilation enabled the downward injection and flow of phyllosilicate-rich materials from the above-lying hemipelagic marls and syn-orogenic deposits toward the carbonate-hosted fault zone (Figs. 11a and 13b). The horizontal component of the displacement and consequently the horizontal dilation are inversely related with fault dip. Accordingly, we explain the ~6 m thick phyllosilicate-rich layer along PSF2 with the occurrence of the gentle dipping (10°-20°) fault segment showed in Fig. 11a. We propose that phyllosilicate-rich layers along carbonate-on-carbonate faults are the result of downward injection of clay into carbonate-hosted pull-aparts concurrent with clay smearing during

fault movement (Lehner and Pilaar, 1997). We refer to injection as the process involving continuous extrusion of plastic clays from a source bed and squeezing along fault zone, enhanced by poor cohesion and soft/plastic behavior of clays (Lehner and Pilaar, 1997). Due to the stratigraphic setting of the central Apennines we infer that injection is mainly downward directed into the carbonate-hosted fault zones. However, we cannot exclude lateral movements of clay along fault surfaces once the injection occurred. Field studies, numerical simulations, and analogue models show that injection and squeezing of soft rocks along faults can occur at depth, if the ratio between the rock strength and the effective stress is sufficiently low to allow flow into voids (e.g., van der Zee et al., 2003; van der Zee and Urai, 2005). Laboratory measurements show that marls have a far lesser strength (3-40 MPa; Altindag, 2012 and references therein) than carbonates and sandstones (46-138 MPa and 35-173 MPa, respectively; Altindag, 2012 and references therein). These observations satisfy the criteria suggested by van der Zee et al. (2003) for clay injection/squeezing, which can occur up to 2 km depth (i.e., the exhumation depth of PSF1 and PSF2) within pull-aparts along extensional faults;

(3) a displacement increase removes the asperity (i.e., pull-apart) generated by the irregular fault trace, which is bypassed by the formation of a smoother fault trace (Fig. 13c; e.g., Schöpfer et al., 2007a, 2007b; Brodsky et al., 2011). In this manner, thick lenses of phyllosilicates, previously isolated within pull-apart (i.e., the PSF2 case), can be thinned, smeared, and concentrated along the carbonate-on-carbonate fault surfaces (i.e., the PSF1 and Fiamignano Fault cases; Figs. 6f and 12a) and mixed within the carbonate-hosted fault core (i.e., the PSF1 case; Figs. 6b-d). Moreover, faulting also juxtaposes the syn-orogenic deposits in the hangingwall with the carbonate deposits in the footwall (Fig. 13d). This process can contribute to clay smearing and mixing along the carbonate principal surface as observed for the Val Roveto Fault and Tre Monti Fault (Figs. 12d and 12g).

We believe that the above-proposed model can be applied to other extensional tectonic settings (e.g., northern Apennines, Rhine Graben, Middle East, Greece) where extensional faults cut

through multilayered stratigraphic succession characterized by strong rheological contrasts (e.g., competent carbonate rocks interbedded with less competent marly and clayey deposits; Bally et al., 1986; Nairn and Alsharhan, 1997; Schumacher, 2002; Kilias et al., 2015). Complementary to the classical clay-smearing model (e.g., Vrolijk et al., 2015), we propose that phyllosilicate-rich materials can also downward inject into fault zones, which could explain the phyllosilicate occurrence along carbonate-on-carbonate faults (Fig. 13b).

9.4 Deformation mechanisms within the phyllosilicate-rich layer (PSF1)

The following observations show that the PSF1 phyllosilicate-rich layer was tectonically sheared:

(1) microstructural observations (Fig. 8d) and clast size distribution (Figs. 9a) show an increase in clasts comminution approaching the principal fault surface. This type of process commonly acts along faults at shallow crustal levels (< 3 km depth) during progressive tectonic deformation and displacement accumulation (e.g., Agosta and Aydin, 2006; Billi et al., 2003; Billi, 2010; Melosh et al., 2014);

(2) foliation planes, phyllosilicate bands, long axes of clasts, and phyllosilicate [001] planes are aligned roughly parallel to the principal fault surface (Figs. 7a, 8a, and 11d). We interpret the concentration and alignment of phyllosilicates within phyllosilicate bands to result from deformation-induced segregation processes (Gibson, 1998), as commonly observed within phyllosilicate-rich fault rocks (e.g., Bos and Spiers, 2001; Ujiie et al., 2011; Haines et al., 2013).

The occurrence of phyllosilicate bands suggest that, in addition to cataclasis, frictional sliding was active during faulting along the principal fault surface. On the other hand, the main deformation mechanisms acting within the carbonate-hosted damage zone of PSF1 were cataclasis, slip localization (i.e., sharp slip surfaces with truncated clasts), and extensional fracturing, as commonly observed within many carbonate fault zones (e.g., Agosta and Aydin, 2006; Billi, 2010; Fondriest et al., 2012; Fondriest et al., 2013; Fondriest et al., 2015; Doglioni et al., 2014; Smeraglia

et al., 2016). Due to little evidence for pressure solution, we suggest that this deformation mechanism played a modest role.

The involvement of phyllosilicates within carbonate-hosted faults has a strong influence both on mechanical behavior of fault rocks and on deformation mechanisms activated during faulting (e.g., Bos et al., 2000; Bos and Spiers, 2002; Haines et al., 2013). In particular, due to the weakness of phyllosilicates with respect to strong carbonates, frictional sliding along phyllosilicates bands (Figs. 8f-h) is energetically favored rather then cataclasis within carbonate rocks (e.g., Tesei et al., 2013; Viti et al., 2014). For this reason, within extensional tectonic settings dominated by massive carbonate rocks with clayey interbeds (e.g., central and northern Apennines, Rhine Graben, Middle East, Greece; Bally et al., 1986; Nairn and Alsharhan, 1997; Schumacher, 2002; Cosentino et al., 2010; Kilias et al., 2015), the occurrence of phyllosilicate-rich layers along carbonate-hosted extensional faults can determine localized and weak deformation zones promoting further displacement accommodation (e.g., Vrolijk et al., 1990).

9.5 Implications for seismic-slip propagation

Experimental studies on clay-bearing fault gouges show that phyllosilicates have a strong influence on the behavior of seismogenic faults in terms of earthquake nucleation and slip propagation (e.g., Faulkner et al., 2011). Wet phyllosilicate-rich gouges deformed at seismic slip rates ($\geq$ 1 m s^{-1}) behave as very weak materials. Hence phyllosilicate-rich zones significantly reduce the resistance to earthquake slip propagation, promoting co-seismic fault slip (e.g., Brantut et al., 2008; Ferri et al., 2010; Ujiie and Tsutsumi, 2010; Ujiie et al., 2011; Bullock et al., 2015). Moreover, scientific drilling through shallow seismogenic fault zones (< 1500 m depth) documented that phyllosilicates frequently concentrate along narrow zones (few millimeters up to few centimeters thick; e.g., Choo and Chang, 2000; Ujiie and Tutsumi, 2010; Sutherland et al., 2012; Chester et al., 2013; Li et al., 2013; Hirono et al., 2014; Warr et al., 2014). Geological observations along these narrow zones suggest that they have accommodated earthquake slip (e.g.,

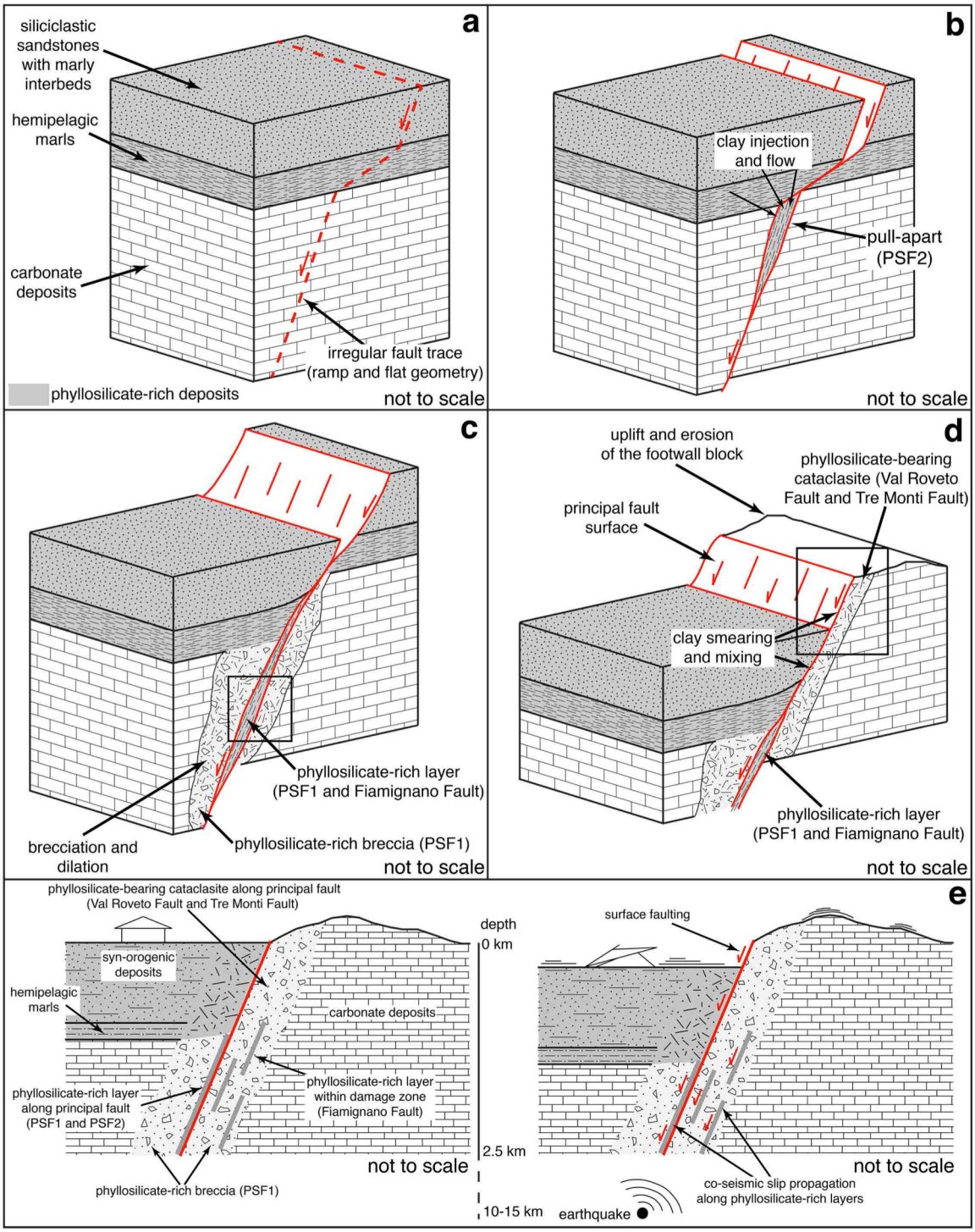


Figure 13. Cartoon showing the conceptual model for phyllosilicate injection and smearing within carbonate-hosted fault zones. **(a)** During the early stage of fault development, the fault propagates upward through a heterogeneous sedimentary succession. The result is a staircase fault geometry with steep fault dips in competent carbonates and sandstones, and shallow fault dips in less competent marls. **(b)** Displacement accumulation along the boundary between carbonates and marls promotes extensional fracturing and dilation along a pull-apart (i.e., dilational jogs). Pull-apart opening enables the downward injection and flow of phyllosilicate-rich materials from the overlying phyllosilicate-rich deposits. Further displacement accumulation concentrates and smears the phyllosilicate-rich material **(c)** into narrow layers along carbonate-on-carbonate faults and **(d)** along fault surfaces juxtaposing phyllosilicate-rich deposits in the hangingwall with the carbonate deposits in the footwall. **(e)** Cartoon showing the effect of phyllosilicate-rich layers within carbonate-hosted faults during earthquake slip propagation up to the Earth's surface. Phyllosilicate-rich layers can behave as a very weak material promoting earthquake-slip propagation up to the Earth's surface and generating co-seismic fault scarps and surface faulting, which are widely documented for recent and historical earthquakes in the central Apennines and elsewhere.

Boullier et al., 2009; Li et al., 2013; Chou et al., 2012; Fulton et al., 2013). It is concluded that narrow zones rich in phyllosilicates facilitate earthquake-slip propagation up to the Earth's surface (e.g., Kameda et al., 2015; Ikari et al., 2015). Accordingly, we suggest that, within shallow (< 3 km depth) carbonate-hosted active faults, that for narrow layers rich in phyllosilicates as in the PSF1 and Fiamignano Fault cases can facilitate co-seismic slip propagation up to the Earth's surface and promote surface faulting (Fig. 13e). This notion can be regionally significant for seismic hazard assessment in the central Apennines of Italy and in other seismically-active extensional tectonic settings, where seismogenic faults cut through sedimentary successions characterized by clayey horizons and/or strong rheological contrasts.

10. Conclusions

We integrated geological mapping with structural and mineralogical analyses of shallow (exhumed from depths < 3 km) potentially-seismogenic extensional faults cutting through the sedimentary succession of the central Apennines and concluded that:

(1) for the first time in the seismically-active extensional setting of the central Apennines, the occurrence of phyllosilicates is documented into carbonate-hosted extensional faults (i.e., carbonate-on-carbonate faults). These phyllosilicates mainly derived from above-lying phyllosilicate-rich deposits, rather than from pressure solution of carbonate host rocks or from other possible processes, and were involved in the fault-zone evolution;

(2) phyllosilicate-rich layers (e.g., PSF1, PSF2 and Fiamignano Fault) originated by downward injection of clay into carbonate-hosted pull-aparts coupled with smearing along fault surfaces. One limitation to our results is that we do not know the maximum depth along faults reached by this downward injection of clays. This theme will be the subject of future studies.

(3) due to further clay smearing along fault surfaces, phyllosilicates mixed within carbonate cataclasites (e.g., Tre Monti Fault and Val Roveto Fault);

(4) even in extensional tectonic settings dominated by high friction lithologies (e.g., carbonate rocks), the occurrence of localized layers rich in weak phyllosilicates along seismogenic faults at depth can be a regionally important control on co-seismic slip propagation up to the Earth's surface with strong implications on seismic hazard.

11. References

Agosta, F., Kirschner, D.L., 2003. Fluid conduits in carbonate-hosted seismogenic normal faults of central Italy. J. Geophys. Res. 108, B42221. doi:10.1029/2002JB002013.

Agosta, F., Aydin, A., 2006. Architecture and deformation mechanism of a basin-bounding normal fault in Mesozoic platform carbonates, central Italy. J. Struct. Geol. 28, 1445–1467. doi:10.1016/j.jsg.2006.04.006.

Alessio, G., Alfonsi, L., Brunori, C. A., Cinti, F. R., Civico, R., Cucci, L., EMERGEO Working Group, 2009. Evidence for surface rupture associated with the Mw 6.3 L'Aquila earthquake sequence of April 2009 (central Italy). Terra Nova 22, 43-51.

Aldega, L., Botti, F., Corrado, S., 2007. Clay mineral assemblages and vitrinite reflectance in the Laga Basin (Central Apennines Italy): what do they record? Clay and Clay Minerals 55, 504-518. doi:10.1346/CCMN.2007.0550505.

Aldega, L., Cuadros, J., Laurora, A., Rossi, A., 2009. Weathering of phlogopite to beidellite in a karstic environment. Am. J. Sci. 309, 689–710. doi:10.2475/08.2009.03.

Altindag, R., 2012. Correlation between P-wave velocity and some mechanical properties for sedimentary rocks. The Journal of The Southern African Institute of Mining and Metallurgy 112, 229-237.

Anigrisani, A.C., Calcaterra, D., Cappelletti, P., Colella, A., Parente, M., Prikryl, R., De Gennaro, M., 2011. Geological features , technological characterization and weathering phenomena of the Miocene Bryozoan and Lithothamnion limestones (central-southern Italy). Ital. J. Geosci. 130, 75–92. doi:10.3301/IJG.2010.25.

Antonellini, M.A., Aydin, A., Pollard, D.D., 1994. Microstructure of deformation bands in porous sandstones at Arches National Park, Utah. J. Struct. Geol. 16, 941-959. doi:10.1016/0191-8141(94)90077-9.

Bally, A.W., Burbi, L., Cooper, C., G.R., 1986. Balanced cross sections and seismic reflecion profiles across the central Apennines. Mem. della Soc. Geol. Ital. 35, 257–310.

Balsamo, F., Aldega, L., De Paola, N., Faoro, I., Storti, F., 2014. The signature and mechanics of earthquake ruptures along shallow creeping faults in poorly lithified sediments. Geology 42, 435–438. doi:10.1130/G35272.1.

Benedetti, L., Manighetti, I., Gaudemer, Y., Finkel, R., Malavieille, J., Pou, K., Arnold, M., Aumaître, G., Bourlès, D., Keddadouche, K., 2013. Earthquake synchrony and clustering on Fucino faults (central Italy) as revealed from in situ ^{36}Cl exposure dating. J. Geophys. Res. Solid Earth 118, 4948–4974. doi:10.1002/jgrb.50299.

Bigi, S., Costa Pisani, P., 2003. The" pre-thrusting" Fiamignano normal fault. Boll. della Soc. Geol. It. 122, 267–276.

Bigi, S., Costa Pisani, P., 2005. From a deformed Peri-Tethyan carbonate platform to a fold-and-thrust-belt: An example from the Central Apennines (Italy). J. Struct. Geol. 27, 523–539. doi:10.1016/j.jsg.2004.10.005.

Bigi, S., Milli, S., Corrado, S., Casero, P., Aldega, L., Botti, F., Moscatelli, M., Stanzione, O., Falcini, F., Marini, M., 2009. Stratigraphy, structural setting and burial history of the Messinian Laga basin in the context of Apennine foreland basin system. J. Mediterr. Earth Sci. 1, 61–84. doi:10.3304/JMES.2009.006.

Billi, A., Salvini, F., Storti, F., 2003. The damage zone-fault core transition in carbonate rocks: implications for fault growth, structure and permeability. J. Struct. Geol. 25, 1779–1794. doi:10.1016/S0191-8141(03)00037-3.

Billi, A., Tiberti, M.M., Cavinato, G.P., Cosentino, D., Di Luzio, E., Keller, J.V.A., Kluth, C., Orlando, L., Parotto, M., Praturlon, A., Romanelli, M., Storti, F., Wardell, N., 2006. First results from the CROP-11 deep seismic profile, central Apennines, Italy: evidence of mid-crustal folding. J. Geol. Soc. London. 163, 583–586. doi:10.1144/0016-764920-002.

Billi, A., 2007. On the extent of size range and power law scaling for particles of natural carbonate fault cores. J. Struct. Geol. 29, 1512–1521. doi:10.1016/j.jsg.2007.06.007.

Billi, A., 2010. Microtectonics of low-P low-T carbonate fault rocks. J. Struct. Geol. 32, 1392–1402. doi:10.1016/j.jsg.2009.05.007.

Bolognesi, F., Bistacchi, A., 2016. Weakness and mechanical anisotropy of phyllosilicate-rich cataclasites developed after mylonites of a low-angle normal fault (Simplon Line, Western Alps). J. Struct. Geol. 83, 1–12. doi:10.1016/j.jsg.2015.11.009.

Bos, B., Peach, C., Spiers, C.J., 2000. Frictional-viscous flow of simulated fault gouge caused by the combined effects of phyllosilicates and pressure solution. Tectonophysics 327, 173–194. doi:10.1016/S0040-1951(00)00168-2.

Bos, B., Spiers, C.J., 2001. Experimental investigation into the microstructural and mechanical evolution of phyllosilicate-bearing fault rock under conditions favouring pressure solution. J. Struct. Geol. 23, 1187–1202. doi:10.1016/S0191-8141(00)00184-X.

Bos, B., Spiers, C.J., 2002. Frictional-viscous flow of phyllosilicate-bearing fault rock: Microphysical model and implications for crustal strength profiles. J. Geophys. Res. 107, 2028. doi:10.1029/2001JB000301.

Bosi, C., 1975. Observazioni preliminari su faglie probabilmente attive nell'Appennino Centrale. Boll. della Soc. Geol. Ital. 94, 827-859.

Boullier, A.M., Yeh, E.C., Boutareaud, S., Song, S.R., Tsai, C.H., 2009. Microscale anatomy of the 1999 Chi-Chi earthquake fault zone. Geochemistry Geophys. Geosystems 10, Q03016. doi:10.1029/2008GC002252.

Brandano, M., Brilli, M., Corda, L., Lustrino, M., 2010. Miocene C-isotope signature from the central Apennine successions (Italy): Monterey vs. regional controlling factors. Terra Nova 22, 125–130. doi:10.1111/j.1365-3121.2010.00925.x.

Brantut, N., Schubnel, A., Rouzaud, J.N., Brunet, F., Shimamoto, T., 2008. High-velocity frictional properties of a clay-bearing fault gouge and implications for earthquake mechanics. J. Geophys. Res. Solid Earth 113, 1–18. doi:10.1029/2007JB005551.

Brodsky, E.E., Gilchrist, J.J., Sagy, A., Collettini, C., 2011. Faults smooth gradually as a function of slip. Earth Planet. Sci. Lett. 302, 185–193. doi:10.1016/j.epsl.2010.12.010.

Bullock, R.J., De Paola, N., Holdsworth, R.E., Trabucho-Alexandre, J., 2014. Lithological controls on the deformation mechanisms operating within carbonate-hosted faults during the seismic cycle. J. Struct. Geol. 58, 22–42. doi:10.1016/j.jsg.2013.10.008.

Bullock, R.J., De Paola, N., Holdsworth, R.E., 2015. An experimental investigation into the role of phyllosilicate content on earthquake propagation during seismic slip in carbonate faults. J. Geophys. Res. Solid Earth 120, 3187–3207. doi:10.1002/2015JB011914.

Carminati, E., Corda, L., Mariotti, G., Brandano, M., 2007. Tectonic control on the architecture of a Miocene carbonate ramp in the Central Apennines (Italy): Insights from facies and backstripping analyses. Sediment. Geol. 198, 233–253. doi:10.1016/j.sedgeo.2006.12.005.

Carminati, E., Lustrino, M., Doglioni, C., 2012. Geodynamic evolution of the central and western Mediterranean: tectonics vs. igneous petrology constraints. Tectonophysics 579, 173–192. doi:10.1016/j.tecto.2012.01.026.

Carminati, E., Corda, L., Mariotti, G., Scifoni, A., Trippetta, F., 2013. Mesozoic syn- and postrifting evolution of the central Apennines, Italy: the role of triassic evaporites. J. Geol. 121, 327–354. doi:10.1086/670730.

Carpenter, B.M., Marone, C., Saffer, D.M., 2011. Weakness of the San Andreas Fault revealed by samples from the active fault zone. Nat. Geosci 4, 251–254. doi:10.1038/ngeo1089.

Carpenter, B.M., Saffer, D.M., Marone, C., 2015. Frictional properties of the active San Andreas Fault at SAFOD: Implications for fault strength and slip behavior. J. Geophys. Res. Solid Earth 120, 5273–5289. doi:10.1002/2015JB011963.

Cavinato, G.P., De Celles, P.G., 1999. Extensional basins in tectonically bimodal central Apennines fold-thrust belt, Italy : Response to corner flow above a subducting slab in retrograde motion. Geology 27, 955–958. doi:10.1130/0091-7613.

Cavinato, G.P., Miccadei, E., 2000. Pleistocene carbonate lacustrine deposits: Sulmona basin (central Apennines, Italy). In Gierlowski-Kordesch, E.H., Kelts, K.R., (Ed.), Lake basins through space and time. AAPG Studies in Geology 46, 517-526.

Cavinato, G.P., Carusi, C., Dall'asta, M., Miccadei, E., Piacentini, T., 2002. Sedimentary and tectonic evolution of Plio-Pleistocene alluvial and lacustrine deposits of Fucino Basin (central Italy). Sediment. Geol. 148, 29–59. doi:10.1016/S0037-0738(01)00209-3.

Cello, G., Deiana, G., Mangano, P., Mazzoli, S., Tondi,

E., Ferreli, L., Maschio, L., Michetti, A. M., Serva, L., Vittori, E., 1998. Evidence for surface faulting during the September 26, 1997, Colfiorito (central Italy) earthquakes. J. Earthq. Eng. 2, 303-324.

Chester, F.M., Rowe, C., Ujiie, K., Kirkpatrick, J., Regalla, C., Remitti, F., Moore, C.J., Toy, V., Wolfson-Schwehr, M., Bose, S., Kameda, J., Mori, J.J., Brodsky, E., Eguchi, E., Toczko, S., Expedition 343 and 343T Scientists, 2013. Structure and composition of the plate-boundary slip zone for the 2011 Tohoku-Oki earthquake. Science 342, 1208-1211. doi: 10.1126/science.1243719

Chiaraluce, L., 2012. Unravelling the complexity of Apenninic extensional fault systems: A review of the 2009 L'Aquila earthquake (Central Apennines, Italy). J. Struct. Geol. 42, 2–18. doi:10.1016/j.jsg.2012.06.007.

Childs, C., Nicol, A., Walsh, J.J., Watterson, J., 1996. Growth of vertically segmented normal faults. J. Struct. Geol. 18, 1389–1397. doi:10.1016/S0191-8141(96)00060-0.

Choo, C.O., Chang, T.W., 2000. Characteristics of clay minerals in gouges of the Dongrae fault, southeastern Korea, and implications for fault activity. Clays Clay Miner. 48, 204–212. doi:10.1346/CCMN.2000.0480206.

Chou, Y.M., Song, S.R., Aubourg, C., Song, Y.F., Boullier, A.M., Lee, T.Q., Evans, M., Yeh, E.C., Chen, Y.M., 2012. Pyrite alteration and neoformed magnetic minerals in the fault zone of the Chi-Chi earthquake (M_w 7.6, 1999): Evidence for frictional heating and co-seismic fluids. Geochemistry, Geophys. Geosystems 13, 1–17. doi:10.1029/2012GC004120.

Ciotoli, G., Etiope, G., Lombardi, S., Naso, G., Tallini, M., 1993. Geological and soil-gas investigation for tectonic prospecting: preliminary results over the Val Roveto fault (central Italy). Geol. Rom. 29, 483-493.

Cipollari, P., Cosentino, D., Parotto, M., 1995. Modello cinematico-strutturale dell'Italia Centrale. Studi Geol. Camerti, Spec. vol. 1995/2, 135-143.

Civitelli, G., Brandano, M., 2005. Atlante delle litofacies e modello deposizionale dei calcari a briozoi e Litotamni nella Piattaforma carbonatica lazialeabruzzese. Boll. della Soc. Geol. It. 124, 611–643.

Collettini, C., Niemeijer, A., Viti, C., Marone, C., 2009. Fault zone fabric and fault weakness. Nature 462, 907–910. doi:10.1038/nature08585.

Compagnoni, B., Galluzzo, F., Giovagnoli, M.C., Lembo, P., Molinari, V., Pampaloni, M.L., Pichezzi, R.M., Rossi, M., Salvati, L., Santantonio, M., Raffi, I., Chiocchini, U., 1993. Note illustrative del foglio 367 "Tagliacozzo". Servizio Geologico d'Italia, Roma.

Corrado, S., Aldega, L., Zattin, M., 2010. Sedimentary vs. tectonic burial and exhumation along the Apennines (Italy). J. Virtual Explor. 36. doi:10.3809/jvirtex.2009.00232.

Cosentino, D., Carboni, M.G., Fabio, Cipollari, P., Di Bella, L., Florindo, F., Laurenzi, M.A., Sagnotti, L., 1997. Integrated stratigraphy of the Tortonian/Messinian boundary: The Pietrasecca composite section (central Apennines, Italy). Eclogae geol. Helv. 90, 229-244. doi:0012-9402/97/020229-16.

Cosentino, D., Cipollari, P., Marsili, P., Scrocca, D., 2010. Geology of the central Apennines; a regional review. J. Virtual Explor. 36. http://dx.doi.org/10.3809/jvirtex.2010.00223.

Critelli, S., La Pera, E., Galluzzo, F., Milli, S., Moscatelli, M., Perrotta, S., Santantonio, M., 2007. Interpreting siliciclastic-carbonate detrital modes in foreland basin system: an example from Upper Miocene arenites of the central Apennines, Italy. Geol. Soc. Am. Special Paper 420, 107-133.

D'Agostino, N., Giuliani, R., Mattone, M., Bonci, L., 2001. Active crustal extension in the Central Apennines (Italy) inferred from GPS measurements in the interval 1994-1999. Geophys. Res. Lett. 28, 2121–2124. doi:10.1029/2000GL012462.

Damiani, A.V., 1977. Osservazioni di campagna sulle litofacies triassiche e liassiche di Filettino (Monti Simbruini-Appennino centrale). Boll. Serv. Geol. Ital. 96, 315–342.

Damiani, A.V., Chiocchini, M., Colacicchi, R., Mariotti, G., Parotto, M., Passeri, M., Praturlon, A., 1991. Elementi litostratigrafici per una sintesi delle facies carbonatiche meso-cenozoiche dell'Appennino centrale. In Tozzi, M., Cavinato, G.P., Parotto, M., (Ed.) Studi preliminari all'acquisizione dati del profilo CROP 11 Civitavecchia-Vasto. Studi Geol. Camerti, Spec. Vol. 1991/2, 187–213.

Demurtas, M., Fondriest, M., Balsamo, F., Clemenzi, L., Storti, F., Bistacchi, A., Di Toro, G., 2016. Structure of a normal seismogenic fault zone in carbonates: The Vado di Corno Fault, Campo Imperatore, Central Apennines (Italy). J. Struct. Geol. 90, 185-206. http://dx.doi.org/10.1016/j.jsg.2016.08.004.

De Vito, C., Ferrini, V., Mignardi, S., Piccardi, L., Tuteri, R., 2004. Mineralogical-petrographic and

geochemical study to identify the provenance of limestone from two archaeological sites in the Sulmona Area (L'Aquila, Italy). J. Archaeol. Sci. 31, 1383–1394. doi:10.1016/j.jas.2004.03.002.

Doglioni, C., 1991. A proposal of kinematic modelling for W-dipping subductions - Possible applications to the Tyrrhenian - Apennines system. Terra Nov. 3/4, 423–434.

Doglioni, C., Gueguen, E., Sàbat, F., Fernandez, M., 1997. The Western Mediterranean extensional basins and the Alpine orogen. Terra Nova. doi:10.1046/j.1365-3121.1997.d01-18.x.

Doglioni, C., D'Agostino, N., Mariotti, G., 1998. Normal faulting vs regional subsidence and sedimentation rate. Mar. Pet. Geol. doi:10.1016/S0264-8172(98)00052-X.

Doglioni, C., Barba, S., Carminati, E., Riguzzi, F., 2014. Fault on–off versus coseismic fluids reaction. Geosci. Front. 5, 767–780. doi:10.1016/j.gsf.2013.08.004.

Dondi, L., Papetti, I., Tedeschi, D., 1966. Stratigrafia del pozzo Trevi 1 (Lazio). Geol. Rom. 5, 249-262.

EMERGEO Working Group, 2016. Terremoto di Amatrice del 24 agosto 2016: Effetti Cosismici doi: 10.5281/zenodo.61566.

Engelder, J.T., 1974. Cataclasis and the Generation of Fault Gouge. Bull. Geol. Soc. Am. 85, 1515–1522. doi:10.1130/0016-7606(1974)85<1515:catgof>2.0.co;2.

Faulkner, D., Lewis, A., Rutter, E., 2003. On the internal structure and mechanics of large strike-slip fault zones: field observations of the Carboneras fault in southeastern Spain. Tectonophysics 367, 235–251. doi:10.1016/S0040-1951(03)00134-3.

Faulkner, D.R., Mitchell, T.M., Behnsen, J., Hirose, T., Shimamoto, T., 2011. Stuck in the mud? Earthquake nucleation and propagation through accretionary forearcs. Geophys. Res. Lett. 38, L18303. doi:10.1029/2011GL048552.

Ferri, F., Di Toro, G., Hirose, T., Shimamoto, T., 2010. Evidence of thermal pressurization in high-velocity friction experiments on smectite-rich gouges. Terra Nov. 22, 347–353. doi:10.1111/j.1365-3121.2010.00955.x.

Ferrill, D.A., Morris, A.P., 2003. Dilational normal faults. J. Struct. Geol. 25, 183–196. doi:10.1016/S0191-8141(02)00029-9.

Ferrill, D.A., Morris, A.P., 2008. Fault zone deformation controlled by carbonate mechanical stratigraphy, Balcones fault system, Texas. Am. Assoc. Pet. Geol. Bull. 92, 359–380. doi:10.1306/10290707066.

Fondriest, M., Smith, S.A.F., Di Toro, G., Zampieri, D., Mittempergher, S., 2012. Fault zone structure and seismic slip localization in dolostones, an example from the Southern Alps, Italy. J. Struct. Geol. 45, 52–67. doi:10.1016/j.jsg.2012.06.014.

Fondriest, M., Smith, S.A.F., Candela, T., Nielsen, S.B., Mair, K., Di Toro, G., 2013. Mirror-like faults and power dissipation during earthquakes. Geology 41, 1175–1178. doi:10.1130/G34641.1.

Fondriest, M., Aretusini, S., Di Toro, G., Smith, S.A.F., 2015. Fracturing and rock pulverization along an exhumed seismogenic fault zone in dolostones: The Foiana Fault Zone (Southern Alps, Italy). Tectonophysics 654, 56–74. doi:10.1016/j.tecto.2015.04.015.

Fossen, H., Schultz, R.A., Shipton, Z.K., Mair, K., 2007. Deformation bands in sandstone: a review. J. Geol. Soc. 164, 755-769. doi:10.1144/0016-76492006-036.

Fujii, Y., Satake, K., 2007. Tsunami source of the 2004 Sumatra-Andaman earthquake inferred from tide gauge and satellite data. Bull. Seismol. Soc. Am. 97, 192–207. doi:10.1785/0120050613.

Fulton, P.M., Brodsky, E.E., Kano, Y., Mori, J., Chester, F., Ishikawa, T., Harris, R.N., Lin, W., Eguchi, N., Toczko, S., 2013. Low Coseismic Friction on the Tohoku-Oki Fault Determined from Temperature Measurements. Science 342, 1214–1217. doi:10.1126/science.1243641.

Galadini, F., Galli, P., 2000. Active tectonics in the central Apennines (Italy)-input data for seismic hazard assessment. Natural Hazards 22, 225-270.

Galadini, F., Messina, P., Giaccio, B., Sposato, A., 2003. Early uplift history of the Abruzzi Apennines (central Italy): Available geomorphological constraints. Quat. Int. 101-102, 125–135. doi:10.1016/S1040-6182(02)00095-2.

Galli, P., Galadini, F., Pantosti, D., 2008. Twenty years of paleoseismology in Italy. Earth-Science Rev. 88, 89–117. doi:10.1016/j.earscirev.2008.01.001.

Galli, P., Giaccio, B., Messina, P., Peronace, E., Zuppi, G.M., 2011. Palaeoseismology of the L'Aquila faults (central Italy, 2009, M_w 6.3 earthquake): implications for active fault linkage. Geophys. J. Int. 187, 1119–1134. doi:10.1111/j.1365-246X.2011.05233.x.

Galli, P., Messina, P., Giaccio, B., Peronace, E., Quadrio, B., 2012. Early Pleistocene to late Holocene activity of the Magnola fault (Fucino fault system, central Italy). Boll. di Geofis. Teor. ed Appl. 53, 435–458. doi:10.4430/bgta0054.

Gibson, R.G., 1998. Physical character and fluid-flow properties of sandstone-derived fault

zones. Geol. Soc. London Spec. Pub. 127, 83-97. doi:10.1144/GSL.SP.1998.127.01.07.

Giorgetti, C., Carpenter, B.M., Collettini, C., 2015. Frictional behavior of talc-calcite mixtures. J. Geophys. Res. Solid Earth 120, 6614–6633. doi:10.1002/2015JB011970.

Gratier, J.P., Thouvenot, F., Jenatton, L., Tourette, A., Doan, M.L., Renard, F., 2013. Geological control of the partitioning between seismic and aseismic sliding behaviours in active faults: Evidence from the Western Alps, France. Tectonophysics 600, 226–242. doi:10.1016/j.tecto.2013.02.013.

Gruppo di Lavoro INGV sul terremoto di Amatrice, 2016. Primo rapporto di sintesi sul Terremoto di Amatrice Ml 6.0 del 24 Agosto 2016 (Italia Centrale), doi: 10.5281/zenodo.61121.

Haines, S.H., Kaproth, B., Marone, C., Saffer, D., van der Pluijm, B.A., 2013. Shear zones in clay-rich fault gouge: A laboratory study of fabric development and evolution. J. Struct. Geol. 51, 206–225. doi:10.1016/j.jsg.2013.01.002.

Hirono, T., Ishikawa, T., Masumoto, H., Kameda, J., Yabuta, H., & Mukoyoshi, H., 2014. Re-evaluation of frictional heat recorded in the dark gouge of the shallow part of a megasplay fault at the Nankai Trough. Tectonophysics 626, 157-169. doi:10.1016/j.tecto.2014.04.020.

Hoffman J., Hower J. 1979. Clay mineral assemblages as low grade metamorphic geothermometers: applications to the thrust faulted disturbed belt of Montana, USA. In: Scholle P.A., Schluger P.R. (Ed.), Aspect of diagenesis. SePM (Society for Sedimentary Geology) Special Publication 26, 55-79.

Holdsworth, R.E., Van Diggelen, E.W.E., Spiers, C.J., De Bresser, J.H.P., Walker, R.J., Bowen, L., 2011. Fault rocks from the SAFOD core samples: Implications for weakening at shallow depths along the San Andreas Fault, California. J. Struct. Geol. 33, 132–144. doi:10.1016/j.jsg.2010.11.010.

Hsu, L., Bürgmann, R., 2006. Surface creep along the Longitudinal Valley fault, Taiwan from InSAR measurements. Geophys. Res. Lett. 33, L06312. doi:10.1029/2005GL024624.

Hunstad, I., 2003. Geodetic strain in peninsular Italy between 1875 and 2001. Geophys. Res. Lett. 30, 1–4. doi:10.1029/2002GL016447.

Ide, S., Baltay, A., Beroza, G.C., 2011. Shallow dynamic overshoot and energetic deep rupture in the 2011 Mw 9.0 Tohoku-Oki earthquake. Science 332, 1426-1429. doi: 10.1126/science.1207020.

Ikari, M.J., Saffer, D.M., Marone, C., 2009. Frictional and hydrologic properties of clay-rich fault gouge. J. Geophys. Res. 114, B05409. doi:10.1029/2008JB006089.

Ikari, M.J., Kameda, J., Saffer, D.M., Kopf, A.J., 2015. Strength characteristics of Japan Trench borehole samples in the high-slip region of the 2011 Tohoku-Oki earthquake. Earth Planet. Sci. Lett. 412, 35–41. doi:10.1016/j.epsl.2014.12.014.

Ikari, M.J., Carpenter, B.M., Marone, C., 2016. A microphysica interpretation of rate- and state dependent friction for fault gouge. Geochem. Geophys. Geosyst. 17, 1660–1677, doi:10.1002/2016GC006286.

Jagodzinski, H., 1949. Eindimensionale fehlordnung in kristallen und ihr einfluss auf die röntgen interferenren. Acta Crystallographica 2, 201-207.

Kameda, J., Shimizu, M., Ujiie, K., Hirose, T., Ikari, M., Mori, J., Oohashi, K., Kimura, G., 2015. Pelagic smectite as an important factor in tsunamigenic slip along the Japan Trench. Geology 43, 155–158. doi:10.1130/G35948.1.

Keranen, K.M., Savage, H.M., Abers, G.A., Cochran, E.S., 2013. Potentially induced earthquakes in Oklahoma, USA: Links between wastewater injection and the 2011 M_w 5.7 earthquake sequence. Geology 41, 699–702. doi:10.1130/G34045.1.

Kettermann, M., Thronberens, S., Juarez, O., Urai, J.L., Ziegler, M., Asmus, S., Krüger, U., 2016. Mechanisms of clay smear formation in unconsolidated sediments - insights from 3D observations of excavated normal faults. Solid Earth Discuss. 1–45. doi:10.5194/se-2016-7.

Kilias, A.D., Vamvaka, A., Falalakis, G., Sfeikos, A., Papadimitriou, E., Gkarlaouni, C.H., Karakostas, B., 2015. The Mesohellenic Trough and the Paleogene Thrace Basin on the Rhodope massif, their structural evolution and geotectonic significance in the Hellenides. J. Geol. Geosci. 4, 1-17, doi: 0.4172/2329-6755.1000198.

Lehner, F.K., Pilaar, W.F., 1997. The emplacement of clay smears in synsedimentary normal faults: inferences from field observations near Frechen, Germany. In: M.ller-Pedersen, P., Koestler, A.G. (Eds.), Hydrocarbon Seals: Importance for Exploration and Production. Norwegian Petroleum Society, Special Publication 7, 39–50.

Li, H., Wang, H., Xu, Z., Si, J., Pei, J., Li, T., Huang, Y., Song, S., Kuo, L., Sun, Z., Chevalier, M., Liu, D., 2013. Characteristics of the fault-related rocks, fault zones and the principal slip zone in the Wenchuan Earthquake Fault Scientific Drilling Project Hole-1 (WFSD-1). Tectonophysics 584, 23–42.

doi:10.1016/j.tecto.2012.08.021.

Ma, K.F., Lee, C.T., Tsai, Y.B., Shin, T.C., Mori, J., 1999. The Chi‐Chi, Taiwan earthquake: Large surface displacements on an inland thrust fault. Eos, Trans. Am. Geophys. Union 80, 605-611.

Mariotti, G., Capotorti, F., 1988. Analisi ed interpretazione di alcuni elementi tettonici recenti nella media valle del Salto (Rieti). Rend. della Soc. Geol. It. 11, 79–84.

Marone, C., Scholz, C., 1989. Particle-size distribution and microstructures within simulated gouge. J. Struct. Geol. 11, 799e814.

Marone C., Richardson, E., 2010. Learning to read fault-slip behavior from fault-zone structure. Geology 38, 767–768. doi:10.1111/j.1365.

Martino, S., Prestininzi, A., Romeo, R., 2014. Earthquake-induced ground failures in Italy. Nat. Hazards Earth Syst. Sci. 14, 799–814. doi:10.5194/nhess-14-799-2014.

Masi, U., Tucci, P., Menichini, G., Azzaro, E., 1996. Chemiostratigrafia e petrografia della parte superiore della formazione dolomitica triassica di Filettino (Monti Simbruini, Lazio). Geol. Rom. 32, 25-33.

Melosh, B.L., Rowe, C.D., Smit, L., Groenewald, C., Lambert, C.W., Macey, P., 2014. Snap, Crackle, Pop: Dilational fault breccias record seismic slip below the brittle–plastic transition. Earth Planet. Sci. Lett. 403, 432–445. doi:10.1016/j.epsl.2014.07.002.

Mildon, Z. K., Roberts, G. P., Walker, J. P. F., Wedmore, L. N., McCaffrey, K. J., 2016. Active normal faulting during the 1997 seismic sequence in Colfiorito, Umbria: Did slip propagate to the surface?. J. Struct. Geol. http://dx.doi.org/10.1016/j.jsg.2016.08.011.

Milli, S., Moscatelli, S., 2000. Facies analysis and physical stratigraphy of the Messinian turbiditic complex in the Valle del Salto and Val di Varri (central Apennines). Giornale di Geologia 62, 57-77.

Mongelli, F., Zito, G., Ciaranfi, N., Pieri, P., 1989. Interpretation of heat flow density of the Apennine chain, Italy. Tectonophysics 164, 267–280. doi:10.1016/0040-1951(89)90020-6.

Montone, P., Salvini, F., 1991. Evidence of strike-slip tectonics in the Apennine Chain near Tagliacozzo (L'Aquila), Abruzzi, central Italy. Boll. della Soc. Geol. It. 110, 707-716.

Montone, P., Salvini, F., 1993. Geologia strutturale dell'area tra Colli di Monte Bove (Carsoli) e Tagliacozzo, Abruzzo, Italia Centrale. Geol. Rom. 29, 15-29.

Moore, D.M., Reynolds, R.C. Jr. 1997. X-Ray diffraction and the identification and analysis of clay minerals. Oxford University Press, Oxford.

Morewood, N.C., Roberts, G.P., 2000. The geometry, kinematics and rates of deformation within an en echelon normal fault segment boundary, central Italy. J. Struct. Geol. 22, 1027–1047. doi:10.1016/S0191-8141(00)00030-4.

Mort, K., Woodcock, N.H., 2008. Quantifying fault breccia geometry: Dent Fault, NW England. J. Struct. Geol. 30, 701–709. doi:10.1016/j.jsg.2008.02.005.

Mostardini, F., Merlini, S., 1986. Appennino centro-meridionale. Sezioni geologiche e proposta di modello strutturale. Mem. della Soc. Geol. It. 35, 177-202.

Nairn, A.E.M., Alsharhan, A.S., 1997. Sedimentary basins and petroleum geology of the Middle East. Elsevier, Amsterdam.

Niemeijer, A.R., Spiers, C.J., 2005. Influence of phyllosilicates on fault strength in the brittle-ductile transition: insights from rock analogue experiments. Geol. Soc. London, Spec. Publ. 245, 303–327. doi:10.1144/GSL.SP.2005.245.01.15.

Oddone, E., 1915. Gli elementi fisici del grande terremoto marsicano-fucense del 13 gennaio 1915. Boll. della Soc. Sism. It. 19, 71–216.

Pantosti, D., Schwartz, D. P., Valensise, G., 1993. Paleoseismology along the 1980 surface rupture of the Irpinia Fault: implications for earthquake recurrence in the Southern Apennines, Italy. J. Geophy. Res. 98, 6561-6577.

Parotto, M., Praturlon, A., 1975. Geological summary of the Central Apennines. In Structural model of Italy, Quad. Ric. Scient. 90, 256-311.

Patacca, E., Scandone, P., Di Luzio, E., Cavinato, G.P., Parotto, M., 2008. Structural architecture of the central Apennines: Interpretation of the CROP 11 seismic profile from the Adriatic coast to the orographic divide. Tectonics 27, 1–36. doi:10.1029/2005TC001917.

Petracchini, L., Antonellini, M., Billi, A., Scrocca, D., 2012. Fault development through fractured pelagic carbonates of the Cingoli anticline, Italy: Possible analog for subsurface fluid-conductive fractures. J. Struct. Geol. 45, 21–37. doi:10.1016/j.jsg.2012.05.007.

Renard, F., Dysthe, D., Feder, J., Bjorlykke, K., Jamtveit, B., 2001. Enhanced pressure solution creep rates induced by clay particles: Experimental evidence in salt aggregates. Geophys. Res. Lett. 28, 1295–1298. doi:10.1029/2000GL012394.

Roberts, G.P., Michetti, A.M., 2004. Spatial and temporal variations in growth rates along active normal fault systems: an example from The Lazio–Abruzzo Apennines, central Italy. J. Struct. Geol. 26, 339–376. doi:10.1016/S0191-8141(03)00103-2.

Roche, V., Homberg, C., Rocher, M., 2012. Architecture and growth of normal fault zones in multilayer systems: A 3D field analysis in the South-Eastern Basin, France. J. Struct. Geol. 37, 19–35. doi:10.1016/j.jsg.2012.02.005.

Rowe, C.D., Meneghini, F., Moore, J.C., 2011. Textural record of the seismic cycle: strain-rate variation in an ancient subduction thrust. Geol. Soc. London, Spec. Publ. 359, 77–95. doi:10.1144/SP359.5.

Saffer, D.M., Marone, C., 2003. Comparison of smectite- and illite-rich gouge frictional properties: application to the updip limit of the seismogenic zone along subduction megathrusts. Earth Planet. Sci. Lett. 215, 219–235. doi:10.1016/S0012-821X(03)00424-2.

Schöpfer, M.P.J., Childs, C., Walsh, J.J., 2006. Localisation of normal faults in multilayer sequences. J. Struct. Geol. 28, 816-833. doi:10.1016/j.jsg.2006.02.003.

Schöpfer, M.P.J., Childs, C., Walsh, J.J., 2007a. Two-dimensional distinct element modeling of the structure and growth of normal faults in multilayer sequences: 1. Model calibration, boundary conditions, and selected results. J. Geophys. Res. 112, B10401. doi:10.1029/2006JB004902.

Schöpfer, M.P.J., Childs, C., Walsh, J.J., 2007b. Two-dimensional distinct element modeling of the structure and growth of normal faults in multilayer sequences: 2. Impact of confining pressure and strength contrast on fault zone geometry and growth. J. Geophys. Res. 112, B10404. doi:10.1029/2006JB004903.

Schumacher, M.E., 2002. Upper Rhine Graben: role of preexisting structures during rift evolution. Tectonics 21, 6-1. doi: 10.1029/2001TC900022.

Smeraglia, L., Trippetta, F., Carminati, E., Mollo, S., 2014. Tectonic control on the petrophysical properties of foredeep sandstones in the central Apennines, Italy. J. Geophys. Res. 119, 9077-9094. doi:10.1002/2014JB011221.

Smeraglia, L., Berra, F., Billi, A., Boschi, C., Carminati, E., Doglioni, C., 2016. Origin and role of fluids involved in the seismic cycle of extensional faults in carbonate rocks. Earth Planet. Sci. Lett. 450, 292-305. doi: 10.1016/j.epsl.2016.06.042.

Smith, S.A.F., Billi, A., Di Toro, G., Spiess, R., 2011. Principal Slip Zones in Limestone: Microstructural Characterization and Implications for the Seismic Cycle (Tre Monti Fault, Central Apennines, Italy). Pure Appl. Geophys. 168, 2365–2393. doi:10.1007/s00024-011-0267-5.

Srodon, J. 1980. Precise identification of illite/smectite interstratifications by X-ray powder diffraction. Clays and clay minerals 28, 401-411.

Srodon, J. 1999. Nature of mixed-layer clays and mechanisms of their formation and alteration. Ann. Rev. Earth Planet. Sci. 27, 19-53. doi:10.1146/annurev.earth.27.1.19.

Storti, F., Billi, A., Salvini, F., 2003. Particle size distributions in natural carbonate fault rocks: Insights for non-self-similar cataclasis. Earth Planet. Sci. Lett. 206, 173–186. doi:10.1016/S0012-821X(02)01077-4.

Sutherland, R., Toy, V.G., Townend, J., Cox, S.C., Eccles, J.D., Faulkner, D.R., Prior, D.J., Norris, R.J., Mariani, E., Boulton, C., Carpenter, B.M., Menzies, C.D., Little, T.A., Hasting, M., De Pascale, G.P., Langridge, R.M., Scott, H.R., Lindroos, Z.R., Fleming, B., Kopf, A.J., 2012. Drilling reveals fluid control on architecture and rupture of the Alpine fault, New Zealand. Geology 40, 1143–1146. doi:10.1130/G33614.1.

Tavani, S., Cifelli, F., 2010. Deformation pattern analysis and tectonic implications of a décollement level within the Central Apennines (Italy). Geol. J. 45, 582–596. doi:10.1002/gj.1198.

Tesei, T., Collettini, C., Carpenter, B.M., Viti, C., Marone, C., 2012. Frictional strength and healing behavior of phyllosilicate-rich faults. J. Geophys. Res. Solid Earth 117, 1–13. doi:10.1029/2012JB009204.

Tesei, T., Collettini, C., Viti, C., Barchi, M.R., 2013. Fault architecture and deformation mechanisms in exhumed analogues of seismogenic carbonate-bearing thrusts. J. Struct. Geol. 55, 167–181. doi:10.1016/j.jsg.2013.07.007.

Tesei, T., Collettini, C., Barchi, M.R., Carpenter, B.M., Di Stefano, G., 2014. Heterogeneous strength and fault zone complexity of carbonate-bearing thrusts with possible implications for seismicity. Earth Planet. Sci. Lett. 408, 307–318. doi:10.1016/j.epsl.2014.10.021.

Toy, V.G., Boulton, C.J., Sutherland, R., Townend, J., Norris, R.J., Little, T.A., Prior, D.J., Mariani, E., Faulkner, D., Menzies, C.D., Scott, H., Carpenter, B.M., 2015. Fault rock lithologies and architecture of the central Alpine fault, New

Zealand, revealed by DFDP-1 drilling. Lithosphere 7, 155–173. doi:10.1130/L395.1.

Tucci, P., Morbidelli, P., 2004. “Apulian marbles” of the Ostuni District (south-eastern Murge, Apulia, Italy). Identification and characterisation of ancient quarries for archeometric purposes. Period. di Mineral. 73, 127–140.

Ujiie, K., Tsutsumi, A., 2010. High-velocity frictional properties of clay-rich fault gouge in a megasplay fault zone, Nankai subduction zone. Geophys. Res. Lett. 37, L24310. doi:10.1029/2010GL046002.

Ujiie, K., Tsutsumi, A., Kameda, J., 2011. Reproduction of thermal pressurization and fluidization of clay-rich fault gouges by high-velocity friction experiments and implications for seismic slip in natural faults. Geol. Soc. London, Spec. Publ. 359, 267–285. doi:10.1144/SP359.15.

Ujiie, K., Tanaka, H., Saito, T., Tsutsumi, A., Mori, J.J., Kameda, J., Brodsky, E.E., Chester, F.M., Eguchi, N., Toczko, S., 2013. Low Coseismic Shear Stress on the Tohoku-Oki Megathrust Determined from Laboratory Experiments. Science 342, 1211–1214.

Valoroso, L., Chiaraluce, L., Piccinini, D., Di Stefano, R., Schaff, D., Waldhauser, F., 2013. Radiography of a normal fault system by 64,000 high-precision earthquake locations: The 2009 L’Aquila (central Italy) case study. J. Geophys. Res. Solid Earth 118, 1156–1176. doi:10.1002/jgrb.50130.

van der Pluijm, B.A., Hall, C.M., Vrolijk, P.J., Pevear, D.R., Covey, M.C., 2001. The dating of shallow faults in the Earth's crust. Nature 412, 172-175.

van der Zee, W., Urai, J.L., Rischard, P.D., 2003. Lateral clay injection into normal faults. GeoArabia 18, 501-522.

van der Zee, W., Urai, J.L., 2005. Processes of normal fault evolution in a siliciclastic sequence: a case study from Miri, Sarawak, Malaysia. Journal of Structural Geology 27, 2281-2300. doi: 10.1016/j.jsg.2005.07.006.

Verberne, B.A., He, C., Spiers, C.J., 2010. Frictional properties of sedimentary rocks and natural fault gouge from the Longmen Shan fault zone, Sichuan, China. Bull. Seismol. Soc. Am. 100, 2767–2790. doi:10.1785/0120090287.

Viti, C., Collettini, C., Tesei, T., 2014. Pressure solution seams in carbonatic fault rocks: mineralogy, micro/nanostructures and deformation mechanism. Contrib. to Mineral. Petrol. 167, 970. doi:10.1007/s00410-014-0970-1.

Vrolijk, P., 1990. On the mechanical role of smectite in subduction zones. Geology 18, 703-707. doi:10.1130/0091-7613(1990)018<0703:OTMROS>2.3.CO;2.

Vrolijk, P., Urai, J.L., Kettermann, M., 2015. Clay Smear: Review of Mechanisms and Applications. J. Struct. Geol. doi:10.1016/j.jsg.2015.09.006.

Warr, L.N., Wojatschke, J., Carpenter, B.M., Marone, C., Schleicher, A.M., Van der Pluijm, B.A., 2014. A “slice-and-view” (FIB–SEM) study of clay gouge from the SAFOD creeping section of the San Andreas Fault at ~2.7 km depth. J. Struct. Geol. 69, 234–244. doi:10.1016/j.jsg.2014.10.006.

Welch, M.J., Davies, R.K., Knipe, R.J., Tueckmantel, C., 2009. A dynamic model for fault nucleation and propagation in a mechanically layered section. Tectonophysics 474, 473–492. doi:10.1016/j.tecto.2009.04.025.

Williams, R.T., Goodwin, L.B., Mozley, P.S., Beard, B.L., Johnson, C.M., 2015. Tectonic controls on fault zone flow pathways in the Rio Grande rift, New Mexico, USA. Geology 43, 723–726. doi:10.1130/G36799.1.

Woodcock, N.H., Mort, K., 2008. Classification of fault breccias and related fault rocks. Geol. Mag. 145, 435–440. doi:10.1017/S0016756808004883.

Woodcock, N.H., Miller, A.V.M., Woodhouse, C.D., 2014. Chaotic breccia zones on the Pembroke Peninsula, south Wales: Evidence for collapse into voids along dilational faults. J. Struct. Geol. 69, 91–107. doi:10.1016/j.jsg.2014.09.019.

Xu, X., Wen, X., Yu, G., Chen, G., Klinger, Y., Hubbard, J., Shaw, J., 2009. Coseismic reverse- and oblique-slip surface faulting generated by the 2008 Mw 7.9 Wenchuan earthquake, China. Geology 37, 515–518. doi:10.1130/G25462A.1.

Chapter 2. Origin and role of fluids involved in the seismic cycle of extensional faults in carbonate rocks

Abstract

We examine the seismically-active right-lateral transtensional-extensional Tre Monti Fault (central Apennines, Italy) with structural and geochemical methods and develop a conceptual evolutionary model of extensional faulting with fluid involvement in shallow (≤ 3 km depth) extensional faults in carbonate rocks. In the analysed fault zone, multiscale fault rock structures include injection veins, fluidized ultracataclasite layers, and crackle breccias, suggesting that the fault slipped seismically. We reconstructed the relative chronology of these structures through cross-cutting relationship and cathodoluminescence analyses. We then used C- and O-isotope data from different generations of fault-related mineralizations to show a shift from connate (marine-derived) to meteoric fluid circulation during exhumation from 3 to ≤ 1 km depths and concurrent fluid cooling from ~68 to < 30 °C. Between ~3 km and ~1 km depths, impermeable barriers within the sedimentary sequence created a semi-closed hydrological system, where prevalently connate fluids circulated within the fault zone at temperatures between 60° and 75 °C. During fault zone exhumation, at depths ≤ 1 km and temperatures < 30 °C, the hydrological circulation became open and meteoric-derived fluids progressively infiltrated and circulated within the fault zone. The role of these fluids during syn-exhumation seismic cycles of the Tre Monti Fault has been substantially passive along the whole fault zone, the fluids being passively redistributed at hydrostatic pressure following co-seismic dilatancy. Only the principal fault has been characterized, locally and transiently, by fluid overpressures. The presence of low-permeability clayey layers in the sedimentary sequence contributed to control the type of fluids infiltrating into the fault zone and possibly their transient overpressures. These results can foster the comprehension of seismic faulting at shallow depths in carbonate rocks of other fold-thrust belts involved in post-collisional seismogenic extensional tectonics.

This study was performed in collaboration with F. Berra, A. Billi, C. Boschi, E. Carminati, and C. Doglioni. This chapter was published as the following paper: Smeraglia L., Berra F., Billi A., Boschi C., Carminati E., Doglioni C., Origin and role of fluids involved in the seismic cycle of extensional faults in carbonate rocks. Earth and Planetary Sciences Letters 450, 292-305, doi: 10.1016/j.epsl.2016.06.042.

1. Introduction

Fluid flow along faults has been widely explored for implications on various topics including hydrocarbon and ore exploration, CO_2 sequestration, groundwater and contaminant transport, and faulting (e.g., Cox, 1995; Williams et al., 2015). Faults and fault zones can be preferential conduits or barriers for the passage of geofluids. Moreover, fault slip behaviors and the seismic cycle are often controlled by the geofluids themselves (e.g., Hickman et al., 1995).

Fluids have been suggested to play either passive or active roles during the seismic cycle (e.g., Sibson, 2014; Fig. 1). For instance, the "fault-valve" model (Fig. 1a) involves an active role of overpressured fluids that can trigger earthquakes (e.g., Miller et al., 2004; Haney et al., 2005). After seismic failure, fluid discharge and sealing mineralizations are favored by hydrofracturing and decompression (stress drop), respectively (e.g., Cox, 1995). Complete fracture sealing allows fluid overpressure to build again and initiate a new seismic cycle. This mechanism can commonly act within fluid-overpressured crustal blocks (e.g., Di Luccio et al., 2010), especially along subduction interfaces, where fluid overpressure is more likely to develop and be sustained (Sibson, 2014). On the other hand, different scenarios involve a passive role of fluids that are redistributed following an earthquake (e.g., Sibson, 2000). Fluid redistribution can be favored by rapid co-seismic dilation and creation of high-permeability fracture networks characterized by subhydrostatic pressure (Fig. 1b, "suction-pump" model) or by crack closure favored by post-seismic stress recovery (Fig. 1c, "mean stress cycling" model). If low-permeability barriers are not created, fluids conserve hydrostatic pressure. These mechanisms can easily act within extensional/transtensional regimes (e.g., Doglioni et al., 2014; Sibson, 2014) in the shallow crust (<5 km), where hydrostatic fluid pressure and high permeability zones have been documented (Townend and Zoback, 2000). These processes can be understood and validated by studying the evidence of seismic-related mineralization and rock-related fluid structures and textures (e.g., Uysal et al., 2009; Rowe and Griffith, 2015). Therefore, the study of the geological record of fluid-fault interactions is a fundamental pre-requisite for general models concerning the origin and role of fluids involved in the seismic cycle. Single case

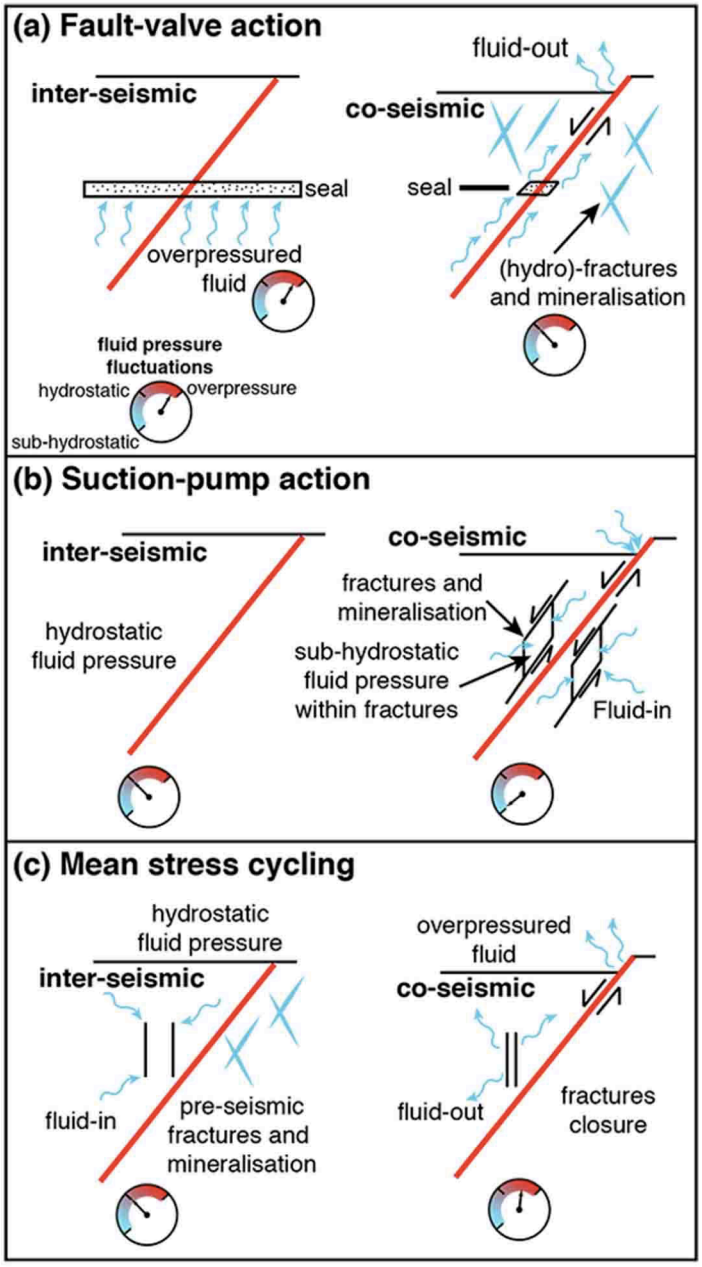


Figure 1. Different models of interaction between fluids and seismic cycles (modified after Sibson, 2000). (a) Fault-valve action. (b) Suction-pump action. (c) Mean stress cycling.

histories are fundamental to build comprehensive conceptual models of seismic-related fluid circulation.

We examine a case study of a major right-lateral transtensional-extensional fault (Tre Monti Fault, TMF, central Apennines, Italy) from a carbonate domain in the central Apennines, Italy (Fig. 2a). The study of this fault is relevant as, at shallow crustal levels (< 10 km depth), fault zones in carbonate rocks represent favorable structures for migration and entrapment of geofluids (e.g., Ghisetti et al., 2001). Moreover, in many seismically active regions worldwide (including our study

area), shallow crustal earthquakes and seismic sequences (e.g., hypocenters at < 10 km depth) nucleate in and propagate upward through carbonate rocks with fluids involvement in the seismic cycle (e.g., Macedonia, Greece, 1995, M_w 6.6 earthquake, Stiros, 1995; Wenchuan, China, 2008, M_w 8.0 earthquake, Chen et al., 2013; L'Aquila, Italy, 2009, M_w 6.3 earthquake, Chiaraluce, 2012).

The TMF has been exhumed from depths ≤ 3 km since about the Pliocene (Galadini et al., 2003) and exhibits excellent exposures allowing geoscientists to study the relationships between fault zone architecture, fluid circulation, and seismic cycle within a tectonically active extensional setting (Smith et al., 2011). As many normal fault earthquakes frequently cause surface ruptures and associated damage and fatalities (Stiros, 1995; Galli et al., 2008), the study of such a shallow fault is relevant for the understanding of the fault zone architecture and fluid circulation at shallow depths (≤ 3 km).

We synthesize the spatio-temporal tectonic evolution and fluid circulation of the TMF into a conceptual model of seismic-related fluid circulation within shallow (≤ 3 km) extensional fault zones. We combine structural, microstructural, mineralogical, and geochemical (cathodoluminescence, stable isotopes, and whole rock geochemistry) methods. The main novelty of this model concerns the origin of geofluids involved in the seismic cycle of exhuming extensional fault zones and their specific role, which is substantially passive along most part of the fault zone except along the principal fault, where fluid overpressures can locally arise during co-seismic phases.

2. Geological Setting

2.1. Apennines evolution and seismotectonic setting

The Central Apennines is a late Oligocene-to-Present fold-and-thrust belt related to the west directed subduction and eastward rollback of the Adriatic plate under the European plate (Doglioni, 1991). Shortening was characterized by the northeastward migration of thrust fronts in a classical forelandward piggy-back sequence of thrust sheets (Cosentino et al., 2010). These tectonic

processes juxtaposed carbonates onto syn-orogenic deposits along NW-SE-oriented thrust faults (Fig. 2a; Cosentino et al., 2010). The thrust sheets consist of ~4-5 km thick Late Triassic-Middle Miocene shallow-water carbonate rocks, whereas the syn-orogenic deposits consist of up to ~3 km thick Late Miocene hemipelagic marls and deep-marine siliciclastic sandstones with intercalated clayey layers (Cosentino et al., 2010).

Since Late Miocene time, while the compressional deformation was still active along the eastern fronts (Adriatic domain), the Apennines belt experienced extension and exhumation in its western and axial parts. This process has been associated with exhumation at rates of ca. 0.3 mm/a in the last 3-5 Ma (e.g., Thomson et al., 2010 for the Northern Apennines). Normal faulting led to crustal thinning related to the development of the Tyrrhenian backarc basin (Doglioni, 1991). This process is still active and has generated a system of NW-SE-oriented basin-bounding active extensional faults and perpendicular strike- to oblique-slip transfer faults (Fig. 2a). Both sets of faults produced large historical and instrumental earthquakes up to M_w 7 (Fig. 2a; e.g., Avezzano, 1915, M_w 7.0 earthquake; L'Aquila, 2009, M_w 6.3 earthquake; Galli et al., 2008; Chiaraluce, 2012). The TMF represents an active transfer fault between two NW-SE-oriented extensional faults (Morewood and Roberts, 2000; Benedetti et al., 2013).

In the Apennines, the imbricated carbonates and syn-orogenic sequences can be traced from the surface to depths of ca. 8–10 km (Patacca et al., 2008). Although some mainshocks nucleated within the underlying crystalline basement (~10 km depth), it is well documented that many foreshocks and aftershocks as well as some mainshocks nucleated and propagated within the overlying sedimentary sequence (Miller et al., 2004; Ventura and Di Giovambattista, 2013). For example, during the 2009 L'Aquila earthquake sequence, large foreshocks and aftershocks (up to M_w 5.5) nucleated at < 5 km depth. Fluid-earthquake interactions at different crustal levels have been instrumentally documented for the most recent earthquakes of the region. For instance, near lithostatic fluid pressure at hypocentral depths triggered both the mainshocks and the aftershocks during the M_w 6.0, 1997 Colfiorito (Miller et al. 2004) and M_w 6.3, 2009 L'Aquila (Di Luccio et al.

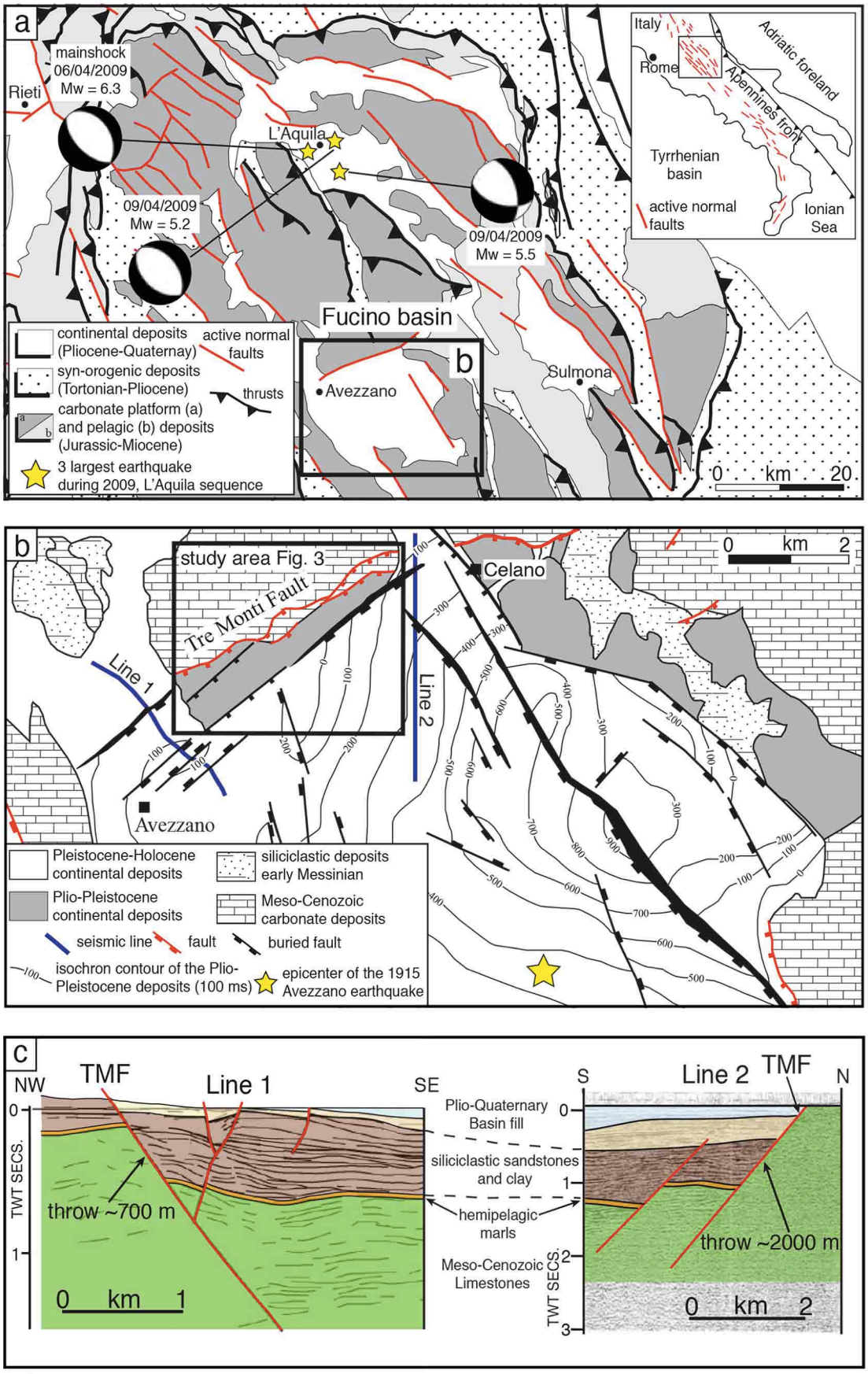


Figure 2. (a) Simplified geological map of the central Apennines (Italy), showing main thrusts and active normal faults. Inset shows a schematic tectonic setting of central-southern Italy with main thrusts and active normal faults. **(b)** Geological setting of the Fucino basin and Tre Monti Fault (TMF) (Cavinato et al., 2002). **(c)** Seismic reflection cross-sections (left cross-section: data line drawing and interpretation; right cross-section: data and interpretation) through the TMF (Cavinato et al., 2002; Patacca et al., 2008). Cross-section traces are shown in (b).

2010) earthquakes. Malagnini et al., (2012) suggested that, during the L'Aquila earthquake, pore fluid pressure diffusion was responsible for the spatial migration of seismicity with the activation of different fault segments.

In the Apennines, earthquakes frequently ruptured the Earth's surface (e.g., Galli et al., 2008; Benedetti et al., 2013). Consequently, the fluids that circulate at shallow crustal levels (< 1 km depth) can enter into and interact with the fault zone, as was the case, for instance, of the L'Aquila earthquake (Amoruso et al., 2011; Doglioni et al., 2013).

2.2. The Tre Monti Fault

The TMF marks the north-western boundary of the Fucino basin, which is an intra-mountain half-graben filled by Late Pliocene–Quaternary continental deposits (Fig. 2b; Cavinato et al., 2002). Paleoseismological investigations suggest that the TMF has been active between Early Pliocene and present times (Benedetti et al., 2013). The TMF is exposed for a length of ~8 km along the southern slope of the Tre Monti Hills as an almost continuous series of ENE-WSW-oriented and SSE-dipping fault surfaces and scarps in Mesozoic limestones (Fig. 2b).

Based on stratigraphic offset and kinematic indicators, the TMF can be defined as an extensional fault with a transtensional right-lateral slip component (e.g., Morewood and Roberts, 2000). Seismic cross-sections through the TMF indicate that the cumulative throw increases from ~0.7 km in the western part to ~2 km in the eastern part (Fig. 2c, Cavinato et al., 2002; Patacca et al., 2008).

The TMF displaces the Tre Monti anticline, an open fold of Mesozoic-Cenozoic carbonate deposits and Late Tertiary syn-orogenic deposits with a north-western periclinal termination (Fig. 3a). The pre-orogenic carbonates crop out for a thickness of ~600 m and are unconformably overlain by syn-orogenic deposits with a minimum thickness of ~150 m (Fig. 3a). Vitrinite reflectance data indicate that, in this area, the syn-orogenic deposits were buried to maximum depths of up to 2 km (Corrado et al., 2010). As the tectonic activity of the TMF started both after

the compressional deformation and after the deposition of syn-orogenic deposits, we infer that the exposed portion of the TMF was exhumed from depths ≤ 3 km.

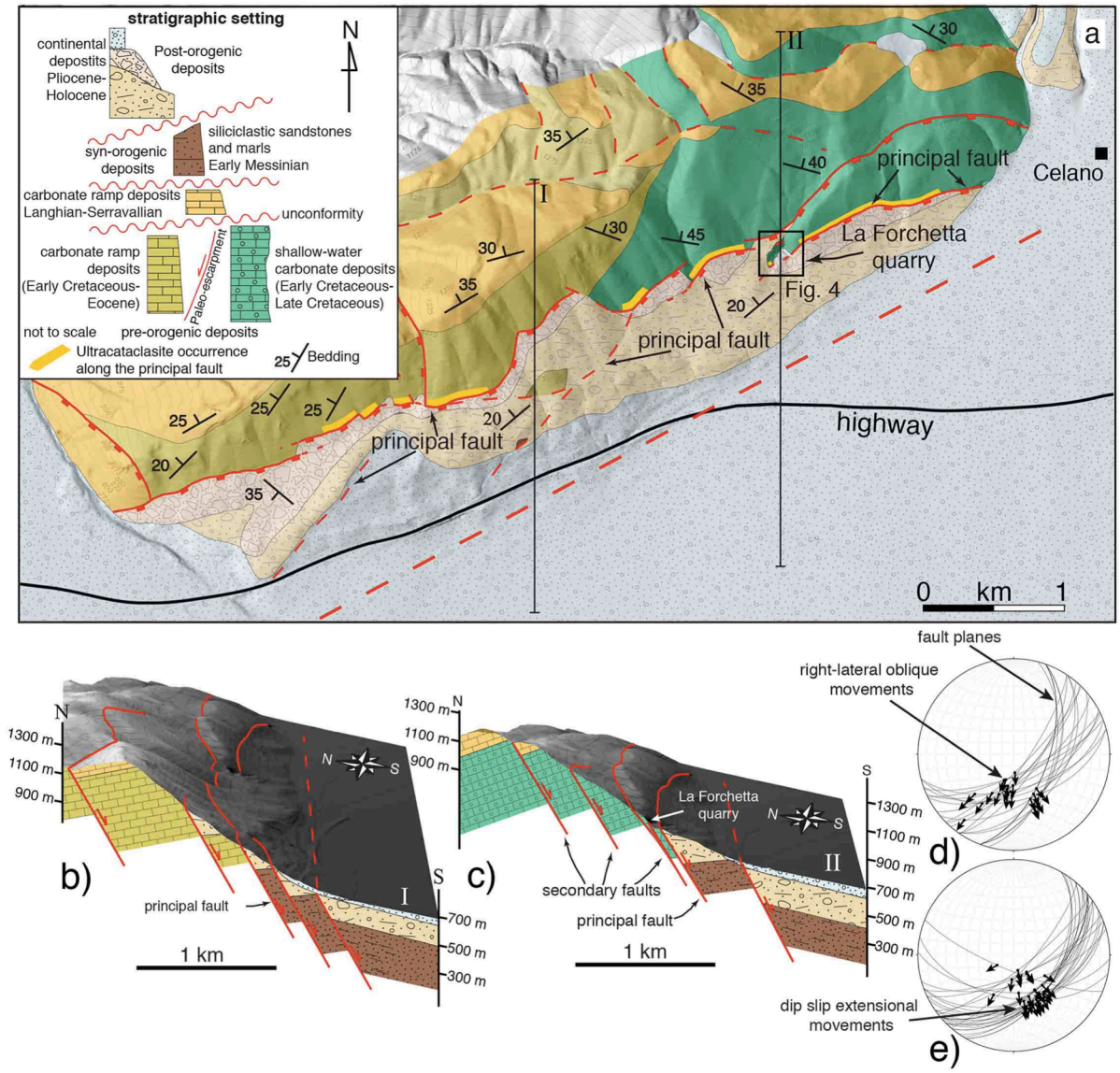


Figure 3. (a) Geological map of the TMF area along the northern boundary of the Fucino basin. Inset shows the stratigraphic-structural relationships in the area. **(b)** and **(c)** Geological cross-sections through the TMF and topographic renditions of the Tre Monti Hills. Cross-section traces in (a). **(d)** Schmidt net (lower hemisphere) showing attitude of meso-scale fault surfaces and related slip vectors (right-lateral transtensional movements). **(e)** Schmidt net (lower hemisphere) showing attitude of meso-scale fault surfaces and related slip vectors (dip-slip extensional movements).

3. Methods

We used the following methods to unravel the TMF architecture and fault-related fluid circulation:

(1) Original field mapping (at 1:5,000 scale or larger) to reconstruct the TMF surface kilometric-scale geometry;

(2) Construction of two geological cross-sections through the TMF to calculate fault displacements and investigate the buried structure. The sections are constrained by field and seismic reflection data;

(3) Detailed structural analyses and systematic sampling within La Forchetta quarry to reconstruct the fault zone internal architecture;

(4) Analysis of fault-rock microstructures using optical microscopy to investigate the deformation mechanisms;

(5) X-ray diffraction analyses (XRD) to determine fault rock mineralogy;

(6) Cathodoluminescence microscopy (CL) employing a cold cathode luminoscope (Nuclide ELM2) to distinguish the different phases of fluid-related mineralizations;

(7) Stable isotope analyses using a mass spectrometer (Finnigan MAT Delta Plus) equipped with Finnigan Gas-Bench II at the Institute of Geosciences and Earth Resources (IGG, CNR, National Research Council, Pisa, Italy). The experimental values were normalized against international (NBS-18) and internal standards. We verified a mean external reproducibility better than 0.1 both for $\delta^{13}C$ and for $\delta^{18}O$. Results are reported according to the conventional δ notations Vienna Pee Dee Belemnite (PDB) and Vienna Standard Mean Ocean Water (SMOW);

(8) Whole fault rock chemical analyses through an inductively coupled plasma-mass spectrometry (ICP-MS) at the Actlabs research laboratories (www.actlabs.com).

4. Structural and Cathodoluminescence Data

4.1. Fault zone setting and general architecture

The TMF is segmented into up to eleven SSE-dipping (45°-65°) fault segments (Fig. 3a). A buried fault segment occurs at the foot of the Tre Monti hills as inferred by seismic reflection data (Cavinato et al., 2002; Fig. 3a). The principal fault surface coincides with the most downhill fault

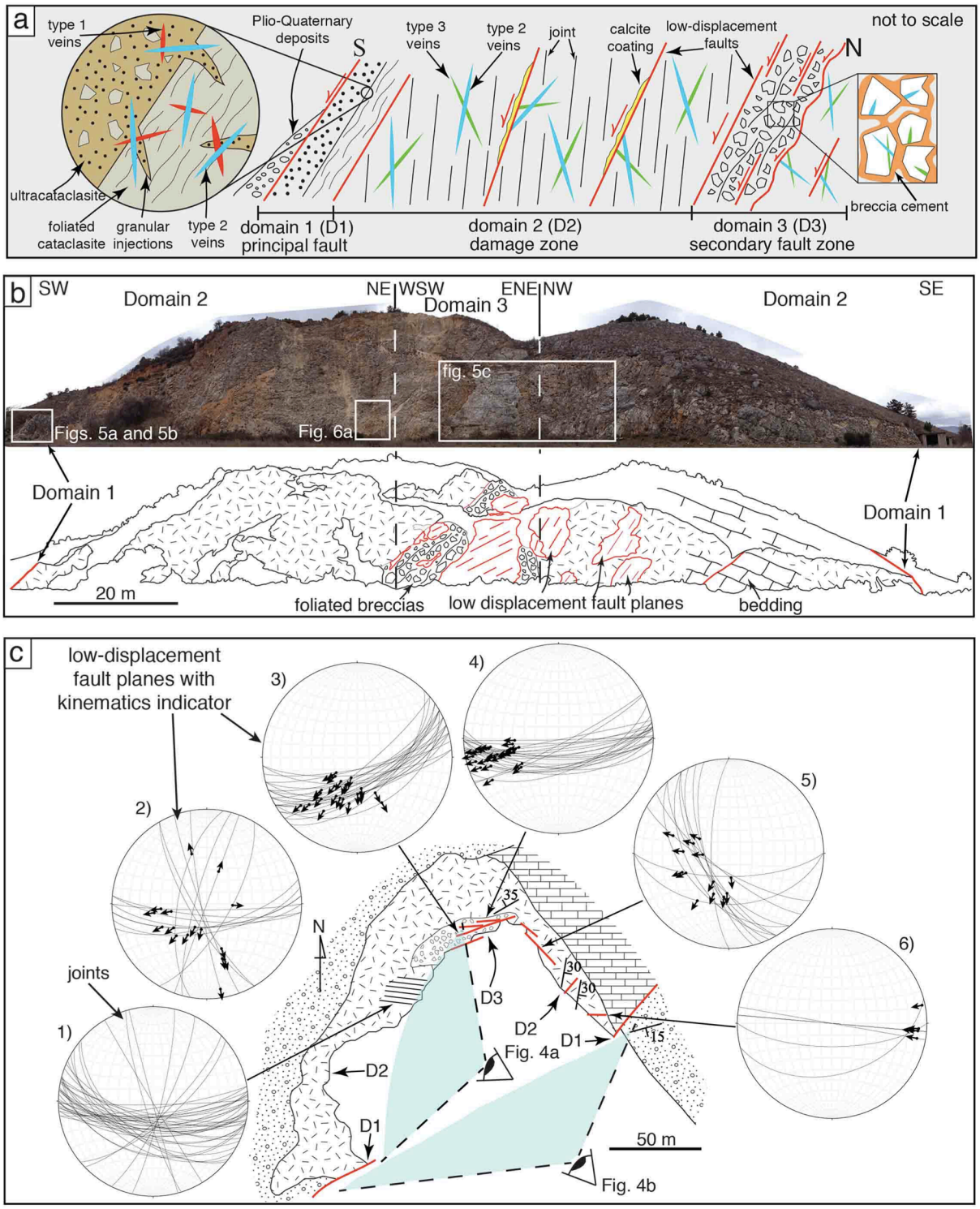


Figure 4. **(a)** Simplified conceptual cross-section through the TMF within La Forchetta quarry, showing the crosscutting relationships and three main structural domains: (principal fault, D1; damage zone, D2; secondary fault zone, D3). This figure represents our index reference for what concerns the three studied structural domains, their spatial distribution, and the crosscutting relationships between structures within each domain (see also Table S2). **(b)** Frontal view of La Forchetta quarry (photograph above and line drawing below), showing exposures of the main structural domains. **(c)** Simplified structural map of La Forchetta quarry. Schmidt nets (lower hemisphere) show attitude of joints (plot 1) and low displacement faults with related slip vectors (plots from 2 to 6). Quarry location: Latitude 42°04'36" N, Longitude 13°29'59" E.

scarp, and juxtaposes carbonate rocks in the footwall with both syn-orogenic marine and post-orogenic continental deposits in the hangingwall (Figs. 3b and 3c). The latter deposits consist of subaerial slope debris composed by carbonate clasts cemented by calcite precipitates.

The principal fault is exposed along a series of en-échelon parallel fault scarps, whereas other segments are buried and inferred by morphological evidence (scarps interpreted as tectonically-controlled) within the continental deposits (Fig. 3a). The principal fault surfaces are commonly striated by sets of slickenlines indicating two main movements: transtensional right-lateral (Fig. 3d) and extensional dip-slip (Fig. 3e). We observed no overprinting relationships between slip indicators. A set of secondary synthetic faults is hosted in the carbonate bedrock behind the principal fault (Figs. 3b and 3c). These faults are characterized by displacements up to a few hundreds of meters.

The La Forchetta quarry is located within a stepover between two en-échelon principal fault segments cutting Early Cretaceous shallow-water carbonates, which include two alternating facies: 1) peritidal white limestone and 2) oolithic grey limestone. In the quarry and nearby areas, as shown in the conceptual cross-section through the fault zone, we identify three main structural domains (Figs. 4a, 4b, and 4c): principal fault (Domain 1, D1); damage zone (Domain 2, D2); secondary fault zone (Domain 3, D3). We describe the three domains in detail as follows.

4.2. Principal fault (D1)

The principal fault (Figs. 4a and 5a) accommodates ~1500 m of throw and concentrates most shear deformation through a fault core that is up to ~1 m thick. The fault core consists of ultracataclasite and foliated cataclasite (Fig. 5b).

(1) The ultracataclasite, brownish in color, forms discontinuous patches and plagues up to ~20 cm thick resting above the underlying foliated cataclasite (Fig. 5b). The ultracataclasite occurs only along the principal fault surface (Fig. 3a) and mostly consists of calcite enriched with ~1.5% of phyllosilicates (mainly illite/smectite) as shown by XRD data (Table S1in supplementary material).

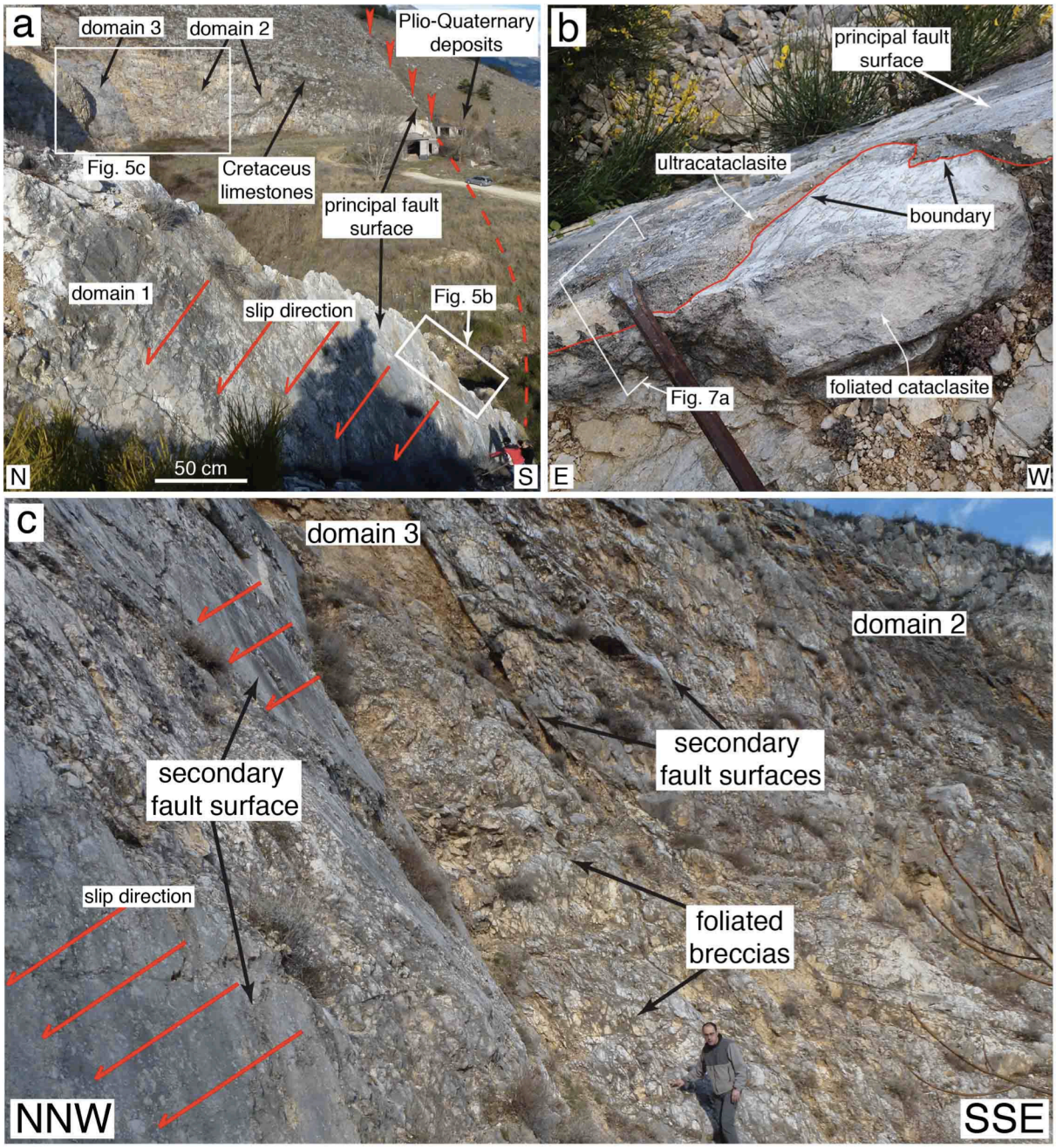


Figure 5. Large-scale outcrop structures of the Tre Monti Fault within the three structural domains: principal fault (domain 1, D1); damage zone (domain 2, D2); secondary fault zone (domain 3, D3). **(a)** Overview of the principal fault surface (D1), which juxtaposes Cretaceous carbonate deposits in the footwall and Plio-Pleistocene continental deposits in the hangingwall. **(b)** Cross-sectional view of the principal fault surface (D1) and related cataclastic fault core, which is ~100 cm thick. The ultracataclasite forms discontinuous patches over the foliated cataclasite. **(e)** Overview of the secondary fault zone (D3) and damage zone (D2). The secondary fault zone is characterized by optimally exposed fault segments and foliated breccias, which rest above fault surfaces.

The occurrence of phyllosilicates and their role during faulting are beyond the scope of this paper. The boundary between the two fault rocks is sharp and continuous or, alternatively, is marked by small, bulbous protrusions of ultracataclasite into the underlying foliated cataclasite, resembling

fluid-like structures (Fig. 7a). Clasts from the foliated cataclasite (between 0.1 and 10 mm in diameter) are dispersed within a ground mass composed by ultrafine-grained material (<0.1 mm in diameter) (Figs. 7a and 8a). Microcrystalline calcite cement pervades the ultracataclasite. The cement is characterized by a low dull red CL color, whereas the clasts and the ultrafine-grained material show black luminescence (Fig. 8b).

(2) The foliated cataclasite is grey and up to ~80 cm thick (Fig. 7a) and XRD data indicate that consists of 100% calcite (Table S1 in supplementary material). The foliation is marked by a series of cataclastic shear zones (Fig. 8c), which encase sigmoids and clasts of host rock affected by extensional microfractures (Fig. 8d). Also in this case, microcrystalline calcite cement pervades the foliated cataclasite. The cement, which represents the groundmass of the foliated cataclasite, and the extensional microfractures are characterized by dull red color under CL light (Fig. 8g).

Within the above-described ultracataclasite and foliated cataclasite, we recognized the following structures:

(1) Extensional fractures filled by fine-grained granular material cutting across the foliated cataclasite, often branching out from the ultracataclasite (Fig. 4a). Based on their geometry, we interpret these filled fractures as granular injections. They form a complex network with sharp boundaries (Figs. 8e and 8f,). Randomly oriented, angular to subangular reworked fragments from the ultracataclasite and/or foliated cataclasite are dispersed throughout the ultrafine matrix of the injections defining a massive and unsorted texture (Figs. 8e and 8g). Granular injections have calcite cement with bright red CL color (Fig. 8g).

(2) Type 1 veins (T1 veins) are randomly oriented calcite-filled veins < 100 μm thick with discontinuous and/or branching geometry that can be recognized only under CL light (Figs. 8g and 8h). T1 veins often branch out from set 2 injections and cut across both the ultracataclasite and the foliated cataclasite (Fig. 8g). Vein filling is composed by anhedreal and equant calcite crystals < 30 μm in diameter with blocky texture (Fig. 8i). Crystals do not show growth competition textures and smooth boundaries form triple junctions textures. No CL zoning is observed within these crystals

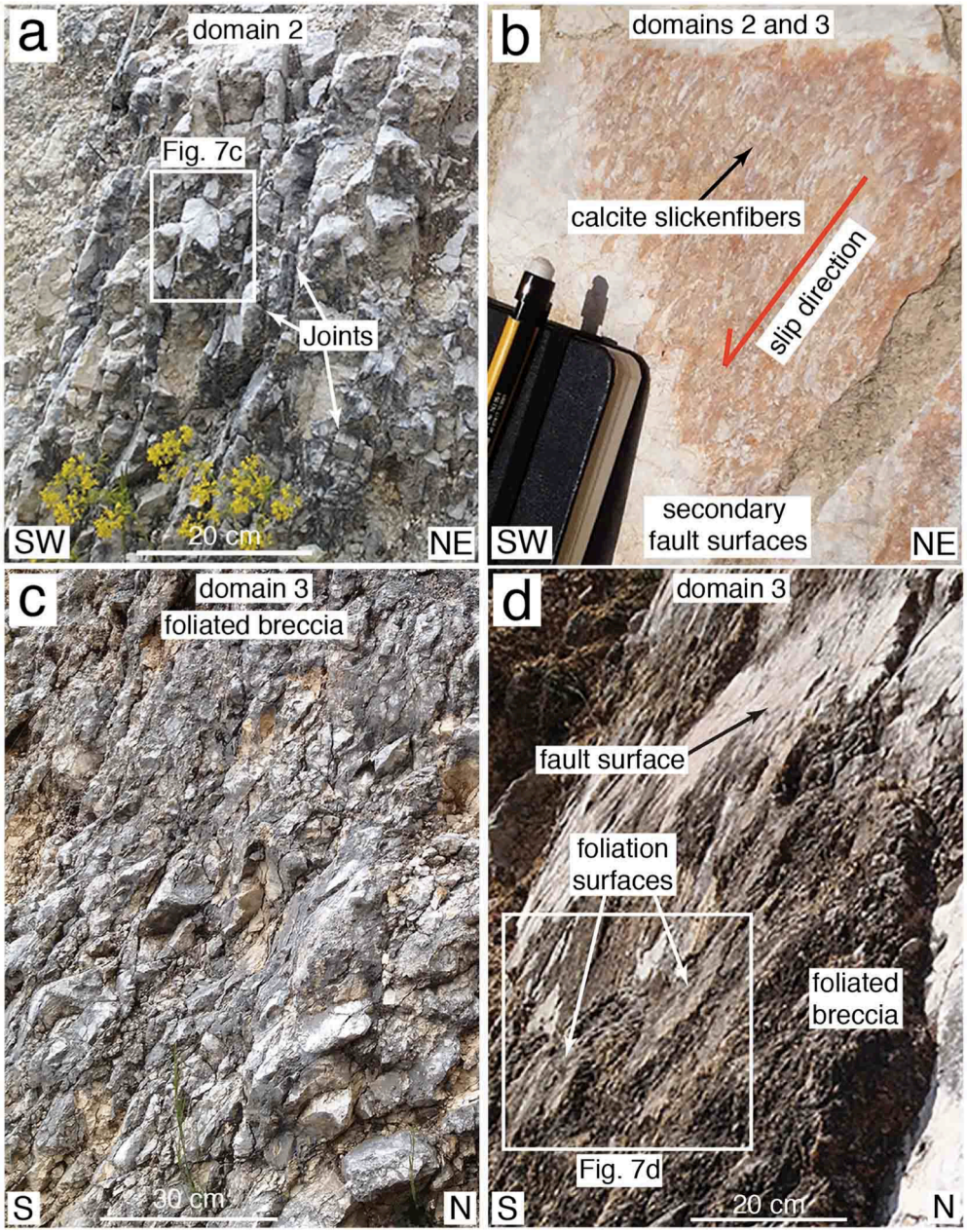


Figure 6. Mesoscale outcrop structures of the Tre Monti Fault within the damage zone (domain 2, D2) and the secondary fault zone (domain 3, D3) **(a)** WNW-ESE-striking subvertical joints (D2), which are spaced between 2 and 10 cm. **(b)** Low-displacement fault surface (D2 and D3) coated with reddish calcite slickenfibers. **(c)** Foliated breccia affected by closely spaced foliation surfaces (D3). **(d)** Foliated breccias resting above a low-displacement fault surface (D3).

that have the same bright red CL color of granular injections (Figs. 8g and 8h). The same fluid probably precipitated the calcite of both T1 veins and granular injections.

(3) Type 2 veins (T2 veins) are up to 1 mm thick extensional calcite-filled veins that are often located in steps and rhomb-shaped pull-apart structures along small Riedel shear fractures (R and P fractures; Fig. 7a). These veins are characterized by sharp boundaries and the filling is composed by

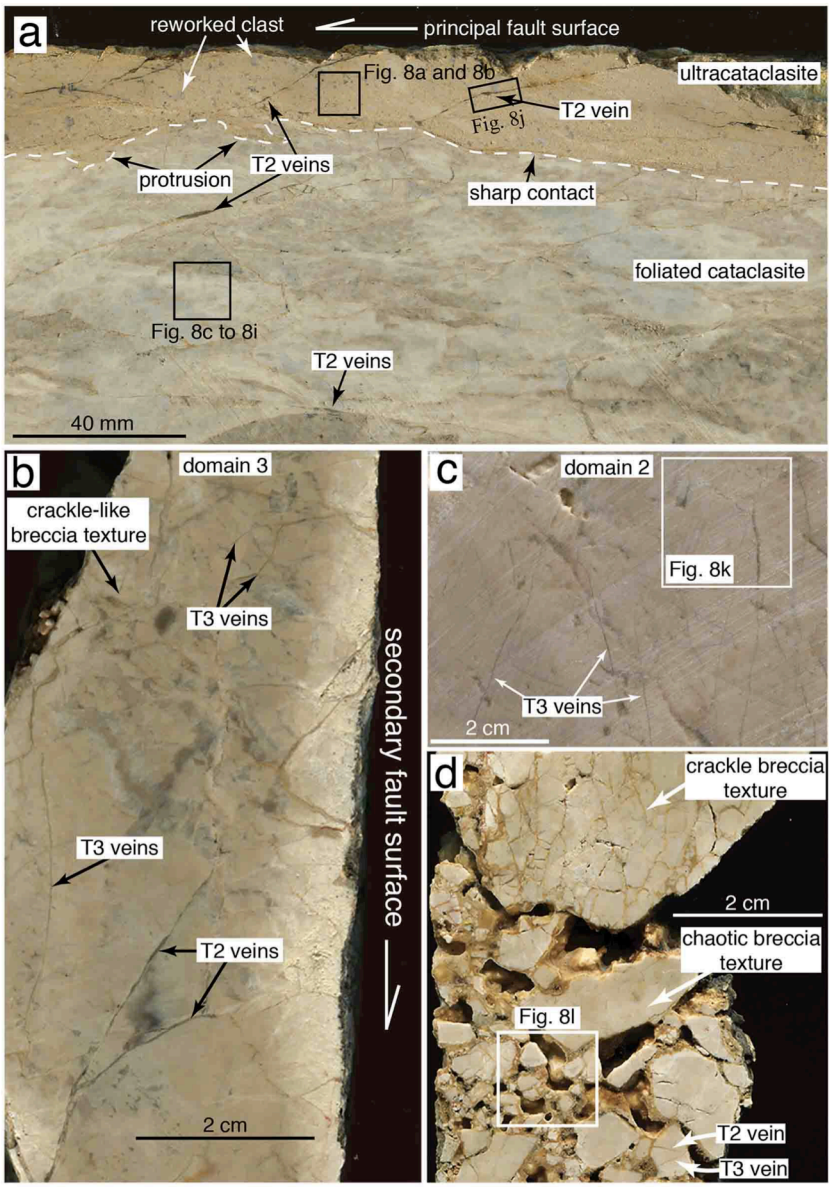


Figure 7. Mesoscale fault rock structures of the Tre Monti Fault within the three structural domains: principal fault (domain 1, D1); damage zone (domain 2, D2); secondary fault zone (domain 3, D3). **(a)** High resolution scan of principal fault sample (D1) cut perpendicularly to the fault surface and parallel to slip direction. The boundary between ultracataclasite and foliated cataclasite is sharp and continuous, but often marked by undulations, protrusions, and fluid-like structures. **(b)** High resolution scan of secondary fault sample (D3) cut perpendicularly to the fault surface and parallel to slip direction characterized by T2 and T3 veins. Note the crackle-like breccia texture created by these veins. **(c)** High resolution scan of rock sample (D2) including T3 veins. **(d)** High resolution scan of fault breccia sample (D3) characterized by chaotic texture. Note that the large clast on top is affected by an inner crackle breccia texture. Note also T2 and T3 veins within clasts.

subhedral calcite crystals up to 200 μm in size with elongate-blocky textures (Fig. 8j). Growth competition textures (e.g., Hilgers et al., 2004) are common with growth directions perpendicular to

vein walls. T2 veins are characterized by no luminescence under CL light and cut across (i.e., postdate) all the previously described structures (Fig. 8g). We recognized T2 veins also within D2 and D3 (Fig. 4a).

4.3. Damage zone (D2)

Within the ~60 m thick damage zone (Figs. 4a, 4b, and 5a), deformation is heterogeneously distributed through calcite-filled veins, patches of joints, and low-displacement (< 3 m) faults (Fig. 4a). These structures are described as follows.

(1) Type 3 veins (T3 veins) are calcite-filled extensional veins up to 1 mm thick and a few centimeters long (Figs. 7b and 7c). The veins are widespread within the entire damage zone with various orientations. Different sets crosscut each other, creating an intersecting network of calcite filled veins. The resulting texture is a crackle-like breccia similar to those described by Woodcock et al. (2014) in carbonate rocks. The crystals filling these veins are characterized by black luminescence under CL light and by textures similar to T2 veins (D1) (Fig. 8k). In D2, we also recognized T2 veins, which systematically cut across T3 veins. T3 veins are absent in D1 and present in D3 (Fig. 4a).

(2) Joints are frequent in D2 with a wide range of orientations. The most continuous and penetrative set is subvertical and WNW-ESE-oriented (plot 1 in Fig. 4c). Joints are not filled and are spaced between 0.5 and 10 cm. They delimit prismatic rock fragments (Fig. 6a) and cut across both T2 and T3 veins (Fig. 4a). Joints are substantially absent in D1.

(3) Low-displacement faults are characterized by two main strikes (N90° and N170°) with slickenfibers indicating oblique-slip and extensional dip-slip motions (plots 2, 5, and 6 in Fig. 4c). Faults and joints are characterized by mutual crosscutting relationships and both cut across T2 and T3 veins (Fig. 4a). Low-displacement faults are also present in D3 and absent in D1. Fault surfaces are commonly striated and coated by reddish calcite slickenfibers (Fig. 6b).

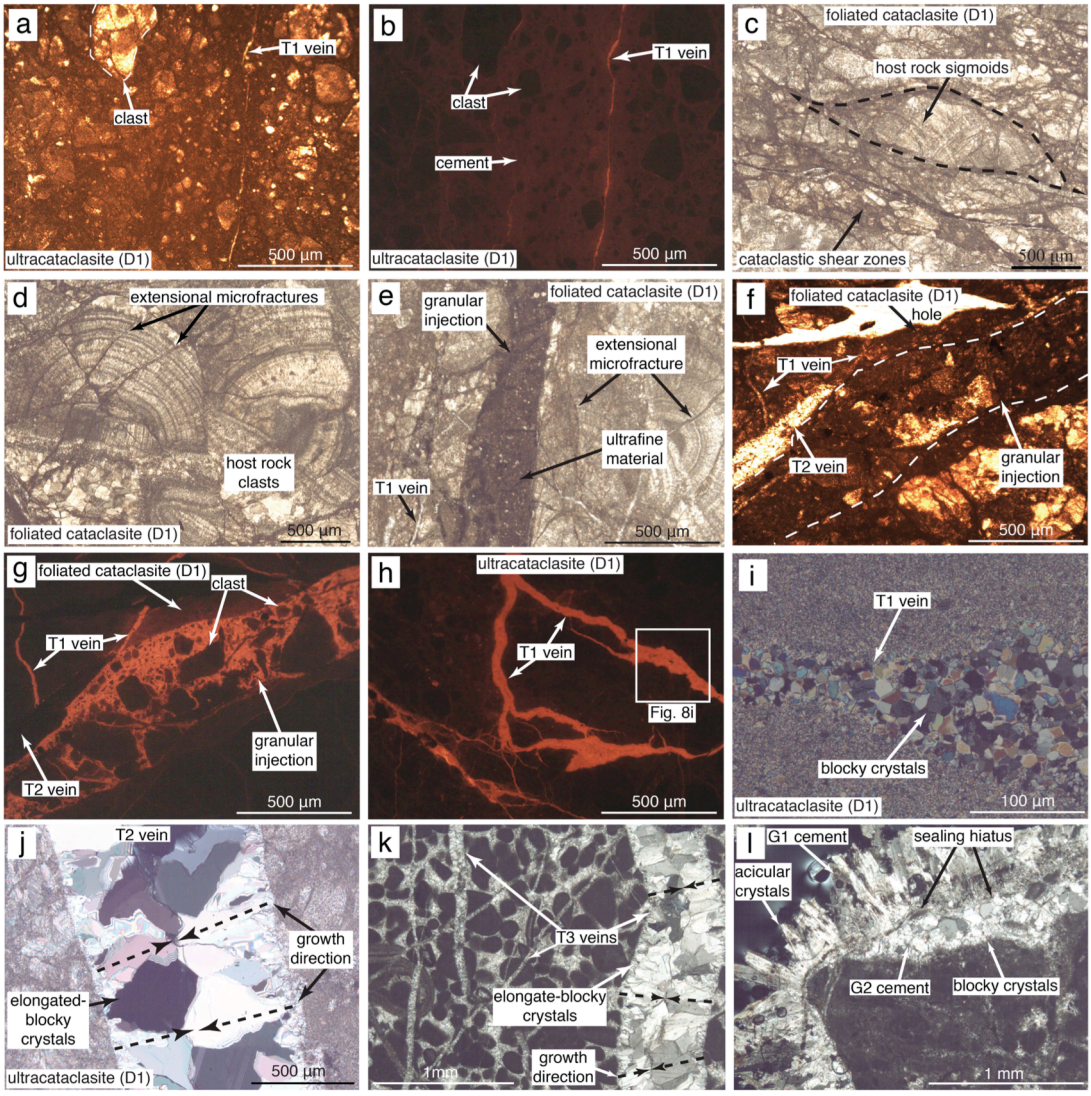


Figure 8. Microphotographs of the principal fault (Domain 1, D1), damage zone (Domain 2, D2), and secondary fault zone (Domain 3, D3) microstructures taken from thin sections under plane-polarized light (PPL), crossed polarized light (CPL), and/or cathodoluminescence light (CL). **(a)** Texture of the ultracataclasite (D1). Note the clasts from the foliated cataclasite dispersed within the ultrafine-grained matrix forming the ultracataclasite (PPL). **(b)** Same as previous microphotograph under CL. Calcite cement has dull red luminescence whereas T1 vein has bright red luminescence. **(c)** Cataclastic shear zones encasing host rock sigmoids (CPL) within the foliated cataclasite (D1). **(d)** Host rock clasts within the foliated cataclasite (D1) with extensional microfractures forming a jigsaw puzzle texture (CPL). **(e), (f)** Granular injections filled by ultrafine material (D1). Note that the injections cut through the foliated cataclasite (PPL). **(g)** Same as previous microphotograph (f) under CL. Granular injection has bright red luminescence. T1 veins have bright red luminescence and branch out from granular injection. Foliated cataclasite have dull red luminescence. T2 veins have black luminescence. Note the massive and unsorted texture of the granular injection, which cuts across the foliated cataclasite. T2 vein has no luminescence and cuts across the foliated cataclasite, T1 veins, and granular injection. **(h)** Bright red luminescence of T1 veins under CL light. **(i)** Vein filling of T1 veins (D1). Anhedral, blocky calcite crystals are characterized by boundaries with triple-junctions (CPL). **(j)** Elongate-blocky calcite crystals within T2 veins (D1). Arrows indicate growth direction and sense of vein crystals (CPL). **(k)** T3 veins characterized by elongate-blocky calcite crystals and by mutual crosscutting relationships (D2). Arrows indicate growth direction of vein crystals (CPL). **(l)** Foliated breccias (D3) with G1 cement characterized by blocky to elongate-blocky calcite crystals, whereas acicular crystals characterize the G2 fibrous cement (CPL). Note the depositional hiatus between G1 and G2 cements.

4.4. Secondary fault zone (D3)

The secondary fault zone (Figs. 4a, 4b, and 5c) consists of a ~30 m long, ~15 m high, and up to ~5 m thick zone of deformation, accommodating a ~50 m of total throw. The zone contains parallel fault segments encasing the following structures.

(1) The best-exposed fault segment (Fig. 5a) is oriented WNW-ESE-oriented with reddish calcite slickenfibers indicating right-lateral oblique-slip movements (plots 3 and 4 Fig. 4c).

(2) In D3, we recognized T2 and T3 veins, and joints. T2 veins systematically cut through T3 veins, and T2 and T3 veins are cut by both the fault surfaces and the joints.

(3) Foliated breccias (Fig. 6c) cemented by calcite are present within D3 and rest above striated fault surfaces (Figs. 5c and 6d). The boundaries between breccias and fault surfaces are sharp. Foliations within these breccias consist of undulated, sharp, and striated fault surfaces, which are roughly parallel to low-displacement faults (Figs. 5c and 6d). In places, foliation planes are also characterized by cataclastic textures. Breccias exhibit a chaotic texture (Fig. 7d; classification of Woodcock et al., 2014) with numerous voids. Clasts are randomly oriented, angular to subangular, and their diameter range from < 0.1 to 10 cm. Several clasts are characterized by inner crackle breccia textures (Fig. 7d). Within the clasts, we recognized T2 and T3 veins (Fig. 7d). Breccias are cemented by reddish calcite precipitates, which occur in two different generations. Generation 1 cement (G1) consists of blocky to elongate-blocky calcite crystals up to 200 μm in diameter (Fig. 8l). This cement fills fractures between clasts. Generation 2 cement (G2) consists of acicular calcite crystals up to 1 mm in length, forming fibrous cement (Fig. 8l). The G2 cement wraps around both carbonate clasts and G1 cement. The breccia is clast-supported, with clasts usually surrounded by G1 and/or G2 cements. “Sealing hiatuses” (sensu Nuriel et al., 2012) between G1 and G2 cements are common (Fig. 8l). Both the G1 and G2 cements show black luminescence under CL light. We synthetize all above-described structures and data in Table S2 in supplementary material.

5. Stable isotope data and whole rock geochemistry

5.1. Sampling strategy

To characterize the origin and the temperature of (parental) fluids responsible for the $CaCO_3$ precipitation (veins and cement), we analyzed the C- and O-isotope ($\delta^{13}C$ and $\delta^{18}O$) of 82 samples collected from the TMF domains and nearby rocks (Fig. 9a and Table S3 in supplementary material). In detail, we powdered bulk rocks from the ultracataclasite and foliated cataclasite (9 samples, "cataclastic rocks") as well as from the cretaceous host rock sampled outside the fault zone (9 samples, "host rock"). Concerning the cataclastic rocks, we sampled and analyzed bulk volumes, where matrix was the most abundant component, as the host rock-derived clasts were too small to be properly sampled without significant contamination from the surrounding rock. In addition, we used a microdrill equipped with spikes down to 0.3 mm in diameter to extract powder from T2 veins (18 samples, D1, D2 and D3), T3 veins (9 samples, D2 and D3), breccia cements (25 samples, D3), calcite slickenfibers on fault surfaces (4 samples, D2 and D3), and post-orogenic Plio-Quaternary deposits cements in the TMF hangingwall (9 samples). We were not able to sample T1 veins, as they are too thin (< 100 μm thick) to be sampled without significant contamination from the surrounding rock. We also determined the whole rock geochemistry of 6 samples from cataclastic rocks (ultracataclasite and foliated cataclasite, D1) and host rock (see detection limits and complete results in Table S4 in supplementary material).

5.2. Results

In Fig. 9a, we distinguished three different end-members characterized by distinct isotope signatures: group 1 (host rock), group 2 (cataclastic rocks and T3 veins), and group 3 (Plio-Quaternary deposits cements, breccia cements, T2 veins, and calcite slickenfibers).

Group 1 (host rock): $\delta^{13}C$ and $\delta^{18}O$ values range between -0.8‰ and 2.4‰, and 26‰ and 31‰, respectively. Isotope values are in agreement with a marine origin (Sharp, 2007). Moreover, whole rock geochemistry analyses indicate that the host rocks are Ca-rich (close to the calcite

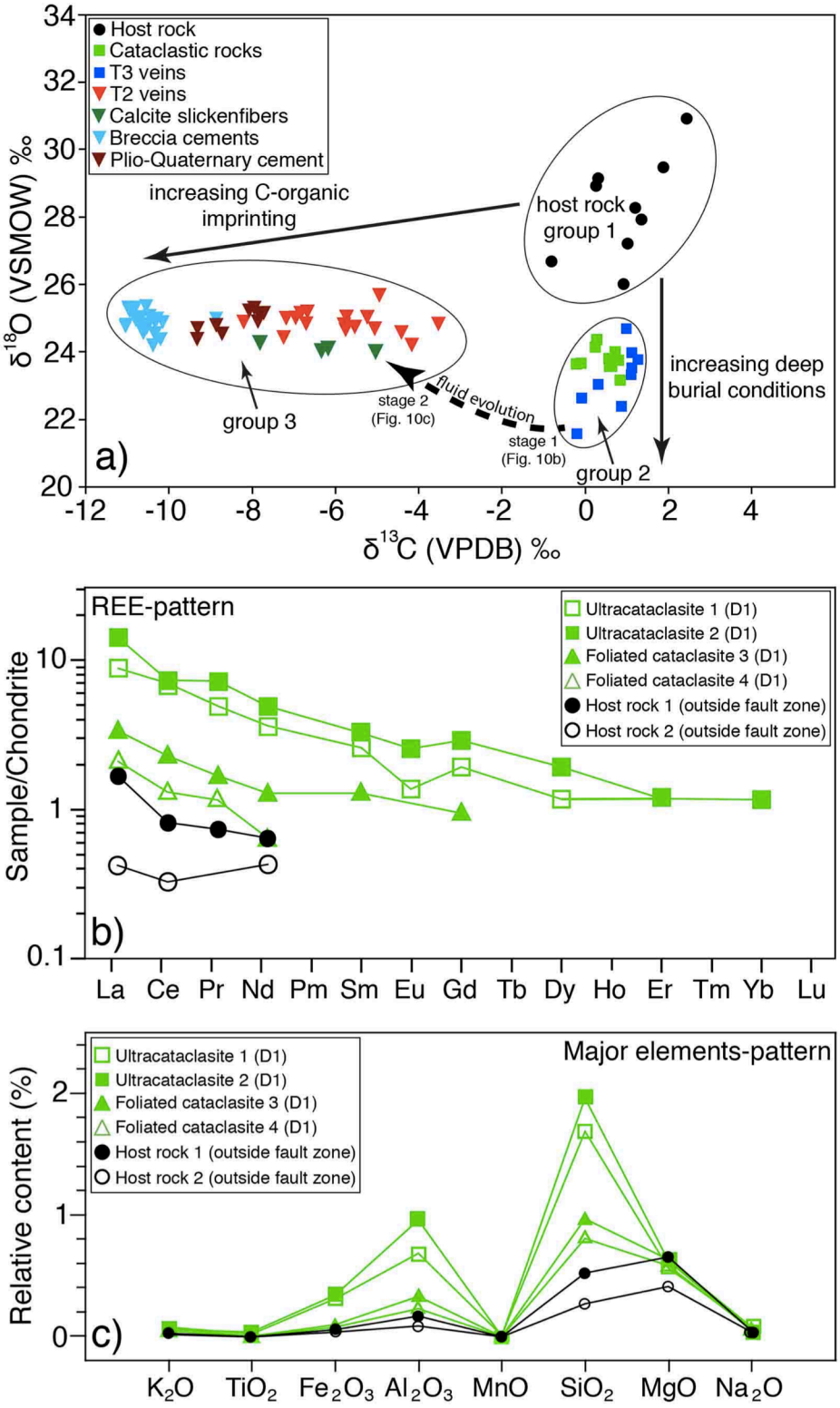


Figure 9. (a) $\delta^{13}C$ (PDB) versus $\delta^{18}O$ (SMOW) diagram for 82 analyzed samples from various carbonate rocks and mineralizations in the studied fault zone domains and surrounding area. **(b)** Chondrite-normalized REE-patterns of ultracataclasite and foliated cataclasite (cataclastic rocks, D1) and of host rocks from TMF. Note the significant REE enrichment of the ultracataclasite. **(c)** Major element pattern of ultracataclasite and foliated cataclasite (cataclastic rocks, D1) and of host rocks from TMF. Note the significant SiO_2, Al_2O_3, Fe_2O_3 enrichment of the ultracataclasite.

composition) and REE (Rare-Earth-Elements)-poor, with Sr concentrations similar to those of Cretaceous marine carbonates in central Italy as reported by Agosta and Kirchner (2003).

Group 2 (cataclastic rocks and T3 veins): in this group, $\delta^{13}C$ and $\delta^{18}O$ range between -0.1‰ and 1.6‰ and between 21.6‰ and 24.4‰, respectively. The average $\delta^{18}O$ value (23‰) is lower with respect to that of host rock (by ~5‰). In addition, whole rock geochemistry analyses indicate that the ultracataclasite, when compared with the host rock, is highly enriched in Sr, SiO_2, Al_2O_3, FeO, and REE, and depleted in CaO (Figs. 9b, 9c, and Table S4 in supplementary material). The depletion of CaO (~2 wt%) is accompanied by a depletion (~1% wt%) in LOI (loss on ignition).

Group 3 (Plio-Quaternary deposits cements, breccia cements, T2 veins, and calcite slickenfibers): in this group $\delta^{13}C$ and $\delta^{18}O$ range between -3.5‰ and -10.2‰ and between 24.1‰ and 25.8‰, respectively. The $\delta^{18}O$ values are characterized by a uniform and narrow range, whereas the $\delta^{13}C$ values are characterized by a broad range.

6. Discussion

6.1 Fluid Sources

Identifying the fluid sources is critical for the development of a correct model of fluid flow in this and similar tectonic contexts. However, as the exact temperature and the O isotope composition of the parental fluids are unknown, fluid sources cannot be unequivocally determined. To partly solve this problem, we discuss different hypotheses under the reasonable assumptions that the analyzed calcite precipitated in 0-3 km depth and 5°-100°C temperature ranges as constrained both by geological and by organic matter maturity data (Corrado et al., 2010). We hypothesize, in particular, two different fluid end-members, which are responsible for the calcite precipitation of group 2 (cataclastic rocks and T3 veins) and group 3 (breccia cement, T2 veins, and calcite slickenfibers):

(a) Group 2 (cataclastic rocks and T3 veins; Fig. 9a): the $\delta^{18}O$ values of group 2 are characterized by a marked depletion compared with those from the host rocks (group 1). In contrast,

$\delta^{13}C$ values are similar to those of the host rocks and marine water (Fig. 9a; Sharp, 2007). The $\delta^{13}C$ values, in particular, are incompatible with calcite precipitation from purely meteoric- and/or groundwater- ($\delta^{13}C < -5‰$) as well as from CO_2-rich thermogene ($\delta^{13}C > 5‰$) fluids. In particular, the measured $\delta^{18}O$ values are similar to those measured on calcite veins precipitated from fluids circulating within deep burial settings (e.g., Kirkwood et al., 2001). The observed depletion can be simply explained by a shift from a shallow marine diagenesis (host rock, group 1) towards a deeper one.

The high concentration of Sr, SiO_2, Al_2O_3, Fe_2O_3, and REE (Figs. 9b and 9c) within the ultracataclasite may account for the observed phyllosilicate enrichment, derived from syn-orogenic deposits in the fault hangingwall. However, Sr enrichment (up to 256 ppm) within the ultracataclasite (Table S4 in supplementary material) is also consistent with calcite cement precipitation in the presence of high-salinity fluids, such as marine-derived fluids trapped within the syn-orogenic deposits. This hypothesis is also consistent with and would explain the occurrence of phyllosilicates along the main fault being their fluid transport mediated by marine fluids trapped within the syn-orogenic deposits.

The $\delta^{18}O$ depletion within the cataclastic rocks is interpreted as mainly due to authigenic calcite cement precipitation from an external fluid circulated along the fault core. In particular, the red luminescence of calcite cement and T1 veins within the cataclastic rocks (Figs. 8b, 8g, and 8h) indicates authigenic calcite precipitation from an external fluid in reducing (rich in Mn^{2+}) and deep burial conditions (e.g., Nuriel et al., 2011). However, as we were not able to separate calcite cement from host rock-derived clasts, based on our geochemical data, we cannot exclude a $\delta^{18}O$ overprint related to other processes, such as calcite dissolution/re-precipitation (i.e., pressure-solution mechanism) commonly acting along fault zones. Hence, $\delta^{18}O$ values of calcite cement could be lower than those measured (i.e., $\delta^{18}O$ values of calcite cement is diluted by $\delta^{18}O$ values of host rock derived clasts). A prevalent role of pressure-solution and re-precipitation is probably excluded by

the fact that the neoformed calcite should have the same black luminescence of host rock clasts, in contrast to what observed.

The $\delta^{18}O$ and $\delta^{13}C$ values of T3 veins (damage zone, D2) are similar to those of cataclastic rocks (Fig. 9a). This evidence suggests that the same fluid responsible for cement precipitation within cataclastic rocks was also associated with a broader circulation within the damage zone, causing T3 veins precipitation. All above-reported observations and inferences suggest, as a most likely scenario, group 2 calcite precipitation within a deep burial environment from marine-derived fluids, such as connate fluid trapped within the marine sedimentary succession (foredeep syn-orogenic deposits and carbonate platform deposits). However, our isotope data are also compatible with other complex fluid origins, such as isotopically evoluted (equilibrated with the host rock for $\delta^{13}C$ values) meteoric and/or groundwater-derived fluids infiltrated at depth and mixed with trapped and/or connate fluids. To calculate the mineralizing fluid temperatures, we assume, in our preferred scenario, calcite precipitation in equilibrium with a marine-like fluid, assuming that this fluid preserved its original isotopic composition (0‰ SMOW). Thermally-activated processes, commonly occurring within narrow (mm-thick) zones along principal faults (for instance during seismic slip; Di Toro et al., 2011), may have increased fluid temperatures within the cataclastic fault core (principal fault, D1). For this reason we calculated precipitation temperatures from T3 veins (located within the damage zone, D2, i.e., most likely unaffected by frictional heating), where fluid temperatures may be controlled only by the geothermal gradient at depth. We used the equation of Kele et al., (2015) for inorganic calcite precipitation in the 6°-95°C temperature range. The calculated precipitation temperatures are in the 60° to 75°C range (average value of ~68°C, Table S2 in supplementary material). These values are consistent with the maximum burial depth of 2.5 km calculated for the TMF (assuming a geothermal gradient of 30°C/km typical of immature extensional tectonic setting).

(b) Group 3 (breccia cement, T2 veins, and calcite slickenfibers; Fig. 9a): the $\delta^{13}C$ values lower than -4‰ are typical of C-organic imprinting (mostly derived from C_3-type vegetation; Sharp,

2007). This evidence is consistent with a parental fluid that circulated trough organic rich soils before infiltrating within the fault zone. In addition, the $\delta^{13}C$ values are similar to those of groundwater measured in carbonate aquifers in central Apennines (e.g., Falcone et al., 2008). Moreover, the isotope values of T2 veins, calcite slickenfibers, and breccia cements are consistent with those of Plio-Quaternary deposits cements, unequivocally deposited in continental environment. Based on the previous considerations, we conclude that group 3 calcite precipitated from a meteoric-derived fluid that circulated trough organic rich soils and then into carbonates groundwater aquifers before infiltrating within the fault zone. We calculated the mineralizing fluid temperatures considering calcite precipitation in equilibrium with meteoric-derived fluids ($\delta^{18}O$ from -7/-8‰ SMOW; Sharp, 2007). Results indicate low precipitation temperatures in the 14° to 26°C range (Table S2 in supplementary material). The calculated temperatures are consistent with in situ temperatures of groundwater aquifers at ≤1 km depth (e.g., Pasquale et al., 2013).

6.2. Spatio-temporal evolution of fault zone architecture and fluid flow

The association of different fluid sources with different styles of structural deformation allowed us to reconstruct two different stages of fault zone evolution and fluid circulation during the burial/exhumation history of the shallow portion (< 3 km depth) of a carbonate-hosted seismogenic fault. We describe the two stages as follows.

(a) After the compressional phase, characterized by folding and thrusting, the Apennines belt experienced extension, exhumation, and seismicity (Doglioni, 1991; Fig. 10a). In the TMF, based on the crosscutting relationships, the first structures were cataclastic rocks (group 2; D1) within the principal fault and T3 veins in the damage zone (group 2; D2) (Fig. 10b). The isotope data together with the calculated precipitation temperatures (in the 60° to 75°C range) indicate calcite precipitation from marine-derived fluids at depths < 3 km. At these depths, deformation was strongly concentrated along the principal fault (D1), which juxtaposed marine syn-orogenic deposits with pre-orogenic carbonate deposits for a total cumulative displacement > 1 km (Fig.

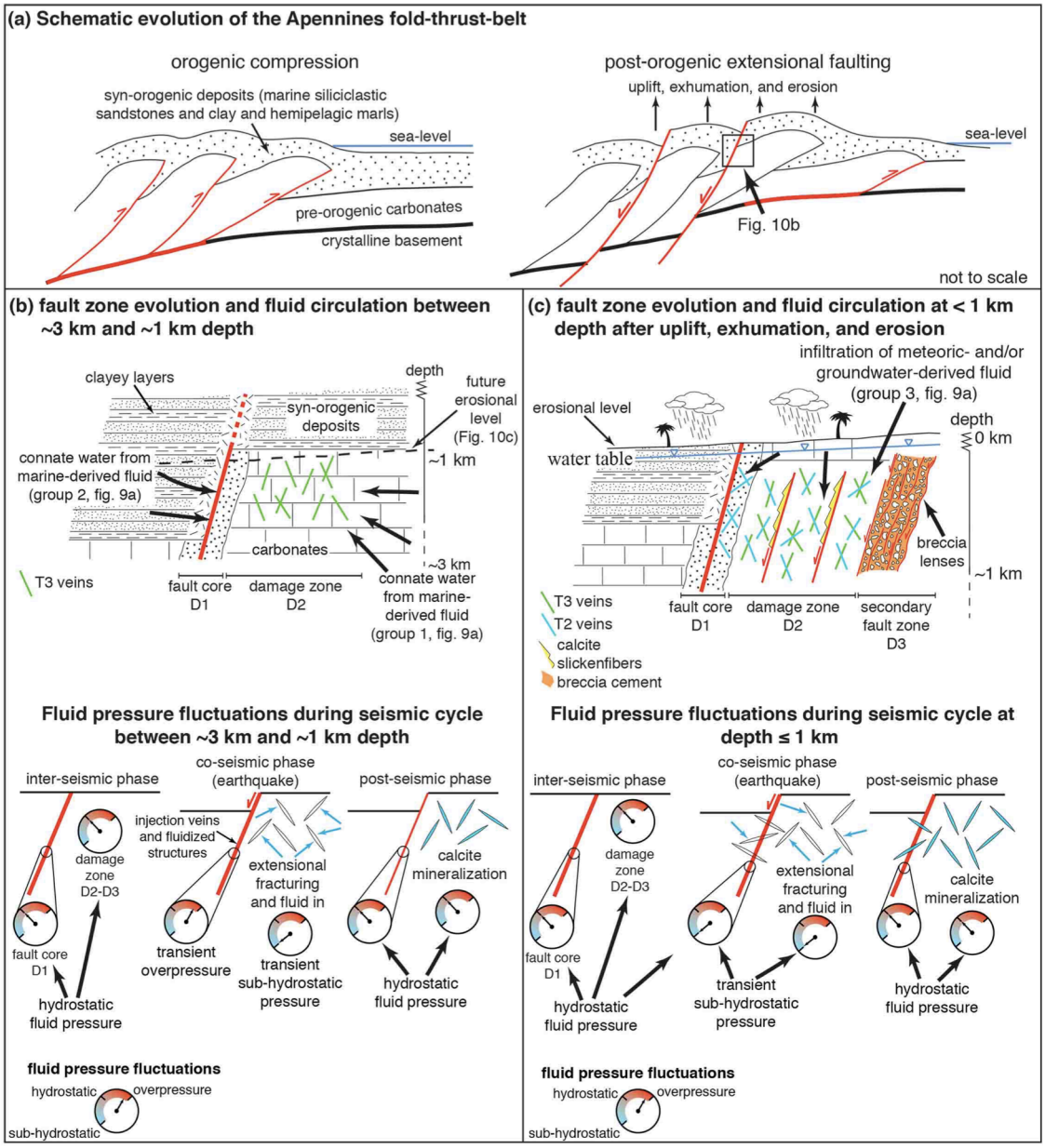


Figure 10. Cartoon showing the conceptual model for the evolution of a shallow (≤ 3 km) extensional fault zone and seismic-related fluid circulation. **(a)** Burial-exhumation history of the Apennines belt involving compression and post-collisional extension. **(b)** In the first stage of fault zone evolution, deformation and fault displacement are concentrated along the principal fault surface (D1), whereas less intense deformation is distributed within the damage zone (D2). The isotope trend in the $\delta^{18}O$-$\delta^{13}C$ space indicates that calcite prevalently precipitated from marine-derived fluids (brines and/or connate waters) between ~3 km and ~1 km depth and at temperature of ~68 °C. At these depths, during co-seismic dilation, fluid pressure instantaneously dropped at sub-hydrostatic pressure conditions within newly created dilatant fractures occurring in the damage zone (D2). This process led to calcite precipitation and mineralization. At the same time, localized and transient suprahydrostatic pressure condition were generated along the principal fault surface (D1). After the co-seismic phase, fluids regained hydrostatic pressure conditions. **(c)** In the second stage of fault zone evolution, deformation and fault displacement are distributed within the damage zone (D2) and the secondary fault zone (D3). The isotope trend in the $\delta^{18}O$-$\delta^{13}C$ space indicates that calcite precipitated from meteoric- and/or groundwater-derived fluids at depths ≤ 1 km and temperatures below 35 °C. At these depths, during co-seismic dilation, fluid pressure instantaneously dropped at subhydrostatic pressure conditions within newly created dilatant fracture in the whole fault zone (D1-D2-D3). This process led to calcite precipitation and mineralization. No evidence of localized and transient suprahydrostatic pressure conditions are present. After the co-seismic phase, fluids regained hydrostatic pressure conditions.

10b). On the other hand, fracturing and veining generated broad and less intense deformation within the damage zone (D2, Fig. 10b). Consequently, marine-derived connate waters trapped within marine syn-orogenic deposits flowed laterally into the principal fault and similar fluids trapped within carbonates deposits flowed into the damage zone (Fig. 10b). Clayey layers within the syn-orogenic deposits may have created low-permeability barriers, which did not allow mixing between connate and external (i.e., meteoric- and/or groundwater-derived fluids) fluids. The different luminescence between calcite precipitates within cataclastic rocks (bright and dull) and T3 veins (black) possibly indicate a difference in the redox conditions within precipitation environments and/or slightly different fluid chemistry within the syn-orogenic deposits with respect to that within the carbonate rocks. In this latter case, the principal fault must have provided a permeability barrier to fluid flow toward the damage zone. This setting suggests semi-closed to closed hydrological conditions as documented in other extensional (e.g., Williams et al., 2015) and compressional tectonic settings (e.g., Ghisetti et al., 2001; Kirkwood et al., 2001; Vannucchi et al., 2010).

(b) In the late stage of fault zone development, the exposed portion of the TMF was exhumed by uplift and erosion of the Apennines belt (Galadini et al., 2003). Owing to low confining pressure, deformation was distributed over a broader volume in the damage zone (D2) and in the secondary fault zone (D3), where patches of joints, breccias, T2 veins, and low-displacement faults developed (Fig. 10c). Displacement was no more accommodated only by the principal fault, but also by low-displacement faults.

Isotope values of T2 veins (group 3; D1, D2, and D3), calcite slickenfibers (group 3; D2 and D3), breccia cements (group 3; D3), and black luminescence of these structures indicate calcite precipitation from meteoric- and/or groundwater-derived fluids in the 14° to 26°C range typical of depths < 1 km. Therefore, we suggest that, during exhumation, the TMF must have intersected shallow (< 1 km depth) groundwater aquifers connected with the Earth's surface so that meteoric-derived fluids infiltrated downward into the fault zone (Fig. 10c) through high-permeability structural conduits (i.e., breccia lenses and joints). The large variation in $\delta^{13}C$ isotope values

suggests different degrees of organic carbon contamination during multiple events of meteoric water infiltrations or variable organic carbon contamination within the aquifer during multiple events of fluid infiltrations. Similar scenarios have been documented in other carbonate fault zones in the same region (e.g., Agosta and Kirschner, 2003) and in other tectonic settings (e.g., Menzies et al., 2014), also in connection with seismic sequences (Amoruso et al., 2011; Doglioni et al., 2013).

6.3. Fluid involvement in the seismic cycle

In this section, we discuss a model for fluid circulation, fluid pressure fluctuations, and fluid redistribution during concurrent exhumation and seismic activity within the shallow portion (≤ 3 km depth) of active fault zones in carbonate rocks, such as the TMF.

(a) Inter-seismic phase: The high permeability networks of fractures and breccias of the TMF allowed the maintenance of hydrostatic fluid pressure up to a depth of ~3 km within critically-stressed faults (e.g., Townend and Zoback, 2000). Fluid pressure was essentially at hydrostatic value between ~3 km and ~1 km depth and at depth ≤ 1 km within the whole fault zone (Figs. 10b and 10c).

(b) Co-seismic phase: crackle and chaotic breccia textures suggest that the TMF slipped seismically with episodic events of co-seismic dilatancy and implosive brecciation within dilational jogs associated with a rapid fluid depressurization (e.g., Sibson, 1986; Woodcock et al., 2014). Cataclasis and shearing may have been either synchronous with co-seismic slip or associated with aseismic creep during interseismic periods (e.g., Stünitz et al., 2010). We propose that extensional fractures and crackle-like brecciation within the damage zone between ~3 km and ~1 km depth (D2 and D3; Fig. 10b) and within the whole fault zone at depth ≤ 1 km (D1, D2, and D3; Fig. 10c) occurred by co-seismic dilatancy at hydrostatic fluid pressure both by rapid tensile pulses propagation (e.g., Ben-Zion and Shi, 2005) and by dilatancy along fault dilational jogs (e.g., Sibson, 2000) rather than by hydrofracturing at near-lithostatic fluid pressure. Dilational jogs commonly develop along strongly undulated fault surfaces, such as those of the secondary fault zone (Fig. 5c).

As tensile strength is small for most sedimentary rocks (1-10 MPa), extensional fracturing and dilatancy can occur down to ~3-4 km depth at hydrostatic fluid pressure (e.g., Sibson, 2000). Even if overpressured fluids were generated at depths of ~5-10 km (e.g., Miller et al., 2004; Haney et al., 2005; Di Luccio et al., 2010), these overpressures could not have been sustained during their upward propagation within high permeability fracture networks and breccias of shallow fault zones (Townend and Zoback, 2000). Thus, hydrofracturing was improbable at shallow crustal depths (≤ 3 km). Immediately after co-seismic dilatancy, the fluid pressure dropped toward subhydrostatic values into newly created extensional fractures allowing the suction of fluids into fractures, CO_2 partial pressure drop and exsolution, and calcite precipitation from a suprasaturated solution (e.g., Uysal et al., 2009; Figs. 10b and 10c). Crosscutting relationships and vein network from TMF suggest multiple events of earthquake-related dilatancy, earthquake-related fluid circulation, and calcite precipitation. However, we found evidence indicating that transient overpressures were only localized into the principal fault (D1) when the fault was active between ~3 km and ~1 km depth (Fig. 10b). Granular injections show texture of injection veins similar to those described by Lin, (2011), indicating that fluid and ultrafine granular material became fluidized to form a solid-liquid system, which was squeezed into the complex network of extensional hydrofractures created by overpressured fluids. Moreover, we interpret fluid-like structures (Fig. 7a) similar to those found at smaller scales in the TMF by Smith et al., (2011) as the result of fluidization of granular material that probably occurred by overpressured fluid release. In addition, calcite crystal textures in T1 veins indicate very high calcite precipitation rate (e.g., Boullier et al., 2004). This is due to large CO_2 pressure drop and exsolution as, at low temperatures (< 100 °C), the larger the CO_2 pressure drop and exsolution, the higher the calcite precipitation rate. Large pressure drops likely occurred during fall from suprahydrostatic fluid pressure (i.e., near-lithostatic) to hydrostatic fluid pressure within newly created hydrofractures.

(c) Post-seismic phase: After co-seismic dilatancy, fluids were passively redistributed at hydrostatic pressure level through the newly created network of high permeable extensional

fractures and breccias (Figs. 10b and 10c). Microstructures of calcite filled veins indicate that extensional fractures remained open at hydrostatic pressure conditions until sealing occurred. Calcite filling is characterized by subhedral crystals with growth competition textures, indicating that crystals slowly precipitated into fluid-filled and open spaces with continuous advection of suprasaturated solution (e.g., Hilgers et al., 2004). Estimated growth rates of natural calcite crystals in tectonic veins precipitated at non-equilibrium conditions range between 10^{-1} and 10^{-2} mm/a (Uysal et al., 2009; Frery et al., 2015). Veins from TMF are only up to 1 mm wide, indicating that they may have been sealed in a few years or months and even less time for thinner veins. Localized and transient fluid pressure (e.g., Hadizadeh et al., 2012) could not have maintained extensional fractures open for such times.

7. Conclusions

We integrated geological mapping and structural analyses together with cathodoluminescence, mineralogical, and geochemical investigations to propose, from a single case history, a conceptual model of seismic fault zone evolution. In the studied case, the stratigraphic-structural setting and burial-exhumation history involved the presence of different types of geofluids (i.e., marine- and meteoric-derived), which have actively or passively assisted the seismic cycle. Between ~3 km and ~1 km depths and temperatures between 60 and 75 °C, prevalently marine-derived fluids trapped within syn-orogenic deposits and carbonate rocks in the hangingwall and footwall, respectively, circulated within the fault zone. Semi-closed hydrological circulation, created by low-permeability barriers within the syn-orogenic deposits (i.e., clayey layers), did not allow substantial mixing with meteoric-derived fluid. During co-seismic dilatancy, fluid pressure shifted toward sub-hydrostatic values in the damage zone and toward an overpressure state along the principal fault, where overpressured fluids actively assisted the co-seismic slip promoting hydrofracturing and granular fluidization. During the post-seismic phase, fluids were passively re-distributed at hydrostatic pressure. With the progressive exhumation toward depths ≤ 1 km, the hydrological circulation

became open due to the formation of high permeability conduits (i.e,, high permeability breccia lenses).. Meteoric-derived fluids infiltrated and circulated within groundwater aquifers and then into the fault zone at temperatures < 30 °C. At these depths, fluid pressure shifted from subhydrostatic to hydrostatic values during co-seismic and post-seismic phases, respectively, without fluid overpressure occurrences. We assess that the proposed model of seismic fluid-fault interaction can be valid elsewhere as the stratigraphic and tectonic setting of the Central Apennines is similar to other seismically active fold-thrust belts characterized by later extension and exhumation. We point out, in particular, the role played by low-permeability compartments that can modulate the type of fluids infiltrating into the fault zone at various levels of exhumation.

8. References

Agosta, F., Kirschner, D.L., (2003). Fluid conduits in carbonate-hosted seismogenic normal faults of central Italy. Journal of Geophysical Research 108, 2221, doi: 10.1029/2002JB002013.

Amoruso, A., Crescentini, L., Petitta, M., Rusi, S., Tallini, M., (2011). Impact of the 6 April 2009 L'Aquila earthquake on groundwater flow in the Gran Sasso carbonate aquifer, Central Italy. Hydrological Processes 25, 1754-1764, doi: 10.1002/hyp.7933.

Ben-Zion, Y., Shi, Z., (2005). Dynamic rupture on a material interface with spontaneous generation of plastic strain in the bulk. Earth and Planetary Science Letters 236, 486-496, doi: 10.1016/j.epsl.2005.03.025.

Benedetti, L., Manighetti, I., Gaudemer, Y., Finkel, R., Malavieille, J., Pou, K., Maurice, A., Aumaitre, G., Bourlès, D., Keddadouche, K., (2013). Earthquake synchrony and clustering on Fucino faults (Central Italy) as revealed from in situ ^{36}Cl exposure dating. Journal of Geophysical Research 118, 4948-4974, doi: 10.1002/jgrb.50299, 2013.

Boullier, A. M., Fujimoto, K., Ohtani, T., Roman-Ross, G., Lewin, E., Ito, H., Pezard, P., Ildefonse, B. (2004). Textural evidence for recent co-seismic circulation of fluids in the Nojima fault zone, Awaji island, Japan. Tectonophysics 378, 165-181, doi: 10.1016/j.tecto.2003.09.006.

Cavinato G.P., Carusi C, Dall'Asta M, Miccadei E, Piacentini T., (2002). Sedimentary and tectonic evolution of Plio–Pleistocene alluvial and lacustrine deposits of Fucino Basin (central Italy). Sedimentary Geology 148, 29-59, PII: S0037-0738(01)00209-3.

Chen, J., Yang, X., Ma, S., Spiers, C.J. (2013). Mass removal and clay mineral dehydration/rehydration in carbonate‐rich surface exposures of the 2008 Wenchuan Earthquake fault: Geochemical evidence and implications for fault zone evolution and coseismic slip. Journal of Geophysical Research 118, 474-496, doi: 10.1002/jgrb.50089.

Chiaraluce, L., (2012). Unravelling the complexity of Apenninic extensional fault systems: A review of the 2009 L'Aquila earthquake (Central Apennines, Italy). Journal of Structural Geology 42, 2-18, doi: 10.1016/j.jsg.2012.06.007.

Corrado, S., Aldega, L., Zattin M., (2010). Sedimentary vs. tectonic burial and exhumation along the Apennines (Italy). In: Beltrando, M., Peccerillo, A., Mattei, M., Conticelli, S., Doglioni, C., (Eds.), The Geology of Italy, Journal of the Virtual Explorer 36, Electronic

Edition, paper 15, 1-37, doi: 10.3809/jvirtex.2010.00232.

Cosentino, D., Cipollari P., Marsili P., Scrocca, D., (2010). Geology of the central Apennines: a regional review. In: Beltrando, M., Peccerillo, A., Mattei, M., Conticelli, S., Doglioni, C., (Eds.), Journal of the Virtual Explorer 36, paper 12, 1-36, doi: 10.3809/jvirtex.2010.00223.

Cox, S.F., (1995). Faulting processes at high fluid pressures: an example of fault valve behavior from the Wattle Gully Fault, Victoria, Australia. Journal of Geophysical Research 100, 12841-12859.

Di Luccio, F., Ventura, G., Di Giovambattista, R., Piscini, A., Cinti, F.R., (2010). Normal faults and thrusts reactivated by deep fluids: The 6 April 2009 Mw 6.3 L'Aquila earthquake, central Italy. Journal of Geophysical Research 115, 1-15, doi: 10.1029/2009JB007190.

Di Toro, G., Han, R., Hirose, T., De Paola, N., Nielsen, S., Mizoguchi, K., Ferri, F., Cocco, M., Shimamoto, T., (2011). Fault lubrication during earthquakes. Nature 471, 494-498, doi:10.1038/nature09838.

Doglioni, C., (1991). A proposal for the kinematic modelling of W-dipping subductions; possible applications to the Tyrrhenian-Apennines system. Terra Nova 3, 423-434.

Doglioni, C., Barba S., Carminati E., Riguzzi F., (2013). Fault on-off versus coseismic fluids reaction. Geoscience Frontiers 5, 767-780, doi: 10.1016/j.gsf.2013.08.004.

Falcone, R.A., Falgiani, A., Parisse, B., Petitta, M., Spizzico, M., Tallini M., (2008). Chemical and isotopic (δ^{18}O‰, δ^{2}H‰, δ^{13}C‰, ^{222}Rn) multi-tracing for groundwater conceptual model of carbonate aquifer (Gran Sasso INFN underground laboratory–central Italy). Journal of hydrology 357, 368-388, doi: 10.1016/j.jhydrol.2008.05.016.

Frery, E., Gratier, J.P., Ellouz-Zimmerman, N., Loiselet, C., Braun, J., Deschamps, P., Blamart, D., Hamelin, B., Swennen, R., (2015). Evolution of fault permeability during episodic fluid circulation: Evidence for the effects of fluid–rock interactions from travertine studies (Utah–USA). Tectonophysics 651, 121-137, doi: 10.1016/j.tecto.2015.03.018

Galadini, F., Messina P., Giaccio B., Sposato, A., (2003). Early uplift history of the Abruzzi Apennines (central Italy): available geomorphological constraints, Quaternary International 101-102, 125–135, doi: 10.1016/S1040-6182(02)00095-2.

Galli, P., Galadini, F. and D., Pantosti, (2008). Twenty years of paleoseismology in Italy. Earth Science Review 88, 89-117, doi: 10.1016/j.earscirev.2008.01.001.

Ghisetti, F., Kirschner, D.L., Vezzani, L., Agosta, F., (2001). Stable isotope evidence for contrasting paleofluid circulation in thrust faults and normal faults of the central Apennines, Italy. Journal of Geophysical Research 106, 8811-8825.

Hadizadeh, J., Mittempergher, S., Gratier, J.P., Renard, F., Di Toro, G., Richard, J., Babaie, H.A., (2012). A microstructural study of fault rocks from the SAFOD: Implications for the deformation mechanisms and strength of the creeping segment of the San Andreas Fault. Journal of Structural Geology 42, 246-260, doi: 10.1016/j.jsg.2012.01.011.

Haney, M.M., Snieder, R., Sheiman, J., Losh, S., (2005). Geophysics: A moving fluid pulse in a fault zone. Nature 437, 46-46, doi: 10.1038/437046.

Hickman, S., Sibson, R., Bruhn, R. (1995). Introduction to special section: Mechanical involvement of fluids in faulting. Journal of Geophysical Research 100, 12831-12840.

Hilgers, C., Dilg-Gruschinski, K., Urai, J.L., (2004). Microstructural evolution of syntaxial veins formed by advective flow, Geology 32, 261-264, doi: 10.1130/G20024.1.

Kele, S., Breitenbach, S.F.M., Capezzuoli, E., Nele Meckler, A., Ziegler, M., Millan, I.M., Kluge, T., Deák, J., Hanselmann, K., John, C.M., Yan, H., Liu, Z., Bernasconi, S.M., (2015). Temperature dependence of oxygen- and clumped isotope fractionation in carbonates: a study of travertines and tufas in the 6-95°C temperature range. Geochimica et Cosmochimica Acta 168, 172-192, doi: 10.1016/j.gca.2015.06.032.

Kirkwood, D., Savard, M. M., Chi, G., (2001). Microstructural analysis and geochemical vein characterization of the Salinic event and Acadian Orogeny: evaluation of the hydrocarbon reservoir potential in eastern Gaspé. Bulletin of canadian petroleum geology 49, 262-281.

Lin, A., (2011). Seismic slip recorded by fluidized ultracataclastic veins formed in a coseismic shear zone during the 2008 MW 7.9 Wenchuan earthquake. Geology 39, 547-550, doi: 10.1130/G32065.1.

Malagnini, L., Lucente, F.P., De Gori, P., Akinci, A., Munafo, I., (2012). Control of pore fluid pressure diffusion on fault failure mode: Insights

from the 2009 L'Aquila seismic sequence. Journal of Geophysical Research 117, B05302, doi: 10.1029/2011JB008911.

Menzies, C.D., Teagle, D.A., Craw, D., Cox, S.C., Boyce, A.J., Barrie, C.D., Roberts, S., (2014). Incursion of meteoric waters into the ductile regime in an active orogen. Earth and Planetary Science Letters 399, 1-13, doi: 10.1016/j.epsl.2014.04.046.

Miller, S.A., Collettini, C., Chiaraluce, L., Cocco, M., Barchi, M., Kaus, B.J.P., (2004). Aftershocks driven by a high-pressure CO_2 source at depth. Nature 427, 724-727, doi: 10.1038/nature02251.

Morewood, N., Roberts, G.P (2000). The geometry, kinematics and rates of deformation within an en échelon normal fault segment boundary, central Italy. Journal of Structural Geology 22, 1027-1047, PII: S0191-8141(00)00030-4.

Nuriel, P., Rosenbaum, G., Uysal, I.T., Zhao, J.-X., Golding, S.D., Weinberger, R., Karabacak, V., Avni, Y., (2011). Formation of fault-related calcite precipitates and their implications for dating fault activity in the East Anatolian and Dead Sea fault zones. In: Fagereng, Å., et al., (eds), Geology of the earthquake source: A volume in honour of Rick Sibson: The Geological Society of London Special Publication 359, 229–248, doi: 10.1144/SP359.13.

Nuriel, P., Weinberger, R., Rosenbaum, G., Golding, S.D., Zhao, J.-X., Uysal, I.T., Bar-Matthews, M., Gross, M.R., (2012). Timing and mechanism of late-Pleistocene calcite vein formation across the Dead Sea Fault Zone, northern Israel. Journal of Structural Geology 36, 43–54, doi: 10.1016/j.jsg.2011.12.010.

Pasquale, V., Chiozzi, P., Verdoya, M., (2013). Evidence for thermal convection in the deep carbonate aquifer of the eastern sector of the Po Plain, Italy. Tectonophysics 594, 1-12, doi: 10.1016/j.tecto.2013.03.011.

Patacca, E., Scandone P., Di Luzio E., Cavinato G.P., Parotto, M. (2008). Structural architecture of the central Apennines: Interpretation of the CROP 11 seismic profile from the Adriatic coast to the orographic divide. Tectonics 27, tc3006, doi:10.1029/2005tc001917.

Rowe, C.D., Griffith, W.A., (2015). Do Faults Preserve a Record of Seismic Slip: A second opinion. Journal of Structural Geology 78, 1-26, doi: 10.1016/j.jsg.2015.06.006.

Sharp, Z., (2007). Principles of stable isotope geochemistry. Pearson Prentice Hall, 344 pp.

Sibson, R.H., (2000). Fluid involvement in normal faulting. Journal of Geodynamics 29, 469-499, PII: S0264-3707(99)00042-3.

Sibson, R.H. (2014). Earthquake Rupturing in Fluid-Overpressured Crust: How Common? Pure and Applied Geophysics 171, 2867-2885, doi: 10.1007/s00024-014-0838-3.

Smith, S.A.F., Billi, A., Di Toro, G., Spiess, R., (2011). Microstructures of Principal Slip Zones in Limestones, and Implications for the Seismic Cycle (Tre Monti fault, central Appennines, Italy). Pure and Applied Geophysics 168, 2365-2393, doi: 10.1007/s00024-011-0301-7.

Stiros, S., (1995). Unexpected shock rocks an 'aseismic' area. Eos, Transactions American Geophysical Union 76, 513-519, doi: 10.1029/95EO00316.

Stünitz, H., Keulen, N., Hirose, T., Heilbronner, R. (2010). Grain size distribution and microstructures of experimentally sheared granitoid gouge at coseismic slip rates–Criteria to distinguish seismic and aseismic faults?. Journal of Structural Geology 32, 59-69, doi: doi:10.1016/j.jsg.2009.08.002.

Thomson, S. N., Brandon, M. T., Reiners, P. W., Zattin, M., Isaacson, P. J., & Balestrieri, M. L. (2010). Thermochronologic evidence for orogen-parallel variability in wedge kinematics during extending convergent orogenesis of the northern Apennines, Italy. Geological Society of America Bulletin,122, 1160-1179, doi:10.1130/B26573.1.

Townend, J., Zoback, M.D., (2000). How faulting keeps the crust strong. Geology 28, 399-402, doi: 10.1130/0091-7613.

Uysal, I.T., Feng, Y., Zhao, J.X., Isik, V., Nuriel, P., Golding, S.D., (2009). Hydrotermal CO_2 degassing in seismically active zones during the Late Quaternary. Chemical Geology 265, 442-454, doi: 10.1016/j.chemgeo.2009.05.011.

Vannucchi, P., Remitti, F., Bettelli, G., Boschi, C., Dallai, L., (2010). Fluid history related to the early Eocene ‐ middle Miocene convergent system of the Northern Apennines (Italy): Constraints from structural and isotopic studies. Journal of Geophysical Research 115, 1978-2012, 115, doi: 10.1029/2009JB006590.

Ventura, G., Di Giovambattista, R., (2013). Fluid pressure, stress field and propagation style of coalescing thrusts from the analysis of the 20 May 2012 ML 5.9 Emilia earthquake (Northern Apennines, Italy). Terra Nova 25, 72-78, doi: 10.1111/ter.12007.

Williams, R.T., Goodwin, L.B., Mozley, P.S., Beard, B.L., Johnson, C.M., (2015). Tectonic controls on fault zone flow pathways in the Rio Grande rift, New Mexico, USA. Geology 43, 723-726, doi: 10.1130/G36799.1.

Woodcock, N.H., Miller A.V.M., Woodhouse, C.D. (2014). Chaotic breccia zones on the Pembroke Peninsula, south Wales: Evidence for collapse into voids along dilational faults. Journal of Structural Geology 69, 91-107, doi: 10.1016/j.jsg.2014.09.019.

9. Supplementary material

Lithology	Quartz (%)	K-feldspar (%)	Plagioclase (%)	Dolomite (%)	Calcite (%)	Clay minerals (%)
Ultracataclasite (D1)	0	0	0	0	98.5	1.5
Foliated cataclasite (D1)	0	0	0	0	100	0

Table S1. Results of X-ray diffraction analyses from cataclastic rocks (D1; ultracataclasite and foliated cataclasite)

	Ultracataclasite (UC)	Foliated cataclasite (FC)	Granular injections (GI)	T1 veins (T1)	T2 veins (T2)	T3 veins (T3)	Breccia cements (BC)	Calcite slickenfibers (CS)
Domain 1 (D1)	X	X	X	X	X			
Domain 2 (D2)					X	X		X
Domain 3 (D3)					X	X	X	X
Crosscutting relationships	UC cuts FC	FC cuts host rock	GI cut FC	T1 cuts UC, FC, GI	T2 cuts UC, FC, GI, T1, T3, and host rock	T3 cuts host rock	BC cuts structure T2, T3, and host rock	CS cuts T2, T3, BC, and host rock
Cathodoluminescence color	Dull red	Dull red	Bright red	Bright red	Black	Black	Black	Black
$\delta^{18}O$ ‰ (Vs SMOW)	23.82	23.82	Not determined	not determined	24.83	24.07	24.92	24.18
$\delta^{13}C$ ‰ (Vs PDB)	0.42	0.42	Not determined	not determined	-5.73	0.74	-10.53	-6.35
Precipitation temperatures	60° - 75°C	60° - 75°C	Not determined	Not determined	14° - 25°C	60° - 75°C	16° - 26° C	20° - 26° C

Table S2. Synthesis of mesostructures, microstructures, cathodoluminescence data, crosscutting relationships, and precipitation temperatures within Domains 1, 2, and 3.

Sample Name	Domain	Mineralogy	$\delta^{13}C$ ‰ (Vs PDB)	$\delta^{18}O$ ‰ (Vs PDB)	$\delta^{18}O$ ‰ (Vs SMOW)
V1 (T2 veins)	D1	calcite	-6.9	-6.7	25.2
V2 (T2 veins)	D1	calcite	-6.7	-6.6	25.3
V3 (T2 veins)	D1	calcite	-5.8	-7.2	24.7
V4 (T2 veins)	D1	calcite	-5.1	-7.1	24.8
V5 (T2 veins)	D1	calcite	-8.2	-6.9	25.0
V6 (T2 veins)	D1	calcite	-7.2	-6.8	25.1
V7 (T2 veins)	D1	calcite	-7.3	-7.4	24.5
V8 (T2 veins)	D1	calcite	-4.4	-7.2	24.7
V9 (T2 veins)	D3	calcite	-4.2	-7.6	24.3
V10 (T2 veins)	D3	calcite	-5.8	-7.0	24.9
V11 (T2 veins)	D3	calcite	-6.7	-7.0	24.9
V12 (T2 veins)	D3	calcite	-5.3	-6.8	25.1
V13 (T2 veins)	D3	calcite	-7.0	-6.8	25.1
V14 (T2 veins)	D3	calcite	-5.6	-7.1	24.8
V15 (T2 veins)	D2	calcite	-3.5	-7.0	24.9
V15 (T2 veins)	D2	calcite	-5.8	-6.8	25.1
V16 (T2 veins)	D2	calcite	-5.0	-6.1	25.8
V17 (T3 veins)	D3	calcite	0.9	-9.5	22.4
V18 (T3 veins)	D3	calcite	1.1	-8.6	23.3
V19 (T3 veins)	D3	calcite	-0.2	-10.3	21.6
V20 (T3 veins)	D3	calcite	-0.1	-9.2	22.7
V21 (T3 veins)	D3	calcite	0.3	-8.8	23.1
V22 (T3 veins)	D2	calcite	1.3	-8.1	23.8
V23 (T3 veins)	D2	calcite	1.0	-7.2	24.7
V24 (T3 veins)	D2	calcite	1.1	-7.9	24.0
V25 (T3 veins)	D2	calcite	1.1	-8.4	23.5
Slickenfiber 1	D3	calcite	-5.1	-7.8	24.1
Slickenfiber 2	D3	calcite	-6.4	-7.8	24.1
Slickenfiber 3	D3	calcite	-6.2	-7.7	24.2
Slickenfiber 4	D3	calcite	-7.8	-7.5	24.4
Cataclastic rock 1	D1	calcite	0.6	-8.3	23.6
Cataclastic rock 2	D1	calcite	-0.2	-8.2	23.7
Cataclastic rock 3	D1	calcite	-0.1	-8.2	23.7
Cataclastic rock 4	D1	calcite	0.2	-7.7	24.2
Cataclastic rock 5	D1	calcite	0.3	-7.5	24.4
Cataclastic rock 6	D1	calcite	0.6	-8.1	23.8
Cataclastic rock 7	D1	calcite	0.7	-7.9	24.0
Cataclastic rock 8	D1	calcite	0.8	-8.1	23.8
Cataclastic rock 9	D1	calcite	0.8	-8.7	23.2
Breccia cement 1	D3	calcite	-10.4	-7.3	24.6
Breccia cement 2	D3	calcite	-10.3	-6.9	25.0
Breccia cement 3	D3	calcite	-10.8	-6.6	25.3
Breccia cement 4	D3	calcite	-10.9	-6.6	25.3
Breccia cement 5	D3	calcite	-10.7	-7.0	24.9
Breccia cement 6	D3	calcite	-10.6	-6.5	25.4
Breccia cement 7	D3	calcite	-11.1	-7.1	24.8
Breccia cement 8	D3	calcite	-10.5	-6.8	25.1
Breccia cement 9	D3	calcite	-10.7	-7.0	24.9
Breccia cement 10	D3	calcite	-11.0	-6.6	25.3
Breccia cement 11	D3	calcite	-10.5	-7.1	24.8
Breccia cement 12	D3	calcite	-10.3	-6.9	25.0
Breccia cement 13	D3	calcite	-10.6	-7.1	24.8
Breccia cement 14	D3	calcite	-10.6	-7.3	24.6
Breccia cement 15	D3	calcite	-10.4	-7.7	24.2
Breccia cement 16	D3	calcite	-10.2	-7.0	24.9
Breccia cement 17	D3	calcite	-11.0	-6.7	25.2
Breccia cement 18	D3	calcite	-11.0	-7.0	24.9

Breccia cement 19	D3	calcite	-10.8	-6.9	25.0
Breccia cement 20	D3	calcite	-10.3	-7.0	24.9
Breccia cement 21	D3	calcite	-10.7	-6.8	25.1
Breccia cement 22	D3	calcite	-10.8	-6.9	25.0
Breccia cement 23	D3	calcite	-8.9	-6.9	25.0
Breccia cement 24	D3	calcite	-10.3	-7.3	24.6
Breccia cement 25	D3	calcite	-10.2	-7.5	24.4
Plio-Quaternary cement 1	No domain	calcite	-9.3	-7.4	24.5
Plio-Quaternary cement 2	No domain	calcite	-8.7	-7.3	24.6
Plio-Quaternary cement 3	No domain	calcite	-9.3	-7.1	24.8
Plio-Quaternary cement 4	No domain	calcite	-8.9	-7.0	24.9
Plio-Quaternary cement 5	No domain	calcite	-7.9	-6.7	25.2
Plio-Quaternary cement 6	No domain	calcite	-7.9	-6.5	25.4
Plio-Quaternary cement 7	No domain	calcite	-7.9	-6.9	25.0
Plio-Quaternary cement 8	No domain	calcite	-8.0	-6.6	25.3
Plio-Quaternary cement 9	No domain	calcite	-7.9	6.7	25.2
Host rock 1	No domain	calcite	1.0	-4.7	27.2
Host rock 2	No domain	calcite	1.2	-3.6	28.3
Host rock 3	No domain	calcite	-0.8	-5.2	26.7
Host rock 4	No domain	calcite	0.9	-5.9	26.0
Host rock 5	No domain	calcite	1.4	-4.0	27.9
Host rock 6	No domain	calcite	0.3	-2.8	29.2
Host rock 7	No domain	calcite	0.3	-3.0	28.9
Host rock 8	No domain	calcite	1.9	-2.4	29.5
Host rock 9	No domain	calcite	2.4	-1.0	30.9

Table S3. Summary of $\delta^{13}C$ ‰ and $\delta^{18}O$ ‰ isotopes analyses.

Host rock 2	Host rock 1	Foliated cataclasite 4 (Domain 1)	Foliated cataclasite 3 (Domain 1)	Ultracataclasite 2 (Domain 1)	Ultracataclasite 1 (Domain 1)	Analysis Method	Detection Limit	Unit Symbol	Analyte Symbol
0.27	0.52	0.80	0.96	1.67	1.94	FUS-ICP	0.01	%	SiO2
0.09	0.17	0.23	0.33	0.68	0.95	FUS-ICP	0.01	%	Al2O3
0.04	0.06	0.08	0.10	0.31	0.34	FUS-ICP	0.01	%	Fe2O3
0.002	0.002	0.004	0.003	0.014	0.007	FUS-ICP	0.001	%	MnO
0.41	0.65	0.58	0.63	0.56	0.62	FUS-ICP	0.01	%	MgO
55.09	54.43	54.00	54.61	53.59	52.09	FUS-ICP	0.01	%	CaO
0.04	0.05	0.06	0.08	0.08	0.05	FUS-ICP	0.01	%	Na2O
0.02	0.03	0.05	0.07	0.08	0.06	FUS-ICP	0.01	%	K2O
0.001	0.002	0.004	0.007	0.025	0.041	FUS-ICP	0.001	%	TiO2
< 0.01	0.03	0.02	0.03	0.05	0.05	FUS-ICP	0.01	%	P2O5
43.69	43.12	43.37	43.23	42.70	42.31	FUS-ICP		%	LOI
125	169	183	191	238	256	FUS-ICP	2	ppm	Sr
0.1	0.4	0.5	0.8	3.4	2.1	FUS-MS	0.1	ppm	La
0.2	0.5	0.8	1.4	4.5	4.3	FUS-MS	0.1	ppm	Ce
< 0.05	0.07	0.11	0.16	0.69	0.47	FUS-MS	0.05	ppm	Pr
0.2	0.3	0.3	0.6	2.3	1.7	FUS-MS	0.1	ppm	Nd
< 0.1	< 0.1	< 0.1	0.2	0.5	0.4	FUS-MS	0.1	ppm	Sm
< 0.05	< 0.05	< 0.05	< 0.05	0.15	0.08	FUS-MS	0.05	ppm	Eu
< 0.1	< 0.1	< 0.1	0.2	0.6	0.4	FUS-MS	0.1	ppm	Gd
< 0.1	< 0.1	< 0.1	< 0.1	< 0.1	< 0.1	FUS-MS	0.1	ppm	Tb
< 0.1	< 0.1	< 0.1	< 0.1	0.5	0.3	FUS-MS	0.1	ppm	Dy
4	< 2	< 2	< 2	5	< 2	FUS-ICP	2	ppm	Y
< 0.1	< 0.1	< 0.1	< 0.1	< 0.1	< 0.1	FUS-MS	0.1	ppm	Ho
< 0.1	< 0.1	< 0.1	< 0.1	0.2	0.2	FUS-MS	0.1	ppm	Er
< 0.05	< 0.05	< 0.05	< 0.05	< 0.05	< 0.05	FUS-MS	0.05	ppm	Tm
< 0.1	< 0.1	< 0.1	< 0.1	0.2	0.2	FUS-MS	0.1	ppm	Yb
< 0.04	< 0.04	< 0.04	< 0.04	< 0.04	< 0.04	FUS-MS	0.04	ppm	Lu
99.65	99.07	99.19	100.00	99.74	98.47	FUS-ICP	0.01	%	Total

Table S4. Whole rock geochemistry data. Analyses performed at Actlabs according to procedures and standards available online at www.actlabs.com.

Chapter 3. Ultra-thin clay layers facilitate seismic slip in carbonate faults

Abstract

Many earthquakes propagate up to the Earth's surface producing surface ruptures. Seismic slip propagation is facilitated by along-fault low dynamic frictional resistance, which is controlled by a number of physico-chemical lubrication mechanisms. In particular, laboratory experiments show that the presence of phyllosilicates within fault gouge is critical for developing dynamic weakening at seismic slip rates. This evidence is crucial for hazard assessment along oceanic subduction zones, where pelagic clays participate to seismic slip propagation. Conversely, the reason why, in continental domains, earthquakes can propagate through high-friction rocks (e.g., limestones or dolostones) up to the Earth's surface is still poorly understood. We document the occurrence of micrometer-thick phyllosilicate-bearing layers along a carbonate-hosted seismogenic extensional fault in the central Apennines, Italy. Using friction experiments, we demonstrate that, at seismic slip rates (1 ms^{-1}), similar calcite gouges with pre-existing phyllosilicate-bearing (clay content ≤ 3 wt.%) micro-layers weaken faster than calcite gouges or mixed calcite-phyllosilicate gouges. We thus propose that, within calcite gouge, ultra-low clay content (≤ 3 wt.%) localized along micrometer-thick layers can facilitate seismic slip propagation during earthquakes in continental domains, possibly enhancing surface displacement.

This study was performed in collaboration with A. Billi, E. Carminati, A. Cavallo, G. Di Toro, E. Spagnuolo, and F. Zorzi. This chapter is currently under review on Scientific Reports as: Smeraglia, L., Billi, A., Carminati, E., Cavallo A., Di Toro G., Spagnuolo E., Zorzi F. Ultra-thin clay layers facilitate seismic slip in carbonate faults.

1. Introduction

Many earthquakes propagate up to the Earth's surface producing surface ruptures, possibly associated with tsunami generation, infrastructure damages, and fatalities (Wells and Coppersmith, 1994; Ambraseys and Jackson, 1994; Martino et al., 2014; Mildon et al., 2016). Seismic slip propagation is facilitated by low dynamic frictional resistance along faults (e.g., Di Toro et al., 2004; Kanamori and Brodsky, 2004; Rice, 2006). Therefore, understanding the mechanisms that lower rock resistance and facilitate seismic slip propagation along faults (e.g., Chang et al., 2012) is relevant for hazard assessment within seismically active regions. To understand such a mechanism, rotary shear experiments simulating natural seismic deformation conditions have been conducted on different natural fault rocks at seismic slip rates ($\geq$1 ms^{-1}) in the past 20 years (e.g., Di Toro et al., 2004; Di Toro et al., 2011). Results show that a number of processes triggered by high mechanical work rates can induce fault weakening (e.g., Di Toro et al., 2006; Han et al., 2007), especially within thermally-unstable rocks such as carbonates (i.e., thermal pressurization and nanopowder lubrication processes; e.g., De Paola et al., 2011; Siman-Tov et al., 2013; Smith et al., 2013). In particular, experiments have revealed the weakening behavior of phyllosilicates, especially in water-saturated conditions, due to their low steady-state dynamic friction and to the absence of peak friction (e.g., Brantut et al., 2008; Ujiie et al., 2011, 2013; Bullock et al., 2015; Oohashi et al., 2015). For this reason, previous studies (e.g., Faulkner et al., 2011; Ujiie et al., 2014; Kameda et al., 2015; Kirkpatrick et al., 2015) suggested that pelagic clay commonly smeared along offshore subduction zones participate to co-seismic fault lubrication, possibly facilitating and enhancing upward co-seismic slip propagation, sometimes associated with tsunamigenic seafloor displacement. Less understood is the origin of surface displacements associated with moderate (M_w $\leq$ 7.0) earthquakes in continental seismically-active regions (e.g., Gudmundsson, 2013; Balsamo et al., 2014; Mildon et al., 2016; see Supplementary Table S1). Here we propose that less than 3 wt.% of phyllosilicates localized within pre-existing ultra-thin layers along carbonate-hosted faults can facilitate co-seismic slip propagation, possibly enhancing surface displacement. In particular, we

first document the occurrence in nature of hitherto unknown phyllosilicate-bearing micrometer-thick layers along the carbonate-hosted seismically-active Tre Monti Fault (e.g., Smith et al., 2011; Benedetti et al., 2013; Smeraglia et al., 2016a) and then we use a rotary shear apparatus to simulate the behavior of this natural setting during co-seismic slip propagation.

The Tre Monti Fault is a shallow (exhumed from depths < 3 km; Smeraglia et al., 2016a) seismogenic extensional fault belonging to the carbonate domain of the central Apennines, Italy (e.g., Roberts et al., 2007; Fig. 1a). The central Apennines is a fold-thrust belt (Oligocene-Quaternary) characterized by imbricate thrust sheets consisting of ~4-5 km thick pre-orogenic massive platform carbonates overlain by ~2 km thick phyllosilicate-rich syn-orogenic deposits (i.e., hemipelagic marls and foredeep clayey-sandstones; e.g., Doglioni 1991; Cosentino et al., 2010; Carminati et al., 2012). Massive carbonate rocks are the main lithology of the central Apennines down to at least 7-8 km depth (e.g., Billi et al., 2006; Patacca et al., 2008). During post-orogenic extension (Pliocene to present time), the fold-thrust belt has been dissected by a system of extensional faults, which bound several intramountain basins filled by Plio-Quaternary continental deposits (e.g., Doglioni et al., 1998; Cavinato and De Celles, 1999). These faults have generated historical and instrumental seismicity up to M_w 7.0 (Fig. 1a; e.g., Avezzano, 1915, M_w 7.0 earthquake; L'Aquila, 2009, M_w 6.1 earthquake; Amatrice-Norcia, 2016, M_w 6.0 and 6.5 earthquakes; e.g., Galli et al., 2008). In this region, earthquakes mainly nucleate at depths ≤ 8 km and co-seismic slip propagates upward along carbonate-hosted faults, often generating surface displacement (e.g., Mildon et al., 2016; Benedetti et al., 2013; Galli et al., 2008; Valoroso et al., 2013; Demurtas et al., 2016; Fig. 1a), as also observed in other seismically-active areas worldwide (see Supplementary Table S1). Therefore, geological and mechanical studies of faults exhumed from shallow depths, such as the Tre Monti Fault, are significant as the small-scale compositional heterogeneity of shallow fault zones can promote or inhibit seismic slip propagation up to the Earth's surface.

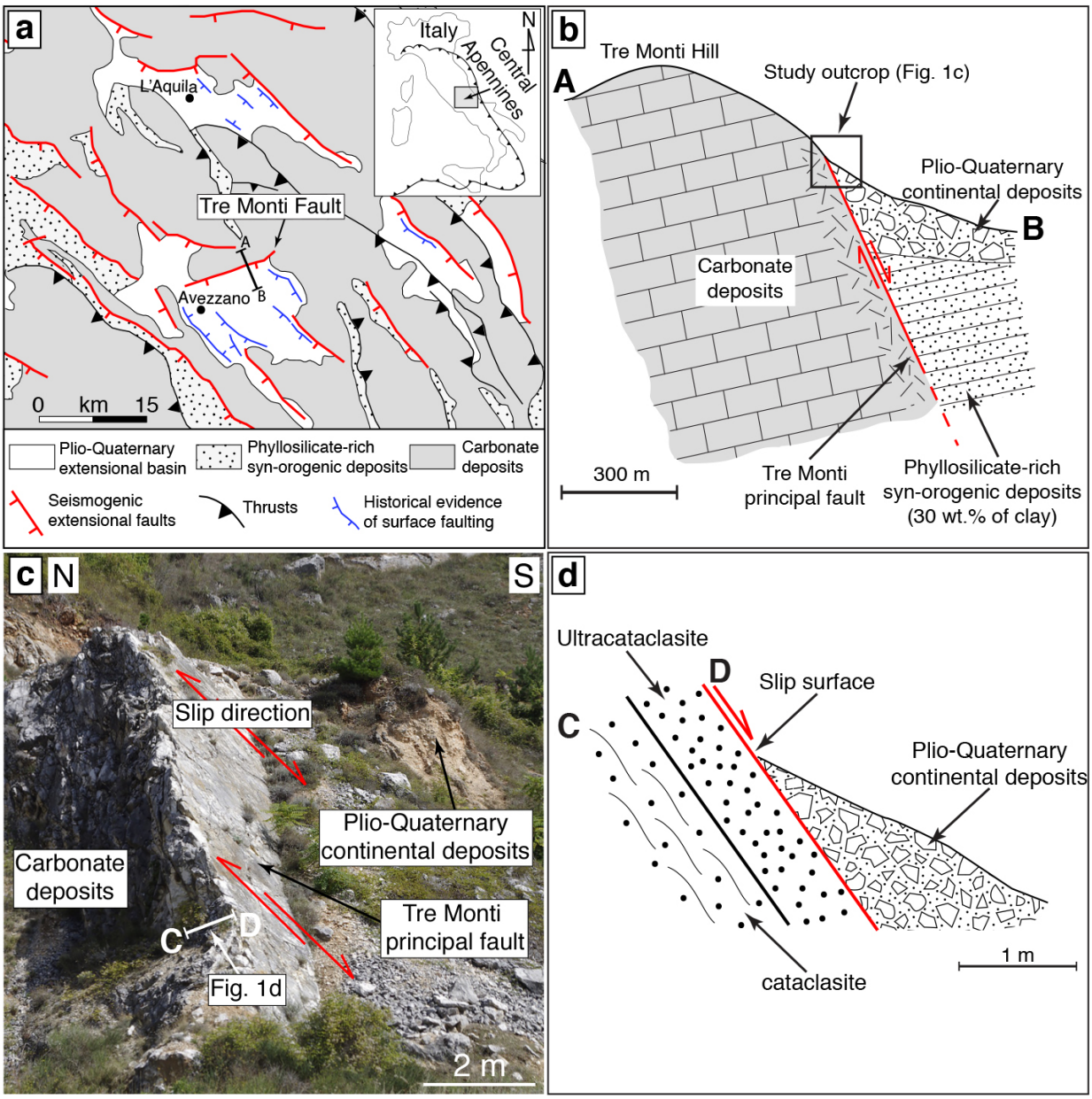


Figure 1. Geological setting. **(a)** Geological setting of the Tre Monti Fault and evidence of surface faulting from historical earthquakes in the central Apennines, Italy. Geological map and base map has been drawn using Adobe Illustrator CS5. **(b)** Simplified geological cross-section through the Tre Monti Fault. Cross-section trace in (a). **(c)** The study outcrop of the Tre Monti principal fault (Latitude 42°04'34" N, Longitude 13°29'58" E). **(d)** Simplified structural cross-section through the Tre Monti principal fault showing the ultracataclasite above the foliated cataclasite.

2. Methods

2.1. Description of starting materials

We used natural materials collected in the field from the foliated carbonate cataclasite and the phyllosilicate-rich deposits to perform high velocity friction experiments (Fig. 2a). The foliated

cataclasite consists of 100% calcite whereas the total phyllosilicate content of the phyllosilicate-rich deposits is ~30% (i.e., the phyllosilicate rich powder used for the experiments contain ~30% of phyllosilicates; Table S2). We used 4.5 g of gouge for each experiments resulting in ring-shaped gouge layers (35/55mm int./ext. diameters), with initial thicknesses of ~3mm (Fig. 3a).

2.2. Description of XRD analysis performed on natural rocks

We performed powder X-ray diffraction (XRPD) analyses and energy dispersive spectroscopy (EDS) to determine the mineralogy of natural fault rocks and experiment materials. In particular, we performed XRPD analyses on the insoluble residue from the ultracataclasite and from the natural phyllosilicate-bearing layers. We isolated the insoluble residues using HCl acid to dissolve calcite. XRPD data were obtained using a PANalytical θ-θ diffractometer equipped with a long fine-focus Cu X-ray tube (operating at 40 kV and 40 mA) and a real-time multiple strip (RTMS) detector (X'Celerator). The scan was performed over the 2θ range of 3–80°, with a virtual 2θ step size of 0.017°, and a counting time of 100 s/step. The program High Score Plus (PANalytical) was used for phase identification and quantitative phase analysis with Rietveld refinement (Rietveld, 1969).

2.3. Descriptions of experimental rotary shear apparatus and gouge holder

We performed friction experiments on the Slow to High Velocity rotary shear Apparatus (SHIVA, Di Toro et al., 2010) at INGV, Roma. The apparatus has a horizontal setup, with the rotary column on one end, the sample chamber in the middle, the axial column and loading system side at the other end. Rotary motion is supplied to the sample pair by two brushless engines of different size. The larger engine operates in a velocity range of 1–3,000 RPM, and owns a peak torque of 932 Nm and a nominal maximum power output of 280 kW. We performed experiments using a dedicated metal sample holder (Fig. 3a) appropriately designed for shearing gouges at high velocities (Smith et al., 2013). Ring-shaped layers of gouge (55mm external diameter, 35mm

internal diameter) are confined by outer and inner rings of tungsten carbide that rotate and slide over a base disc of the same material. The base disc and the rotary base plate are etched with a cross-hatch pattern to provide roughness at the boundaries of the gouge layer. The normal load, exerted by an air actuator, was applied on the gouge layer by the stationary column of SHIVA. Normal load applied to the outer and inner rings is independent of that applied to the gouge layer, and is modulated by five outer springs and one inner spring: normal load is proportional to the spring stiffness and to the amount of compression during each experiment. Given that we used the same layer thickness for each experiment, we consider the normal load on the outer and inner rings to be the same for each experiment. Calibration of the gouge holder is discussed in detail in Smith et al. (2013).

2.4. Description of experimental conditions

We conducted dry experiments at room humidity conditions, whereas, in water-saturated experiments, we water damped gouges with 0.5 ml of distilled water. Gouge materials for tests were hoven-dried at 40°C for days before the experiments. Experimental slip rates were set at 0.001 ms^{-1} and 1 ms^{-1}, for a total sliding displacement of 0.5 meter under water-saturated (wet) and dry conditions. We held normal stress constant at 8.5 MPa and 5 MPa for dry and wet experiments, respectively. The SHIVA apparatus does not allow the measurement/control of pore pressure during the wet experiments. Accordingly the measured friction should be considered as apparent (or effective), as suggested by Chen et al. (2017), for the unknown pore pressure within the gouge. The experimental sequence progressed as follows: gouges were initially pre-sheared at 1 cms^{-1} for 10 cm of total slip under 0.5 MPa of normal load, both in low velocity and in high velocity experiments and both in dry and in wet conditions. In all experiments, gouges were initially pre-sheared at 0.01 ms^{-1} for 10 cm of total slip under 0.5 MPa of normal load. This procedure was done to properly simulate the behaviour of our natural fault rocks (Fig. 2b), which were (pre-) sheared by multiple slip events and to limit the pressurization effects due to gouge compaction, as also done in

previous experiments in rotary shear apparatuses (e.g., Chen et al., 2017). After, gouges were loaded to the target normal stress and were sheared up to the target displacement. For high velocity experiments, acceleration and deceleration rates were of 24 ms^{-2}**.** After the experiments, gouges were cohesive and flinty. We impregnated gouge fragments under vacuum using a LR-white resin. We then prepared petrographic sections from the impregnated gouges cut perpendicular to the gouge layers and approximately parallel to the slip direction. We studied micro- and nano-structures (both natural and experimental) through scanning electron microscope on polished thin sections ~30 μm thick. All samples were uniformly coated with 1-2 nm thick chrome particles. We used three different facilities. (1) A thermal FE-SEM Zeiss Merlin Gemini 2 with 0.7 nm of resolution and four detectors (two in lens detector for high resolutions) at CERTEMA (Multidisciplinary technology laboratory, Grosseto, Italy). This device is equipped with a high sensitivity EDS detector (active area of 50 mmq) and with a 5 crystals WDS spectrometer. (2) A thermal FE-SEM JEOL (jsm6500f) at INGV (National Institute of Geophysics and Volcanology), Rome, with 2.5 nm of resolution and two detectors. EDS has an active area of 25 mmq. (3) A FE-SEM Zeiss Auriga at CNIS (Center for Nanotechnologies Applied to Engineering, Sapienza University of Rome, Italy) with 1 nm of resolution and three detectors (one in lens detector for high resolutions). All thin-sections were examined under optical microscope at various magnifications prior than SEM analyses.

3. Results

3.1. Natural fault zone structures

The Tre Monti Fault juxtaposes pre-orogenic carbonate deposits (footwall) with both syn-orogenic phyllosilicate-rich deposits (Fig. 1b; average phyllosilicate content ~30%, see Supplementary Table S2) and overlying continental (fluvial, lacustrine, and slope) deposits (hangingwall). The fault displays a dip of ~60° and a maximum displacement of ~1,500-2,000 m

(Cavinato et al., 2002; Smeraglia et al., 2016a). The principal fault surface is excellently exposed along a ~8 km long carbonate-hosted fault scarp (Cavinato et al., 2002; Smith et al., 2011; Benedetti et al., 2013; Smeraglia et al., 2016a; Fig. 1c) exhumed by multiple surface faulting events (Benedetti et al., 2013). The principal fault is associated with a ~1 m-thick cataclastic fault core, which consists of an ultracataclasite lying above a cataclasite (Smeraglia et al., 2016a; Figs. 1d, 2a-c). The ultracataclasite shows more intense grain comminution than the cataclasite (Fig. 2c) and forms discontinuous patches and plagues above the cataclasite owing to fault scarp erosion. X-ray Powder diffraction (XRPD) and energy dispersive spectroscopy (EDS) analyses revealed that the cataclasite consists solely of calcite, whereas the ultracataclasite consists of calcite, phyllosilicates (~1.5 wt.%; mainly smectite, illite, and kaolinite; see Supplementary Fig. S1 and Supplementary Table S2), detrital micas, quartz, K-feldspar, and plagioclase (< 1%; see Supplementary Fig. S2 and Supplementary Table S3), which are also present within the syn-orogenic deposits (Critelli et al., 2007; Smeraglia et al., 2014).

Phyllosilicates are concentrated within slip-parallel micrometer-thick (from ~30 μm up to ~1 mm in thickness) layers at the boundary between the ultracataclasite and the cataclasite (Figs. 2b and 2c). The average phyllosilicate content within these layers is ~5 wt.% (see Supplementary Fig. S2 and Table S2). Phyllosilicate-bearing layers have sharp boundaries, which truncate calcite clasts (Figs. 2b and 2c). Within these layers, calcite clasts are scattered within a phyllosilicate matrix and are usually wrapped by phyllosilicates creating a continuous film (Fig. 2d). At the nanoscale, phyllosilicates consist of granular zones and elongated fibers comprising clumped and chained ~50-nm-thick nanospherules and nanotubes (Figs. 2e and 2f).

Due to lack of dissolution seams and teeth-shaped margins (i.e., typical of stylolites; e.g., Tesei et al., 2013; Viti et al., 2014) close to the phyllosilicate-bearing layers, we exclude that these layers formed by residual processes connected with pressure solution of carbonates. Hence, we infer that the phyllosilicates derived from the phyllosilicate-rich syn-orogenic deposits at the fault

hangingwall, and that they were smeared and mixed into the ultracataclasite during fault activity (Smeraglia et al., 2016b).

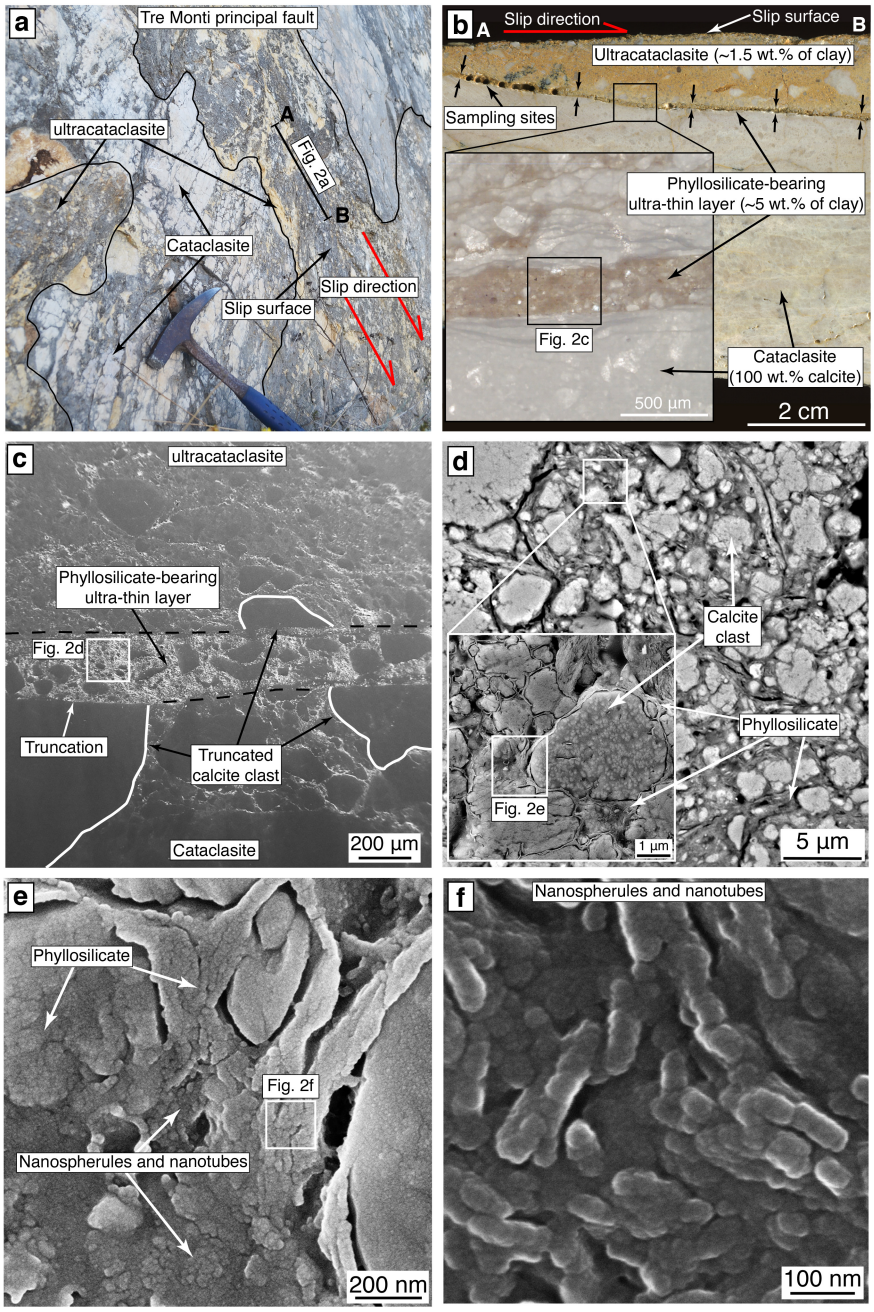


Figure 2. Phyllosilicate occurrence within the carbonate-hosted Tre Monti Fault. **(a)** Detail of the Tre Monti principal fault showing patches of ultracataclasite above the foliated cataclasite. **(b)** Phyllosilicate-bearing layer at the boundary between the ultracataclasite and the foliated cataclasite. Inset shows a microphotograph under optical microscope showing a detail of the phyllosilicate-bearing layer. **(c)** FE-SEM image of micrometer-thick phyllosilicate-bearing layer, which truncates calcite clasts. **(d)** FE-SEM image of carbonate clasts within a phyllosilicate matrix. Inset shows calcite clasts wrapped by a continuous phyllosilicates film. **(e-f)** FE-SEM images of nanostructures of natural phyllosilicates from the phyllosilicate-bearing layers characterized by clumped and chained nanospherules and nanotubes.

3.2. Laboratory experiments and comparison with natural fault products

Based on the previously-reported field, mineralogical, and microscopic observations, we conducted low to high velocity rotary shear friction experiments (see Methods) to investigate the frictional behavior of micrometer-thick phyllosilicate-bearing layers within synthetic calcite gouges reproducing those observed along the Tre Monti Fault (Figs. 2b and 2c). We performed experiments on 3 mm-thick gouge layers obtained by crushing and sieving (<125 μm) the natural foliated cataclasite (100% calcite) and the phyllosilicate-rich syn-orogenic deposits (~30% of phyllosilicates), both under dry and under water-saturated (wet) conditions.

Experimental slip rates were set at 0.001 ms^{-1} and 1 ms^{-1} to simulate subseismic and co-seismic slip rates, respectively. We held the normal stress constant at 8.5 MPa and 5 MPa in dry and wet experiments, respectively, consistently with lithostatic load at shallow depth (< 0.5 km). We set normal stress to 5 MPa under wet conditions to avoid gouge extrusion from the gouge holder. We sheared the gouges imposing a total slip of 0.5 meter, both during low- (0.001 ms^{-1}) and high-velocity (1 ms^{-1}) experiments, to simulate, in the latter case, the amount of co-seismic slip occurring at depth < 0.5 km during a M_w 6.0-6.5 earthquake (e.g., Anzidei and Pondrelli, 2016). We carried out experiments using three different gouge configurations (Fig. 3a) aimed at understanding the mechanical effect of a small percentage of clay concentrated along ultra-thin layers within the calcite gouge. The configurations are: (1) 10% of phyllosilicate-rich deposits randomly mixed with 90% of calcite ("mixed gouge experiments"; total phyllosilicate content of ~3 wt.%); (2) 2 mm-thick layer of 100% calcite overlain by a 1 mm-thick layer consisting of a random mixture of 10% of phyllosilicate-rich deposits and 90% of calcite ("layered gouge experiments"; total phyllosilicate content in the 1-mm thick layer of ~3 wt.%); this configuration, in particular, simulates the phyllosilicate-bearing layers observed within natural samples from the Tre Monti Fault (Figs. 2b and 2c). For this configuration, we also performed a non-shear compression experiment to study the pre-shear microstructures (compare Supplementary Fig. S3 with Fig. 3a "layered gouge"

configuration); (3) 100% calcite gouge ("calcite gouge experiments"). Complete experimental procedures and results are listed in the method section and Supplementary Table S4.

At subseismic slip rates (0.001 ms^{-1}), all gouges have a similar friction coefficient evolution from the first peak value to a steady-state value (0.7-0.8; Fig. 3b). At seismic slip rates (1 ms^{-1}), all experiments are characterized by a dynamic weakening behavior. In particular, the decay of friction (i.e., weakening phase) towards a steady-state value (~0.4) occurs after a strengthening phase defined as the distance (i.e., slip) to the onset of dynamic weakening (D_{ow}, Smith et al., 2013; Fig. 3c). We calculated the D_{ow} values considering the maximum distance reached by the strengthening phase until the start of the weakening phase (Fig. 3c). Remarkably, we recognize a general trend showing that layered gouges weaken faster than mixed gouges, which, in turn, weaken faster than carbonate gouges both in dry and in wet conditions (Fig. 3c). In particular, layered gouges have a D_{ow} shorter than those measured for mixed and calcite gouges, both in dry and in wet conditions (Figs. 3c and 3d). Overall, wet gouges show a lower steady-state dynamic friction values than dry gouges, as previously observed within water-saturated gouges (e.g., Ujiie et al., 2011, 2013; Bullock et al., 2015; Fig. 3c).

To verify the reproducibility of the mechanical data, we replicated a set of six additional experiments both in wet (three experiments: mixed, layered, and calcite gouge experiments) and in dry conditions (three experiments: mixed, layered, and calcite gouge experiments; see Supplementary Fig. S4 and Fig. S5). Despite the high heterogeneity of the tested materials (i.e., natural rocks such as syn-orogenic deposits), these experiments reproduce well the previously observed mechanical trend: layered gouges weaken faster than mixed gouges, which, in turn, weaken faster than calcite gouges both in wet and dry conditions (see Supplementary Figs. S4 and S5).

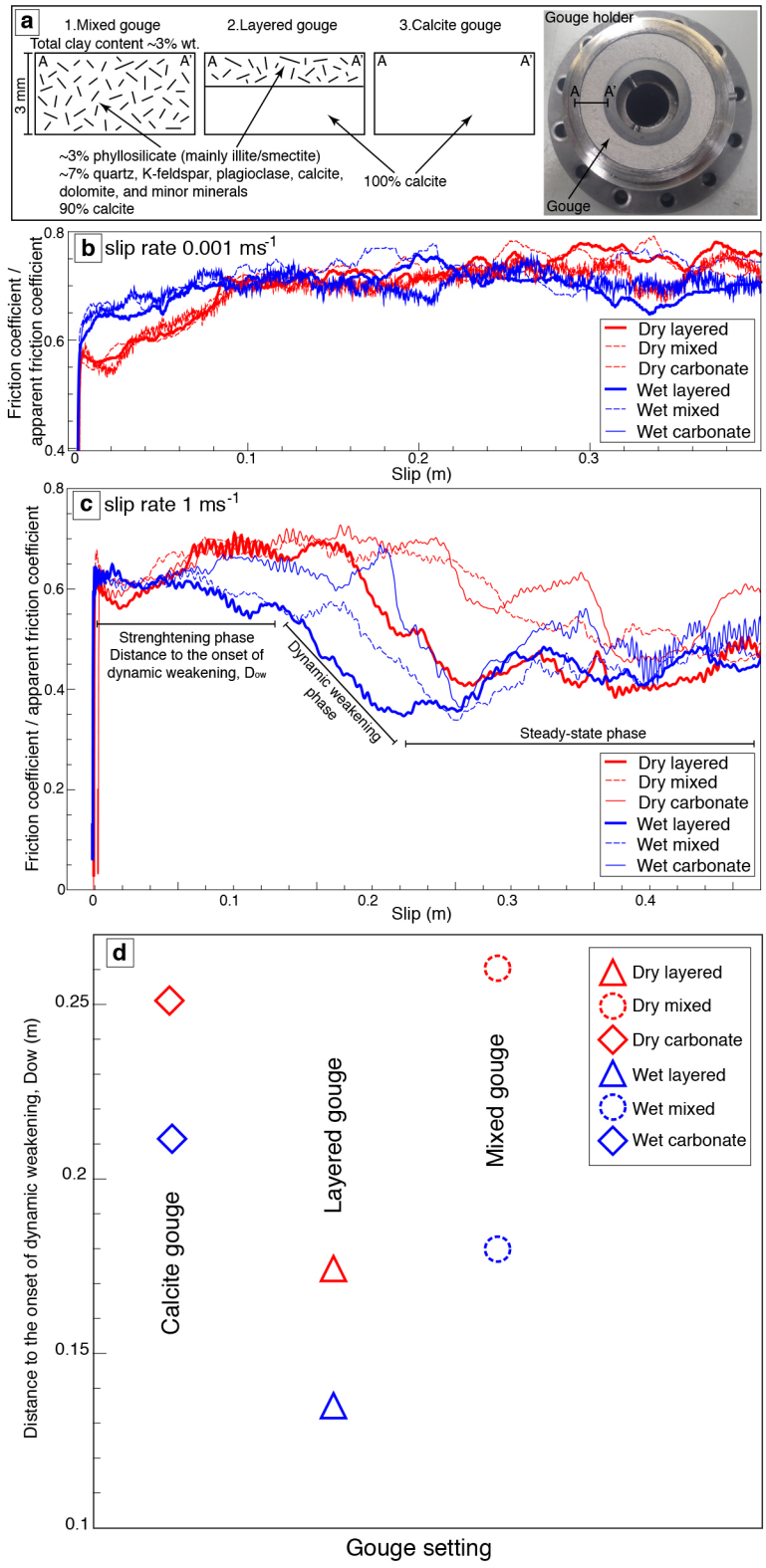


Figure 3. Results from friction experiments. **(a)** experimental setup: (left) the three different configurations of tested gouges and (right) the gouge holder. **(b)** Friction coefficient versus slip during experiments at subseismic (0.001 ms^{-1}) slip rate. **(c)** Friction coefficient versus slip during experiments at seismic (1 ms^{-1}) slip rate. **(d)** Distance to the onset of dynamic weakening, D_{ow}, versus clay content. Layered gouges are characterized by a D_{ow} lower than those of mixed and calcite gouges, both in dry and in wet conditions.

Using FE-SEM, we investigated the micro- and nano-structures obtained from the experimental gouges. Layered and mixed gouges sheared at subseismic velocity have a fabric consisting of randomly distributed particles of phyllosilicates and calcite (Fig. 4a). On the contrary, both in layered and in mixed configurations and both in wet and in dry conditions, gouges sheared at high velocity (i.e., seismic slip rate) are characterized by phyllosilicate segregation and concentration along micrometer-thick layers (Figs. 4b, 4c, and 4d). These layers were absent within the pre-sheared gouges (see Supplementary Fig. S3). Phyllosilicate-bearing layers form discontinuous patches rather than continuous layers and include carbonate clasts floating within a fine-grained matrix consisting of phyllosilicate lamellae wrapping around clasts (Figs. 4b and 4c). These microstructures are identical to those of natural micrometer-thick phyllosilicate-bearing layers observed within the Tre Monti Fault ultracataclasite (Fig. 2d).

Mixed and layered gouges sheared at seismic slip rates, both in wet and dry conditions, have similar microstructures characterized by reduced grain size within a ~500 μm-thick deformation zone along the slip surface (Figs. 4b-d). This evidence suggests that the layered vs. mixed configurations have no influence on the final gouge microstructure. On the contrary, mechanical data show that layered gouges weaken faster than mixed gouges (Fig. 3c). This evidence suggests that the initial gouge setting (layered vs. mixed) exerts a strong mechanical control on the weakening behaviour of the gouges regardless of the final microstructures.

Mixed and layered gouges in dry conditions show extreme grain size reduction and shear localization along a ~50 μm-thick principal slip zone (Fig. 4d). This principal slip zone is a mixture of phyllosilicates and calcite consisting of slip-parallel ~50 nm thick fibers composed by an array of nanospherules and nanotubes (Fig. 4d). In places, individual nanospherules clump together to form granular bulbous zones. These structures are very similar to phyllosilicate nanostructures observed within the Tre Monti Fault phyllosilicate-bearing layers (Figs. 2e and 2f). On the contrary, the principal slip zones of experiments conducted at subseismic slip rates are not characterized by nanospherules or nanotubes (Fig. 4a). Given the very slow creep rates and large cumulative slips

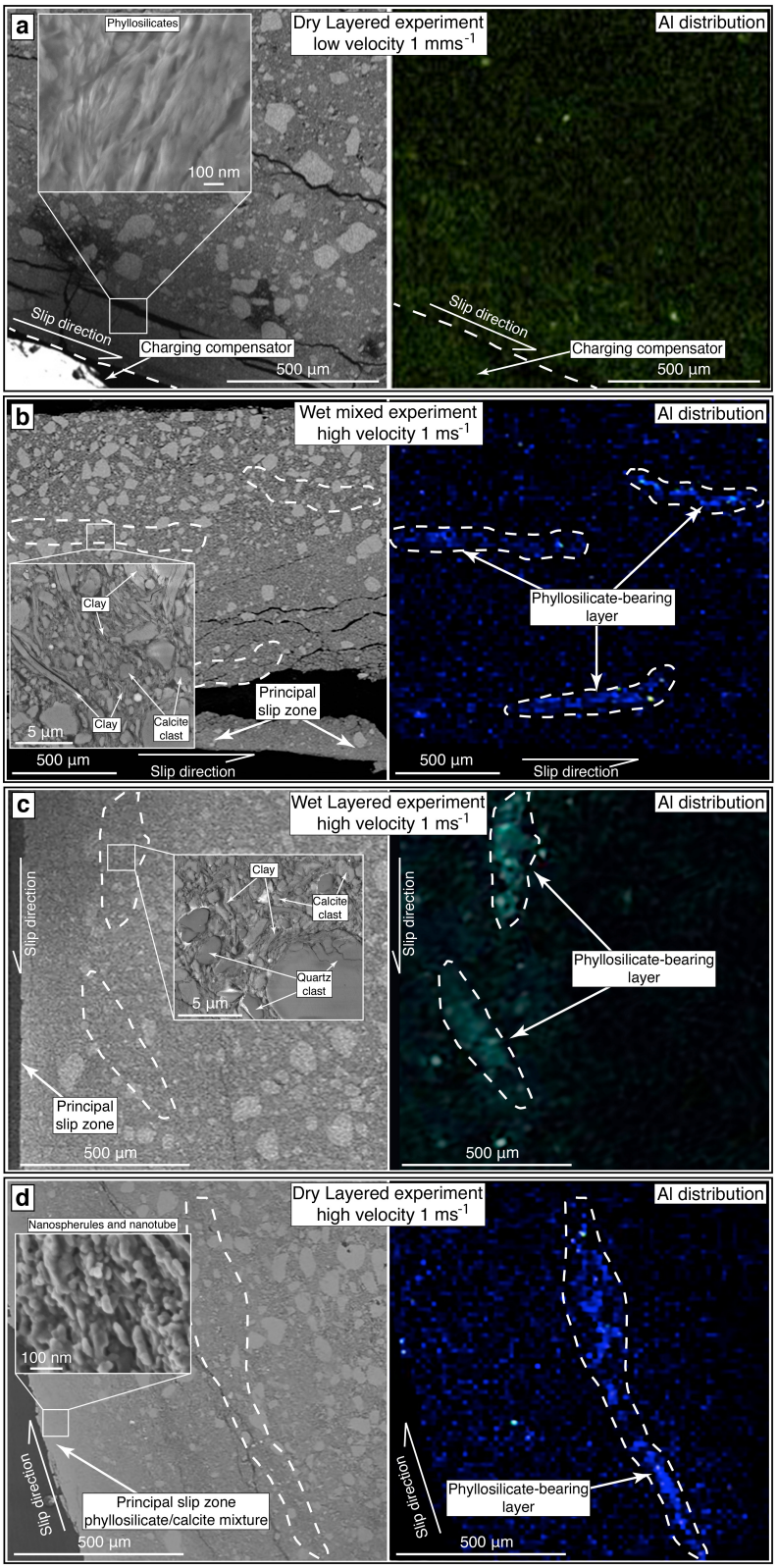


Figure 4. Experimental microstructures. **(a)** Left: FE-SEM image of dry layered gouge experimentally-sheared at subseismic velocity (0.001 ms^{-1}). Grain size reduction occurs toward the principal slip zone. Inset shows a detail of phyllosilicate lamellae showing no nanospherules or nanotubes that occur, in contrast, in samples from experiments at seismic velocity (see d). Right: EDS map showing no concentration and segregation of phyllosilicates along distinct layers that occur, in contrast, in samples from experiments at seismic velocity (see b-d). FE-SEM image of **(b**, left**)** wet

mixed gouge experiment and **(c**, left**)** wet layered gouge experiment sheared at seismic-slip velocity (1 ms^{-1}) showing grain size reduction toward the principal slip zone. EDS map shows segregation and concentration of phyllosilicates along micrometer-thick layers both for mixed (**b**, right) and for layered (**c**, right) gouges under wet conditions. Insets show carbonate clasts within phyllosilicate-bearing layer wrapped by phyllosilicates. **(d)** Left: FE-SEM image of dry layered gouge experiment sheared at seismic-slip velocity (1 ms^{-1}) showing, toward the principal slip surface, grain size reduction and compaction stronger than wet gouges. Inset shows the nanostructures from the principal slip zone. These structures consist of clumped and chained nanospherules and nanotubes identical to those observed within phyllosilicates along the Tre Monti principal fault (see Figs. 2e and 2f). Right: EDS map showing concentration and segregation of phyllosilicates along a micrometer-thick layer.

possibly accommodated by natural slipping zones, we cannot rule out that clay nanospherules and nanotubes within the Tre Monti Fault (Figs. 2e and 2f) may have formed aseismically, as suggested for nanospherules within calcite gouges sheared at subseismic velocity (e.g., slip velocity 1 μm/s; Verberne et al., 2014). However, in the case of the Tre Monti Fault, the coexistence of (1) clay nanospherules and nanotubes within phyllosilicate-bearing layers (Figs. 2e and 2f) similar to those observed within other phyllosilicates sheared at co-seismic slip-rates (compare with Fig. 9c in Ujiie et al., 2011), (2) truncated carbonate clasts (observed only within calcite gouges sheared at co-seismic slip rates; Fondriest et al., 2013) along phyllosilicate-bearing layers (Fig. 2c), and (3) co-seismic displacements documented by *in-situ* ^{36}Cl fault scarp exposure dating (Benedetti et al., 2013), possibly suggests that phyllosilicate-bearing layers formed during fault slip at co-seismic slip rates. Moreover, we emphasize that no nanospherules and nanotubes were generated during low-velocity experiments both in dry and in wet conditions (Fig. 4a). Accordingly, we hypothesize that the Tre Monti Fault hosted co-seismic slip propagation along phyllosilicate-bearing layers up to shallow levels.

4. Discussion and conclusions

We conclude that calcite gouges with an illite/smectite content as low as 3% localized along slip-parallel micrometer layers (Fig. 3a) weaken faster than calcite and mixed calcite-phyllosilicate gouges (Figs. 3c and 3d) at seismic slip rates (1 ms^{-1}). Therefore, this type of gouge can be

responsible for fault weakening within carbonate-hosted faults, facilitating co-seismic slip propagation up to the Earth's surface in continental domains characterized by high friction rocks (e.g., carbonates). The steady-state friction coefficient measured in our experiments (~0.4) is somewhat higher than that (~0.2) resulting from previous experiments in carbonate rocks at co-seismic slip rates[5]. This slight difference is likely due to the shorter slip distance (50 cm) set in our experiments to simulate co-seismic slip at depth < 500 m (e.g., Anzidei and Pondrelli, 2016). For larger slips, we would indeed expect a further reduction (i.e., below 0.4) of the friction coefficient also in our experimental setting. Nonetheless**,** our experiments certainly point out that the occurrence of thin layers with ultra-low clay content (3 wt.%) promote a faster weakening of layered gouges with respect to mixed and calcite gouges (Fig. 3c). Clay-bearing layers can also be produced during co-seismic slip by clay segregation and localization from an initial mixture of clay and calcite (Figs. 4b-d). The segregation of clay into numerous phyllosilicate-bearing layers can act as a self-enhancing process, promoting further fault weakening during earthquakes along newly formed phyllosilicate-bearing layers.

In summary, we propose that the 3 wt.% of clay concentrated within pre-existing ultra-thin layers could be the lower boundary for facilitating dynamic weakening during earthquake slip at shallow crustal levels in continental domains. The dynamic weakening effect can be even stronger if the phyllosilicate content exceeds 3 wt.% (e.g., Bullock et al., 2015).

5. References

Ambraseys, N.N., & Jackson, J.A. Faulting associated with historical and recent earthquakes in the Eastern Mediterranean region. *Geophys. J. Int.* 133, 390-406 (1998).

Anzidei, M. & Pondrelli, S. (Eds.). The Amatrice seismic sequence: preliminary data and results. *Annals of Geophysics* 59, (2016).

Balsamo, F., Aldega, L., De Paola, N., Faoro, I., & Storti, F. The signature and mechanics of earthquake ruptures along shallow creeping faults in poorly lithified sediments. *Geology* 42, 435-438 (2014).

Benedetti, L. *et al.* Earthquake synchrony and clustering on Fucino faults (central Italy) as revealed from in situ ^{36}Cl exposure dating. *J. Geophys. Res.* 118, 4948–4974 (2013).

Billi, A., *et al.* First results from the CROP-11 deep seismic profile, central Apennines, Italy: evidence of mid-crustal folding. *J. Geol. Soc. London.* 163, 583–586 (2006).

Brantut, N., Schubnel, A., Rouzaud, J. N., Brunet, F., & Shimamoto, T. High-velocity frictional properties of a clay-bearing fault gouge and implications for earthquake mechanics. *J. Geophys. Res.* 113, B10401 (2008).

Bullock, R.J., De Paola, N., & Holdsworth, R.E. An experimental investigation into the role of phyllosilicate content on earthquake propagation during seismic slip in carbonate faults. *J. Geophys. Res.* 120, 3187-3207 (2015).

Carminati, E., Lustrino, M., & Doglioni, C. Geodynamic evolution of the central and western Mediterranean: tectonics vs. igneous petrology constraints. *Tectonophysics* 579, 173-192 (2012).

Cavinato, G.P., & De Celles, P.G. Extensional basins in tectonically bimodal central Apennines fold-thrust belt, Italy: Response to corner flow above a subducting slab in retrograde motion. *Geology* 27, 955–958 (1999).

Cavinato, G.P., Carusi, C., Dall'asta, M., Miccadei, E., & Piacentini, T. Sedimentary and tectonic evolution of Plio-Pleistocene alluvial and lacustrine deposits of Fucino Basin (central Italy). *Sediment. Geol.* 148, 29–59 (2002).

Chang, J.C., Lockner, D.A., & Reches, Z. Rapid acceleration leads to rapid weakening in earthquake-like laboratory experiments. *Science* 338, 101-105 (2012).

Chen, J., Niemeijer, A., Yao, L., & Ma, S. Water vaporization promotes coseismic fluid pressurization and buffers temperature rise. *Geophysical Research Letters*, doi: 10.1002/2016GL071932, (2017).

Cosentino, D., Cipollari, P., Marsili, P., & Scrocca, D. Geology of the central Apennines; a regional review. *J. Virtual Explor.* 36, 12 (2010).

Critelli, S., *et al*. Interpreting siliciclastic-carbonate detrital modes in foreland basin system: an example from Upper Miocene arenites of the central Apennines, Italy. *Geol. Soc. Am. Special Paper* 420, 107-133 (2007).

De Paola, N., *et al*. Fault lubrication and earthquake propagation in thermally unstable rocks. *Geology* 39, 35-38 (2011).

Demurtas, M., *et al.* Structure of a normal seismogenic fault zone in carbonates: The Vado di Corno Fault, Campo Imperatore, Central Apennines (Italy). *J. Struct. Geol. 90*, 185-206 (2016).

Di Toro, G., *et al*. Fault lubrication during earthquakes. *Nature* 471, 494-498 (2011).

Di Toro, G., *et al.* From field geology to earthquake simulation: a new state-of-the-art tool to investigate rock friction during the seismic cycle (SHIVA). *Rendiconti dei Lincei* 21, 95-114 (2010).

Di Toro, G., Goldsby, D. L., & Tullis, T. E. Friction falls towards zero in quartz rock as slip velocity approaches seismic rates. *Nature* 427, 436-439 (2004).

Di Toro, G., Hirose, T., Nielsen, S., Pennacchioni, G., & Shimamoto, T. Natural and experimental evidence of melt lubrication of faults during earthquakes. *Science* 311, 647-649 (2006).

Doglioni, C. A proposal of kinematic modelling for W-dipping subductions - Possible applications to the Tyrrhenian - Apennines system. *Terra Nova* 3/4, 423–434 (1991).

Doglioni, C., D'Agostino, N., & Mariotti, G. Normal faulting vs regional subsidence and sedimentation rate. *Mar. Pet. Geol.* 15, 737-750 (1998).

Faulkner, D.R., Mitchell, T.M., Behnsen, J., Hirose, T., & Shimamoto, T. Stuck in the mud? Earthquake nucleation and propagation through accretionary forearcs. *Geophys. Res. Lett.* 38, L18303 (2011).

Fondriest, *et al*. Mirror-like faults and power dissipation during earthquakes. *Geology* 41, 1175-1178 (2013).

Galli, P., Galadini, F., & Pantosti, D. Twenty years of paleoseismology in Italy. *Earth-Science Rev.* 88, 89–117 (2008).

Gudmundsson, A. Great challenges in structural geology and tectonics. *Frontiers in Earth Science* 1, 1-10 (2013).

Han, R., Shimamoto, T., Hirose, T., Ree, J.-H. & Ando, J. Ultralowfriction of carbonate faults caused by thermal decomposition. *Science* 316, 878–881 (2007).

Kameda, J. *et al*. Pelagic smectite as an important factor in tsunamigenic slip along the Japan Trench. *Geology* 43, 155-158 (2015).

Kanamori, H., & Brodsky, E.E. The physics of earthquakes. *Reports on Progress in Physics*, 67, 1429 (2004).

Kirkpatrick, J.D., *et al.* Structure and lithology of the Japan Trench subduction plate boundary fault. *Tectonics* 34, 53-69 (2015).

Martino, S., Prestininzi, A., & Romeo, R.W. Earthquake-induced ground failures in Italy from a reviewed database. *Nat. Hazards Earth Syst. Sci*. 14, 799-814 (2014).

Mildon, Z.K., *et al.* Active normal faulting during the 1997 seismic sequence in Colfiorito, Umbria: did slip propagate to the surface? *J. Struct. Geol.* (2016).

Oohashi, K., Hirose, T., Takahashi, M., & Tanikawa, W. Dynamic weakening of smectite-bearing faults at intermediate velocities: implications for subduction zone earthquakes. *J. Geophys. Res.* 120, 1572-1586 (2015).

Patacca, E., Scandone, P., Di Luzio, E., Cavinato, G.P., & Parotto, M. Structural architecture of the central Apennines: Interpretation of the CROP 11 seismic profile from the Adriatic coast to the orographic divide. *Tectonics* 27, 1-36 (2008).

Rice, J.R. Heating and weakening of faults during earthquake slip. *J. Geophys. Res.* 111, B05311 (2006).

Rietveld, H.M. A profile refinement method for nuclear and magnetic structures. *Journal of applied crystallography* 2, 65-71 (1969).

Roberts, G.P. Multi-seismic cycle velocity and strain fields for an active normal fault system, central Italy. *Earth and Plan. Sci. Lett.* 251, 44-51 (2007).

Siman-Tov, S., Aharonov, E., Sagy, A., & Emmanuel, S. Nanograins form carbonate fault mirrors. *Geology* 41, 703-706 (2013).

Smeraglia, L., Trippetta, F., Carminati, E., & Mollo, S. Tectonic control on the petrophysical properties of foredeep sandstones in the central Apennines, Italy. *J. Geophys. Res.* 119, 9077-9094 (2014).

Smeraglia, L., *et al*. Origin and role of fluids involved in the seismic cycle of extensional faults in carbonate rocks. *Earth and Plan. Sci. Lett.* 450, 292-305 (2016a).

Smeraglia, L., Aldega, L., Billi, A., Carminati, E., & Doglioni, C., Phyllosilicate injection along carbonate-hosted faults and implications for co-seismic slip propagation: Case studies from the central Apennines. *Journal of Structural Geology* 93, 29-50 (2016b).

Smith, S.A.F., Billi, A., Di Toro, G., & Spiess, R. Principal Slip Zones in Limestone: Microstructural Characterization and Implications for the Seismic Cycle (Tre Monti Fault, Central Apennines, Italy). *Pure Appl. Geophys.* 168, 2365–2393 (2011).

Smith, S.A.F., *et al*. Co-seismic recrystallization during shallow earthquake slip. *Geology* 41, 63-66 (2013).

Smith, S.A.F., Nielsen, S., & Di Toro, G. Strain localization and the onset of dynamic weakening in calcite fault gouge. *Earth and Plan. Sci. Lett.* 413, 25-36 (2015).

Tesei, T., Collettini, C., Viti, C., & Barchi, M.R., 2013. Fault architecture and deformation mechanisms in exhumed analogues of seismogenic carbonate-bearing thrusts. *Journal of Structural Geology* 55, 167–181, (2013).

Ujiie, K. *et al*. Low coseismic shear stress on the Tohoku-Oki megathrust determined from laboratory experiments. *Science* 342, 1211-1214 (2013).

Ujiie, K., & Kimura, G. Earthquake faulting in subduction zones: Insights from fault rocks in accretionary prisms. *Progress in Earth and Planetary Science* 1, (2014).

Ujiie, K., Tsutsumi, A., & Kameda, J. Reproduction of thermal pressurization and fluidization of clay-rich fault gouges by high-velocity friction experiments and implications for seismic slip in natural faults. *Geol. Soc. London, Spec. Publ.* 359, 267–285 (2011).

Valoroso, L., *et al*. Radiography of a normal fault system by 64,000 high-precision earthquake locations: The 2009 L'Aquila (central Italy) case study. *J. Geophys. Res.* 118, 1156-1176 (2013).

Verberne, B.A., Pluümper, O., De Vinter, M.D.A., & Spiers, C.J. Superplastic nanofibrous slip zones control seismogenic fault friction. *Science* 346, 1342-1344 (2014).

Viti, C., Collettini, C., & Tesei, T. Pressure solution seams in carbonatic fault rocks: mineralogy, micro/nanostructures and deformation mechanism. *Contribution to Mineral. Petrol.* 167, 970, (2014).

Wells, D.L., & Coppersmith, K.J. New empirical relationships among magnitude, rupture length, rupture width, rupture area, and surface displacement. *Bull. Seismol. Soc. Am.* 84, 974-1002 (1994).

6. Supplementary material

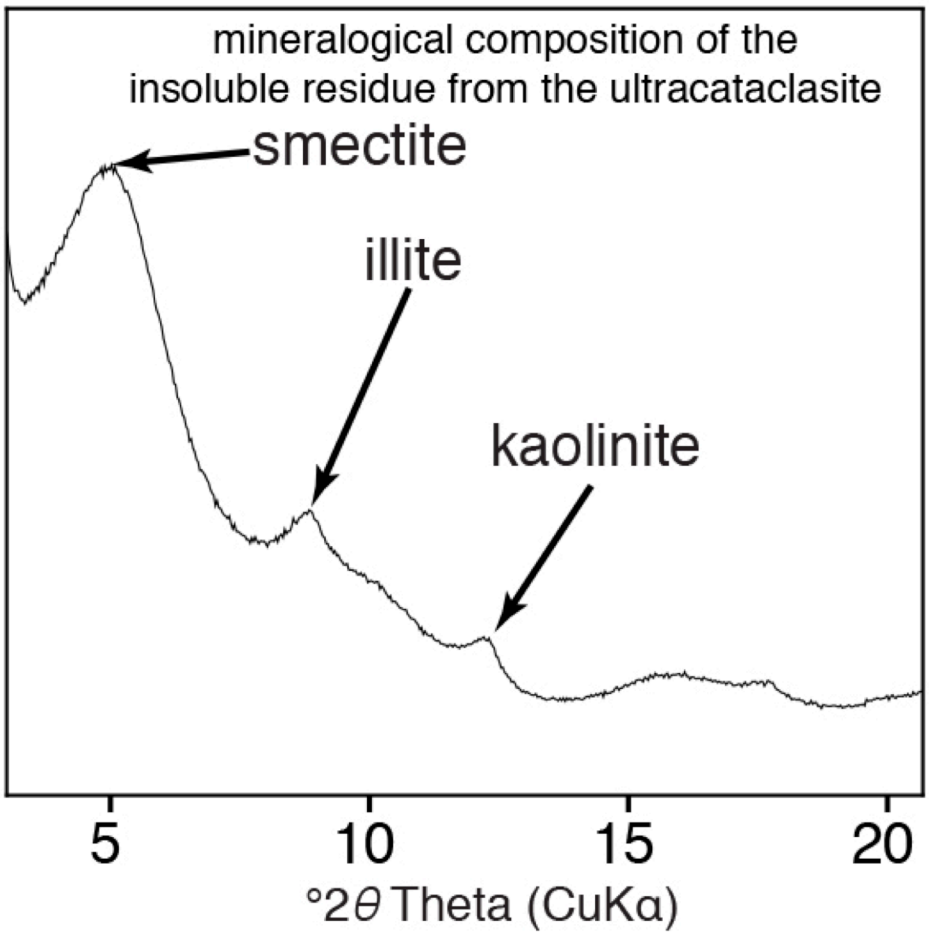


Figure S1. Powder X-ray diffraction (XRPD) traces of the insoluble residue from the ultracataclasite. Diffraction peaks showing the occurrence illite, smectite and kaolinite within the insoluble residue (~1.5% wt.) from the ultracataclasite.

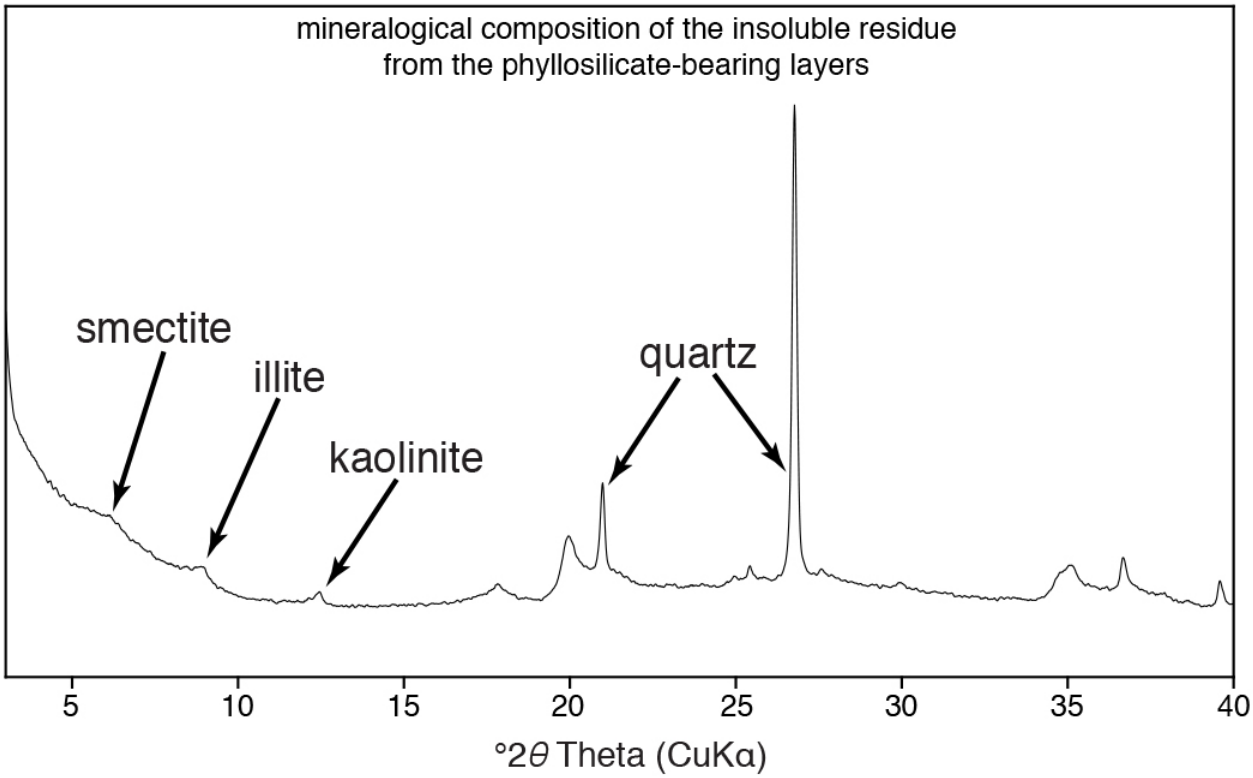


Figure S2. Powder X-ray diffraction (XRPD) traces of the insoluble residue from the phyllosilicate-bearing layer within the ultracataclasite**.** Diffraction peaks showing the occurrence illite, smectite, kaolinite, and quartz within the insoluble residue (~8.6% wt.) from the phyllosilicate-bearing layer within the ultracataclasite.

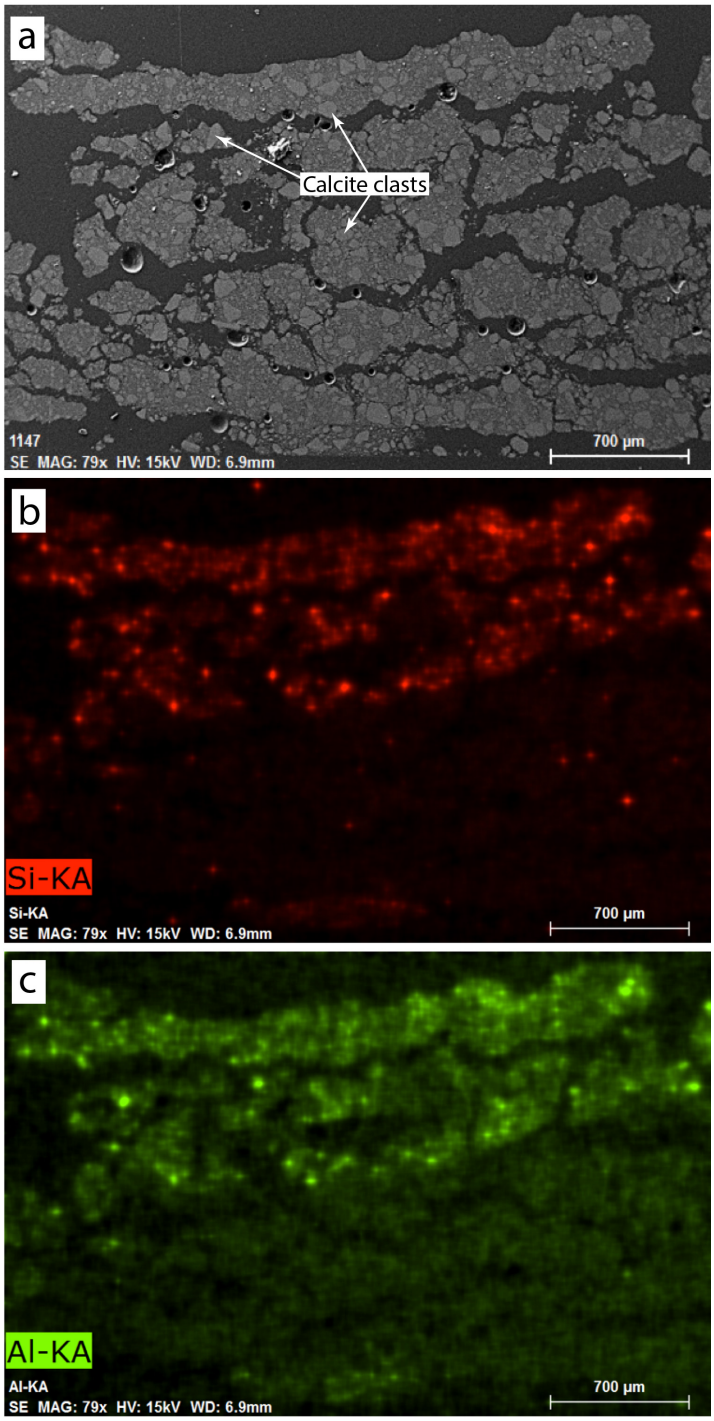


Figure S3. Pre-shear configuration of dry layered experiment. (a) FE-SEM image showing microstructures of pre-shear configuration of dry layered experiment. EDS maps showing any silica (b) and aluminum (c) concentration along the phyllosilicate-rich layer. Silica and aluminum are indicative of the presence of phyllosilicate.

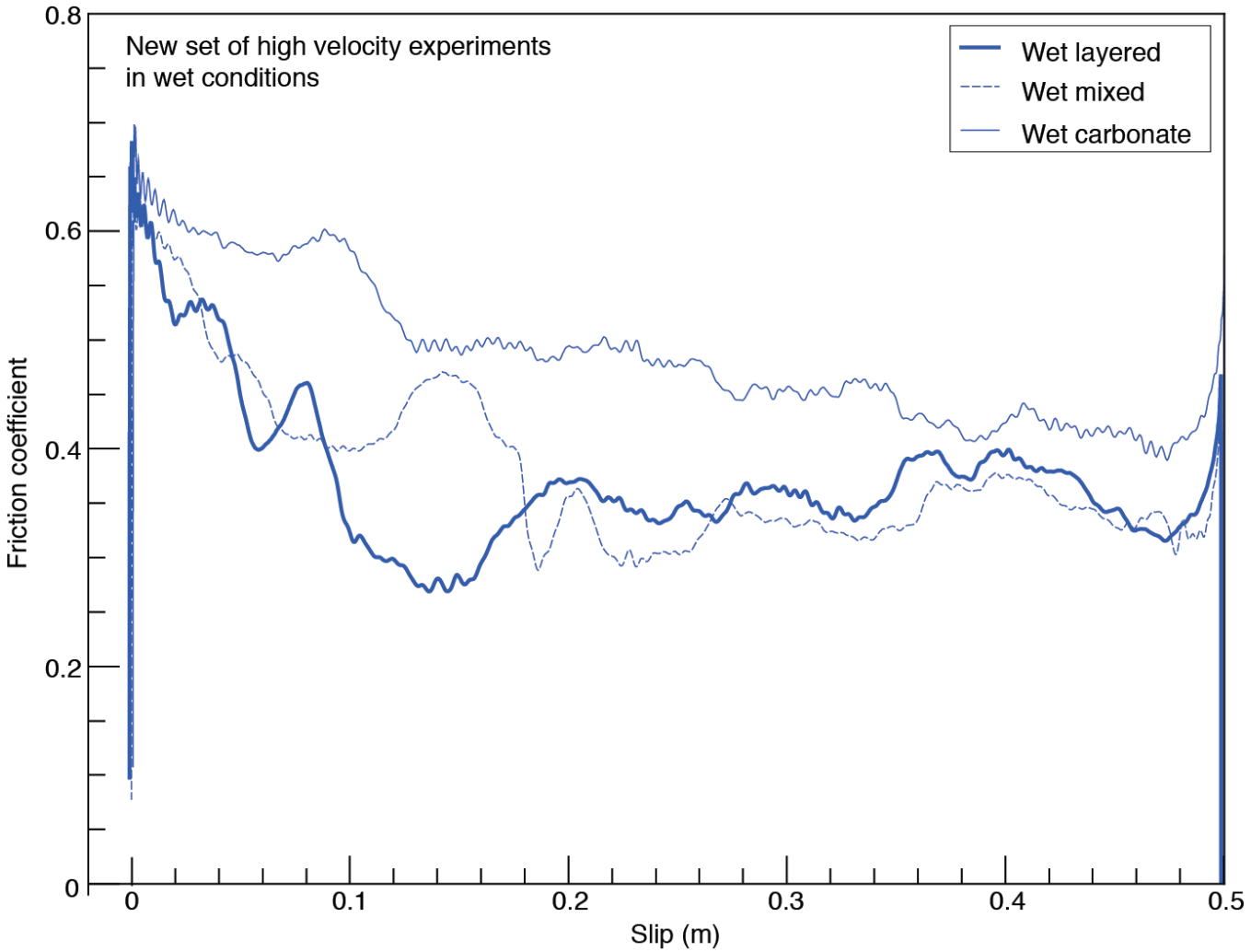


Figure S4. Friction coefficient versus slip of additional experiments at seismic (1 ms^{-1}) slip rate in wet conditions. The new experiments confirm the observed mechanical trend: the layered gouge is weaker than the mixed gouge experiments, which in turn is weaker than pure calcite gouges.

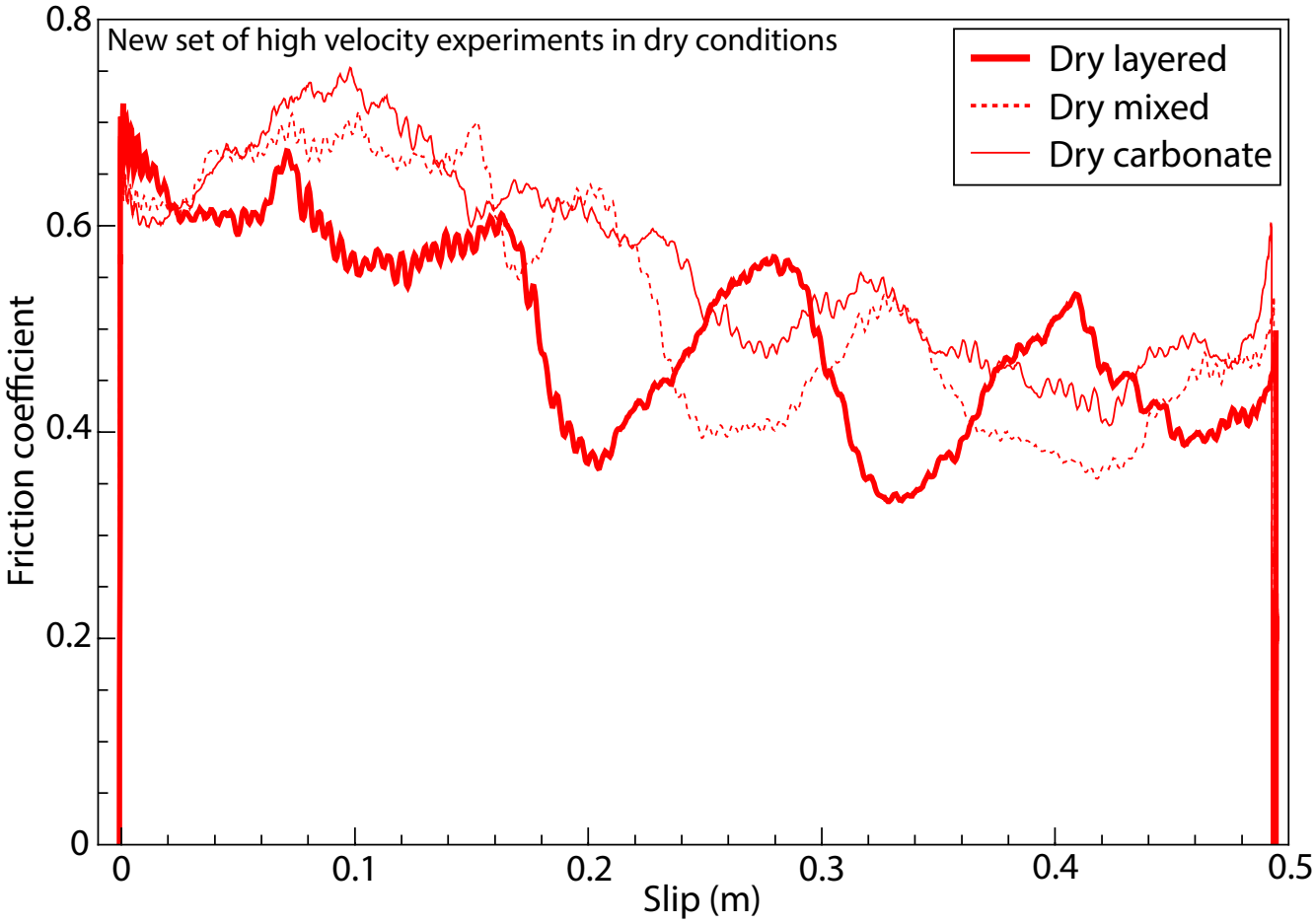


Figure S5. Friction coefficient versus slip of additional experiments at seismic (1 ms^{-1}) slip rate in dry conditions. The new experiments confirm the observed mechanical trend: the layered gouge is weaker than the mixed gouge experiments, which in turn is weaker than pure calcite gouges.

Location	Earthquake	Date	Slip Type	Magnitude	Surface rupture length (km)	Surface displacement (m)
Greece	Sparta	–	N	–	20	3.50
Turkey	Menderes	22/02/1653	N	7.1	70	3.00
Iran	Vostiza	26/12/1861	N	6.6	13	2.20
Greece	Fokis	01/08/1870	N	6.7	6+	2.00
Greece	Civril	03/05/1875	N	6.5	10	1.10
Turkey	Emiralan	29/07/1880	N	6.5	10	0.40
Turkey	Banaz	30/09/1887	N	6.3	10	0.50
Turkey	Martin	27/04/1894	N	6.9	40	1.00
Greece	Mender	20/09/1899	N	6.9	40	1.00
Turkey	Struma	4/4/1904	N	7.2	25	2.00
Bulgaria	Scutari	1/6/1905	N	6.3	10	1.00
Albania	Marmara	9/8/1912	NR	7.4	50	3.00
Turkey	Burdur	3/10/1914	NR	7.0	23	1.50
Italy	Avezzano	13/1/1915	N	7.0	20	2.0
USA	Pleasant Valley	3/10/1915	N	7.6	62	5.8
Kenya	Laikipia	1/6/1928	N	7.0	31	3.3
Turkey	Plovdiv	14/4/1928	N	6.8	–	0.50
Bulgaria	Papazili	18/4/1928	N	6.9	50	3.5
Iran	Ieriss	26/9/1932	N	6.9	15	1.80
Greece	Saphane	25/6/1944	NR	6.0	18	0.30
Peru	Ancash	10/11/1946	N	7.2	21	2.1
USA	Fort Sage Mtns.	14/12/1950	N	5.6	9.2	0.20
Turkey	Sofades	30/4/1954	N	6.7	30	0.90
USA	Rainbow Mountain	6/7/1954	N	6.3	18	0.31
USA	Stiliwater	24/8/1954	N	6.9	34	0.76
Greece	Velestin	8/3/1957	NL	6.6	1	0.20
USA	Hebgen Lake	18/8/1959	N	7.6	26.5	6.1
Greece	Manyas	16/10/1964	NR	6.8	40	0.10
Turkey	Megalop.	1/9/1966	N	5.6	2	0.05
Greece	Acarnania	29/10/1966	N	5.8	4	0.40
Greece	Debar	30/11/1967	NL	6.6	10	0.50
Turkey	Alasehir Valley	28/3/1969	N	6.5	32	0.82
Turkey	Gediz	28/3/1970	N	7.1	41	2.8
Turkey	Burdur	12/5/1971	N	6.2	4	0.30
USA	Oroville	1/8/1975	N-RL	5.6	3.8	0.06
Greece	Thessaloniki	20/6/1978	N	6.4	19.4	0.22
Turkey	Volvi	20/6/1978	N	6.4	32	0.20
Greece	Almyros	9/7/1980	N	6.4	5.3	0.2
Italy	South Apennines	23/11/1980	N	6.9	38	1.15
Greece	Corinth	25/2/1981	N	6.4	19	1.5
Greece	Corinth	4/3/1981	N	6.4	13	1.1
Yemen	Dhamer	13/12/1982	N	6.0	15	0.03
USA	Borah Peak	28/10/1983	N-LL	7.3	34	2.7
Peru	Cuzco	5/4/1986	N	4.6	2.5	0.1
Greece	Kalamata	13/9/1986	N	5.8	15	0.18
New Zealand	Edgecumbe	2/3/1987	N	6.6	18	2.90
USA	Eureka Valley	17/5/1993	N	5.8	4.4	0.02
Greece	Kozani	13/5/1995	N	6.5	15	0.05
Turkey	Dinar	1/10/1995	NR	6.2	10	0.30
Italy	L'Aquila	7/4/2009	N	5.5	6	0.30
Mexico	El Mayor-Cucapah	4/4/2010	N	6.88	–	0.30

Table S1. Non-exhaustive list of onshore extensional fault earthquakes, which caused surface displacement. Historical and instrumental extensional fault earthquakes that generated surface faulting up to about six meters of vertical displacement in different regions worldwide (e.g., Wells and Coppersmith, 1994; Ambraseys and Jackson, 1998; Martino et al., 2014). *E = extensional; RL = right lateral; LL = left lateral. For earthquakes with an oblique component of slip, the subordinate sense of slip is listed after the primary slip type.

Lithology	Quartz (%)	K-feldspar (%)	Plagioclase (%)	Dolomite (%)	Calcite (%)	Clay minerals (%)
Ultracataclasite	0	0	0	0	98.5	1.5
Phyllosilicate-rich layers (ultracataclasite)	3	0	0	0	92	5
Cataclasite	0	0	0	0	100	0
Syn-orogenic deposit (Hemipelagic marls)	26	0	0	5	24	45
Syn-orogenic deposit (Siliciclastic sandstones)	31	3	13	11	12	30

Table S2. Powder X-ray diffraction (XRPD) mineralogical composition of natural fault rocks and tested materials. The ultracataclasite consists of calcite (98.5% wt.) and clay minerals (1.5% wt.). Phyllosilicate-bearing layers consist of calcite (93% wt.), quartz (2% wt.), and clay minerals (5% wt.). The foliated cataclasite consists solely of calcite (100% wt.). Siliciclastic sandstones (Syn-orogenic deposits) consist of quartz (24%), k-feldspar (3%), plagioclase (11%), dolomite (11%), calcite (16%), pyrite (1%), muscovite/illite (21%), chlorite (9%), serpentine (3%), and non quantifiable low amount of smectite and kaolinite. Hemipelagic marls (Syn-orogenic deposits) consist of of quartz (16%), plagioclase (5%), dolomite (3%), calcite (32%), Mg-calcite (21%), muscovite/illite (12%), chlorite (4%), kaolinite (3%), serpentine (4%), and non quantifiable low amount of smectite.

wt%	Phyllosilicates	Detrital Mica	Plagioclase (albite)	K-feldspar	Quartz
Na_2O	0.4	0.7	11.6	0.9	0.1
MgO	3.9	5.4	0.0	0.3	0.2
Al_2O_3	23.4	29.1	19.0	17.3	0.8
SiO_2	55.0	48.8	68.6	69.3	96.1
K_2O	2.7	3.6	0.0	11.8	0.2
CaO	5.0	5.8	0.8	0.0	0.6
TiO_2	1.4	1.1	0.0	0.4	0.3
MnO	0.7	1.6	0.0	0.0	1.3
Fe_2O_3	6.4	2.3	0.0	0.0	0.5
sum	99.0	98.4	100.0	100.0	100.0

Table S3. Average EDS composition of the non-carbonate minerals within the ultracataclasite. Results show the occurrence of phyllosilicates, detrictal mica (mainly illite/muscovite), plagioclase, K-feldspar, and quartz. The chemical data suggest that phyllosilicates and detrital mica are an assemblage of muscovite, illite, chlorite, and smectite.

Number of experiment	Type of experiment	Velocity (m/s)	Normal stress (Mpa)	Distance to the onset of dynamic weakening (m)	Steady state friction	Fracture energy (MJ/m^2)	Total displacement (m)
1146	Dry Layered	1	8.5	0.1743	0.4054	0.461	0.5
1147	Dry Random	1	8.5	0.2604	0.4793	0.473	0.5
1155	Dry Carbonate	1	8.5	0.2511	0.4517	0.570	0.5
1150	Wet Layered	1	5	0.135	0.3467	0.217	0.5
1149	Wet Random	1	5	0.1799	0.3357	0.232	0.5
1156	Wet Carbonate	1	5	0.2115	0.3629	0.262	0.5
1276	Wet Layered	1	5	0.0089	0.2679	0.112	0.5
1275	Wet Random	1	5	0.0216	0.2863	0.193	0.5
1274	Wet Carbonate	1	5	0.097	0.4065	0.386	0.5

Table S4. Summary of experimental conditions and mechanical results of friction experiments.

Chapter 4. Seismic cycles in carbonate/clay-hosted faults

Abstract

In many regions worldwide, moderate to large earthquakes nucleate in and/or propagate through carbonate and marly rocks. The upward propagation of co-seismic slip along faults can cause strong ground motions and surface displacements with associated fatalities and infrastructure damages. In this multi-disciplinary and multi-methodological work, microstructural observations from an extensional fault zone are combined with micromechanical property analyses (Contact Resonance Atomic Force Microscopy, CR-AFM) of fault rocks and with slow to high velocity friction experiments (SHIVA rotary apparatus) to find evidence of past seismic cycles and understand the nanoscale rheology of a seismically-active carbonate/clay-hosted fault. Fault-related microstructures and crosscutting relationships indicate that multiple fast and slow deformation events occurred during co-seismic slip (e.g., fluidized structures, truncated clasts, and phyllosilicate nanospherules and nanotubes) and postseismic/interseismic periods (e.g., clay-assisted pressure-solution seams, clumped clasts, foliation planes, and mantled clasts), respectively. These multiple deformation mechanisms are influenced by fault rock rheology as suggested by CR-AFM measurements showing that ultra-low clay content (~5 wt.%) within the carbonate-hosted gouges can significantly weaken the fault zone. This evidence is confirmed by high-velocity friction experiments showing that the occurrence of ultra-thin phyllosilicate-bearing (≤ 3 wt.%) layers within calcite gouges, as those observed in the natural fault, can facilitate the upward propagation of co-seismic slip, thus possibly leading to Earth's surface displacement. These results can explain some seismological, paleoseismological, and geodetic observations such as the short- to long-term mechanical behavior of faults.

This study was performed in collaboration with A. Bettucci, A. Billi, E. Carminati, A. Cavallo, G. Di Toro, M. Natali, D. Passeri, M. Rossi, and E. Spagnuolo and is under review on Journal of Geophysical Research.

1. Introduction

Understanding the short and long-term mechanical behavior and deformation mechanisms of seismogenic faults is the prerequisite to properly model seismic cycles of active faults and eventually contribute to physically-based probabilistic earthquake forecasting or, at least, mitigate earthquake effects (e.g., Dieterich et al., 1994; Hainzl et al., 2010). Detailed fault mechanical models require indeed, among other parameters, the complete understanding of rheology, frictional behaviors, fluid pressure fluctuations, and deformation mechanisms acting along faults during the seismic cycle (e.g., Li et al., 2011; Hadizadeh et al., 2012; Ben-Zion and Sammis, 2013; Tesei et al., 2014).

Crustal deformation related to seismic cycles has been recorded and studied with paleoseismological, seismological, and geodetic techniques (GPS and InSAR); however, the short-term records of instrumental seismology (less than one century) and geodesy (about 25 years), as well as the non-continuous record of paleoseismology, have limited the long-term understanding of the seismic cycle. For these reasons, the direct study (in situ) of the geological record preserved within fault zones is fundamental to understand the spectrum of deformation mechanisms and mechanical parameters necessary to model the intermediate- to long-term active fault behavior during the seismic cycle (e.g., Smith et al., 2011; Collettini et al., 2014; Fondriest et al., 2012; Demurtas et al., 2016).

Such studies can be accomplished studying seismogenic faults through deep boreholes (e.g., Solum et al., 2006; Gratier et al., 2011) or through the analysis of exhumed faults (e.g., Balsamo et al., 2013; Demurtas et al., 2016). Results from these direct surface studies are complementary to and can explain some seismological and geodetic observations (e.g., Milliner et al., 2016) and are therefore relevant to understand fault deformation mechanisms during the seismic cycle including how the fault zone structure can promote or inhibit seismic slip propagation up to the Earth's surface.

In this paper, we present a multi-disciplinary research starting from the natural case of the exposed extensional seismically-active Tre Monti Fault (TMF) within the carbonate-dominated seismic domain of the central Apennines, Italy (Smith et al., 2011; Benedetti et al., 2013; Smeraglia et al., 2016a). The TMF has been exhumed from shallow depths (≤ 3 km; Smeraglia et al., 2016a) and can hence be considered as an exposed analogue for shallow seismogenic faults. In particular, we focus our study on the ~1 m thick carbonate/clay-hosted Tre Monti principal fault core, which accommodated up to ~2,000 m of total displacement (Smeraglia et al. 2016a). To do so, we combine microstructural, chemical, and mineralogical analyses with laboratory micromechanical analyses and low- to high-velocity friction experiments that simulate the natural setting under laboratory-controlled conditions (Di Toro et al., 2010). We integrate results from previous studies on this fault (Smith et al., 2011; Benedetti et al., 2013; Smeraglia et al., 2016a) with new data to elaborate a synthetic model of deformation mechanisms acting during seismic cycles and to properly highlight how nanoscale rheological contrasts along carbonate/clay-hosted faults influence the bulk fault zone rheology and deformation mechanisms. In particular, we show that microstructures representative of deformation mechanisms acting during the co-seismic and interseismic phases are strongly influenced fault rheology at the nanoscale. We demonstrate that ultra-low clay content (3-5% wt.) within a carbonate-hosted fault zone can weaken the fault zone at the nanoscale and facilitate co-seismic slip propagation. These results can explain some seismological, paleoseismological, and geodetic observations and the short- to long-term mechanical behavior of faults.

2. Geological setting

The Central Apennines are a late Oligocene-to-Present fold-and-thrust belt related to the west directed subduction and eastward rollback of the Adriatic plate under the European plate (e.g., Doglioni, 1991). Shortening was characterized by the northeastward migration of NW-SE-oriented thrust faults, which off-scraped and piled-up the sedimentary succession of the Adriatic plate (e.g.,

Cosentino et al., 2010). Thrust faults juxtaposed ~4,000-5,000-m-thick Late Triassic-Middle Miocene shallow-water carbonate rocks above ~2,000-m-thick Late Miocene syn-orogenic deposits (hemipelagic marls and siliciclastic sandstones with clayey and marly interbeds; Fig. 1a; Cosentino et al., 2010). Seismic reflection profiles show that imbricated carbonate deposits occur from the surface down to a depth of ~7,000-8,000 m (e.g., Billi et al., 2006).

Since Early Pliocene time, the axial part of the Central Apennines belt experienced uplift and extensional tectonics in connection with the development of the Tyrrhenian backarc basin (Doglioni, 1991). This process is still active and has generated intra-mountain grabens bounded by NW-SE-oriented extensional faults and less frequent ENE-WSW-oriented strike- to oblique-slip transfer faults (Fig. 1a). This fault network has produced large historical and instrumental earthquakes up to M_w 7 (Fig. 1a; e.g., Avezzano, 1915, M_w 7.0 earthquake, Galli et al., 2008; L'Aquila, 2009, M_w 6.3 earthquake, Valoroso et al., 2013; Amatrice, 2016, M_w 6.0 and Norcia, 2016, M_w 6.5 earthquakes, Anzidei and Pondrelli, 2016). The TMF belongs to this active tectonic setting representing an extensional-to-transtensional transfer fault between two NW-SE-oriented extensional faults (e.g., Morewood and Roberts, 2000).

Although in the Central Apennines several seismic mainshocks nucleated at depths < 10 km probably in crystalline rocks, it is well documented that many foreshocks and aftershocks as well as some mainshocks nucleated in and propagated upward through the carbonate sedimentary succession (e.g., Valoroso et al., 2013). In particular, co-seismic slip often propagate up to the surface, causing ground displacements and surface faulting, as documented for the recent cases of the 2009 L'Aquila and 2016 Amatrice-Norcia earthquakes (e.g., Anzidei and Pondrelli, 2016) and as shown by paleoseismological observations (e.g., Galli et al., 2008). For instance, during the 2016 Amatrice-Norcia seismic sequence, two mainshocks (M_w 6.0 and M_w 6.5) nucleated at ~7-8 km depth and seismic slip propagated upward through carbonate rocks causing a ~15 km long and up to 200 cm high surface rupture (Anzidei and Pondrelli, 2016). Moreover, many aftershocks of the 2016 Amatrice-Norcia mainshocks nucleated at shallow depths (< 5 km) along carbonate-hosted

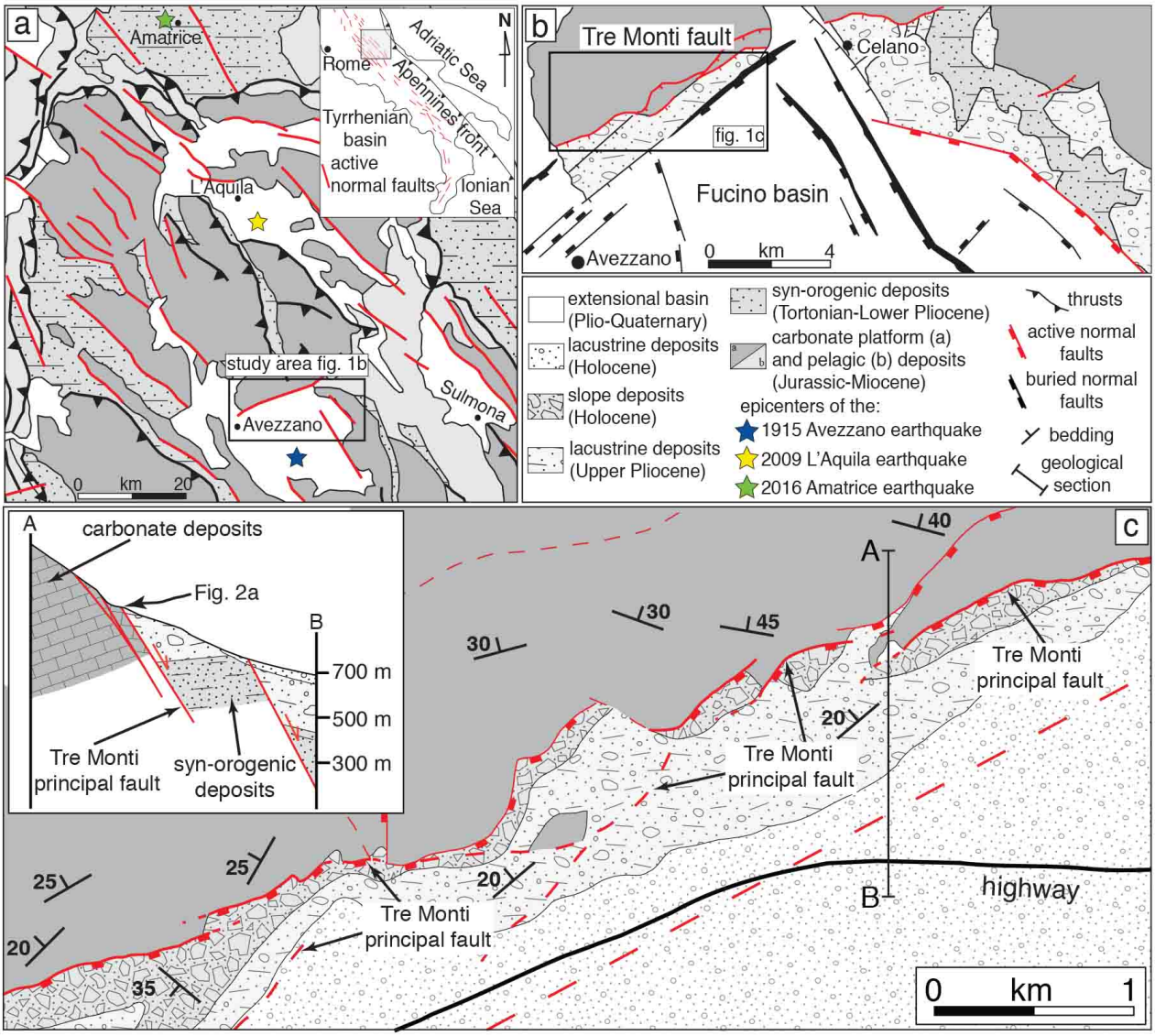


Figure 1. Geological setting and structure of the Tre Monti Fault. **(a)** Geological map of the central Apennines, Italy, showing active faults. Stars indicate the epicenters of the 1915, M_w 7.0, Avezzano, 2009, M_w 6.3, L'Aquila, and 2016, M_w 6.0, Amatrice earthquakes. **(b)** Geological map of the northern boundary of the Fucino basin, including the Tre Monti Fault that is studied in this paper. **(c)** Geological map of the TMF showing principal and secondary faults. Simplified cross-section (inset) through the TMF, showing the principal fault outcrop.

faults and also the maximum slip patches (up to ~2.5 m) of the mainshocks were located at ~4-7 km depth probably within carbonate rocks (Anzidei and Pondrelli, 2016). This evidence indicates that the shallow fault zone structure must have strongly modulated the observed earthquake-related deformation processes and slip recorded at shallow depths and at the surface.

The TMF is a SSE-dipping and ~8 km long extensional/transtensional fault, which delimits the north-western boundary of the Fucino basin, an intramountain half-graben filled by Late Pliocene–

Quaternary continental deposits (Fig. 1b; Morewood and Roberts, 2000; Cavinato et al., 2002; Smith et al., 2011; Smeraglia et al., 2016a). Paleoseismological investigations suggest that the TMF has been active between Early Pliocene and recent-present times (Benedetti et al., 2013). The TMF has been exhumed from depths ≤ 3 km accumulating up to ~2,000 m of cumulative displacement along the principal fault (Cavinato et al., 2002; Smith et al., 2011; Smeraglia et al., 2016a). The principal fault is exposed along the foothills of the Tre Monti Hills and juxtaposes carbonate deposits in the footwall with both syn-orogenic clay-rich deposits and post-orogenic continental sediments (i.e., lacustrine, fluvial, and slope debris deposits) in the hangingwall along a series of ENE-WSW-oriented fault scarps in Mesozoic limestones (Fig. 1c; Benedetti et al., 2013; Smeraglia et al., 2016a). On the contrary, synthetic secondary faults are hosted within the carbonate bedrock of the footwall and juxtapose Mesozoic carbonates and Plio-Quaternary continental deposits in the hangingwall with Mesozoic carbonates in the footwall (Smith et al., 2011; Smeraglia et al., 2016a).

Using geochemical methods, Smeraglia et al. (2016a) showed that the cataclastic rocks of the TMF principal fault developed at ~2-3 km depth. Therefore, in this work, we propose that the inferred deformation mechanisms acted along the TMF principal fault at depths ≤ 3 km.

3. Methods

To finalize this multidisciplinary research, we used the following methods:

(1) Optical and electron microscopy (FE-SEM Zeiss Auriga at the CNIS Laboratory, Sapienza University, Rome, and FE-SEM Zeiss Merlin at the CERTEMA Multidisciplinary Laboratory, Grosseto) to investigate micro- and nano-deformation mechanisms on twenty oriented thin sections of fault rocks.

(2) X-ray powder diffraction (XRPD, at the Padova University laboratories) and Energy Dispersive X-ray analysis (EDS, using FE-SEM Zeiss Auriga at the CNIS Laboratory, Sapienza University, Rome, and FE-SEM Zeiss Merlin at the CERTEMA Multidisciplinary Laboratory, Grosseto) to investigate both natural and experimental fault rock mineralogy and chemistry.

(3) Contact Resonance Atomic force measurements (CR-AFM; Passeri et al., 2013) to measure in situ mechanical properties (Young's modulus and viscoelasticity) within natural samples (at the CNIS Laboratory, Sapienza University, Rome). Detailed method description is provided in Appendix A of Supplementary material.

(4) Pulse-echo ultrasonic technique (at the CNIS Laboratory, Sapienza University, Rome) to measure the elastic properties (i.e., Young's modulus and Poisson ratio) of host carbonate rock and to calibrate the CR-AFM measurements. Detailed method description is provided in Appendix B of Supplementary material.

(5) Low to high velocity friction experiments using SHIVA (Slow- to High-Velocity rotary-shear friction Apparatus, at INGV HP-HT Laboratory, Rome; Di Toro et al., 2010) to investigate frictional properties of natural fault rocks. During these experiments we recorded also gas emission through a mass spectrometer. Moreover, to quantitatively constrain the behavior of shear and normal stress, we performed a zero-lag cross-correlation analysis to quantify the correlation between the imposed normal stress and the recorded shear stress. Detailed method description is provided in Appendix C of Supplementary material.

4. Field- to nano-scale observations on the Tre Monti principal fault

The architecture of the Tre Monti principal fault has been partially documented in previous studies (Smith et al., 2011; Smeraglia et al., 2016). Here we discuss new observations (i.e., fluid-like structures, Figs. 2d and 2e; ultra-thin phyllosilicate-bearing layers, Figs. 2c and 2f; pressure-solution seams, Figs. 3b, 3d, and 3e; foliation planes Fig. 3c; mantled clasts, Fig. 3c; and clumped clasts, Figs. 3d and 3h) concerning fault deformation mechanisms and microstructures.

The principal fault (Fig. 2a) accommodated tectonic deformation along a ~1 m thick fault core, which consists of two different fault rocks: ultracataclasite and foliated cataclasite (Figs. 2b and 2c). XRPD analyses show that the ultracataclasite consists of calcite (~98.5 wt.%) and phyllosilicates (~1.5 wt.%, mainly illite/smectite and kaolinite; Table S1 in Supplementary material

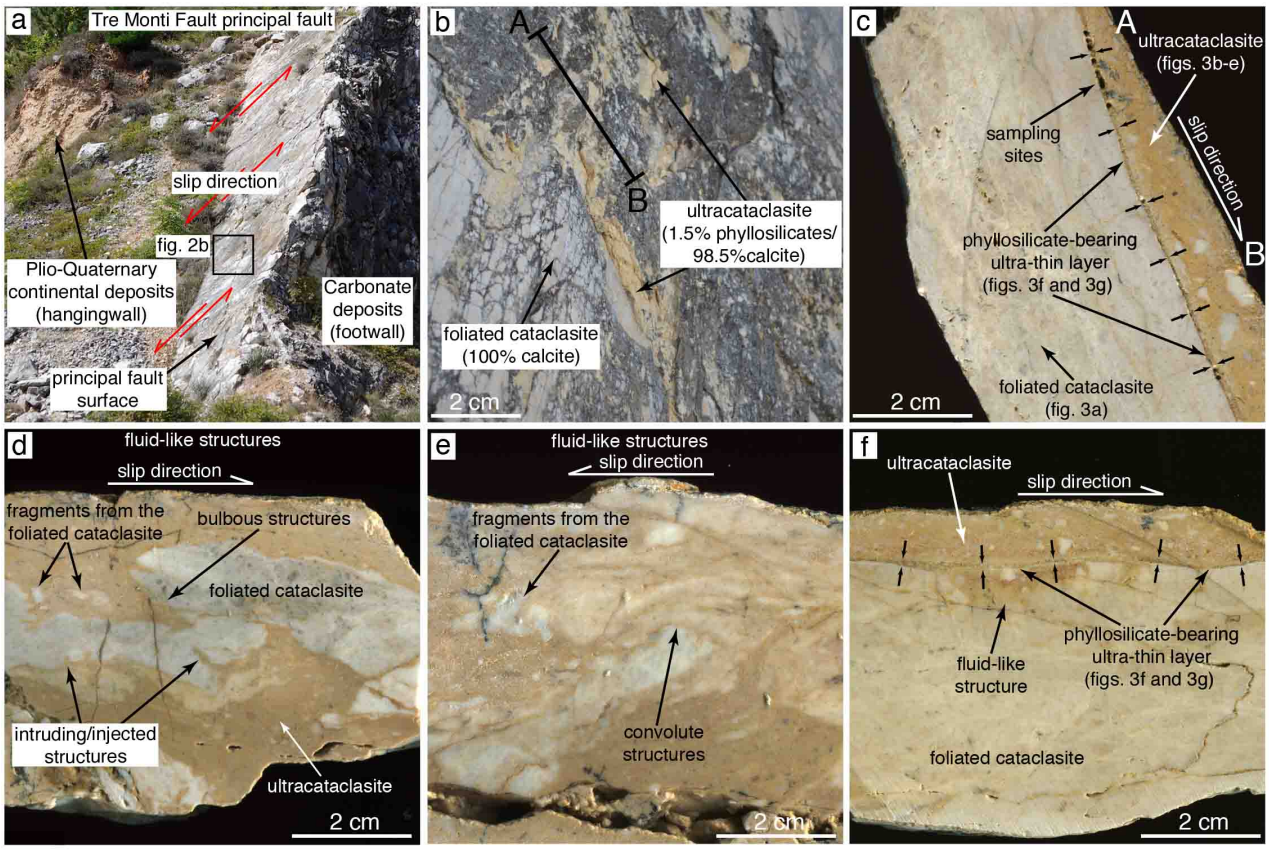


Figure 2. Rocks of the Tre Monti fault. **(a)** Overview of the Tre Monti principal fault, which juxtaposes, in the study outcrop, Plio-Quaternary continental deposits in the hangingwall with carbonate deposits in the footwall. **(b)** Detail of the principal fault surface showing patches and plagues of ultracataclasite (with 1.5 wt.% of phyllosilicates) above the foliated cataclasite (100 wt.% calcite). **(c)** High resolution scan of sample cut perpendicular to the principal fault surface, showing the sharp contact between the ultracataclasite and the foliated cataclasite marked by the phyllosilicate-bearing layers laying between the two fault rocks. **(d, e)** High resolution scans of samples cut perpendicular to the principal fault surface, showing fluid-like structures characterized by irregular margins and bulbous/convolute structures with injection of the ultracataclasite into the foliated cataclasite. **(f)** High resolution scan of sample cut perpendicular to the principal fault surface showing a fluid-like injection of the ultracataclasite into the foliated cataclasite cut by the phyllosilicate-bearing layer.

and Smeraglia et al., 2016b). On the contrary, the foliated cataclasite consists solely of calcite (Table S1 in Supplementary material). Phyllosilicates in the ultracataclasite mainly derived from incorporation, smearing and mixing, along the principal fault, of phyllosilicate-rich syn-orogenic deposits in the hangingwall (Smeraglia et al., 2016b). The ultracataclasite forms patches and plagues, up to ~10 cm thick, above the foliated cataclasite (Fig. 2b). The boundary between these two fault rocks is often sharp and continuous (Fig. 2c); however, in places, the two fault rocks are

mingled together showing fluid-like structures at the centimeter scale (Figs. 2d and 2e). These structures show irregular/convolute margins (Fig. 2e) with bulbous protrusion, up to several cm-thick, of the ultracataclasite into the foliated cataclasite. The irregular margins are characterized, in places, by load-like or intruded/injected structures (Fig. 2d). Moreover, fragments from the foliated cataclasite are, in places, completely enclosed within the ultracataclasite (Fig. 2d). These fluidized structures develop at distances up to 10 cm from the principal slip surface (Figs. 2d and 2e). Similar fluid-like structures have been previously documented along the TMF only at the millimeter-scale (Smith et al., 2011). In this latter case, in particular, the micrometer-thick bulbous protrusions were intruded only for small distances (i.e., a few microns) between the different cataclastic layers (Smith et al., 2011).

The foliated cataclasite is characterized by calcite clasts derived from the host rock (i.e., Mesozoic limestones; Fig. 3a). Foliation planes consist of slip-parallel shear planes bounding calcite sigmoids affected by extensional microfractures (Fig. 3a). The ultracataclasite consists of calcite clasts (millimeter to micrometer in size) derived from the underlying foliated cataclasite, scattered within an ultra-fine phyllosilicate-bearing reddish matrix (Fig. 3b). Clasts are sub-angular to well-rounded and, in places, are in reciprocal contact showing indented and teeth-shaped margins, typical of pressure solution seams (i.e., stylolites; Fig. 3b). The ultracataclasite is characterized, in places, by foliation planes roughly parallel to the slip direction (Fig. 3c). Within these foliation planes, calcite clasts are scattered within the ultra-fine phyllosilicate-bearing reddish matrix (Fig. 3c). In particular, large calcite clasts are characterized by mantled-like structures (e.g., Passchier and Trouw, 2005) showing elongate trails of smaller calcite clasts aggregates, stretched parallel to the foliation (Fig. 3c). These small calcite clasts are in reciprocal contact showing indented and teeth-shaped margins, typical of pressure solution seams (Fig. 3c).

The ultra-fine phyllosilicate-bearing reddish matrix consists of micro- to nano-meter-thick sub-angular to well-rounded calcite clasts and phyllosilicates (Figs. 3d and 3e). In particular, phyllosilicates represent ~1.5 wt.% of the bulk volume of the ultracataclasite (Table S1 in

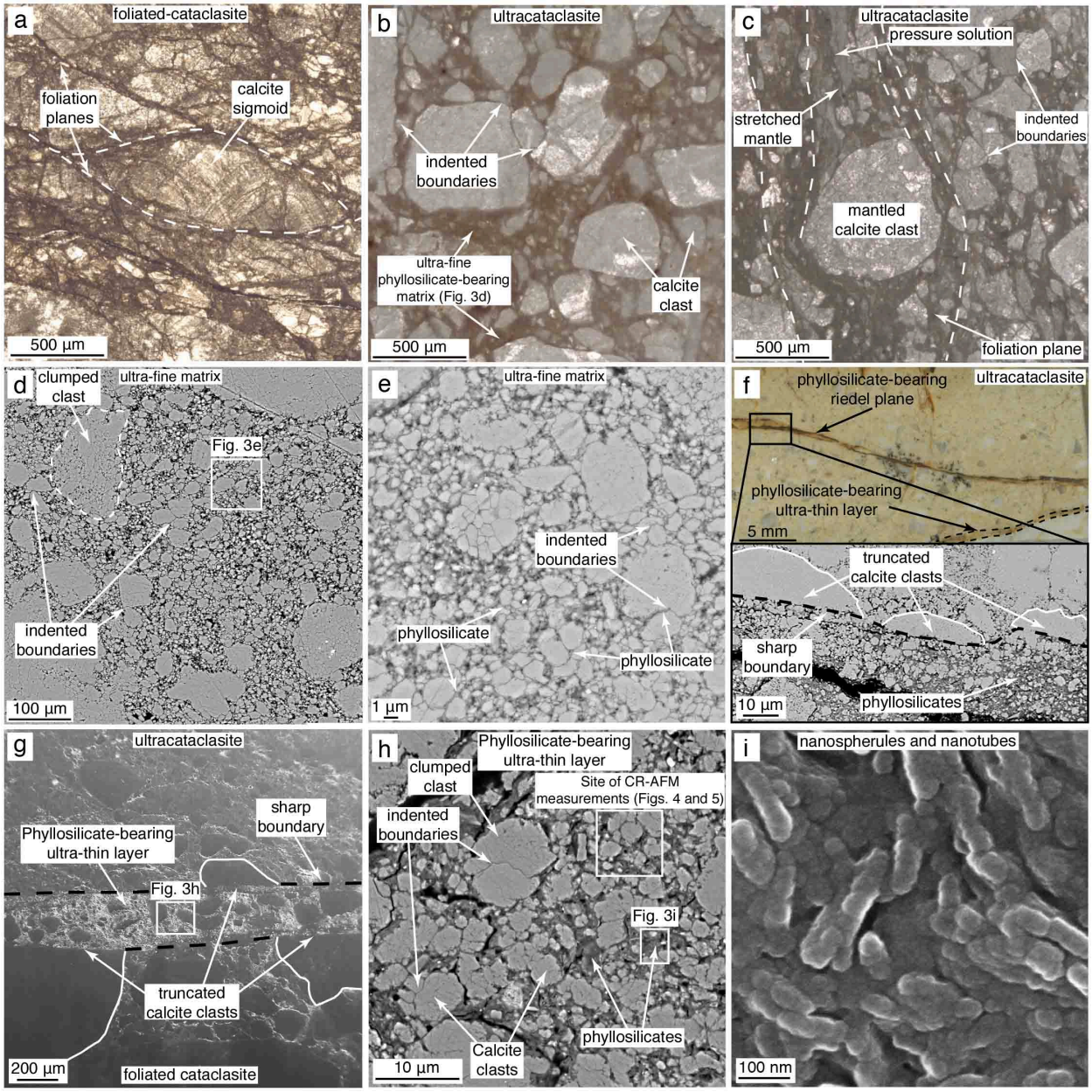


Figure 3. Microphotographs of thin sections showing representative fault rock textures along the TMF under optical (OPT) and field emission scanning electron microscope (FESEM). **(a)** Texture of the foliated cataclasite showing foliation planes defined by cataclastic shear zones encasing host rock sigmoids. **(b)** Texture of the ultracataclasite showing calcite clasts scattered within an ultra-fine reddish phyllosilicate-bearing matrix. Clasts that are in contact with one another show indented and teeth-shaped margins. **(c)** Texture of the ultracataclasite showing foliation planes defined by shear zones rich in ultra-fine reddish phyllosilicate-bearing matrix. Large clasts in this foliation planes are characterized by mantled structures showing an elongate trail of smaller calcite clasts. **(d, e)** FESEM images of the texture of the ultra-fine matrix from the ultracataclasite. Calcite clasts that are in contact with one another show indented and teeth-shaped margins. In places, an ultra-thin phyllosilicate film is interposed between clasts. Small calcite clasts are welded together to form larger clasts. **(f)** High resolution scan of sample cut perpendicular to the TMF, showing phyllosilicate-bearing layers along a riedel shear planes and the boundary between the ultracataclasite and the foliated cataclasite. Inset shows a FESEM image of the sharp boundary with truncated clasts between the phyllosilicate-bearing layer (i.e., along the riedel shear plane) and the ultracataclasite. **(g)** FESEM image of the phyllosilicate-bearing

layer between the ultracataclasite and the foliated cataclasite showing a sharp boundary, which truncates calcite clasts. **(h)** Detail of the phyllosilicate-bearing layer showing calcite clasts scattered within phyllosilicate layers. Calcite clasts that are in contact show indented and teeth-shaped margins. **(i)** Detail of phyllosilicate nanostructures (i.e., clumped nanospherules and nanotubes) within the phyllosilicate-bearing layer.

Supplementary material). Contacts between calcite clasts show indented and teeth-shaped geometries down to the microscale, defining a highly compact and low-porosity texture (Figs. 3e), also due to ultra-thin phyllosilicate lamellae (a few hundreds of nm thick) often interposed between clast margins (Fig. 3e). In places, clumps of small calcite clasts are welded together to form larger and distinct clasts (Figs. 3d and 3e). These larger clasts are reworked within the ultracataclasite (Figs. 3d and 3e).

Microstructural observations and XRPD analyses (Table S1 in Supplementary material) within the ultracataclasite show that phyllosilicates (mainly illite/smectite and kaolinite) concentrate within ultra-thin (up to ~1 mm-thick) and localized layers (in the following "phyllosilicate-bearing layers"). The average phyllosilicate content within these layers is ~5 wt.%, thus higher than the phyllosilicate content within the ultracataclasite (~1.5 wt.%). Phyllosilicate-bearing layers occur along the sharp boundaries between the ultracataclasite and the foliated cataclasite (Fig. 2c), along some riedel-shear planes cutting across the ultracataclasite (Fig. 3f) or, in places, cutting across fluid-like structures (Fig. 2f), delineating a pervasive network along the Tre Monti principal fault. In addition, these crosscutting relationships suggest that phyllosilicate-bearing layers postdate the ultracataclasite, the foliated cataclasite, and the fluid-like structures.

Layer margins are sharp and continuous, truncating calcite clasts (Figs. 3f and 3g). In these layers, carbonate clasts are well rounded and scattered within a phyllosilicate-bearing matrix. Calcite clasts that are in reciprocal contact show indented and teeth-shaped margins, typical of pressure solution seams (i.e., stylolites; Fig. 3h). We found clumped calcite clasts, as those observed within the ultracataclasite matrix (Figs. 3d and 3e), reworked within the phyllosilicate-bearing layers (Fig. 3h). Down to the nanoscale, phyllosilicates are characterized by fibrous or

massive morphologies, which, in detail, consist of 50 nm-thick clumped and chained nanospherules and nanotubes (Fig. 3i). We found these peculiar phyllosilicate microstructures only within the phyllosilicate-bearing layers.

5. In situ elastic property micromeasurements

Figures 4a and 5a are topographic CR-AFM maps of two areas (16 μm^2 and ~2 μm^2, respectively) within the phyllosilicate-bearing layer (Fig. 3d). Detailed method description is provided in Appendices A and B in Supplementary material. In these maps, we observe several calcite clasts (few microns to some tens of nanometers in size), scattered within a phyllosilicate-bearing matrix. Phyllosilicates are characterized by first contact resonance frequency (f_1) and by first quality factor (Q_1) values lower than those of calcite clasts (Figs. 4b, 4c, 5b, and 5c). This setting is confirmed by second contact resonance frequency (f_2) and by second quality factor (Q_2) values (Figs. 4d, 4e, 5d and 5e). From these values, we calculated the indentation modulus, which can be treated as the Young's modulus of the study material, as explained in Appendix A in Supplementary material.

Quantitative maps of indentation modulus (i.e., Young's modulus; Figs. 4f, and 5f) show that calcite clasts and phyllosilicates are characterized by indentation moduli of 49±8 GPa and 7±3 GPa, respectively (i.e., measurements at ambient pressure). The indentation modulus of phyllosilicates is consistent with that previously calculated with CR-AFM (Prasad et al., 2002). On the contrary, the indentation modulus of calcite clast is smaller than Young's modulus of TMF carbonate host rock (80±5 GPa; Appendix B in Supplementary material) and smaller than Young's modulus previously measured in intact carbonate rocks at low confining pressure (~5 MPa; e.g., Agosta et al., 2007).

Calcite clasts are characterized by loss tangent and loss modulus values of 0.01±0.002 and 450±150 MPa, respectively (Figs. 4g, 4h, 5g, and 5h). On the contrary, the same maps show that

phyllosilicates are characterized by a loss tangent and loss modulus values of 0.023±0.004 and 160±30 MPa, respectively (Figs. 4g, 4h, 5g, and 5h). These data indicate a more viscous response of phyllosilicates than calcite.

Overall, the analyzed areas from the phyllosilicate-rich layers can be considered as two-phase nanocomposite within which phyllosilicates roughly represents ~50% of the total volume (Figs. 4a and 5a). Thus, the effective composite modulus (i.e., indentation modulus of phyllosilicates together with calcite clasts) of these areas calculated using the Voight Model is about 28 GPa, which is smaller than Young's modulus of TMF carbonate host rock (80±5 GPa; Appendix B in Supplementary material) and smaller than Young's modulus previously measured in carbonate-hosted cataclastic rocks (e.g., Agosta et al., 2007).

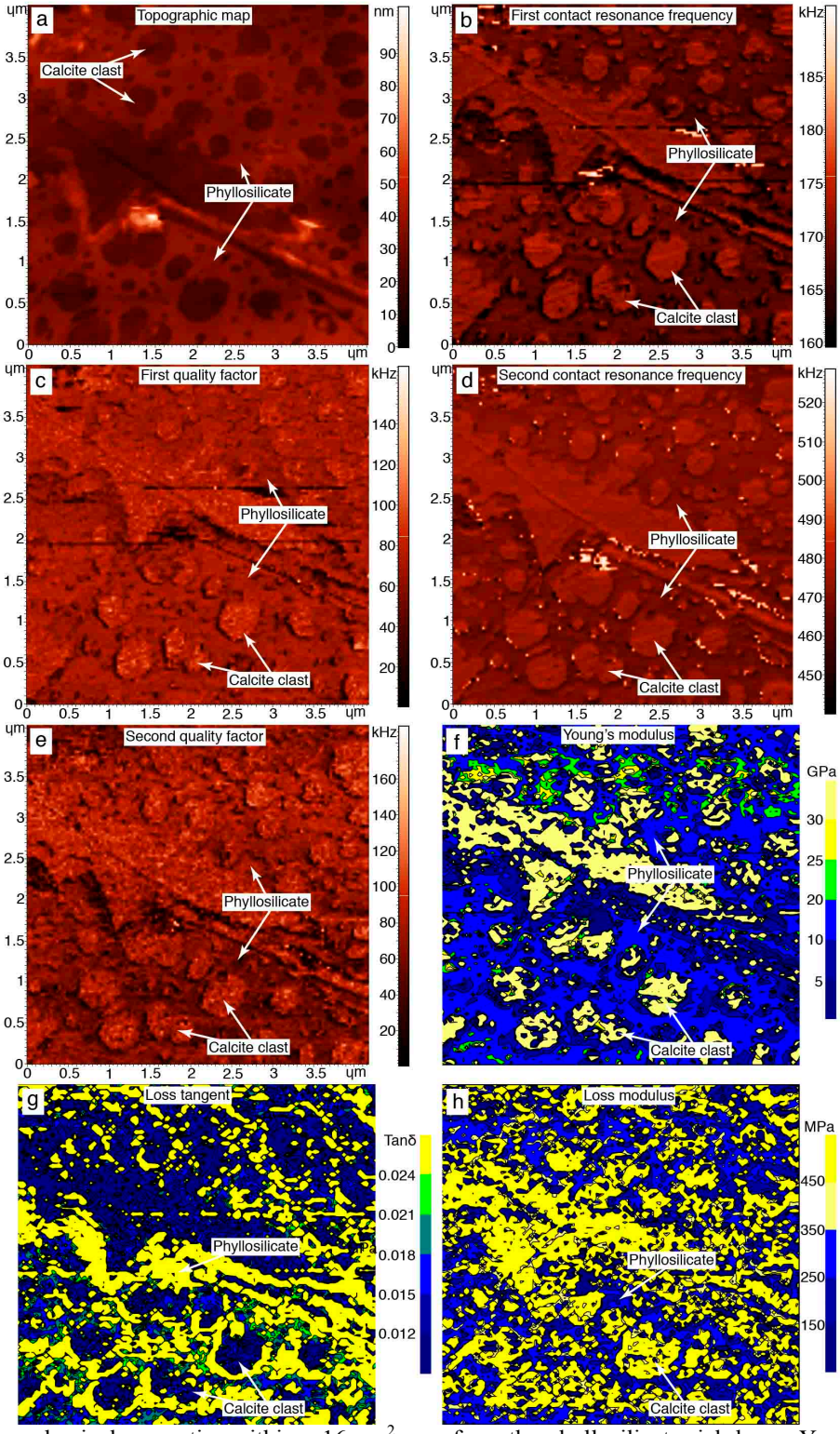


Figure 4. In situ mechanical properties within a 16 μm^2 area from the phyllosilicate-rich layer. Young's modulus and viscosity are calculated through Atomic Force Microscopy (AFM). **(a)** Topographic maps showing calcite clasts (black) scattered within phyllosilicates (red). Maps of the **(b)** first and **(d)** second contact resonance frequency (f_1 and f_2) and of the **(c)** first and **(e)** second quality factor (Q_1 and Q_2) values showing that calcite clasts are stiffer than phyllosilicates. **(f)** Map of the Young's modulus values showing that calcite clasts have higher Young's modulus than that of phyllosilicates. Maps of **(g)** loss tangent (tanδ) and **(h)** loss modulus (E'') values showing that phyllosilicates behave in a less viscous manner (i.e., higher loss tangent and lower loss modulus values than calcite) than calcite clasts, which have an elastic behavior.

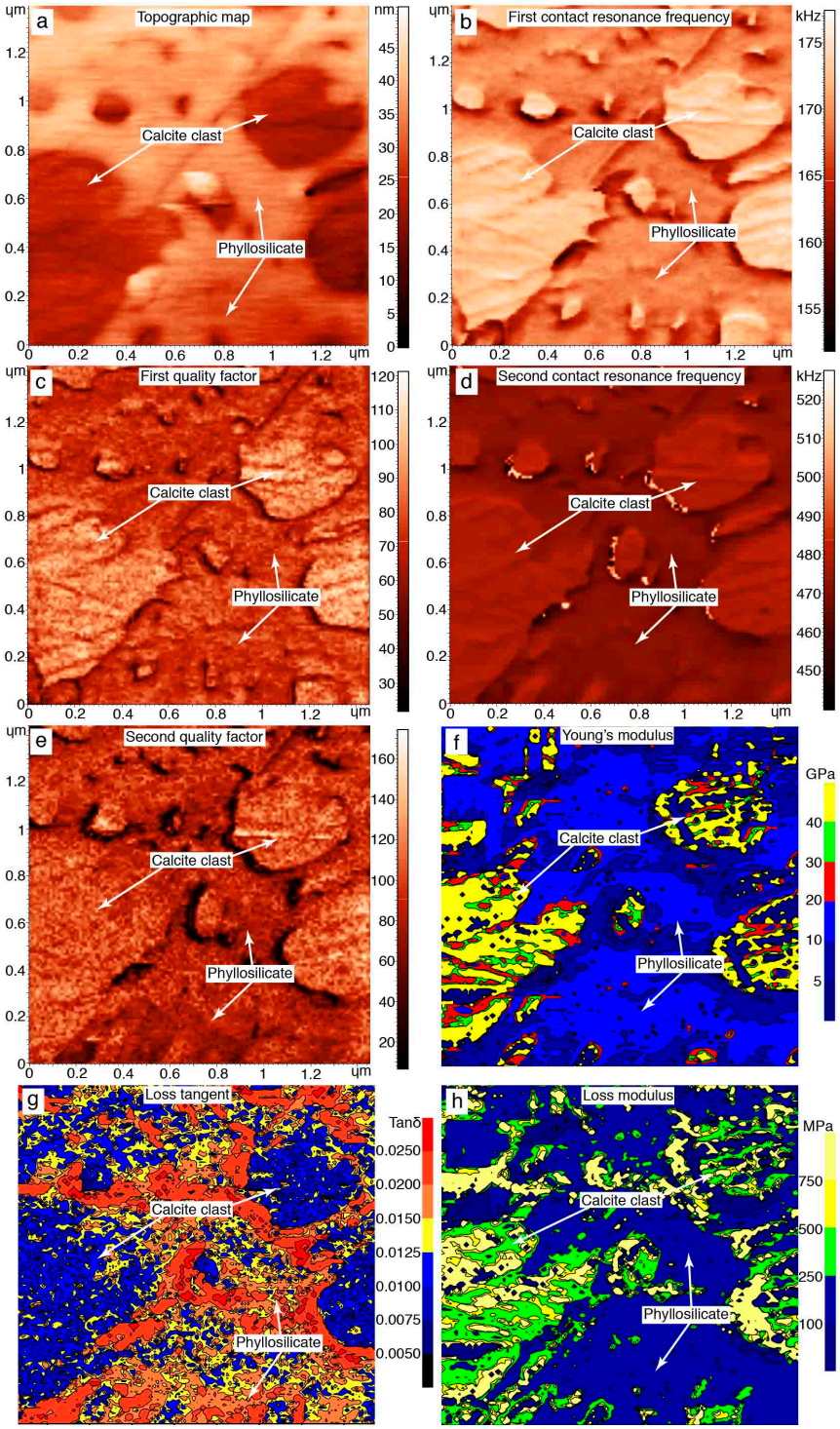


Figure 5. In situ mechanical properties within a ~2 μm^2 area from the phyllosilicate-rich layer. Young's modulus and viscoelastic property are calculated through Atomic Force Microscopy (AFM). **(a)** Topographic maps showing calcite clasts (black) scattered within phyllosilicates (red). Maps of the **(b)** first and **(d)** second contact resonance frequency (f_1 and f_2) and of the **(c)** first and **(e)** second quality factor (Q_1 and Q_2) values showing that calcite clasts are stiffer than phyllosilicates. **(f)** Map of the Young's modulus values showing that calcite clasts have higher Young's modulus than that of phyllosilicates. Maps of **(g)** loss tangent (tanδ) and **(h)** loss modulus (E'') values showing that phyllosilicates behave in a more viscoelastic manner (i.e., higher loss tangent and lower loss modulus values than calcite) than calcite clasts, which show an elastic behavior.

6. Low to high velocity friction experiments

6.1. Experimental procedure

Field and microstructural observations show the occurrence of low percentage (~5% wt.%) of phyllosilicates concentrated along ultra-thin and discrete layers. To understand the frictional behavior and unravel the origin of such layers within calcite-bearing fault rocks, we conducted rotary-shear experiments reproducing the natural setting observed in nature.

We prepared the starting gouge material using natural rocks collected in the field. To obtain a pure calcite powder, we crushed and sieved (<125 μm) the foliated cataclasite (100% calcite, Table S1 in Supplementary material), whereas, to obtain a phyllosilicate-rich powder, we crushed and sieved (<125 μm) the syn-orogenic deposits (~38% of phyllosilicates content; Table S1 in Supplementary material). We used 4.5 g of gouge for each experiment creating ring-shaped gouge layers with initial thicknesses of ~3 mm (Fig. 6b).

We carried out experiments using three different gouge settings (Fig. 6b). Mixed gouge (Fig. 6b, left panel) consists of 10% of phyllosilicate-rich powder mixed with 90% of pure calcite powder (total phyllosilicates content of ≤ 3 wt.%). Layered gouge (Fig. 6b, middle panel) consists of a ~1 mm-thick layer made of 10% of phyllosilicate-rich powder mixed with 90% of calcite powder overlain by a ~2 mm-thick layer of pure calcite powder. This configuration simulates the ultra-thin phyllosilicate-bearing layers observed along the TMF (Figs. 2c, 2f, 3f, and 3g). Calcite gouge (Fig. 6b, right panel) consists of pure calcite powder used as an end member and representing the bulk composition of the TMF.

We performed experiments at 0.001 ms^{-1} (i.e., almost subseismic slip velocity) and 1 ms^{-1} (i.e., typical seismic slip velocity) slip-rates under water-damped (hereafter wet) and room-humidity (hereafter dry) conditions. Water-damped gouges were saturated with 0.5 ml of distilled water in the case of wet experiments. Helding the normal stress constant at 8.5 MPa and 5 MPa for dry and wet experiments, respectively, we sheared gouges for a total displacement of 0.5 meter. We set these boundary conditions to simulate the calculated co-seismic slip (i.e., in the case of high

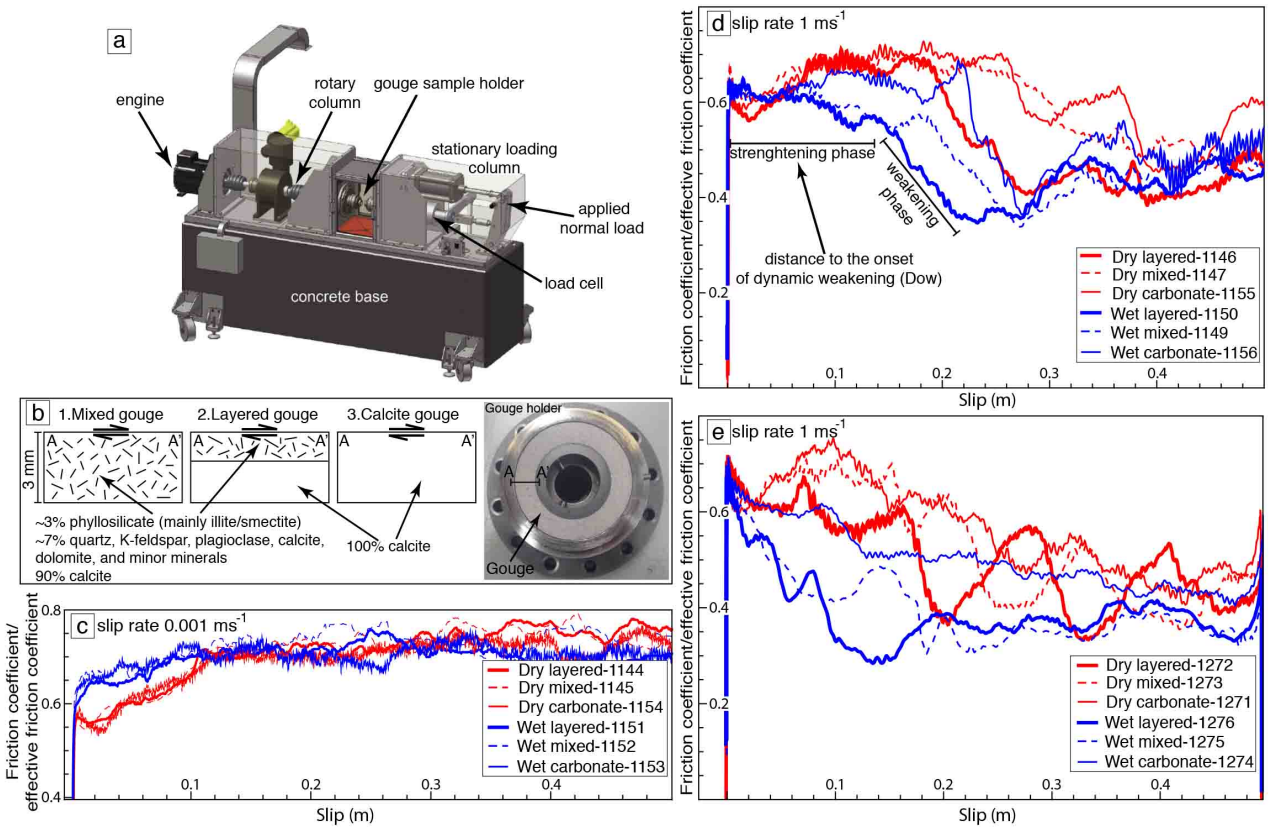


Figure 6. Experimental apparatus, gouge configurations, and mechanical results (evolution of friction coefficient versus slip) of low to high velocity shear experiments. **(a)** SHIVA apparatus with main components labeled (modified from Smith et al., 2015). **(b)** Gouge configurations showing the three different setup: mixed, layered, and pure calcite gouges. **(c)** Evolution of friction coefficient versus slip during experiments at subseismic (0.001 ms^{-1}) slip rate. Friction coefficient reached the 0.7-0.8 values and remained stable during all experiments. **(d, e)** Evolution of friction coefficient versus slip during experiments at seismic (1 ms^{-1}) slip rate. Layered gouges are weaker (i.e., they have a lower distance to the onset of dynamic weakening, D_{ow}) than mixed gouges, which are, in turn, weaker than pure clacite gouges, both in dry and wet conditions.

velocity experiment) occurring along a shallow (i.e., at depth <0.5 km) fault zone during M_w 6.0-6.5 earthquakes (e.g., Anzidei and Pondrelli, 2016).

The experimental procedure consists of the following steps: (1) samples were initially pre-sheared at 1 cms^{-1} for 10 cm of slip at 1 MPa of normal load, both in dry and in wet conditions. We pre-sheared gouges to properly simulate our natural analogues, within which the fault rocks are naturally pre-sheared due to fault displacement accumulation, (2) samples were loaded to the target normal stress and were then sheared with acceleration and deceleration rates of 24 ms^{-2}, up to the total displacement, (3) during the experiment we measured gas emission with a Pfeiffer Quadstar

quadrupole mass spectrometer (see Appendix C in supplementary material), (4) after experiments, flinty fragments of sheared samples were collected and impregnated under vacuum using low-viscosity epoxy. The impregnated gouges were cut perpendicularly to the surface and approximately parallel to slip direction. Then, we prepared petrographic thin sections ~30 μm thick for microstructural observations. Complete mechanical results are reported in Table S2 in Supplementary material.

6.2. Results

At 0.001 ms^{-1}, both in dry and in wet conditions, the effective friction coefficient (i.e., note that, in the wet experiments, the pore fluid pressure cannot be measured; hence the term "effective") achieves a peak of ~0.6 at slip initiation and then increases almost monotonically towards a constant value of 0.7-0.8 that is eventually achieved after ~0.5 m of slip (Fig. 6c). On the contrary, at seismic slip rates (1 ms^{-1}), gouges in the three configurations (both in dry and in wet conditions) show a strong dynamic weakening (i.e., friction drop) after a strengthening phase, which is defined here as the distance to the onset of dynamic weakening, D_{ow} (Figs. 6d and 6e; Smith et al., 2015). Overall, both in dry and in wet conditions, we recognized a general trend: layered gouges weaken faster than mixed gouges, which, in turn, weaken faster than calcite pure gouges (Fig. 6d).

To test the reproducibility of this trend, we replicated high velocity experiments (with layered, mixed, and calcite gouges) both in dry and in wet conditions. The major relevant difference from the previous experiments is observed in the weakening stage of wet experiments, which can suffer from slightly different ambient conditions, sample saturation, and holding time. However, despite the large heterogeneity of natural materials used for gouges, the replicated experiments are in good agreement with the previously observed mechanical trends (i.e., layered gouges weaken faster than mixed gouges, which, in turn, weaken faster than calcite pure gouges Fig. 6e).

During high velocity dry experiments, we observed a normal stress increase in correspondence with the shear stress increase (i.e., during the strengthening phase; Fig. 7a). This is

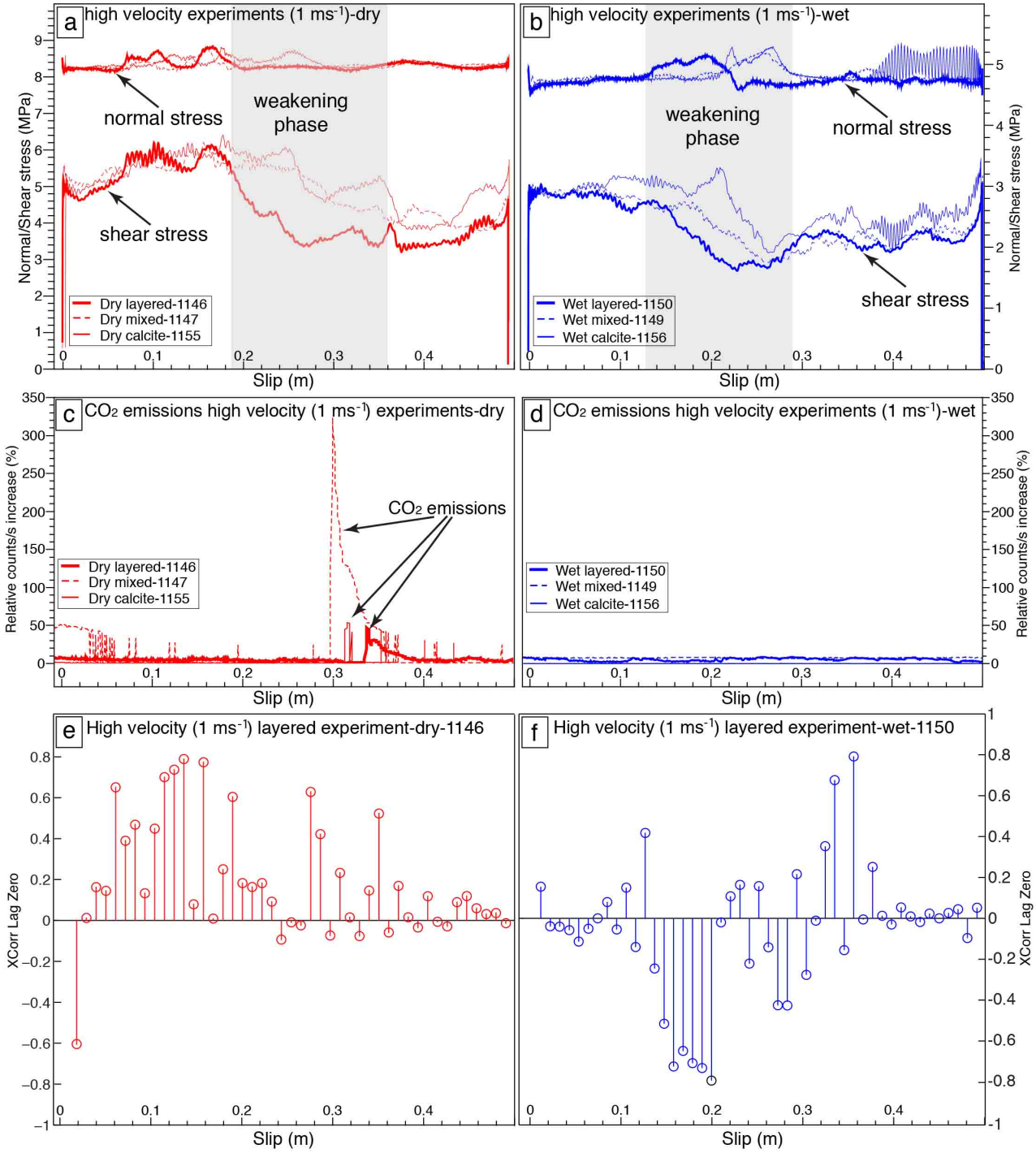


Figure 7. Mechanical and mass spectrometer data for high velocity experiments both in dry (red curves, left column) and in wet (blue curves, right column) conditions. **(a, b)** Evolution of shear stress versus normal stress. Wet experiments show an increase in the normal stress in correspondence of friction drop (i.e., during the weakening phase). On the contrary, dry experiments show an increase in the normal stress in correspondence of the strengthening phase. **(c, d)** CO_2 emissions were recorded only during dry experiments. **(e, f)** Evolution of cross-correlation (Lag0) coefficient. Dry experiments show a positive correlation during most experiments, indicating an in-phase oscillation between normal and shear stress. On the contrary, wet experiments show a negative correlation during the central part of the experiment (i.e., the weakening phase), indicating an increase of normal stress during a decrease in shear stress (i.e., out of phase oscillation).

consistent with zero-lag cross-correlation analyses (see Appendix C in Supplementary material) showing that high velocity experiments in dry conditions are characterized by a positive correlation (Fig. 7e, S1, and S2 in Supplementary material). In particular, a positive correlation can be attributed to: (1) the coupling between the rotary column (supplying the shear force) and the stationary column (supplying the normal load) through a strong frictional interface (i.e., irregularities in the gouge contact surface) or (2) a slightly misalignment between the rotary and the stationary columns.

On the contrary, during high velocity wet experiments, we observed an increase in the normal stress in correspondence with the shear stress decrease (i.e., during the weakening phase; Fig 7b). This is consistent with zero-lag cross-correlation analyses (see Appendix C in Supplementary material) showing that high velocity experiments in wet conditions are characterized by a negative correlation in correspondence with the weakening phase (Fig. 7f, S1, and S2 in Supplementary material). A negative correlation is relevant for the experiment mechanics and is further explained in the discussion section.

Low velocity experiments under dry conditions are characterized by normal stress oscillations (Fig. 8a), whereas low velocity experiments under wet conditions show a constant normal stress (Fig. 8b). In particular, under dry conditions, normal stress oscillations are in phase with shear stress oscillations (Fig. 8a). Low velocity experiments under both wet and dry conditions show an alternation between positive and negative correlation during all experiments (Fig. 8e, 8f, and S3 in Supplementary material).

Significant gas emissions (CO_2) were detected only during high velocity experiments under dry conditions (compare Fig. 7c with Fig 7d) and in correspondence with the weakening phase (Fig. 7c). Instead, gas emissions were not detected (i.e., or gas emissions were below the instrumental detection limit) in the low velocity experiments performed both under dry and under wet conditions (Figs. 8c and 8d).

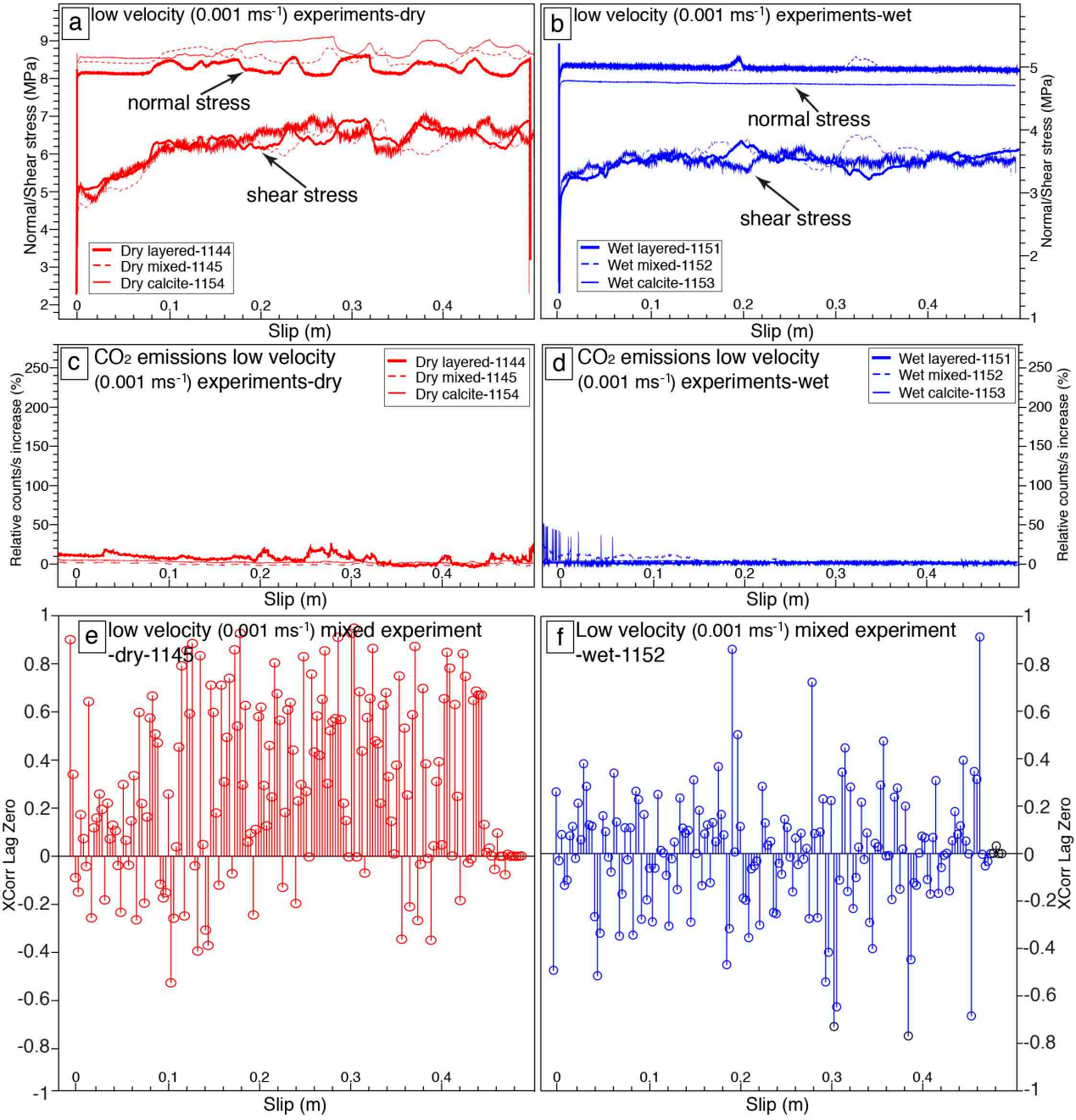


Figure 8. Mechanical and mass spectrometer data for low velocity experiments both in dry (red curves, left column) and in wet (blue curves, right column) conditions. **(a, b)** Evolution of shear stress versus normal stress. Wet experiments show constant normal stress, whereas dry experiments show normal stress oscillations, which are in phase with shear stress oscillations. **(c, d)** No CO_2 emissions were recorded both in dry and wet conditions. **(e, f)** Evolution of cross-correlation (Lag0) coefficient, showing positive to negative cross-correlation coefficient oscillations. This indicates an alternation of in-phase and out-of-phase normal stress and shear stress oscillation probably due to axial column misalignment of friction effects within the gouge.

6.3. Experimental microstructures

Microstructures of gouges from low velocity experiments under both dry and wet conditions are characterized by grain comminution towards the principal slip surface in all cases regardless of the gouge configuration (i.e., layered and mixed; Figs. 9a-d). We observed a similar grain comminution trend within gouges from high velocity experiments, both in dry and in wet conditions (Figs. 9e-h). However, the ~200 µm-thick principal slip zone of gouges from high velocity experiments under dry conditions is characterized by a compact and welded texture (Figs. 9e and 9f). At the nano-scale, this texture is characterized by slip-parallel ~50-nm-thick fibers composed by arrays of 50 nm-thick clumped nanospherules and nanotubes consisting of a mixture of phyllosilicates and calcite (Figs. 9e and 9f). In places, individual nanospherules clump together to form granular zones (Figs. 9e and 9f). These nanostructures are very similar to phyllosilicate nanostructures observed within natural phyllosilicate-bearing layers along the TMF (Fig. 3i). On the contrary, nanospherules or nanotubes are absent in the principal slip zones of gouges from low velocity experiments, both in wet and in dry conditions (Figs. 9a and 9b).

Element distribution maps (i.e., from EDS analyses) show that gouges from low velocity experiments (layered, mixed, calcite gouges) under both dry and wet conditions are characterized by mixed distribution of phyllosilicate and calcite particles (Figs. 9a-d). On the contrary, gouges from high velocity experiments under both dry and wet conditions are characterized by phyllosilicate segregation and concentration along slip-parallel micrometer-thick layers (Figs. 9e-h). These layers consist of calcite clasts scattered within phyllosilicates, with thin clay lamellae wrapping calcite clasts. These layers show microstructures similar to those observed within phyllosilicate-bearing layers along the TMF (Fig. 3h).

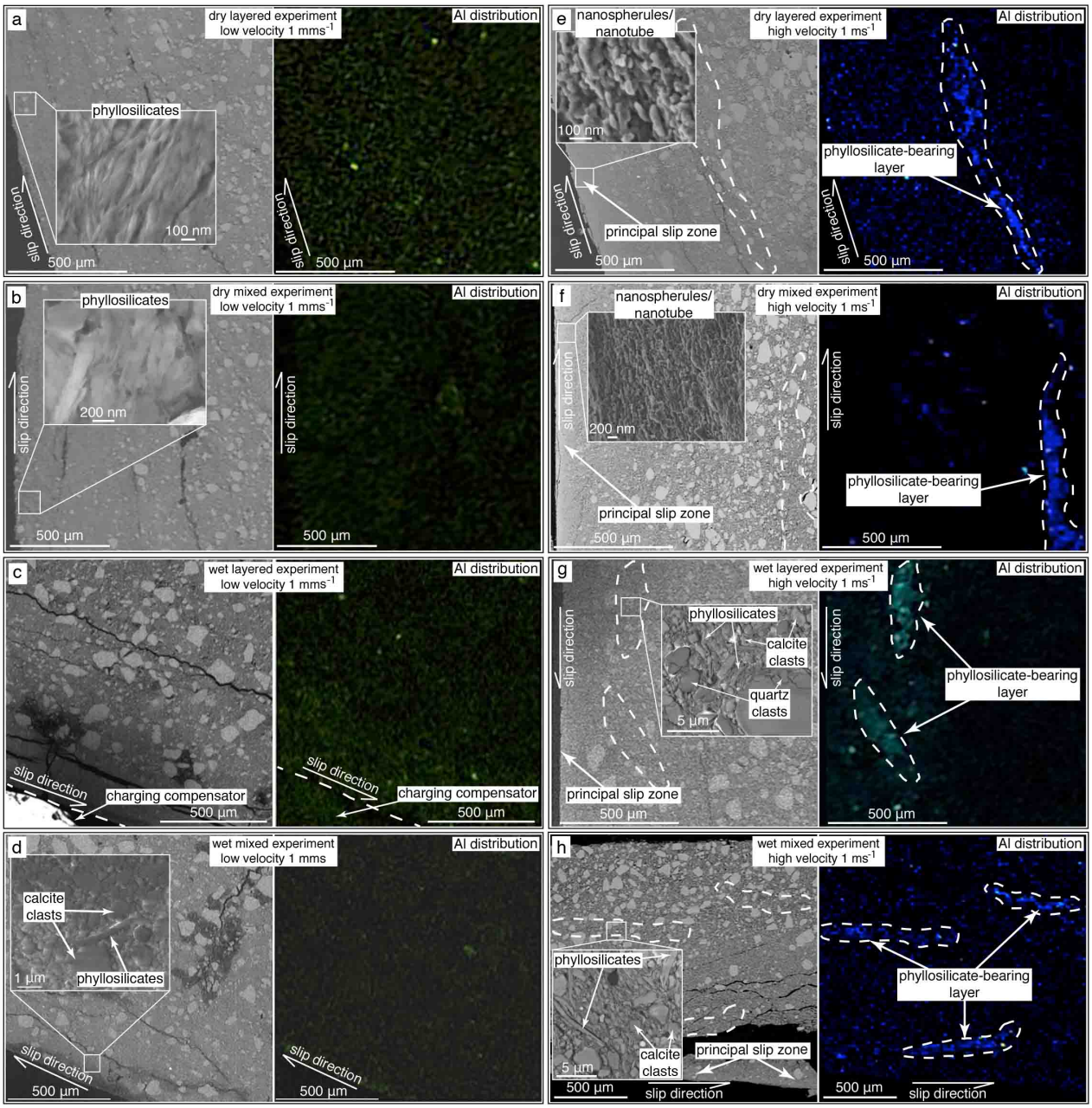


Figure 9. FESEM images (left) and EDS maps (right) of experimental microstructures. **(a-b)** Wet gouges (layered and mixed configurations) sheared at subseismic velocity (0.001 ms^{-1}) showing grain size reduction toward the principal slip zone. EDS maps show no concentration of phyllosilicates along distinct layers. **(c-d)** Dry gouges (layered and mixed configurations) sheared at subseismic velocity (0.001 ms^{-1}) showing grain size reduction toward the principal slip zone. Inset shows a detail of phyllosilicate lamellae chracterized by no nanospherules and nanotubes. Grain comminution is more intense than that observed within wet gouges. EDS maps show no segregation and concentration of phyllosilicates along distinct layers. **(e, f)** Wet gouges (layered and mixed configurations) sheared at seismic velocity (1 ms^{-1}) showing grain size reduction toward the principal slip zone. EDS map show segregation and concentration of phyllosilicates along micrometer-thick layers for both layered and mixed configurations. Insets show calcite clasts within phyllosilicate-bearing layers scattered within phyllosilicates. These microstructures are identical to those observed along the Tre Monti Fault (Fig. 3h). **(g, h)** Dry gouges (layered and mixed configurations) sheared at seismic velocity (1 ms^{-1}) showing grain size reduction toward the principal slip zone. Grain comminution is more intense than that

observed within wet gouges. Inset shows the nanostructures from the principal slip zone both for layered and for mixed configurations. These structures consist of clumped and chained nanospherules and nanotubes similar to those observed within phyllosilicate layers along the TMF (Fig. 3i).

7. Discussion

7.1. Rationale

First, we discuss how our observations and results can contribute to build a model of seismic cycles valid for carbonate/clay-hosted faults. We compare, in particular, our observations with previously-documented fault-related microstructures, which have been interpreted in terms of deformation mechanisms acting during seismic cycles. Second, we discuss some significant implications of our microstructural observations and mechanical data to explain seismological observations.

7.2. Synthetic model of seismic cycles

Co-seismic phase. Fluid-like structures (Figs. 2d-f), truncated clasts (Figs. 3f-g), clay nanospherules and nanotubes (Fig. 3i), and phyllosilicate-rich layers (Figs. 2c, 2f, 3f, and 3g) indicate deformation at high strain-rate and high temperature owing to fast co-seismic slip.

(1) Fluid-like structures (Figs. 2d-f) suggest that both the ultracataclasite and the foliated cataclasite behaved, in part, as a mobile, cohesionless, and fluidized granular material (Fig. 10a). Such fluid structures have been previously documented within the TMF (Smith et al., 2011; Smeraglia et al., 2016a) and in other carbonate-hosted faults (e.g., Fondriest et al., 2012; Demurtas et al., 2016) and are interpreted as the result of fast and instantaneous fluidization of granular materials during co-seismic slip triggered by thermal decomposition of carbonates (e.g., De Paola et al., 2011) or by pressurized fluids trapped or injected within the fault gouge (e.g., Fondriest et al., 2012; Rowe et al., 2012). This inference is consistent with our laboratory simulations showing a negative correlation between normal and shear stress during the weakening phase of high velocity experiments in wet conditions (Fig. 7f, S1, and S2 in Supplementary material). In particular, such

negative correlation can be explained by a fluid (i.e., water) pressure increase. Fluid pressure increase would indeed expand the slipping zone (i.e., due to gouge dilatancy) and exert a spurious force on the load cell, which is installed between the gouge holder and the axial piston (Fig. 6a). The increase in normal stress would result from the contribution of the normal stress applied by the piston, on one side of the load cell, and from the spurious pressure exerted by the pressurization of the gouge, on the other side of the load cell (see discussion in Ferri et al, 2010). However, in our high-velocity experiments, both in dry and in wet conditions, we did not record any gouge dilatancy (Fig. S4 in Supplementary material). This evidence can be explained by the occurrence of a slight gouge extrusion during experiments (i.e., and consequently gouge compaction), thus buffering the gouge dilatancy. The fluid pressure increase contributed to gouge weakening and could be due to impulsive and confined fluid pressurization related to rapid undrained gouge compaction (e.g., Kameda et al., 2010). During high velocity experiments under wet conditions, we did not measure gas emissions. This can be due to water occurrence in wet experiments that limited the temperature rise within a range unsuitable for the generation of thermally-activated processes (e.g., decarbonation).

On the contrary, we recorded CO_2 emissions during high velocity experiments in dry conditions (Figs. 7b). The CO_2 emissions during experiments can be probably related to thermo-chemical processes such as calcite decarbonation (e.g., De Paola et al., 2011) activated at high friction temperatures. However, positive correlation between normal and shear stress during high velocity experiments in dry conditions (Fig. 7d, S1, and S2 in Supplementary material) suggest no pore pressure increase within fault gouge. This is consistent with CO_2 detection externally from the gouge holder, which indicates that CO_2 was able to scape from the gouge and dissipates its overpressure (if any).

(2) truncated clasts along ultra-thin phyllosilicate-bearing layer margins (Figs. 3f and 3g) are symptomatic of high strain-rate and fast (i.e., co-seismic) slip localization along layer margins (Fig. 10a). In particular, truncated clasts are observed along carbonate-hosted mirror-like fault surfaces

and are observed along sharp slip surfaces only during experiments conducted at seismic slip rates (~1 ms^{-1}; Fondriest et al., 2013).

(3) phyllosilicate-bearing layers formed only during high velocity experiments (i.e., at co-seismic slip rates, 1 ms^{-1}) under both dry and wet conditions (Figs. 9e-h).

(4) nanospherules and nanotubes developed only during high velocity experiments under dry conditions (Figs. 9e-f) and are lacking within the principal slip zone of low velocity experiments (i.e., almost subseismic slip rate; Figs. 9a-d). Such nanospherules and nanotubes are similar to phyllosilicates nanostructures along the TMF (Fig. 3i). In particular, nanospherules and nanotubes in the phyllosilicate-bearing layers along the TMF (Figs. 3i and S5a in Supplementary material) are similar to those observed within phyllosilicate-bearing gouges after experimental deformation at seismic slip velocities (≥ 1 ms^{-1}) after high temperature rise (~250-570 °C, Ujiie et al., 2011; Fig. S5b in Supplementary material) and to those observed within other natural phyllosilicate-rich faults (Fig. S5c in Supplementary material). In addition, nanospherules and nanotubes are similar to those observed within phyllosilicates affected by hydrothermal processes (at ~200-250 °C, Fig. S5d and S5e in Supplementary material). On the contrary, the phyllosilicate nanospherules and nanotubes differ markedly from the typical nanostructures of detrital phyllosilicates (Fig. S5f in Supplementary material). This evidence suggests that the observed nanospherules and nanotubes within the TMF probably developed at high temperatures associated with co-seismic slip propagation along the phyllosilicate-bearing layers.

In addition to the above-mentioned evidence, we also point out that in-situ ^{36}Cl exposure dating over the TMF fault scarp showed the probable occurrence of seismic events along this fault (Benedetti et al., 2013).

Post-seismic/interseismic phases. Teeth-shaped clasts margins (Figs. 3b-e), clumped clasts (Figs. 3d and 3e), foliation planes (Fig. 3c), and mantled clasts (Fig. 3c) imply deformation at low strain-rate owing to slow (e.g., aseismic) deformation during the post-seismic/interseismic phases (Fig. 10b).

(1) Teeth-shaped clast margins are identical to those produced by intergranular pressure solution of carbonate grains during slow compaction experiments performed in the 30°-150°C temperature range and 20-47 MPa effective stress range (Zhang et al., 2010). Moreover, intergranular pressure solution has been widely documented within carbonate-hosted faults exhumed from depths < 4 km (e.g., Billi, 2003). These temperature-depth constraints are identical to those inferred during tectonic deformation along the TMF before exhumation (Smeraglia et al., 2016). In addition, pressure-solution processes can be enhanced by the occurrence of phyllosilicates between indented clasts (e.g., Renard et al., 2001), as observed between teeth-shaped clast margins within the ultra-fine matrix of the ultracataclasite (Fig. 3e).

(2) We propose that foliated cataclasite (Fig. 3a) and foliation planes within the ultracataclasite (Fig. 3c) were generated through slow and continuous (i.e., aseismic) deformation along the TMF during postseismic/interseismic phases (Fig. 10b). Slow and continuous deformation is also consistent with mantled structures of calcite clasts (Fig. 3e), which are similar to those observed in mylonitic rocks deformed at low strain-rate within the lower crust (e.g., Passchier and Trouw, 2005). This inference is consistent with geological evidence and laboratory investigations showing that foliated fault rocks typically develop along faults through slow and stable slip (e.g., Tesei et al., 2014). However, recent experimental investigations showed that foliated carbonate fault rocks could form also at seismic slip rates (Smith et al., 2016). In this case foliation planes are often associated with sharp slip surfaces (Smith et al., 2016). However, in our case, the occurrence of indented teeth-shaped margins within clasts of the foliation planes (Fig. 3c) and the lack of any sharp slip surface along or near the foliation planes (Fig. 3c) suggests a slow (i.e., aseismic) and continuous deformation along foliation planes.

(3) Reworked clumped clasts (i.e., derived by clasts aggregation and compaction through pressure solution; Figs. 3d and 3e) and teeth-shaped margins of such clasts within both the ultracataclasite and phyllosicate-bearing layers suggest multiple seismic cycles with several events

of compaction (i.e., pressure solution during both the postseismic/interseismic phases) clasts reworking (during the co-seismic phase), and then re-compaction.

Evidence of multiple deformation events is also visible for co-seismic structures. In fact, phyllosilicate-bearing layers cutting through fluidized structures (Fig. 2f) indicate multiple events of fluidization and slip localization affecting, in alternating moments, different patches of the principal faults during different seismic cycles.

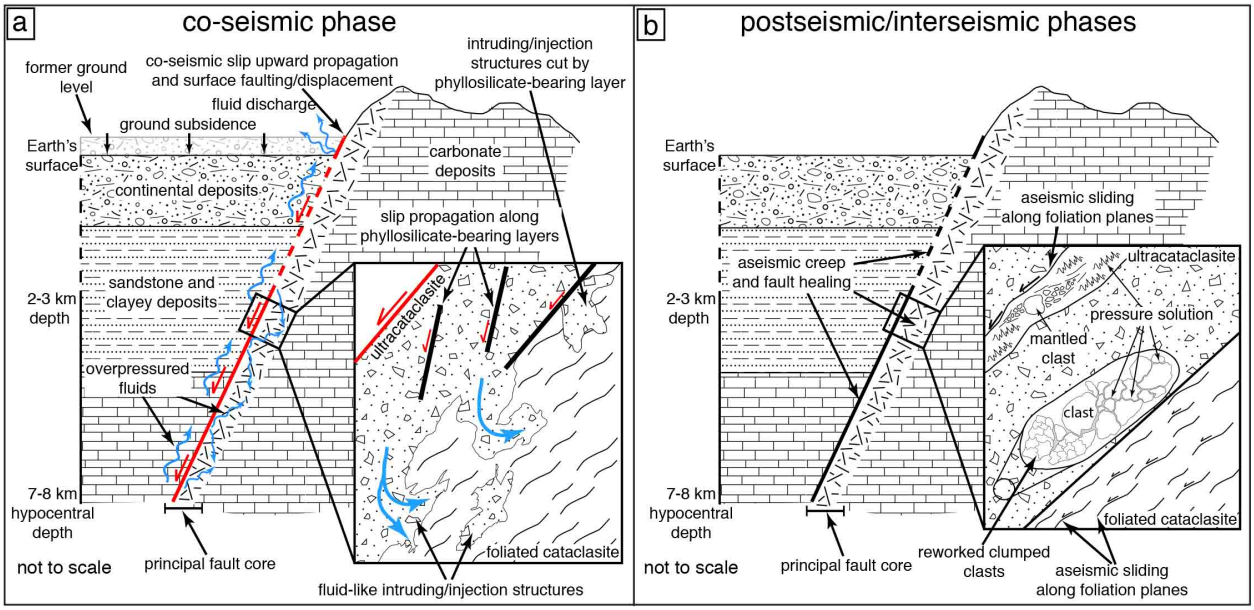


Figure 10. Synthetic model for the seismic cycle within carbonate/clay hosted principal fault cores in the brittle upper crust (depths < 2-3 km). **(a)** During the co-seismic phase, earthquake-related slip is facilitated along phyllosilicate-bearing layers, which can promote co-seismic clip propagation up to the Earth's surface, possibly enhancing surface faulting. Fault weakening can also be assisted by fluid overpressure as testified by fluid-like fault rock structures. **(b)** During the interseismic phase, slow deformation processes are accommodated by clay-assisted pressure-solution mechanisms (i.e., promoting fault healing and re-strengthening) and frictional sliding along foliation planes (i.e., promoting aseismic creep).

7.3 Implications

Our microstructural observations and mechanical data can explain the following seismological observations.

(1) The occurrence of fluid overpressures along faults during earthquakes (e.g., Terakawa et al., 2010) is consistent with fluidized fault rock textures preserved along the TMF (Fig. 2d-e), testifying for episodic and impulsive fault rock fluidization during co-seismic slip (Fig. 10a).

(2) We suggest that slow and continuous deformation along foliation planes (Figs. 3a and 3c) and mantled clasts (Fig. 3c) can promote aseismic creep and tectonic stress relaxation (Fig. 10b). On the contrary, we suggest that intergranular pressure solution, as observed within the ultracataclasite (Fig. 3b-e), can promote fault healing and strength recovery, which is responsible for fault locking and tectonic elastic strain energy accumulation (Fig. 10b). These features are consistent with seismological and geodetic observations, suggesting that active faults can move slowly (i.e., dissipating elastic strain energy) through aseismic creep during the interseismic/postseismic phase or can be locked (i.e., storing elastic strain energy) between two earthquakes (e.g., Johanson and Burgman, 2005; Wilkinson et al., 2010). Both locked and creeping portions can be present along the same fault segment (e.g., Johanson and Burgman, 2005; Tong et al., 2013). We explain this fault behavior as the result of the interplay between frictional sliding and intergranular pressure solution occurring along the same fault segment, as also observed along the TMF (Figs. 3a-e).

(3) High-velocity laboratory experiments on phyllosilicate-rich gouges (down to 10 wt.% of phyllosilicate content) show that phyllosilicates facilitate earthquake-slip propagation (e.g., Bullock et al., 2015). In addition, our experimental results show that even ultra-low clay content ($\leq$ 3 wt.%) localized in ultra-thin layers within carbonate-hosted gouges is sufficient to facilitate co-seismic slip propagation through the shallow part of fault zones (depths < 0.5 km; Figs. 6d-e, and 10b). The segregation and concentration of clay into newly-formed phyllosilicate-bearing layers (Figs. 9e-h) during co-seismic slip can promote further weakening during future earthquakes along the

previously formed phyllosilicate-bearing layers. This inference is consistent with paleoseismological and direct observations showing that moderate to large earthquakes can propagate up to the Earth's surface causing surface faulting (e.g., Galli et al., 2008; Anzidei and Pondrelli, 2016).

(4) Seismological observations and numerical modeling showed that earthquake-slip and displacement are heterogeneously distributed along fault planes during earthquakes and are affected by fault structural complexity and mechanical properties of fault rocks (e.g., Peltzer et al., 1999; Gudmundsson, 2004; Anzidei and Pondrelli, 2016; Milliner et al., 2016). In this work, we show that the occurrence of ultra-low clay content (~5 wt.%), as observed within ultra-thin phyllosilicate-bearing layers, is sufficient to strongly reduce the fault rock stiffness down to nanoscale, where we measured indentation moduli (i.e., Young's modulus) of comminuted calcite clasts (49±8 GPa), phyllosilicates (7±3 GPa), and of the whole phyllosilicate-rich layers (28 GPa) as far lower than Young's modulus of the carbonate host rock (80±5 GPa). We suggest that the different indentation moduli of calcite clasts and intact calcite host rock can be due to the development of very comminuted clasts characterized by microfractures and junctions between clumped clasts (Figs. 3d, 3e, and 3h). This inference is consistent with measurements on macroscopic samples of brecciated and fractured fault rocks, which are characterized by Young's moduli smaller than those of intact host rocks (e.g., Agosta et al., 2007; Kahraman and Alber, 2008). Although we are aware that our data have been collected in the absence of a confining pressure, we show that the bulk fault rock stiffness at the nanoscale can be as low as ~28 GPa, which is far lower than ~60-80 GPa previously measured from macroscopic samples of carbonate cataclastic rocks at only ~5 MPa of confining pressure (e.g., Agosta et al., 2007). Therefore, we suggest that microdeformation mechanisms (i.e., fast slip localization, thermally-activated weakening mechanisms, pressure-solution, and others) acting along fault cores during the seismic cycle are affected by fault rock stiffness at the nanoscale. Accordingly, we suggest that strong stiffness heterogeneity occurring down to the nanoscale along faults (i.e., due to different fault rocks mineralogy; Figs. 4 and 5) is one of the factors (i.e.,

including stress drop, fault geometry, fluid pressure, and so on) that can influence earthquake-slip and displacement heterogeneities along faults as observed through seismological techniques (e.g., Milliner et al., 2016). Our inference is consistent with numerical modeling showing that, at the microscale, a network of weak shear zones can strongly reduce the bulk fault rock strength, thus influencing fault rheology and seismic-mechanical behaviors (Gerbi et al., 2016).

8. Conclusions

The study of the carbonate/clay-hosted Tre Monti Fault, exhumed from depths < 3 km, allowed us to:

(1) document microstructures developed during different stages of the seismic cycle. In particular, fluidized fault rocks, truncated calcite clasts, and ultra-thin phyllosilicate-bearing layers are interpreted as the result of co-seismic deformation. On the contrary, clay assisted intergranular pressure solution and foliation planes are interpreted as the result of slow compaction processes and aseismic sliding, respectively, during postseismic/interseismic phases;

(2) link microstructures and micromechanical properties to seismological observations. In particular, fluidized fault rocks are consistent with seismologically inferred fluid overpressure along faults. We propose that ultra-low clay content (≤ 3 wt.%) localized along ultra-thin layers could alone facilitate earthquake slip up to the Earth's surface possibly enhancing surface displacement as observed by both direct and paleoseismological studies. Clay assisted intergranular pressure solution and foliation planes can explain fault healing and re-strengthening (i.e., fault locking and tectonic stresses increase) and aseismic sliding (i.e., tectonic stresses dissipation), respectively;

(3) constrain micromechanical fault rock properties. In particular, strong rheological contrasts, at the nanoscale, due to the occurrence of even ultra-low phyllosilicate content (~5 wt.%) within fault rocks, can influence microdeformation mechanisms and hence seismic behavior of faults, possibly affecting both earthquake-slip and deformation mechanism distributions.

In summary, multidisciplinary studies, such as this one, can improve the knowledge of the mechanical behavior of faults during the seismic cycle and explain some seismological and geodetic observations, thus advancing the geoscientists' predictive capability of seismic cycles and earthquakes mechanics.

9. References

Agosta, F., M. Prasad, and A. Aydin (2007), Physical properties of carbonate fault rocks, fucino basin (Central Italy): implications for fault seal in platform carbonates, *Geofluids*, 7, 19-32.

Anzidei, M., and S. Pondrelli (Eds.), (2016), The Amatrice seismic sequence: preliminary data and results, *Annals of Geophysics*, 59.

Balsamo, F., L. Aldega, N. De Paola, I. Faoro, and F. Storti (2014), The signature and mechanics of earthquake ruptures along shallow creeping faults in poorly lithified sediments, *Geology,* 42, 435–438. doi:10.1130/G35272.1.

Benedetti, L., I. Manighetti, Y. Gaudemer, R. Finkel, J. Malavieille, K. Pou, M. Arnold, D. Aumaître, G. Bourlès, and K. Keddadouche (2013), Earthquake synchrony and clustering on Fucino faults (central Italy) as revealed from in situ ^{36}Cl exposure dating, *J. Geophys. Res. Solid Earth*, 118, 4948–4974. doi:10.1002/jgrb.50299.

Ben-Zion, Y., and C. G. Sammis (2013), Shear heating during distributed fracturing and pulverization of rocks, *Geology*, 41, 139-142.

Billi, A. (2003), Solution slip and separations on strike-slip fault zones: theory and application to the Mattinata Fault, Italy, *J. Struct. Geol.*, 25, 703-715.

Billi, A., M. M. Tiberti, G. P. Cavinato, D. Cosentino, E. Di Luzio, J. V. A. Keller, C. Kluth, L. Orlando, M. Parotto, A. Praturlon, M. Romanelli, F. Storti, and N. Wardell (2006), First results from the CROP-11 deep seismic profile, central Apennines, Italy: evidence of mid-crustal folding, *J. Geol. Soc. London*., 163, 583–586. doi:10.1144/0016-764920-002.

Bullock, R.J., N. De Paola, and R.E. Holdsworth (2015), An experimental investigation into the role of phyllosilicate content on earthquake propagation during seismic slip in carbonate faults, *J. Geophys. Res.*, 120, 3187–3207. doi:10.1002/2015JB011914.

Burchfield, B.C., L.H. Royden, R.D. van der Hilst, and B.H. Heger (2008), A geological and geophysical context for the Wenchuan earthquake of 12 May 2008, Sichuan, People's Republic of China, *Geol. Soc. Am.*, 18, 4-11.

Cavinato, G.P., C. Carusi, M. Dall'asta, E. Miccadei, and T. Piacentini (2002), Sedimentary and tectonic evolution of Plio-Pleistocene alluvial and lacustrine deposits of Fucino Basin (central Italy), *Sediment. Geol.*, 148, 29–59. doi:10.1016/S0037-0738(01)00209-3.

Collettini, C., B.M. Carpenter, C. Viti, F. Cruciani, S. Mollo, T. Tesei, F. Trippetta, L. Valoroso, and L. Chiaraluce (2014), Fault structure and slip localization in carbonate-bearing normal faults: An example from the Northern Apennines of Italy, *J. Struct. Geol.*, 67, 154-166, doi: 10.1016/j.jsg.2014.07.017.

Cosentino, D., P. Cipollari, P. Marsili, and D. Scrocca (2010), Geology of the central Apennines; a regional review, *J. Virtual Explor.*, 36. http://dx.doi.org/10.3809/jvirtex.2010.00223.

De Paola, N., N. Hirose, T. Mitchell, G. Di Toro, C. Viti, and T. Shimamoto (2011), Fault lubrication and earthquake propagation in thermally unstable rocks, *Geology*, 39, 35–38, doi: 10.1130/G31398.1.

Demurtas, M., M. Fondriest, F. Balsamo, L. Clemenzi, F. Storti, A. Bistacchi, and G. Di Toro (2016), Structure of a normal seismogenic fault zone in carbonates: The Vado di Corno Fault, Campo Imperatore, Central Apennines (Italy), *J. Struct. Geol.*, 90, 185-206, doi: org/10.1016/j.jsg.2016.08.004.

Dieterich, J. (1994), A constitutive law for rate of earthquake production and its application to earthquake clustering, *J. Geophys. Res.*, 99, 2601-2618.

Di Toro, G., A. Niemeijer, A. Tripoli, S. Nielsen, F. Di Felice, P. Scarlato, G. Spada, R. Alessandroni, G. Romeo, G. Di Stefano, S. Smith, E.

Spagnuolo, and S. Marisano (2010), From field geology to earthquake simulation: a new state-of-the-art tool to investigate rock friction during the seismic cycle (SHIVA), *Rendiconti dei Lincei*, 21, 95-114, doi:10.1007/s12210-010-0097-x.

Doglioni, C. (1991), A proposal of kinematic modelling for W-dipping subductions - Possible applications to the Tyrrhenian - Apennines system, *Terra Nova*, 3/4, 423–434.

Ferri, F., G. Di Toro, T. Hirose, and T. Shimamoto (2010), Evidence of thermal pressurization in high-velocity friction experiments on smectite-rich gouges, *Terra Nova*, 22, 347-353.

Fiore, S., F. J. Huertas, F. Huertas, and J. Linares (1995), Morphology of kaolinite crystals synthesized under hydrothermal conditions, *Clays and Clay Minerals*, 43, 353-360.

Fondriest, M., S. A. F. Smith, G. Di Toro, D. Zampieri, S. Mittempergher (2012), Fault zone structure and seismic slip localization in dolostones, an example from the Southern Alps, Italy, *J. Struct. Geol*., 45, 52–67. doi:10.1016/j.jsg.2012.06.014.

Fondriest, M., S. A. F. Smith, T. Candela, S. B. Nielsen, K. Mair, and G. Di Toro (2013), Mirror-like faults and power dissipation during earthquakes, *Geology*, 41, 1175–1178. doi:10.1130/G34641.1.

Galli, P., F. Galadini, and D. Pantosti (2008), Twenty years of paleoseismology in Italy, *Earth-Science Rev.*, 88, 89–117. doi:10.1016/j.earscirev.2008.01.001.

Gerbi, C., S. E. Johnson, D. Shulman, and K. Klepeis (2016), Influence of microscale weak zones on bulk strength, *Geoch. Geophys. Geosys.,* doi:10.1002/2016GC006551.

Gratier, J.P., J. Richard, F. Renard, S., Mittempergher, M.L. Doan, G. Di Toro, J. Hadizadeh, and A.M. Boullier (2011), Aseismic sliding of active faults by pressure solution creep: Evidence from the San Andreas Fault Observatory at Depth, *Geology*, 39, 1131-1134, doi:10.1130/G32073.

Gudmundsson, A. (2004), Effects of Young's modulus on fault displacement, *C. R. Geoscience*, 336, 85-92, doi:10.1016/j.crte.2003.09.018.

Hadizadeh, J., S. Mittempergher, J.P. Gratier, F. Renard, G. Di Toro, J. Richard, and H.A. Babaie (2012), A microstructural study of fault rocks from the SAFOD: implications for the deformation mechanisms and strength of the creeping segment of the San Andreas Fault, *J. Struct. Geol.*, 42, 246–260, doi:org/10.1016/j.jsg.2012.01.011.

Hainzl, S., G.B. Brietzke, and G. Zöller (2010), Quantitative earthquake forecasts resulting from static stress triggering, *J. Geophys. Res.*, 115, B11311, doi:10.1029/2010JB007473.

Hearn, E.H., and W.R. Thatcher (2015) Reconciling viscoelastic models of postseismic and interseismic deformation: Effects of viscous shear zones and finite length ruptures, *J. Geophys. Res.*, 120, 2794-2819, doi:10.1002/2014JB011361.

Johanson, I.A., and R. Bürgmann (2005), Creep and quakes on the northern transition zone of the San Andreas fault from GPS and InSAR data, *Geophys. Res. Lett.*, 32, L14306, doi:10.1029/2005GL023150.

Kahraman, S., and M. Alber (2008), Triaxial strength of a fault breccia of weak rocks in a strong matrix, *Bulletin of engineering geology and the environment*, 67, 435-441.

Kameda, J., Y. Yamamoto, and G. Kimura (2010), Smectite swelling in the Miura–Boso accretionary prism: Possible cause for incipient décollement zone formation, *Tectonophysics*, 494, 75-84.

Laurich, B., J. Urai, G. Desbois, C. Vollmer, and C. Nussbaum (2014), Microstructural evolution of an incipient fault zone in Opalinus Clay: Insights from an optical and electron microscopic study of ion-beam polished samples from the Main Fault in the Mt-Terri Underground Research Laboratory, *J. Struct. Geol.*, 67, 107-128.

Li, Q., T.E. Tullis, D. Goldsby, and R.W. Carpick (2011), Frictional ageing from interfacial bonding and the origins of rate and state friction, *Nature*, 480, 233-236, doi: 10.1038/nature10589.

Milliner, C. W. D., C. Sammis, A. A. Allam, J. F. Dolan, J. Hollingsworth, S. Leprince, and F. Ayoub, (2016), Resolving fine-scale heterogeneity of co-seismic slip and the relation to fault structure, *Scientific reports*, *6*, 27201.

Morewood, N. C., and G. P. Roberts (2000), The geometry, kinematics and rates of deformation within an en echelon normal fault segment boundary, central Italy, *J. Struct. Geol*., 22, 1027–1047. doi:10.1016/S0191-8141(00)00030-4.

Passchier, C.W., and R. A. J. Trouw (2005), Microtectonics. Springer.

Passeri, D., M. Rossi, J.J. Vlassak (2013), On the tip calibration for accurate modulus measurement by contact resonance atomic force microscopy,

Ultramicroscopy, 128, 32-41, doi: org/10.1016/j.ultramic.2013.02.003.

Peltzer, G., F. Crampé, and G. King (1999), Evidence of nonlinear elasticity of the crust from the M_w7.6 Manyi (Tibet) earthquake, *Science*, 286, 272-276.

Prasad, M., M. Kopycinska, U. Rabe, W. Arnold (2002), Measurement of Young's modulus of clay minerals using atomic force acoustic microscopy, *Geophys. Res. Lett.*, 29, 131-134, doi: 10.1029/2001GL014054.

Renard, F., D. Dysthe, J. Feder, K. Bjørlikke, and B. Jamtveit (2001), Enhanced pressure solution creep rates induced by clay particles: experimental evidence in salt aggregates, *Geophys. Res. Lett.*, 28, 1295-1298, doi: 10.1029/2000GL012394.

Setti, M., L. Marinoni, and A. Lopez-Galindo (2009), Clay mineral assemblage as indicator of hydrothermalism in the basal part of the CP-3 core (Victoria Land Basin, Antartica), *Clay Minerals*, 44, 389-404.

Smeraglia, L., F. Berra, A. Billi, C. Boschi, E. Carminati, and C. Doglioni (2016a), Origin and role of fluids involved in the seismic cycle of extensional faults in carbonate rocks, E*arth Planet. Sci. Lett.*, 450, 292-305, doi: 10.1016/j.epsl.2016.06.042.

Smeraglia, L., L. Aldega, A. Billi, C. Carminati, and C. Doglioni (2016b), Phyllosilicate injection along extensional carbonate-hosted faults and implications for co-seismic slip propagation: Case studies from the central Apennines, Italy, *J. Struct. Geol.*, 93, 29-50, doi: 10.1016/j.jsg.2016.10.003.

Smith, S. A. F., A. Billi, G. Di Toro, and R. Spiess (2011), Microstructures of Principal Slip Zones in Limestones, and Implications for the Seismic Cycle (Tre Monti fault, central Appennines, Italy), *Pure and App. Geophys.*, 168, 2365-2393, doi: 10.1007/s00024-011-0301-7.

Smith, S. A. F., S. Nielsen, G. Di Toro (2015), Strain localization and the onset of dynamic weakening in calcite fault gouge, *Earth and Plan. Sci. Lett.*, 413, 25-36.

Smith, S. A. F., J. Griffiths, M. Fondriest, G. Di Toro, and M. Demurtas (2016), "Coseismic foliations" in gouge and cataclasite: experimental observations and consequences for interpreting the fault rock record, Paper presented at EGU General Assembly Conference, Vienna, Abstract 18, 2531.

Solum, J. G., S. H. Hickman, D. A. Lockner, D. E. Moore, B. A. van der Pluijm, A. M. Schleicher, and J. P. Evans (2006), Mineralogical characterization of protolith and fault rocks from the SAFOD main hole, *Geophys. Res. Lett.*, 33, L21314, doi:10.1029/2006GL027285.

Terakawa, T., A. Zoporowski, B. Galvan, and S. A. Miller (2010), High-pressure fluid at hypocentral depths in the L'Aquila region inferred from earthquake focal mechanisms, *Geology*, 38, 995-998.

Tesei, T., C. Collettini, M. R. Barchi, B. M. Carpenter, and G. Di Stefano (2014), Heterogeneous strength and fault zone complexity of carbonate-bearing thrusts with possible implications for seismicity, *Earth Planet. Sci. Lett.*, 408, 307–318. Doi:10.1016/j.epsl.2014.10.021.

Tong, X., D. T. Sandwell, and B. Smith-Konter (2013), High-resolution interseismic velocity data along the San Andreas fault from GPS and InSAR, *J. Geophys. Res.*, 118, 369-389, doi: 10.1029/2012JB009442.

Ujiie, K., A. Tsutsumi, and J. Kameda (2011), Reproduction of thermal pressurization and fluidization of clay-rich fault gouges by high-velocity friction experiments and implications for seismic slip in natural faults, *Geol. Soc. London, Spec. Publ.*, 359, 267–285. doi:10.1144/SP359.15.

Valoroso, L., L. Chiaraluce, D. Piccinini, R. Di Stefano, D. Schaff, and F. Waldhauser (2013), Radiography of a normal fault system by 64,000 high-precision earthquake locations: The 2009 L'Aquila (central Italy) case study, *J. Geophys. Res.*, 118, 1156–1176. doi:10.1002/jgrb.50130.

Wilkinson, M., K. J. W. McCaffrey, G. P. Roberts, P. A. Cowie, R. J. Phillips, A. M. Michetti, E. Vittori, L. Guerrieri, A.M. Blumetti, A. Bubeck, A. Yates, and G. Sileo (2010), Partitioned postseismic deformation associated with the 2009 Mw 6.3 L'Aquila earthquake surface rupture measured using a terrestrial laser scanner, *Geophys. Res. Lett.*, 37, 10, doi: 10.1029/2010GL043099.

Zhang, X., C. J. Spiers, C. J. Peach (2010), Compaction creep of wet granular calcite by pressure solution at 28°C to 150°C, *J. Geophys. Res.*, 115, B09217, doi: 10.1029/2008JB005853.

10. Supplementary materials

Appendix A: In situ elastic property measurements

We performed elastic property measurements at the nanometer scale using a Contact Resonance Atomic Force Microscopy setup (CR-AFM, Solver, NT-MDT, made in Russia; Passeri et al., 2013) equipped with a commercial Si cantilever (CSG10, NT-MDT, made in Russia). A piezoelectric transducer replaced the sample holder in order to excite out-of-plane oscillations, at ultrasonic frequencies. The relative position (r) of the tip on the cantilever (i.e., $r = L_1/L$, where L_1 is the tip position and L is the cantilever length) defines the modes in which the cantilever tip can be in contact with the sample. We carried out measurements collecting the resonance frequencies and the quality factors for two contact modes (f_1 and Q_1 and f_2 and Q_2), after determining their corresponding free values in air both for the first mode (f^0_1 = 27.2 kHz and Q^0_1 = 150) and for the second mode (f^0_2 = 181.1 kHz and Q^0_2 = 180). All experiments were conducted at room conditions.

We performed the CR-AFM measurements on a ~30 μm thick thin section cut through the phyllosilicate-rich layer (Fig. 3h). In this setup, we set an area of the sample under the CR-AFM tip into oscillation through a piezoelectric transducer. The tip-sample contact can be described as a spring with the elastic constant represented by the contact stiffness (k), which determines the first and the second contact resonance frequencies (f_1 and f_2) and the corresponding quality factors (Q_1 and Q_2) of the system. The $f_{1\text{-}2}$ and the $Q_{1\text{-}2}$ are used to characterize the mechanical properties of the sample. In particular, assuming the sample perfectly elastic, we used the contact stiffness (k) values to determine the sample indentation modulus (M), which can be treated as the sample Young's modulus, after calibration of the CR-AFM measurements with two reference materials with known indentation modulus (Passeri et al., 2013). M is defined as $E/(1-\nu^2)$, where E is the Young's modulus and ν the Poisson ratio. As reference, we used the indentation modulus of highly oriented pyrolytic graphite (HOPG, M = 20 GPa) and of carbonate host rock (M =

89±7 GPa) sampled away from the TMF to calibrate phyllosilicates and carbonate fault rocks, respectively. We determined M of the carbonate host rock calculating Young's modulus (E=80±5 GPa) and Poisson ratio (ν=0.32±0.3) by measuring P-Wave and S-Wave velocity through a pulse-echo ultrasonic technique (see Appendix B). On the contrary, in the case of a viscoelastic sample, the elastic modulus consists of a real part (E', storage modulus) and of an imaginary part (E'', loss modulus). Using CR-AFM measurements, we determined the E''/E' ratio, namely the loss tangent (tanδ), without any calibration procedure. Assuming E'=M, we determined E'' as M*tanδ.

Appendix B: Pulse-echo ultrasonic measurements

A pulse-echo ultrasonic technique has been exploited for measuring both the longitudinal and the shear wave velocity in the samples. An ultrasonic pulser/receiver (Panametrics Model 500 PR) has been used to generate ultrasonic pulses through a 7.5 MHz longitudinal wave transducer (Panametrics V320) and 2.25 MHz shear wave transducer (Panametrics V154). The longitudinal wave velocity (Vl) and shear wave velocity (Vs) have been determined measuring the time of flight of ultrasonic pulses. The longitudinal wave velocity (Vl) and shear wave velocity (Vs) are 6,570 ± 25 m/s and 3,365 ± 40 m/s, respectively. Consequently, using the measurement of longitudinal and shear wave velocities, the Young's modulus and the Poisson's ratio are E = 80 ± 5 GPa and ν = 0.32 ± 0.03, respectively.

Appendix C: Rotary shear experiments

The SHIVA apparatus (Di Toro et al., 2010) has a horizontal rotary column on one side, the sample holder in the middle, and the axial column/loading system at the other side. Rotary shear is provided to the axial column by two engines. We used a sample holder designed for incohesive materials (gouge) confinement (Smith et al., 2015). The sample holder consists of a base plate and inner and outer rings (35/55 mm internal/external diameter) and of a set of springs

designed to discharge the metal rings of the full applied normal load. This assembly prevents gouge extrusion from sample holder during the experiments. Moreover, we isolated the gouge holder from the external environment through glass windows and, within this sample chamber, we measured gas emission with a Pfeiffer Quadstar quadrupole mass spectrometer. The detector (capillar) was placed 1 cm far from the sheared surface consequently the mass spectrometer data are affected by a temporal delay due to the flight time and the measurement time. Results are given in terms of percentage counts relative to the ambient amount. To quantitatively constrain the behavior of shear and normal stress, we performed a zero-lag cross-correlation (at zero time dephasing with a control window which depends on the recording rate) analysis comparing the normal and shear stress curves. If normal stress increases together with shear stress (i.e., the two signals vary in-phase), the result is a positive correlation (> 0; i.e., the two signals behave in the same manner). On the contrary, if normal stress increases and shear stress decreases at the same time (i.e., the two signals are out-of-phase), the result is a negative correlation (< 0; i.e., the two signals behave in the opposite manner).

Lithology	Quartz (%)	K-feldspar (%)	Plagioclase (%)	Dolomite (%)	Calcite (%)	Clay minerals (%)
Ultracataclasite	0	0	0	0	98.5	1.5
Phyllosilicate-rich layers (ultracataclasite)	3	0	0	0	92	5
Cataclasite	0	0	0	0	100	0
Syn-orogenic deposit (Hemipelagic marls)	26	0	0	5	24	45
Syn-orogenic deposit (Siliciclastic sandstones)	31	3	13	11	12	30

Table S1. Powder X-ray diffraction (XRPD) mineralogical composition of natural fault rocks and tested materials. The ultracataclasite consists of calcite (98.5% wt.) and clay minerals (1.5% wt.). Phyllosilicate-bearing layers consist of calcite (93% wt.), quartz (2% wt.), and clay minerals (5% wt.). The foliated cataclasite consists solely of calcite (100% wt.). Siliciclastic sandstones (Syn-orogenic deposits) consist of quartz (24%), k-feldspar (3%), plagioclase (11%), dolomite (11%), calcite (16%), pyrite (1%), muscovite/illite (21%), chlorite (9%), serpentine (3%), and non quantifiable low amount of smectite and kaolinite. Hemipelagic marls (Syn-orogenic deposits) consist of of quartz (16%), plagioclase (5%), dolomite (3%), calcite (32%), Mg-calcite (21%), muscovite/illite (12%), chlorite (4%), kaolinite (3%), serpentine (4%), and non quantifiable low amount of smectite.

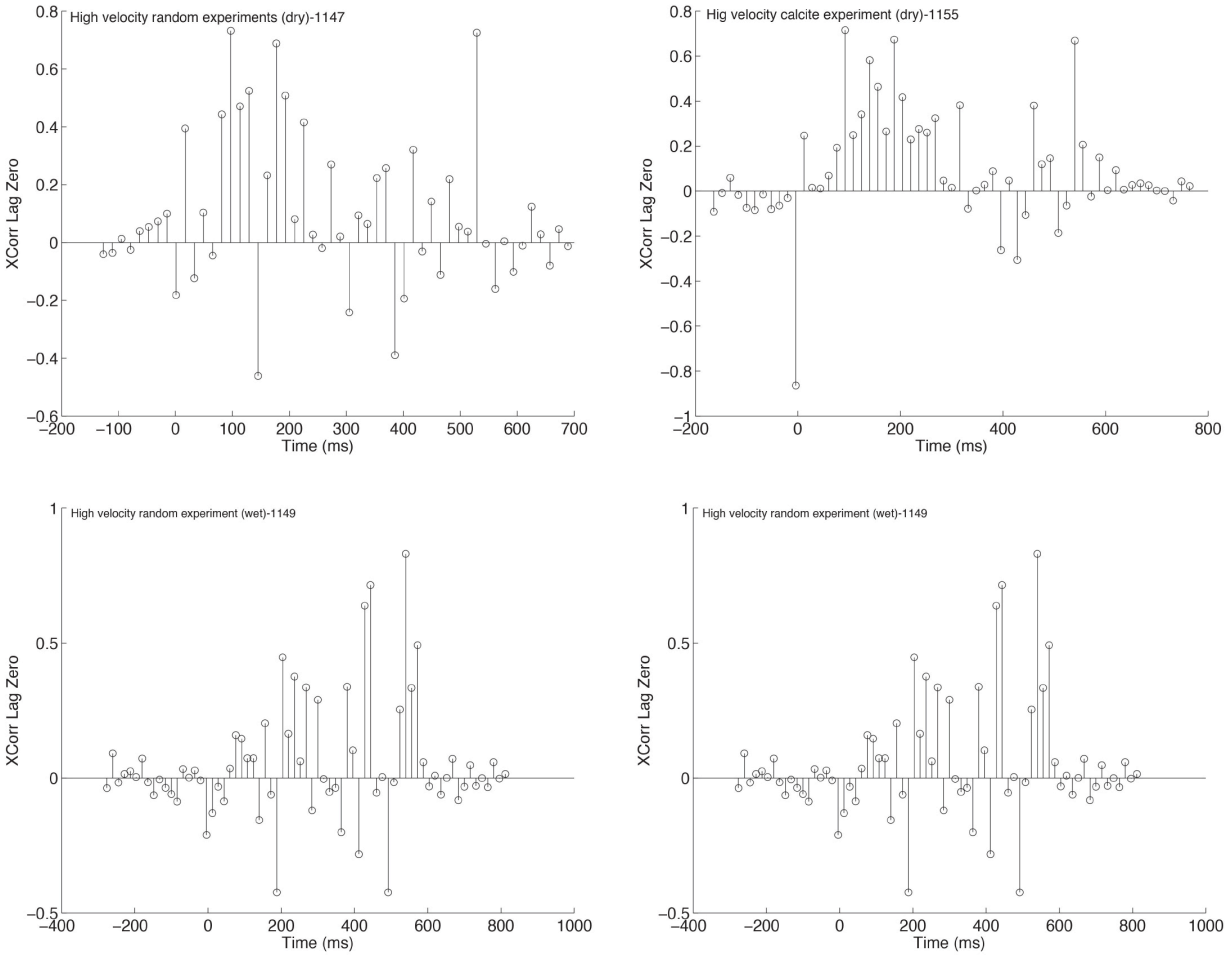


Figure S1. Evolution of cross-correlation (Lag0) coefficient during high velocity experiments both in dry (upper raw) and wet (lower raw) conditions. High velocity dry experiments show a positive correlation roughly during all the experiments indicating an in-phase oscillation between normal and shear stress. On the contrary, high velocity wet experiments show a negative correlation roughly during the central part of the experiment (i.e., the weakening phase) indicating an increase of normal stress during a decrease in shear stress (i.e., out of phase oscillation).

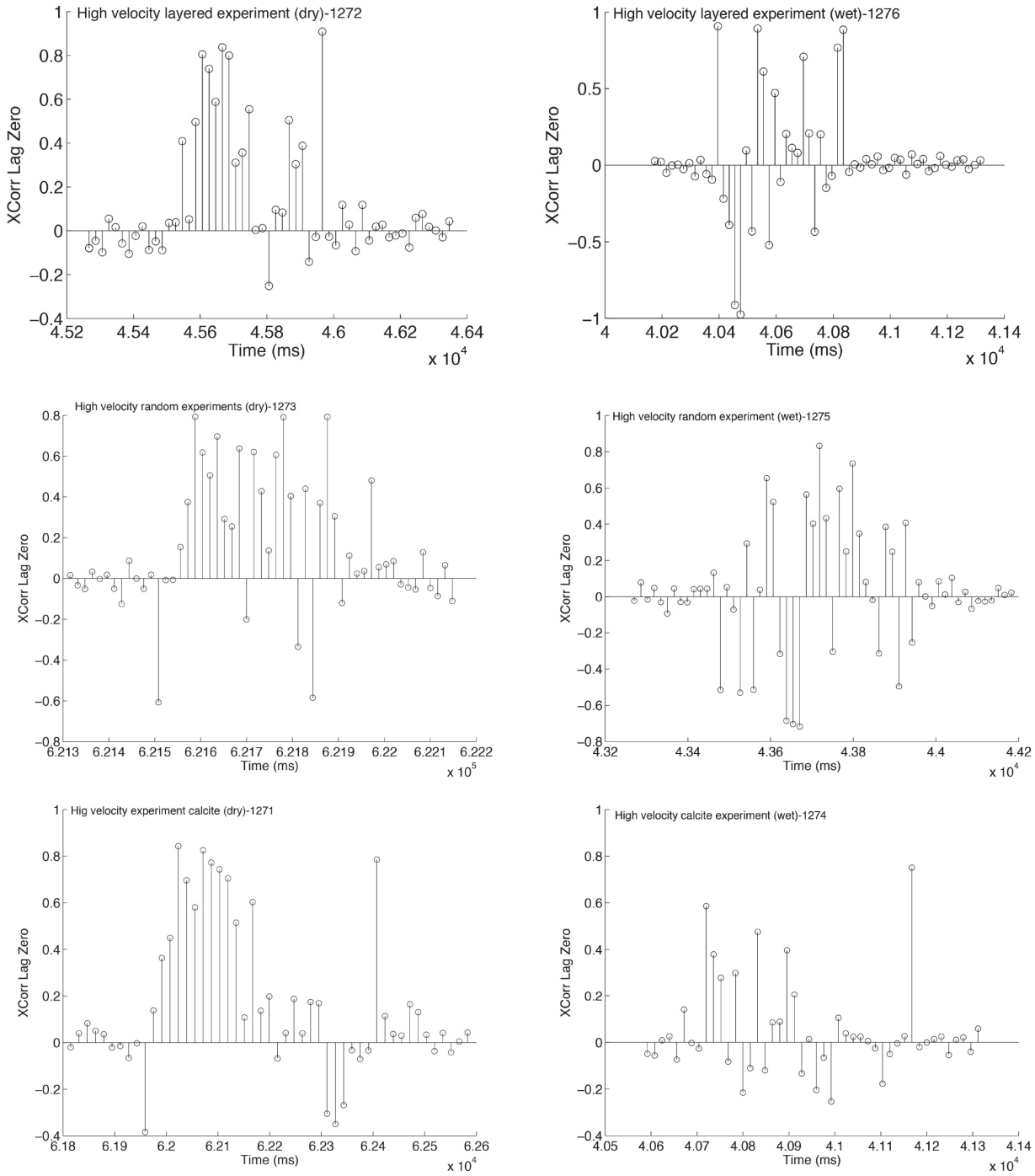


Figure S2. Evolution of cross-correlation (Lag0) coefficient during high velocity experiments both in dry (left column) and wet (right column) conditions for the new experiments. High velocity dry experiments show a positive correlation roughly during all the experiments indicating an in-phase oscillation between normal and shear stress. On the contrary, high velocity wet experiments show a negative correlation roughly during the central part of the experiment (i.e., the weakening phase) indicating an increase of normal stress during a decrease in shear stress (i.e., out of phase oscillation).

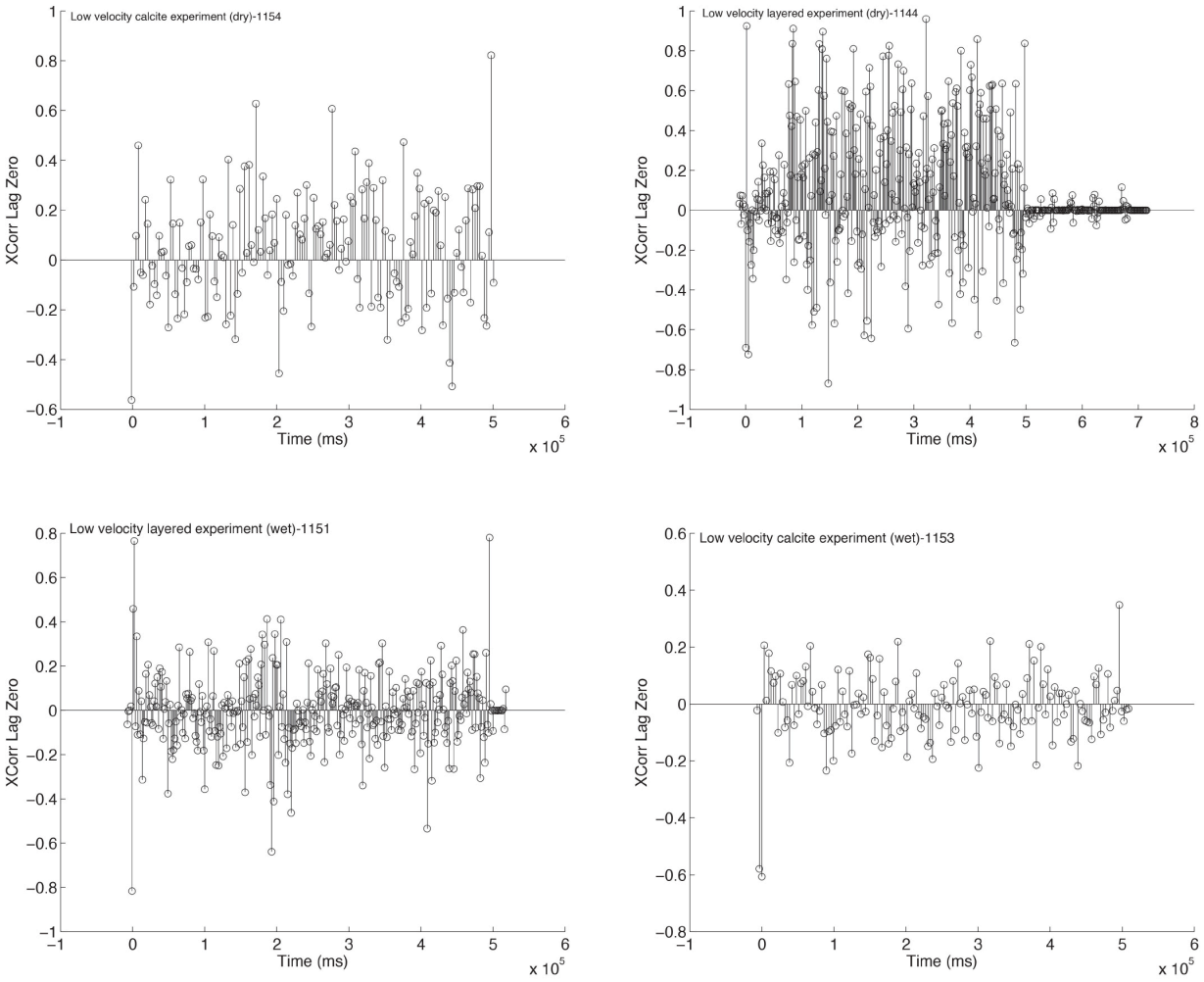


Figure S3. Evolution of cross-correlation (Lag0) coefficient during low velocity experiments showing positive to negative cross-correlation coefficient oscillations. This indicates an alternation of in-phase and out of phase normal stress and shear stress oscillation.

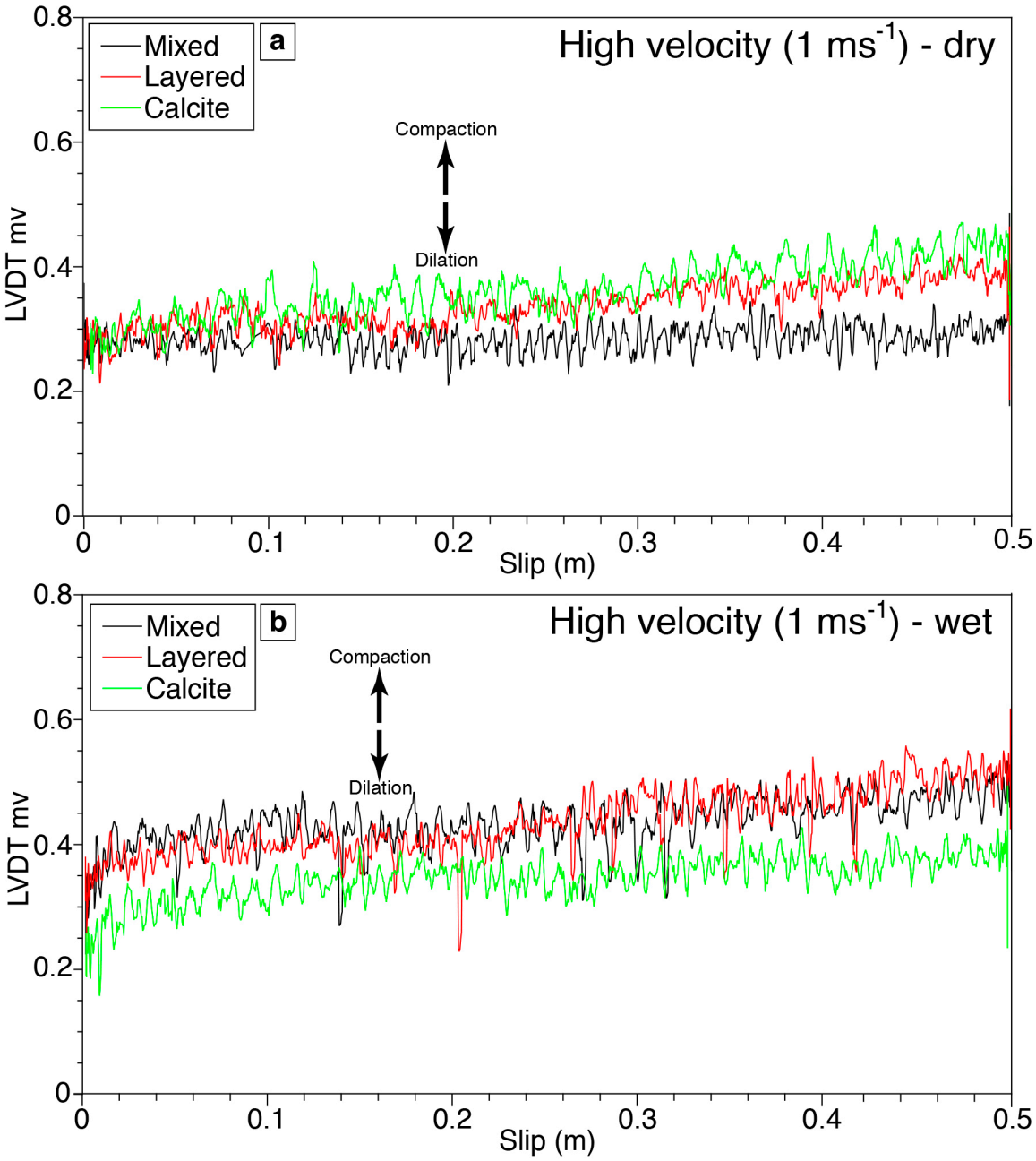


Figure S4. Gouge dilatancy/compaction vs. slip during high velocity experiments both in dry **(a)** and wet **(b)** conditions. During all the experiments gouges show small compaction also due to slight gouge extrusion during tests.

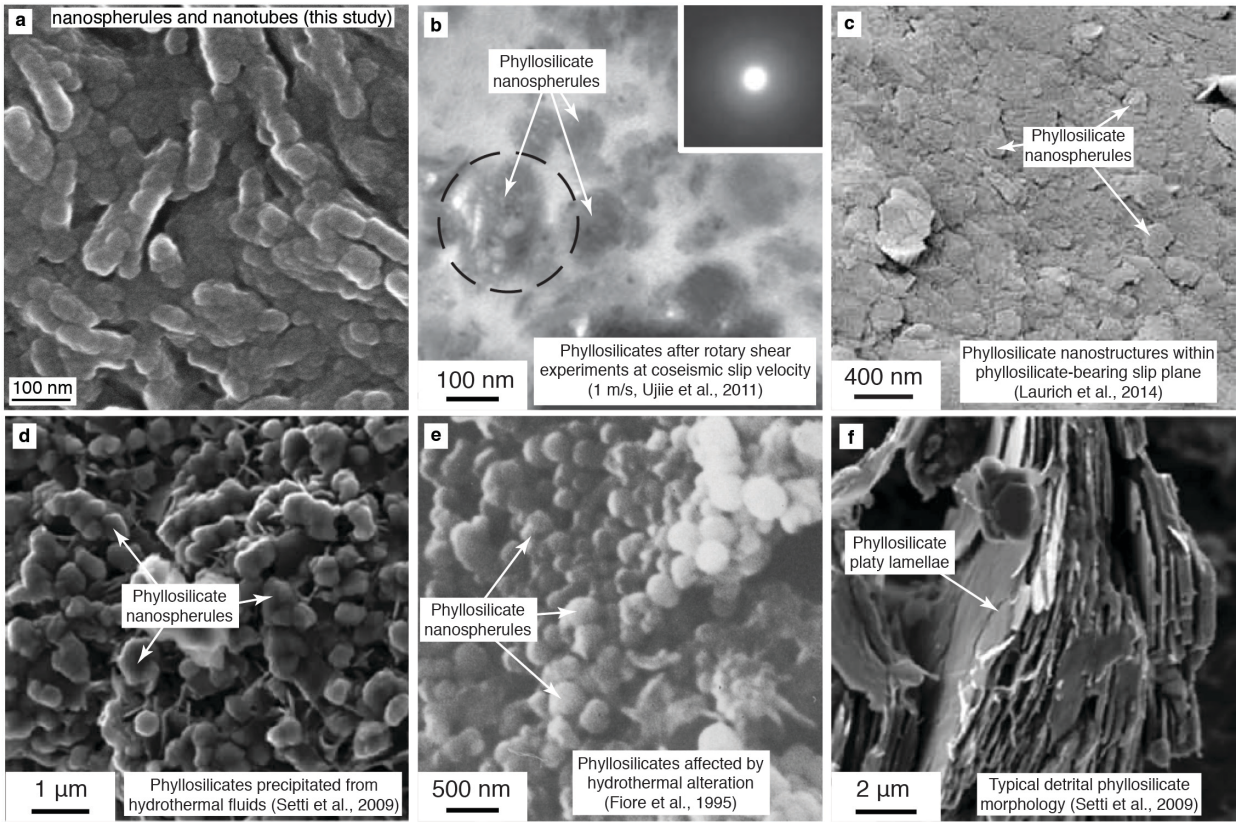


Figure S5. Figure of comparison between phyllosilicate nanostructures from the Tre Monti Principal fault and from other studies. **(a)** FESEM (Zeiss Auriga) image of phyllosilicate nanostructures from the phyllosilicate-bearing layers (Tre Monti Principal fault) characterized by clumped aggregates of nanospherules (~50 nm in size) and nanotubes (up to a few hundreds of nm long). **(b)** Tem image (modified after Ujiie et al., 2011) of phyllosilicate nanostructures after rotary shear experiments at coseismic slip velocity (1 ms^{-1}) and temperatures up to ~570 °C showing phyllosilicate nanospherules. **(c)** SEM image of aggregated phyllosilicate nanospherules within phyllosilicate-bearing fault plane (modified after Laurich et al., 2014). **(d, e)** SEM images of aggregates of phyllosilicate nanospherules after precipitation from (d) and alteration by (e) hydrothermal fluids at up to ~250 °C (modified after Fiore et al., 1995 and Setti et al., 2009). **(f)** SEM image showing clumped platy phyllosilicate lamellae typical of detrital and/or authigenic phyllosilicates (modified after Setti et al., 2009).

General conclusions and future perspectives

In many seismically-active regions earthquakes nucleate in and upward propagate through shallow fault zones cutting carbonate to clayey sedimentary successions. Therefore, structures, mechanics, and fluid circulations within carbonate/clay-hosted faults can significantly affect the mechanics of earthquakes and seismic cycles. In this thesis, I used a multidisciplinary approach combining (I) detailed geological mapping and structural analyses of exhumed carbonate/clay-hosted seismogenic faults, (II) microstructural and mineralogical investigations of fault rocks, (III) stable isotope geochemistry of fault-related calcite mineralizations, (IV) in situ mechanical analyses of natural fault rocks, (V) rock deformation experiments under conditions similar to those of earthquake-slip propagation. This multidisciplinary approach allowed me to identify fault zone evolution, fluid circulation, and mechanical behavior of carbonate/clay-hosted seismogenic faults from the central Apennines, Italy. In synthesis, I conclude that:

1) phyllosilicate-rich layers (e.g., Pietrasecca 1 and 2 faults and Fiamignano Fault) can occur along carbonate-hosted fault planes and are originated by downward injection of clay into carbonate-hosted pull-aparts coupled with smearing along fault surfaces. These phyllosilicates mainly derived from above-lying phyllosilicate-rich deposits within the sedimentary succession. These observations imply that, in extensional tectonic settings dominated by high friction lithologies (e.g., carbonate rocks), the occurrence of localized layers rich in weak phyllosilicates along seismogenic faults at depth can be a regionally important control on co-seismic slip propagation up to the Earth's surface with strong implications on seismic hazard;

2) fluid circulation within carbonate/clay hosted faults is characterized by a shift from connate (marine-derived) to meteoric fluid circulation during exhumation from 3 to $\leq$ 1 km depths and concurrent fluid cooling from ~68 to < 30 °C. Microstructural evidence show that the role of these fluids during syn-exhumation seismic cycles has been substantially passive along the whole fault zone, the fluids being passively redistributed at hydrostatic pressure following co-seismic dilatancy. Only the principal fault shows evidence of local and transient fluid overpressures;

3) ultra-thin phyllosilicate-bearing layers with an illite/smectite content as low as 3 wt.% weaken faster than calcite and mixed calcite-phyllosilicate gouges at seismic slip rates (1 ms^{-1}) and can be responsible for fault weakening within carbonate-hosted faults, thus facilitating co-seismic slip propagation up to the Earth's surface in continental domains characterized by high friction rocks (e.g., carbonates). I propose that the 3 wt.% of clay concentrated in ultra-thin layers could be the lower boundary for facilitating dynamic weakening during earthquake slip at shallow crustal levels;

4) fault rock microstructures and micromechanical properties can be strongly correlated with seismological observations. In particular, fluidized fault rocks are consistent with seismologically inferred fluid overpressure at hypocentral depths. Clay assisted intergranular pressure solution and foliation planes can explain fault healing and re-strengthening (i.e., fault locking and elastic strain energy accumulation) and aseismic sliding (i.e., elastic strain energy dissipation), respectively. Moreover, strong rheological contrasts, at the nanoscale, due to the occurrence of little amount of phyllosilicates within fault rocks, can strongly modulate the bulk mechanical and seismic behavior of faults, affecting both earthquake-slip and deformation mechanism distributions.

My final intent in this thesis was to point out how such a multidisciplinary study (i.e., integrating field and laboratory observations) can contribute to a better comprehension of fault zone architecture and deformation mechanisms relevant for earthquake mechanics and seismic cycles. Moreover, I emphasize the use of direct in situ studies of fault rock friction (i.e., low- to high-velocity friction experiments) and mechanical properties (i.e., through Atomic Force Microscopy measurements) as new and fundamental instruments to obtain natural parameters to be used in the near future for seismic cycle modeling. In particular, earthquake-slip distribution, stress drop, and fault friction are intimately correlated with fault rock mechanical and rheological properties. Although indirect estimations or assumptions of these parameters are fundamental to model short- to long-term fault mechanical behaviors, I strongly believe that in situ (i.e., studying exhumed seismogenic faults) micromeasurements of such parameters can significantly advance our

knowledge of earthquakes and seismic cycles. Future perspectives concerning earthquake models must be complemented by geological studies and in situ rheological parameter measurements within exhumed fault zones, which can represents analogues of seismogenic faults at depth.

Ringraziamenti

Alla fine di questi tre anni di dottorato ci tengo a ringraziare tutte le persone che hanno reso possibile questo lavoro, sia umanamente sia scientificamente, senza di loro tutto ciò sarebbe stato impossibile.

Grazie a Eugenio e Andrea che in questi tre anni, ma anche prima, mi hanno sempre sostenuto e aiutato, anche con consigli e suggerimenti che vanno al di là degli aspetti puramente scientifici. Grazie per aver creduto in me, per la pazienza e per non avermi mai fatto mancare il vostro supporto! Grazie a Carlo, con il quale ho iniziato questa ricerca, ed è sempre stato presente con consigli fondamentali e con il suo supporto.

Grazie a tutte le persone che hanno contribuito alla raccolta dei dati di questa tesi: Andrea Cavallo, Elena Nazzari e Piergiorgio Scarlato (FESEM e microsonda, INGV), Giulio Di Toro, Elena Spagnuolo, Li-Wei Kuo e Stefano Aretusini (per gli esperimenti con SHIVA, INGV), Luca Aldega, Federico Zorzi e Stefano Stellino (per le analisi ed interpretazione dei dati diffrattometrici), Fabrizio Berra (catodoluminescenza), Chiara Boschi, Simone Vezzoni e Ilaria Baneschi (isotopi stabili), Sabrina Sarto e Francesco Mura (FESEM), Marco Rossi, Daniele Passeri, Marco Natali, e Andrea Bettucci (Forza Atomica ed analisi ad ultrasuoni), Alessio Fazioli (rilievi di terreno).

Un grazie speciale a Domenico Mannetta per le decine e decine di sezioni sottili preparate. Grazie per l'infinita pazienza e disponibilità, il tuo lavoro è stato fondamentale!

Grazie a tutte le persone con le quali ho avuto modo di condividere la mia ricerca e che mi hanno fornito molti consigli utili: Marco Brandano, Gian Paolo Cavinato, Cristiano Collettini, Irene Cornacchia, Domenico Cosentino, Michele Fondriest, Carolina Giorgetti, Li-Wei Kuo, Silvio Mollo, François Passelegue, Steve Smith, Stefano Tavani, Telemaco Tesei, Fabio Trippetta.

Un grazie speciale va alla mia famiglia e alla mia fidanzata che nonostante tutte le difficoltà mi sono stati sempre vicino non facendomi mancare mai nulla per cercare di vivere "serenamente" questi tre anni.

Grazie a tutti i miei amici, vicini e lontani, e a quelli che mi hanno accompagnato varie volte sul terreno.